OVERCOMING GLIOBLASTOMA INTRACTABILITY: PRE-CLINICAL CHARACTERISATION OF TRAIL SENSITISATION BY MARIZOMIB AND NOVEL TREATMENT PERSPECTIVES

Von der Fakultät Energie-, Verfahrens- und Biotechnik
der Universität Stuttgart

zur Erlangung der Würde eines
Doktors der Naturwissenschaften (Dr. rer. nat.) genehmigte Abhandlung

Vorgelegt von

Chiara Boccellato

aus Marino Laziale (Rom)

Hauptberichter: Prof. Dr. Markus Morrison

Mitberichter: Prof. Dr. Jörn Lausen

Tag der mündlichen Prüfung: 22.02.2022

Institut für Zellbiologie und Immunologie der Universität Stuttgart

2022

Universität
Stuttgart

OVERCOMING GLIOBLASTOMA INTRACTABILITY:

PRE-CLINICAL CHARACTERISATION OF TRAIL SENSITISATION BY MARIZOMIB AND NOVEL TREATMENT PERSPECTIVES

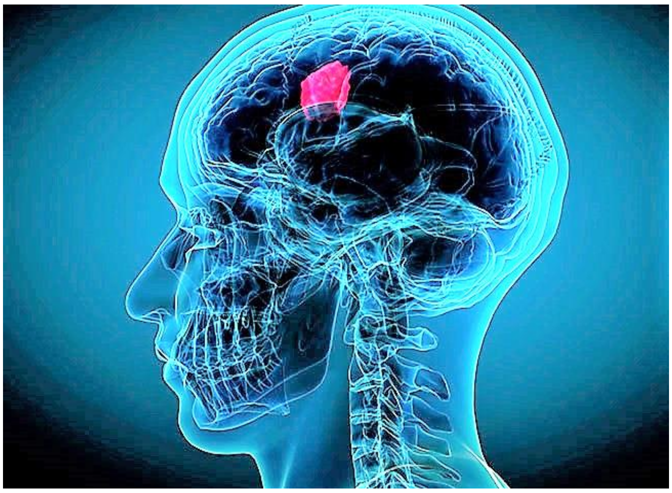

PhD Dissertation

Chiara Boccellato

2022

“*Attitudes are more important than abilities,*
Motives are more important than methods,
Character is more important than cleverness
And the heart takes precedence over the head”
Denis Parsons Burkitt

This work is dedicated to my beloved grandmother Eleonora,
the proud warrior who taught me never to give up.

Table of contents

Table of contents

Declaration/Erklärung

Declaration

I, Chiara Boccellato, hereby declare that I have independently prepared and written this thesis entitled "Overcoming glioblastoma intractability: pre-clinical characterisation of TRAIL sensitisation by marizomib and novel treatment perspectives" and have written it independently. Only the indicated aids were used. All information taken verbatim or in the sense of other works are marked with the source, as are the contributions by other persons. The thesis has not yet been published in this form or presented elsewhere as a doctoral dissertation.

Erklärung

Hiermit versichere ich, Chiara Boccellato, diese Arbeit mit dem Titel "Overcoming glioblastoma intractability: pre-clinical characterisation of TRAIL sensitisation by marizomib and novel treatment perspectives" eigenständig angefertigt und verfasst zu haben. Es wurden nur die angegebenen Hilfsmittel verwendet. Alle Angaben, die wörtlich oder sinngemäß anderen Werken entnommen wurden, sind unter Angabe der Quelle kenntlich gemacht, wie auch Beiträge anderer Personen. Die Arbeit ist in dieser Form noch nicht veröffentlicht oder in anderweitig als Promotionsleistung vorgelegt worden.

Chiara Boccellato

Publications, conferences, secondments

Publications

(on which parts of this thesis are based)

- **Boccellato, C**., and Rehm, M. TRAIL-induced apoptosis signalling and its modulation by proteasome inhibition (*In preparation*).
- **Boccellato, C**., and Rehm, M. Glioblastoma, from disease understanding towards optimal cell-based in vitro models. *Cellular Oncology* (2022).
- **Boccellato, C.**, Kolbe, E., Peters, N., Juric, V., Fullstone, G., Verreault, M., Idbaih, A., Lamfers, M. L. M., Murphy, B. M., Rehm, M. Marizomib sensitizes primary glioma cells to apoptosis induced by a latest-generation TRAIL receptor agonist. *Cell Death & Disease* **12**, 647 (2021).
- Lincoln, F.A., Imig, D., **Boccellato, C.**, Juric, V., Noonan, J., Kontermann, R.E., Allgöwer, F., Murphy, B.M., Rehm, M. Sensitization of glioblastoma cells to TRAIL-induced apoptosis by IAP- and Bcl-2 antagonism. *Cell Death & Disease* **9**, 1112 (2018).

Conferences and Workshops

- 15th European Association of Neuro-Oncology (EANO) annual meeting, Glasgow, United Kingdom. September 2020 - Poster presentation. *Cancelled due to COVID-19 pandemic.*
- 12th European Workshop on Cell Death (EWCD), Fiuggi, Italy. April 2020 - Oral presentation. *Cancelled due to COVID-19 pandemic.*
- 27th Conference of the European Cell Death Organization (ECDO), Dresden, Germany. September 2019 - Poster presentation.
- 13th PhD Workshop on Molecular Mechanisms and Therapeutic Approaches in Cancer, Feldberg, Germany. September 2019 - Oral presentation.

Secondments

- Royal College of Surgeons in Ireland (RCSI), Dublin, Ireland. Group: Dr. Brona M. Murphy. April - June 2019.
- Erasmus Medical Center (EMC), Rotterdam, Netherlands. Group: Dr. Martine L.M. Lamfers. February 2018.

List of abbreviations

2D	two dimensional
3D	three dimensional
ABC	ATP-binding cassette
ACD	accidental cell death
AML	acute myeloid leukemia
APAF-1	apoptotic protease activating factor 1
ATCC	american type culture collection
ATF	activating transcription factor
ATP	adenosine triphosphate
BAD	Bcl-2 associated agonist of cell death
BAK	Bcl-2 homologous antagonist/killer
BAX	Bcl-2-associated X protein
BBB	Blood-Brain Barrier
Bcl-2	B-cell lymphoma 2
Bcl-xL	B-cell lymphoma-extra large
BCRP	breast cancer resistance protein
bFGF	fibroblast growth factor beta
BH3	Bcl-2 homology 3
BID	BH3-interacting domain death agonist
BIM	Bcl2-interacting mediator of cell death
BIR	baculovirus IAP repeat
BME	basement membrane extract
BSA	bovine serum albumin
BTZ	bortezomib
CAD	caspase-activated Dnase
CARD	caspase activation and recruitment domain
CDK	cyclin-dependent kinase
c-FLIP	cellular FLICE-like inhibitory protein
CHOP	C/EBP homologous protein
CI	combination index
cIAP	cellular inhibitor of apoptosis protein
C-L	caspase-like
CLL	chronic lymphocytic leukemia
CNS	central nervous system
CO_2	carbon dioxide
COX	cyclooxygenase
CP	catalytic (core) particle
CT-L	chymotrypsin-like
Da	dalton
DAMPs	damage-associated molecular patterns
DCs	dendritic cells
DD	death domain
ddH_2O	double-distilled water
DED	death effector domain
DFO	deferoxamine
DIABLO	direct inhibitor of apoptosis binding protein with low pI
DISC	death-inducing signalling complex
DMEM	dulbecco's modified eagle medium
DMSO	dimethyl sulfoxide
DNA	deoxyribonucleic acid
DR	death receptor
DTT	dithiothreitol
DUB	deubiquitinating enzymes
ECM	extra cellular matrix
EDTA	ethylenediaminetetraacetic acid
EGF	epidermal growth factor
EGFR	epidermal growth factor receptors
EGTA	ethylene glycol tetraacetic acid
EMA	european medicines agency
EMC	erasmus medical center

List of abbreviations

EMT	epithelial–mesenchymal transition
erastin	eradicator of RAS and ST-expressing cells
ERK	extracellular signal-regulated kinase
ER	endoplasmic reticulum
FADD	Fas-associated death domain protein
FBS	fetal bovine serum
Fc	fragment crystallizable region
FcRn	neonatal Fc receptor for IgG
FDA	food and drug administration
Fer-1	ferrostatin-1
FITC	fluorescein isothiocyanate
g	gravitational force
GBM	glioblastoma (multiforme)
GFP	green fluorescent protein
GPX	glutathione peroxidase
GSC	glioma stem cell
GSH	glutathione
Gy	gray unit
HeLa	henrietta lacks
I.V	intravenous
IAP	inhibitor of apoptosis
IC_{50}	half-maximal inhibitory concentration
ICM	institut du cerveau et de la moelle épinière
IDH	isocitrate dehydrogenase
IFN	interferon
IKK	IκB kinase
ISR	integrated stress response
IZI	institute for cell biology and immunology
JNK	c-Jun N-terminal kinase
LOX	lipoxygenase
LPCAT	lysophosphatidylcholine acyltransferase
LPS	lipopolysaccharides
LUBAC	linear ubiquitin chain assembly complex
Mcl-1	myeloid cell leukemia 1
MDM2	mouse double minute 2
MDMX	murine double minute X
MEK	mitogen-activated ERK kinase
MGMT	O6-methylguanine-DNA methyltransferase
MHC	major histocompatibility complex
MLKL	mixed lineage kinase domain like pseudokinase
MM	multiple myeloma
MMP	mitochondrial membrane potential
MOMP	mitochondrial outer membrane permeabilization
MRP	multidrug resistance protein
MRZ	marizomib
NAD(P)H	nicotinamide adenine dinucleotide phosphate
NCCD	nomenclature committee on cell death
NEMO	NF-κB essential modulator
NFR2	nuclear factor erythroid 2-related factor 2
NF-κB	nuclear factor 'kappa-light-chain-enhancer' of activated B-cells
NK	natural killer
NS	neurosphere
NSCLC	non-small cell lung cancer
NTRK	neurotrophic tyrosine receptor kinase
OPG	osteoprotegerin
OS	overall survival
OVs	oncolytic viruses
PARP	poly (ADP-ribose) polymerase
PBS	phosphate buffered saline
PC	phosphatidylcholine
PDAC	pancreatic ductal adenocarcinoma
PDCLs	patient derived cell lines
PEI	polyethylenimine
PFS	progression-free survival
P-gp	P-glycoprotein
PI	propidium iodide
PIs	proteasome inhibitors

PL	phospholipids
PTEN	phosphatase and tensin homolog
PUFA	polyunsaturated fatty acids
PUMA	p53 upregulated modulator of apoptosis
Q-VD-OPh	quinoline-val-asp-difluoro phenoxymethylketone
RAF	rapidly accelerated fibrosarcoma
RAS	rat sarcoma
RCD	regulated cell death
rcf	relative centrifugal force
RCSI	royal college of surgeons in ireland
rhTRAIL	recombinant human TRAIL
RING	really interesting new gene
RIP-1	receptor-interacting serine/threonine-protein kinase 1
RIP-3	receptor-interacting serine/threonine-protein kinase 3
RNA	ribonucleic acid
ROS	reactive oxygen species
RPMI	roswell park memorial institute
RSL	RAS-selective lethal
RT	room temperature
scTRAIL	single chain TRAIL
SDS-PAGE	sodium dodecyl sulphate–polyacrylamide gel electrophoresis
SD	standard deviation
SEM	standard error of mean
SLC7A11	solute carrier family 7, member 11
Smac	second mitochondria-derived activator of caspases
tBID	truncated BID
TBS	tris-buffered saline
TERT	telomerase reverse transcriptase
TFRC1	transferrin receptor 1
TIC	tumour initiating cell
T-L	trypsin-like
TMZ	temozolomide
TNBC	triple negative breast cancer
TNF	tumor necrosis factor
TNF-R	tumor necrosis factor receptor
TP53	tumor protein 53
TRAF	TNF receptor-associated factor
TRAIL	tumor necrosis factor related apoptosis inducing ligand
TRAIL-R	TRAIL receptor
UBA	ubiquitin-associated
UPS	ubiquitin-proteasome system
VDAC	voltage-dependent anion channel
VEGF	vascular endothelial growth factor
WBL	whole-blood lysates
WEHI-539	walter and eliza hall institute-539
WHO	world health organisation
Wnt	wingless-related integration site
XIAP	X-linked inhibitor of apoptosis protein

List of figures

Lists of tables and equations

Abstract

Glioblastoma (GBM) is the most aggressive cancer of the central nervous system (CNS). Surgical resection, adjuvant temozolomide-based chemotherapy and radiation are the primary treatments, yet the outcome of GBM patients remains poor with a median life expectancy of 15 to 17 months. Therefore, novel and effective treatment options are required, as are reliable pre-clinical experimental models that are suitable for exploratory studies on novel drugs and drug combinations.

In this work, patient-derived cell line models (PDCL), generated from fresh primary or recurrent glioblastoma tumours, have been examined to assess prevalence of responsiveness to a highly stable hexavalent format of TRAIL receptor agonist (IZI1551) and to the blood brain barrier (BBB)-permeant proteasome inhibitor marizomib (MRZ). Serum-free medium and limited cultivation times of both 2D and 3D cancer cell cultures were adopted to maintain the characteristics of primary tumour cells. The degree of BBB permeability of marizomib was evaluated in the human hCMEC/D3 cell line model, which was also employed to test the efficacy of the IZI1551+MRZ combination in pre-clinical settings.

It was found that IZI1551 and marizomib acted synergistically to induce apoptosis in the majority of low-passage PDCLs, both under 2D and 3D cultivation conditions. Altering the relative timing of drug exposure, specifically marizomib pre-treatment, led to even enhanced responses and allowed to lower drug concentrations without losing treatment efficacy. Importantly, the amount of marizomib that can cross the simple BBB model was sufficient to confer sensitisation to IZI1551. In cases of treatment resistance against IZI1551 and marizomib, lowering the mitochondrial apoptosis threshold with BH3 mimetics appeared sufficient to restore apoptosis sensitivity.

Taken together, these results demonstrated that marizomib is a potent sensitiser of apoptosis induced by a 2nd generation TRAIL receptor agonist in glioblastoma. The optimized synergism between marizomib and IZI1551 in time-shifted treatment schedules, together with the ability of marizomib to cross the BBB, suggests this combination as a promising strategy to be tested in clinical settings.

In the second part of this work, an alternative cell death pathway, namely ferroptosis, has been investigated as a strategy to bypass the obstacle of the apoptosis refractory state of highly resistant cancers such as glioblastoma.

Ferroptosis is a recently identified form of iron-dependent regulated cell death that presents distinct features compared to apoptosis and that is characterised by the accumulation of toxic lipid peroxides.

Here it was shown that the U-87 MG, a *bona-fide* glioblastoma cell line that was reported to be TRAIL resistant, displays a dose-dependent cell death response to the ferroptosis inducer RSL3. Surprisingly, it was found that BH3 mimetics antagonised this cytotoxicity. The unexpected consequences of combining these agents highlight the need to better understand the interactions between these drugs in order to advance their use as cancer therapeutics.

Overall, this thesis presents diverse treatment options against glioblastoma that exploit either drugs classically inducing apoptosis or the alternative cell death modality of ferroptosis. Considering the limited availability of approved treatments, studies aiming at expanding the choice of glioblastoma therapeutics, such as those conducted in this work, are of particular importance and pave the way for their implementation at a clinical and pre-clinical level.

Zusammenfassung

Das Glioblastom (GBM) ist die aggressivste Krebsart des zentralen Nervensystems und chirurgische Resektion, adjuvante Chemotherapie auf Temozolomid-Basis sowie Bestrahlung sind die primären Behandlungsmethoden. Leider ist die Prognose von Glioblastom-Patienten, mit einem durchschnittlichen medianen Überleben von 15 bis 17 Monaten, trotzdem nach wie vor sehr schlecht. Deshalb ist es von größter Wichtigkeit, bessere Behandlungsmöglichkeiten in Form neuer Medikamente oder Medikamentenkombinationen zu erforschen. Um eine gute Übertragbarkeit der in vitro gewonnenen Erkenntnisse zu gewährleisten, ist es außerdem unerlässlich mit zuverlässigen vorklinischen Versuchsmodellen zu arbeiten.

In dieser Studie wurden deshalb Zelllinien verwendet, die aus frischen primären oder rezidivierenden Tumoren von Glioblastom-Patienten stammten. An diesem Modell wurde dann die Wirksamkeit einer Kombinationstherapie aus einem neuartigen hexavalenten TRAIL-Rezeptor Agonisten (IZI1551) und einem, für die Blut-Hirn-Schranke (BHS) durchlässigen Proteasom-Inhibitor, marizomib (MRZ), getestet. Um die Eigenschaften der primären Tumorzellen zu erhalten, wurde hierbei sowohl für 2D- als auch für 3D-Zellkulturen serumfreies Medium eingesetzt und relativ kurze Kultivierungszeiten eingehalten. Die Fähigkeit von marizomib die BHS zu passieren, wurde außerdem in einem Modell aus menschlichen hCMEC/D3-Zellen verifiziert. Dieses Modell wurde im Anschluss auch dazu verwendet, die Kombinationstherapie aus IZI1551 und marizomib weiterführend zu untersuchen.

Es zeigte sich, dass IZI1551 in Kombination mit marizomib, sowohl unter 2D- als auch unter 3D-Kultivierungsbedingungen, synergistisch Apoptose in der Mehrzahl der untersuchten, kurzzeitig-kultivierten Glioblastom Zelllinien auslöste. Die Änderung des relativen Zeitpunkts der Medikamentenexposition, genauer gesagt die Vorbehandlung mit marizomib, führte zu einer noch stärkeren Sensitivierung und ermöglichte es, insgesamt niedrigere Medikamentenkonzentrationen zu verwenden ohne dass dies die Wirksamkeit der Kombinationsbehandlung beeinträchtigte. Dabei hervorzuheben ist, dass die Menge an marizomib, die die BHS im Modellversuch überwinden konnte, ausreichte, um die Krebszellen gegenüber IZI1551-induzierter Apoptose zu sensitiveren. In den wenigen Glioblastom-Zelllinien, die sich als resistent gegenüber der Kombinationstherapie herausstellten, konnte durch eine Behandlung mit BH3 Mimetika, kleiner Moleküle die zu einer schnelleren Permeabilisierung der Mitochondrien führen, eine Resensitivierung der Krebszellen erreicht werden.

Zusammenfassend lässt sich sagen, dass marizomib ein potenter Sensibilisator für die durch TRAIL-Rezeptor-Agonisten ausgelöste Apoptose in Glioblastom ist. Der optimierte zytotoxische Effekt von marizomib und IZI1551 in zeitlich versetzten Behandlungsschemata sowie die Fähigkeit von marizomib, die BHS zu überwinden, lässt diese Kombinationstherapie sehr vielversprechend für Untersuchungen in der klinischen Praxis erscheinen.

Im zweiten Teil dieser Arbeit wurde untersucht, ob in Apoptose-resistenten Glioblastom-Zelllinien ein alternativer Zelltodweg, nämlich Ferroptose, ausgelöst werden kann. Ferroptose ist eine erst kürzlich identifizierte Form eines eisenabhängigen regulierten Zelltods, die sich von Apoptose unterscheidet und durch die Anhäufung toxischer Lipidperoxide gekennzeichnet ist.

Es konnte hierbei gezeigt werden, dass der Ferroptose-auslösende Stoff RSL3 zytotoxisch auf eine klassische, TRAIL-resistente Glioblastom-Zelllinie, U-87 MG, wirkte. Überraschenderweise wurde des Weiteren festgestellt, dass BH3-Mimetika diese Zytotoxizität antagonisieren. Die unerwarteten Folgen der Kombination dieser Wirkstoffe machen deutlich, dass es notwendig ist, Wechselwirkungen zwischen diesen Medikamenten besser zu verstehen, um ihren Einsatz als Krebstherapeutika voran zu treiben.

Insgesamt werden in dieser Arbeit verschiedene Behandlungsmöglichkeiten gegen Glioblastom vorgestellt, welche entweder klassisch Apoptose, oder den erst kürzlich beschriebenen Zelltodweg, Ferroptose, in den Krebszellen auslösen. In Anbetracht der begrenzten Verfügbarkeit zugelassener Behandlungen sind Studien wie diese, die darauf abzielen, die Auswahl an Glioblastom-Therapeutika zu erweitern, von höchster Wichtigkeit da sie den Weg für die Untersuchung dieser Medikamente in klinischen Studien ebnen.

Introduction

1. Glioblastoma (GBM)

1.1 GBM epidemiology and classification

Glioblastoma is the most common form of primary malignancy of the central nervous system (CNS) in adults. It was described in 1863 by the German pathologist Dr. Rudolf Virchow [1], who identified it as is a form of glioma. Gliomas are tumours arising from glial or precursor cells and comprise astrocytomas - with glioblastoma being one of them -, oligodendrogliomas, ependymomas, oligoastrocytoma and a few other rare histologies. Although considered a rare tumour, with an incidence rate of less than 5 cases per 100,000 people, glioblastoma accounts for 14.5% of all brain and CNS tumours and for 48.6% of the malignant ones. According to recent statistics of the central brain tumour registry of the United States (CBTRUS; data for 2014-2018) it affects men more than women, the median age at diagnosis being 65 and the five-years survival rate being of approximately 6.8% depending on patients' characteristics and tumour histology [2].

Glioblastoma is mostly found in cerebral hemispheres, especially in the frontal and temporal lobes, while only a few percent occurs in the cerebellum, brainstem and spinal cord [3]. Its infiltrative properties are long known and difficulties in identifying a discrete border zone between the tumour and the normal brain parenchyma were already reported in 1928 [4]. Depending on the functional role of the area of the brain affected, clinical presentations include persistent weakness, numbness, loss of vision or alteration of the language. Headache is a very common initial symptom while seizure only occurs in approximately 25% of patients [5].

The aetiology of this tumour type is still obscure. Only 20% of glioblastoma patients have a family history of cancer and susceptibility genes have not been clearly identified yet [6]. However, some familial cases have been found to be associated with rare genetic syndromes like Li-Fraumeni syndrome and neurofibromatosis of types 1 and 2 [7]. Among all the risk factors analysed, only high doses of ionizing radiation have been confirmed as such, while no association was ever proved with lifestyles that include alcohol or drug consumption, cigarettes smoking or specific diets [8,9].

The term glioblastoma was used for the first time in 1927 by the neuropathologist Dr. Percival Bailey and the neurosurgeon Dr. Harvey Cushing, who have provided the first systematic classification and histological description of gliomas [10]. Since then, several updates on more appropriate classification and nomenclature systems followed. Most recently, in 2021, the world health organisation (WHO) revised the classification of CNS tumours (WHO CNS5) by including molecular parameters in addition to histological features for the definition of diagnostic categories and a grading system [11]. Of note, the nomenclature was already revised in the fourth edition of the WHO Classification of Tumours of the Central Nervous System and the term “multiforme” was abolished, even though the abbreviation “GBM” is still widely used and will also be utilized in this thesis [12]. Based on the WHO CNS5 classification, a mutated IDH gene now separates astrocytomas (specifically astrocytoma, IDH-mutant of CNS WHO grade 4) from glioblastomas. IDH1 is a protein found in the cytoplasm, peroxisomes and endoplasmic reticulum and its function is to catalyse the oxidative decarboxylation of isocitrate to α-ketoglutarate. IDH2 has a function similar to IDH1, but it is found in the mitochondria. In contrast to IDH mutated astrocytoma, glioblastomas are defined as an adult-type of diffuse astrocytic tumours displaying a wild-type status of the IDH gene (Glioblastoma, IDH-wildtype) and assigned to CNS WHO grade 4. More precisely, in the setting of an IDH-wildtype diffuse and astrocytic glioma in adults, a glioblastoma is diagnosed if microvascular proliferation or necrosis, TERT promoter mutation, EGFR gene amplification or a combined gain of the entire chromosome 7 and loss of the entire chromosome 10 [+7/−10] is observed.

1.2 The challenges of GBM treatment

The treatment of glioblastoma patients is extremely challenging. The difficulties in finding an effective therapy are mainly due to four reasons: its invasive properties, its heterogeneity, its rapid development of resistance to radio-chemotherapy, and the presence of the blood-brain barrier (BBB), which most drugs cannot cross.

Glioblastoma cells have the ability to infiltrate into normal brain tissue, penetrating the brain parenchyma and the perivascular space by degrading the extra cellular matrix (ECM). Due to their aggressive migrative behaviour, glioblastoma cells escape the complete surgical resection and therefore, the tumour usually re-occurs within a few centimetres from its original location [13,14]. Numerous studies have been conducted on glioblastoma invasiveness, trying to clarify patterns and directionalities as well as the mechanisms responsible for the invasive behaviour. For example, it was found that while certain brain regions are more frequently invaded by glioblastoma cells, others such as the hippocampus are normally spared [15]. The processes that allow glioblastoma cells to invade the surrounding tissue have been extensively studied and are reviewed elsewhere [16]. In general, they comprise peculiar cell-to-cell and cell-to-ECM adhesion mechanisms, ECM and cytoskeletal remodelling and epithelial-mesenchymal transition (EMT). Unfortunately, possibly due to the complex networks of the signalling pathways involved, this knowledge could not yet be translated into efficient therapeutic strategies in the clinic.

Introduction

Tumour heterogeneity encompasses both inter-tumour heterogeneity, which refers to the distinct genetic alterations and differing tumour architectures found among different patients, and intra-tumour heterogeneity, which refers to the diversity of cell-to-cell and tissue contexture within an individual tumour. Genome wide transcriptome analyses of high-grade gliomas has led to the classification of three subtypes that could be prognostically relevant [17–19]. These are referred to as proneural (PN), classic (Class), and mesenchymal (Mes) subtypes. An additional subtype, the so-called neural (Neu) subtype, has been removed from the classification as it could be traced by normal neural lineage contamination [20–22]. Treatment outcomes among individuals of the same tumour subtype are not homogeneous, likely due to the abovementioned heterogeneities. One caveat of the subtyping process is that classification must be based on the analysis of a specific site of the tumour from which a biopsy is taken. However, biopsies from different regions of the tumour of a patient can result in the assignment to a different molecular subtype [23,24]. Moreover, single-cell RNA analysis has shown that a patient tumours can comprise cells of all these three subtypes [25,26]. Recent spatial analyses of tumour heterogeneity revealed that the peripheral (vascular) portion of the tumour core preferentially expresses the proneural genes while the central core portion (hypoxic region) more frequently consists of cells that can be assigned to the mesenchymal subtype [27]. A more detailed description of the features of distinct regions of a glioblastoma tumor can be found in the anatomical atlas that was compiled in 2018 by Puchalski and colleagues, who integrated mutation and gene expression data obtained from morphologically distinct parts of the tumour [28]. Due to the pronounced intra-tumour heterogeneity, it is understandable that among the different sub-populations that coexist within a tumour some are spared from the treatment and can cause relapse. Hence, this adds another level of complexity to prognostication but at the same time exemplifies why interest in and understanding of intra-tumour heterogeneity continues to increase [29]. In an effort to categorize this complexity, interesting work has been conducted by N. Bergmann and colleagues [30]. Based on the immunoreactivity to nine relevant markers (AlDH1; CA-IX; EGFR; GFAP; MAP2; Mib1; Nestin; NeuN; Vimentin), they found that the different areas of a glioblastoma tumour could be clustered into five pathophysiological groups that reoccur throughout the tumour mass. Interestingly, the characteristic marker profile of these groups resembles that of the abovementioned glioblastoma subtypes (PN; Class and Mes), thereby offering means to bridge the divide between intra-tumour and inter-tumour heterogeneity classifications. Importantly, as the five groups do not exclude each other but rather co-exist in diverse regions of the same tumour, it needs to be noted that glioblastoma subtyping without spatial contexture can inappropriately homogenize the intra-tumour heterogeneity and will be dominated by tumour regions that are quantitatively predominant in the respective biopsies.

A common assumption was that the source of tumour heterogeneity could be ascribed to a population of cells referred to as cancer stem cells (CSCs), which thus became targets for the development of therapeutic strategies [31,32]. Glioma stem-like cells (GSCs) owe their name to the similarities with normal neural stem cells (NSCs) in terms of self-renewal properties, ability of differentiate into different cell types, expression of neurogenic markers like CD133, CD15 and Nestin and also transcriptional stemness factors including Sox2, Olig2, Nanog, and c-Myc [33–37]. By employing single-cell transcriptomics, A. Bhaduri and colleagues showed the existence of heterogeneous GSCs subtypes that coexist within a single tumour and among them they identified the outer radial glia (oRG) cells as an invasive population with a behaviour that is typically only observed during human development. Together with the presumed reactivation of developmental programs in these cells, they concluded that heterogeneous GSCs may be responsible for the aggressive invasive properties of glioblastoma [38]. However, as reviewed by J.N. Rich, both the definition of cancer stem cell itself and also how they give rise to tumour heterogeneity are still matters of debate [39]. The emergence of the concept of cellular plasticity implies a dynamic equilibrium between GSCs and differentiated non-GSCs, with a potential for non-GSCs to revert (dedifferentiate) to GSCs [40–42]. For example, it has been reported that conditions like hypoxia- or radiation-induced stress can promote dedifferentiation into a stem-like cell state [43–45]. That is why recent studies warn against the exclusive targeting of stem-like cell subpopulations, as these need to be considered “moving targets” with a state that adapts to changing microenvironments [46]. Instead, efforts are underway to better understand the plasticity of tumour cells and the mechanisms that influence their state transitions [47]. The process of these transitions, rather than aiming at the so-called stem cells, might indeed be promising targets for designing improved treatments to prevent tumour re-occurrence and repopulation.

Another feature that complicates the treatment of glioblastoma is the presence of the BBB. The BBB is a blood-to-brain interface that mechanically and biochemically segregates the brain from the parenchyma, strictly controlling the passage of substances in and out of the CNS. This physical separation is achieved by special brain capillary endothelial cells which do not have fenestrae and form a tight barrier that most polar, water-soluble molecules bigger than 450 Da cannot cross [48]. As such, the BBB also protects the CNS from harmful compounds or infections. Of note, the BBB endothelial cells express proteins of the ATP-binding cassette (ABC) superfamily that hydrolyse ATP to actively pump out substances against their concentration gradient. These integral membrane transporters can recognise a wide variety of substrates and thanks to such low specificity they carry out a crucial function in protecting the brain from diverse toxins. Unfortunately, since this can also impair the passage of therapeutics, ABC transporters can contribute to establishing drug resistance [49–51]. In fact, ABC transporters at the BBB, but also in tumour cells, are often highly expressed and enhance the multidrug resistance of glioblastoma [52–54]. For example, P-glycoproteins (P-gp), that are encoded by the ABCB1 (or MDR1) gene, typically recognise hydrophobic substrates, including traditional drugs used for the treatment of glioblastoma such as the alkylating agent carmustine and the standard of care temozolomide (TMZ) [55,56]. Many chemotherapeutics are also recognized by the breast-cancer resistance protein (BCRP), which is encoded by the ABCG2 gene. Interestingly, BCRP shares some substrate specificity with P-gp and with the multidrug resistance protein 1 (MRP1/ABCC1), a redundancy that has probably evolved to ensure protection also in case of mutations in any of these proteins [57,58]. In summary, these transporters play a crucial role in preventing therapeutics from reaching the brain and the target sites of the tumour.

1.3 GBM treatment options

GBM patients are notoriously difficult to treat and progress towards novel and improved treatment options is slow. Currently, the standard of care is still based on the Stupp protocol which more than fifteen years ago proved that the addition of concomitant and adjuvant TMZ to fractionated focal irradiation of 60 Gy improves overall survival from 12.1 to 14.6 months compared to radiotherapy alone [59]. TMZ exerts its cytotoxicity by transporting a methyl group that attaches to guanines at their O^6 position during the process of DNA replication. By this, an O^6-methylguanine (O^6-MG) is formed which then pairs with a thymine base nucleotide instead of a cytosine. Such a mismatched base pairing provokes DNA breaks, with consequent cell cycle arrest at the G_2/M transition of the cell cycle, followed by apoptotic cell death. Radiochemotherapy with TMZ, followed by six cycles of adjuvant TMZ and preceded by maximal safe surgery, is nowadays still the first line treatment for glioblastoma. Unfortunately, the survival benefit provided by TMZ is very modest and many patients do not respond at all to such treatment. Innate or acquired resistance to TMZ has been investigated comprehensively [60]. A follow-up report on the Stupp protocol study and also the more recent DIRECTOR trial on recurrent glioblastoma identified the methylation status of the promoter of the O^6-methylguanine-DNA methyltransferase (MGMT) gene as a positive prognostic marker of TMZ responsiveness [61,62]. MGMT is a DNA repair enzyme that removes alkyl and methyl adducts formed at the O^6 position of guanines, therefore antagonising the lethal effects of alkylating agents like TMZ. MGMT protein expression is under epigenetic control, meaning that the methylation of its promoter results in the silencing of the gene. As it was found that MGMT promoter methylation correlates with improved progression-free and overall survival in patients treated with alkylating agents, several studies have focused on trying to modulate the expression of this enzyme [63,64]. Interestingly, the methylation status of MGMT changes throughout the progression of the tumour, and can be affected by TMZ treatment itself [65,66]. In particular, it has been shown that tumours with an initial methylation of the MGMT promoter frequently reoccur with a decreased methylation if treated with TMZ [67,68].

The resistance to TMZ, together with the practical infeasibility of surgically removing the entire tumour mass, inevitably leads to relapse. Although the treatment of recurrent glioblastomas is not standardised, a follow up surgery (when feasible) and/or radiotherapy (rare) represent the approaches most commonly applied. The second line chemotherapy consists of either nitrosourea-based regimens, like lomustine (CCNU) alone, or the combination of lomustine plus alkylating agents (like TMZ) plus bevacizumab, or bevacizumab alone [69–72]. The use of lomustine in the treatment of recurrent glioblastoma provides a median overall survival of 8 to 9 months and a median progression-free survival of almost 3 months [72,73].

Bevacizumab (brand name Avastin®) is a recombinant humanized anti-vascular endothelial growth factor (VEGF) monoclonal antibody. By binding to circulating VEGFs, it inhibits their recognition by the respective cell surface receptors, therefore reducing the growth of blood vessels [74,75]. Bevacizumab was first studied for the treatment of metastatic colorectal cancer and in 2006 received the approval of the American food and drug administration (FDA) [76]. Later, its use against glioblastoma has been evaluated in several clinical trials, both for recurrent cases and as a first line treatment, but with no reported improvement in the overall survival of patients [77,78]. It was hypothesized that the limited efficacy of bevacizumab, as well as that of other monoclonal antibodies like the EGFR inhibitor cetuximab, might be due to their size and therefore difficulty in penetrating the BBB [79].

Several studies have focused on common mutations in glioblastoma and the possibility to devise associated treatment regimens. For example, tyrosine kinase receptor pathways are among the most frequently mutated pathways in glioblastoma and strategies to target them with the small multi-kinase inhibitor Regorafenib are now being evaluated in the AGILE and Regoma studies (NCT03970447 and NCT02926222), with promising initial results [80]. In the human genome, genes for three neurotrophic tyrosine receptor kinases (NTRK) can be found, and in cancer cells these can appear as fusion genes that lead to constitutively active TRKs that drive tumour cells proliferation [81]. NTRK inhibitors targeting NTRK fusion-positive cancers are now under study in glioblastoma [82].

Glioblastoma displays an overall strong resistance to conventional therapies. Hence, additional strategies to eradicate this tumour are under development. For example, oncolytic virotherapy is an approach that prospectively could provide advances to glioblastoma disease management and therapy [83]. Oncolytic viruses (OVs) can destroy the tumour cells in which they are hosted (oncolysis), and the consequent release of tumour antigens stimulates the immune system. The possibility of modifying OV genomes allows arming them with cell suicide genes [84]. Since Martuza's group in 1991 have engineered the first virus for oncolytic purposes, oncolytic virotherapy has further been explored [85]. Apart from Herpes simplex, many other viruses have been trialled and this led, in 2015, to the first FDA-approved oncolytic virus for the treatment of melanoma [86,87]. In glioblastoma, viruses from ten different families have been tested, some with very promising results [88]. For example, PVS-RIPO is an engineered variant of the poliovirus type 1 vaccine whose internal ribosomal entry site (IRES) has been replaced with that of the human rhinovirus type 2 in order to reduce its neuro-toxicity. The entry site of the virus is the cell receptor CD155/Necl5 which, by being upregulated in glioblastoma cells, provides the necessary tumour specificity and safety profile that allows the use of a poliovirus as a therapeutic agent [89,90]. This recombinant non-pathogenic polio-rhinovirus chimera proved to be very effective in early stages of clinical trials, with 20% of patients still being alive three years after initiating the treatment [91].

Among the approved treatments against glioblastoma, it is also relevant to mention the Tumour Treating Fields (TTFields). This treatment modality consists of the delivery of low intensity (< 3 V/cm) and medium frequency (200 KHz) electric fields that alter spindle formation and subsequently lead to mitotic arrest or cell division delay [92]. The first FDA-approved TTF device was the NovoTTF-100A (Optune®), pioneered by the company Novocure. Clinical studies have shown that the addition of TTF to TMZ increased patients' overall survival compared to chemotherapy alone, paving the way for more studies on this technology [93–95].

As mentioned before, the difficulties in treating glioblastoma are also due to the presence of the BBB, a physical and biochemical obstacle to the delivery of drugs to the brain. Considering that the first line treatment of basically every glioblastoma patient involves a surgery, implantable polymers can be placed in the tumor cavity at this stage. In particular, implants loaded with the chemotherapeutic carmustine have been developed and are available as Gliadel® Wafer. These wafers have been clinically tested, also in combination with TMZ, and already received FDA approval [96–98]. Nevertheless, modalities to improve drug delivery to the brain represent a growing area of research, with hydrogel and nanocarrier technologies being optimised in the last years for their use against glioblastoma [99].

Finally, it is important to mention that non-invasive ways of temporarily opening the BBB to allow drug penetrance are also under investigation. In particular, the BBB can be disrupted in a controlled manner by using focused ultrasounds. The safety of this technology has started to be assessed in both mice and humans and ultrasound delivering devices, like the SonoCloud by CarThera, are currently under clinical evaluation (NCT02253212) [100,101].

The above list of therapeutic options does not claim to be exhaustive, but serves to highlight the scarcity of approved therapies for glioblastoma and, thus, the urgent need to find new effective therapies.

2. GBM *in vitro* tumour models

One of the reasons for the limited success of many drug candidates entering clinical trials is the poor correlation between their efficacy in *in vitro* tumour models and in *in vivo* scenarios. The cell culture methods currently in use fail to account for all the factors that are responsible for the complexity of glioblastoma. Hence, depending on the biological question to address, all the available experimental models should be examined to select for the most suitable ones. With regards to the pre-clinical *in vitro* models, multiple options are available. First, the cells to utilise can be either immortalised cell lines or patient-derived cell lines (PDCLs). Then, culturing conditions have to be selected. These include the choice of medium composition and the age of the culture that, for primary cells, should be limited by a defined number of cell passages. Additionally, depending on the cell-to-cell and cell-to-ECM interactions that are relevant to reproduce, plastic cultureware can be appropriately pre-treated and the cells can either be cultivated as monolayers or as 3D spheroids.

The following paragraphs provide an overview of the experimental *in vitro* models that are available for glioblastoma research, with a focus on those adopted in this thesis.

2.1 Immortalized cell lines

Traditionally, cell-based studies on glioblastoma have been performed on immortalised cell lines, most commonly U-87 MG; U-251 MG; LN-229 and A172. Such widely used cell lines have been developed from patient tumours often decades ago, sometimes also by artificially manipulating the cells such that they would proliferate indefinitely. The advantage of these well-characterised cell lines is that they constitute a simple system comprising one single cell type that can be maintained easily in serum-containing medium. This supports experimental replicability and reproducibility, and also comparative studies between multiple international laboratories. Commercially available cell lines are a continuous source of cell material, therefore allowing large scale studies such as drug screens. Moreover, the content of so-called GSCs can be increased in such cells lines, for example when culturing these as spheroids, thereby allowing studies on stem-like subpopulations [102]. Unfortunately, established cell lines come with drawbacks. First, as they have been established a long time ago, back tracing and authentication of such cell lines sometimes is difficult. Genetic analyses of the cell line U-87 MG revealed, for example, that although it is considered to be a *bona fide* human glioblastoma cell line, its actual origin is uncertain [103]. While established in 1966 at Uppsala University in

Sweden from what was thought to be the glioblastoma of a 44-year-old woman, fifty years later it is available in the American Type Culture Collection (ATCC) as an authenticated cell line derived from a male patient [104]. Another important limitation is that such cell lines have been passaged *in vitro* uncountable times. As such, they have been selected over time for those with the highest proliferation rate, and at the expense of the genetic heterogeneity that is a hallmark of glioblastoma and that might have been present in the original isolates. Moreover, successive and prolonged passaging can lead to genetic drift, which may result in alterations in both the genotype and phenotype of these cells, thereby broadening the gap between the cell line model and the actual *in vivo* tumour [105,106]. Nevertheless, established glioblastoma cell lines can be considered as a convenient model for a fast screening of drug candidates and for obtaining preliminary results. However, these would need further validations in other study systems.

2.2 Patient derived cells

The use of primary early passage cells obtained from fresh tumour samples is becoming more common and begins to replace the use of traditional cell lines. Such cell materials are often referred to as patient-derived cell lines (PDCLs), even though obviously also traditional cell lines are derived from patient materials. To obtain PDCLs, fresh biopsies are processed within 2-3 h post-resection based on protocols that preserve the characteristics of the original tumour [107,108]. PDCLs are now considered state-of-the-art preclinical models for glioblastoma studies, as they have been found to maintain the gene expression profiles present in the parental tumour [109,110]. However, depending on the conditions adopted for their subsequent culturing, the behaviour of these cells and, most importantly, the fraction of GSCs within the culture, can vary broadly [111]. One major issue arises from the use of serum-supplemented media, which reduces the relative proportion of GSC subpopulations and appears to induce their differentiation into more committed cells [112,113]. This can be avoided by culturing PDCLs in the absence of serum and, instead, in the presence of defined supplements. The most commonly used medium for this purpose is Dulbecco's Modified Eagle Medium (DMEM) in 1:1 ratio with Nutrient Mixture F-12, that contains high concentrations of D-glucose (3151mg/L), amino acids, vitamins and inorganic salts. The growth factors normally added to this medium comprise epidermal growth factor (EGF) and basic fibroblast growth factor (bFGF), plus additional supplements such as N2 or B27, which contain lipid components that have been shown to promote the proliferation of glioblastoma cells [114]. Compared to standard cell cultures, the maintenance of cells in serum-free, supplemented medium, has been shown to preserve the genetic aberrations and gene expression profile of the tumour of origin [109,112]. Nevertheless, besides the culturing medium, another crucial aspect for the maintenance of these cells is the life of the cultures. For a PDCL to be considered a reliable model of a glioblastoma tumour, its culture time should be limited to a maximum of about twenty passages. In fact, it has been reported that older cultures start to accumulate transcriptional changes that affect important signalling pathways like that of mTOR and Wnt [115].

Glioblastoma PDCLs can be cultured either as monolayers (2D) or as spheroids (3D). 2D cultures are convenient as they allow an efficient propagation of the cells that are homogeneously exposed to the growth factors contained in the medium. Cells in 2D cultures exhibit a different morphology compared to those grown as 3D models and, therefore, drug sensitivities may differ between these conditions [116]. However, this might not always be the case, so the requirement for 3D-cultured PDCLs as models for the screening of drug responsiveness in glioblastoma needs to be assessed on a case-by-case basis [117,118].

The culture of PDCLs in 2D can be improved by treating the plastic of the culturing flasks with coating polymers that reduce the stiffness of the surfaces and allow cells to interact from multiple sides. Plastic indeed provides an unnaturally stiff environment to which cells react with an altered behaviour in terms of invasion properties and proliferation rates [119,120]. To provide an environment that more closely resembles that of the tumour, hydrogels containing different ECM components have been developed. For example, Matrigel is a natural hydrogel derived from the ECM of mouse sarcoma tumours and it has been adapted for culturing glioblastoma cells. Matrigel, just like other ECM-derived hydrogels that have been developed, contains mostly laminin and collagen IV [121]. This composition is well-suited to mimic the ECM of several tissues, but does not appropriately reflect that of the brain. Indeed, the brain ECM is richer in proteoglycans and glycoproteins, especially hyaluronic acid and heparan sulfate. On the other side, laminin is the main component of the wall of the blood vessels and GSCs are known to mostly reside in the perivascular niche [122]. Therefore, the use of such coating polymers still provides a valid approximation of the brain environment and are surely preferable over plastic surfaces.

Overall, the short-term cultivation of PDCLs in EGF and bFGF-supplemented serum-free medium and on ECM coatings represents the best and cheapest option to recapitulate the characteristics of the parental tumour. Moreover, PDCLs allow for the analysis of tumour cell diversity among individual patients, which is a step closer towards the study of inter-tumour heterogeneity. Considering that PDCLs can also grow as spheroids, 2D PDCL models can be complemented with 3D culture systems. This is described in the following paragraph together with the most advanced 3D culturing methods.

2.3 3D tumour models

Bidimensional cultivation of cells, although an efficient way of expanding a culture, has the intrinsic drawback of oversimplifying the complex cell-to-cell interactions found in tumours [123,124]. In order to circumvent this problem, serum-free cultured glioblastoma PDCLs can be grown suspended in medium over non-adhesive substrates, such as ultra-low attachment plates or cultureware treated with anti-adherence rinsing solutions. GBM cells then form typical aggregates referred to as spheroids, or more specifically neurospheres (NS) or gliomaspheres. Spheroids kept under these conditions have been shown to maintain cellular subpopulations with stem-like properties[125]. Spheroids originate from the spontaneous aggregation of multiple single cells and can vary greatly in size and thus cell number, an aspect to be taken into account when analysing the differences or similarities in cellular responses between spheroids and between repeat experiments [126]. If clonal identity between spheroid cells is required, limited dilution assays can be employed [127]. These allow to grow spheres from individual starting cells and also provide an indication for the tumour initiating capacity of such cells [128]. In a simplified view, cells that depend on cell-to-cell contacts for continued growth would be assumed to undergo anoikis, whereas GSCs would be expected to grow in suspension in serum-free medium and to form spheres. However, in conditions of low cell density paracrine signals are missing, cell growth can be very slow and can come at the cost of losing the cellular heterogeneity of the starting cultures or cell isolates. Nevertheless, PDCLs grown as spheres/spheroids are a cheap and relatively convenient model that, especially when used in combination with 2D PDCLs, represent a widely used standard employed in most of the laboratories for pre-clinical studies.

More elaborated experimental models have been developed to overcome the limitations of neurospheres. For example, organotypic glioma spheroids are slice cultures directly derived from a biopsy that comprise several cell types and structures of the glioblastoma microenvironment like non-malignant cells, ECM and blood vessel structures. Because of these features, organotypic slice cultures are particularly suitable for studying migration and invasion properties of glioblastoma. Such spheroids not only reconstruct the tumour microenvironment, but they also appear to be genetically stable and could be used to test TMZ susceptibility [129,130]. Unfortunately, as an *ex-vivo* system, slice cultures are cost and time consuming, individually unique and due to their nature as tissue samples do not lend themselves for repeat experiments or for well-controlled reference experimental systems.

In order to study cell-to-cell as well as cell-to-matrix interactions in a 3D model, a variety of hydrogel-coated scaffolds have been developed with different biomaterials and coatings that try to mirror the brain ECM. The list ranges from the first Matrigel-coated polystyrene scaffolds to hyaluronic acid ones. Relatively cheap and easy to scale up for high-throughput experiments, these scaffolds have already found several applications, such as drug response studies as well as proliferation and invasion experiments [116,131]. However, the stiffness of the scaffold, that is known to influence cell behaviour, represents a limitation of these models. Additionally, throughout the cell passaging, an inevitable selection process takes place that favours those cells that attach more loosely to the matrix and that, therefore, are more easily retrieved, an effect that may bias invasiveness studies.

A tumour is a dynamic entity that adapts to the changes of the microenvironment. 3D cultures instead, are far more static because the surrounding medium conditions remain largely stable. To better represent the variability of the tumour microenvironment, and therefore the variable conditions to which tumour cells are exposed, microfluidic systems like the “tumour-on-chip” have been developed. In such systems, cells are grown in hydrogel tubes filled with circulating media whose composition can be time-controlled in terms of nutrients and factors to be added. Also, brain-specific ECM components, like hyaluronic acid, can be included to create a more a realistic glioblastoma microenvironment. This technology has been applied for the long-term cultivation (>50 days) of glioblastoma tumour initiating cells (TICs), such that stem cell properties could be maintained. Cells can be pumped into alginate hydrogel tubes (AlgTubes) and continuously grown along them to form strands of spheres expressing GSC markers [132]. Hence, this may represent an efficient and relatively cost-ineffective method for the mass production of TICs.

A recently emerged platform for the study of glioblastoma development and its pathology is represented by brain organoids or “mini-brains”. Organoids are structures resembling a whole organ and are generated starting from stem cells that develop and differentiate in three-dimensional systems. In 2013, M.A. Lancaster from the group of J.A. Knoblich, developed a protocol for deriving cerebral organoids from induced pluripotent stem cells (iPSCs), which were first cultured as embryoid bodies and then induced to differentiate towards the neuroectoderm. The cells, embedded in a Matrigel pellet, were cultured in a differentiation medium in the presence of EGF/FGF2 and then moved to a spinning bioreactor. These cerebral organoids developed different and interdependent brain regions such as the cerebral cortex, with progenitor cells that self-organised to originate mature cortical neurones [133,134]. In 2016, a pioneering work by C.G Hubert, applied this “mini-brain” model to glioblastoma in order to generate brain tumour organoids. These organoids grew for months and showed regional heterogeneity, with an outer region of quickly dividing cells that were positive for stemness marker such as SOX2, OLIG2, and TLX. Importantly, cells of this region were sensitive to radiotherapy, while senescent and quiescent cells of the hypoxic core were overall more radio-resistant. Furthermore, a hypoxic gradient that spatially correlated with reduced SOX2 expression could be observed within the organoid. Successful orthotopic implantation into mouse brains demonstrated the tumourigenic capacity of this model. This work showed that brain tumour organoids can be employed to study tumour heterogeneity and drug sensitivity in a sophisticated model of the primary patient tumour, with a superior level of complexity compared to simple patient-derived sphere cultures [135].

Recently, a biobank of patient-derived glioblastoma organoids, recapitulating the mutational profiles of the parental tumours, has been generated [136]. This biobank can be interrogated to test personalised therapies by correlating the glioblastoma organoid mutational profiles with responses to certain drugs. Overall, compared to conventional cell cultures, tumour organoids better recapitulate the original tumour architecture and its microenvironmental gradients. Additionally, they preserve the cellular heterogeneity of the parental tumour and, for that, they represent a valid option for the pre-clinical research on glioblastoma.

Due to the process of self-assembly, tumour organoids may have a variable cellular composition and structure. In order to gain a better control over both the cellular and the ECM components, 3D bio-printed models of glioblastoma tumours have been developed. This technology exploits novel biomaterials and recent advances of tissue engineering techniques to reconstruct 3D models that are based on clinical images of the tumour. These images are sliced into 2D sections such that a bioprinter can generate well-defined structures in all three dimensions. A variety of natural or synthetic biocompatible scaffolds that can reproduce the brain ECM are available, like hydrogels of chitosan-alginate and hyaluronic acid, or synthetic polymers like poly-lactide co-glycolide and polyethylene-glycol [137–139]. The bio-printing can be performed using a so-called extrusion method, which consists of the continuous depositing, layer-by-layer, of filaments of biomaterial or of inkjet droplets released from a nozzle. Alternatively, photo-crosslinking can be used to induce the photopolymerization of the bioink to form 3D structures [140]. Several cell types can be encapsulated into this bio-printed ECM, such that a “mini-brain” structure, replicating the tumour architecture and the interactions among different cell types, can be built. The choice of cellular components, biomaterial and bio-printing method depends on the biological issue that researchers want to address. For example, M.A. Heinrich and colleagues developed a brain model in which they first printed a scaffold that encapsulated mouse macrophages. These were placed such that a cavity was left empty for being filled with methacryloyl/gelatin bioink-embedded mouse glioblastoma cells. Finally, the whole construct was photo-crosslinked [141]. In this 3D bio-printed mini-brain the location of the tumour allowed cellular cross-talk to occur similarly to that in an *in vivo* situation and, therefore, the model was used to study the interactions between cancer cells and macrophages. M.A Hermida and colleagues instead, used the extrusion method to established a model comprising glioblastoma cells and stromal cells co-printed in a matrix of alginate, hyaluronic acid and collagen-1 crosslinked with calcium [142]. Although cost-effective and limited by the availability of suitable biomaterials that do not affect the normal tissue development, 3D-bioprinted models have the advantage of facilitating the study of the tumour microenvironment and its influence on the tumor cells.

The experimental models described in this section have been developed in an effort to narrow the gap between *in vitro* and *in vivo* settings and all of them contributed to the understanding of different aspects of the glioblastoma biology. Depending on the scientific question that has to be addressed, the limitations and the advantages listed above should all be taken into account such that the most suitable model can be selected. Nevertheless, it has to be considered that reliable results are always those arising from comparative studies performed in more than a single model system.

3. Apoptosis

Cell death, like cell proliferation, is a physiological process that is necessary for both tissue development and homeostasis [143]. It occurs not only in multicellular organisms but, in simplified modalities, also in unicellular eukaryotes organised in colonies [144]. According to the guidelines by the Nomenclature Committee on Cell Death (NCCD), cell death modalities can broadly be divided into regulated cell death (RCD) and accidental cell death (ACD) [145]. While ACD is an uncontrollable form of cell death that is due to a severe physical, chemical, or mechanical insult, RCD is a molecularly controlled cell suicide. RCD is induced in response to stress conditions or cell external cues. The first discovered and best characterised form of RCD is apoptosis [146]. Apoptosis manifests with typical and unique morphological changes of the cell that include membrane blebbing, cell shrinkage, nuclear fragmentation, chromatin condensation, chromosomal DNA fragmentation and loss of adhesion to the ECM. Biochemical alterations include the activation of cysteine aspartyl proteases, named caspases, and the scramblase-mediated flipping of phosphatidylserine from the inner leaflet of the plasma membrane to the cell surface. The activation of caspases is the event ultimately leading to cell death, while the exposure of phosphatidylserine represents a phagocytosis signal for macrophages that remove dying cells [147]. Depending on the origin of the activating stimulus, apoptosis initiation can follow the intrinsic (mitochondria-mediated) or the extrinsic (death receptor-mediated) pathway, with both routes eventually converging on the same execution phase.

The extrinsic apoptosis pathway is activated by the binding of extracellular ligands to cell-surface death receptors (DRs). Such DRs are type I transmembrane proteins that belong to the tumor necrosis factor (TNF) receptor superfamily, a group of almost thirty proteins involved in cell death as well as in cell survival, differentiation and also in immune functions [148]. Most members of this superfamily are characterised, at their N-terminal, by the occurrence of a cysteine-rich extracellular domain while, at the C-terminus, a sixty amino acids-long cytoplasmic “death domain” (DD) is present [149]. In the superfamily of TNF receptors, six members are counted as death receptors and they include: cluster of differentiation 95 (CD95/Apo-1/Fas), TNF receptor 1 (TNFR1), TNF-related apoptosis-inducing ligand-receptor 1 (TRAIL-R1/Apo-2/DR4), TNF-related apoptosis-inducing ligand-receptor 2 (TRAIL-R2/DR5), DR3 (TRAMP/Apo-3/WSL-1/LARD) and DR6 (TR7). The ligands of these receptors are: fibroblast associated surface antigen ligand (CD95L/FasL), TNF, TRAIL (Apo-2L) and TWEAK (DR3L/Apo-3L). The ligand of DR6 instead is not yet clearly defined [150]. Based on the cell type and the DR signalosome composition, the binding of these ligands to their cognate receptors can activate non-cytotoxic signalling pathways that regulate cell proliferation and differentiation, the production of chemokines, inflammatory responses and tumour-promoting activities [151]. Additionally, in conditions where extrinsic apoptosis is blocked, an alternative cell death pathway named necroptosis can be initiated [152,153]. Otherwise, the binding of DRs to their ligands leads to the activation of initiator caspases and apoptosis execution.

The intrinsic pathway is activated by non-receptor-mediated stimuli that provoke an intrinsic cellular stress, like for example irradiations, viral infections, chemotherapeutics, reactive oxygen species (ROS) overload and others [154–157]. In these cases, the key event is the permeabilization of the outer mitochondrial membrane (MOMP), which is governed by proteins of the Bcl-2 family. This results in the release of apoptogenic factors from the mitochondrial intermembrane space and in the subsequent activation of the apoptosis execution phase [158].

3.1 TRAIL-mediated apoptosis signalling and its regulation

TRAIL is a cytokine found as a soluble trimer or as a type II trans-membrane protein with an extra-cellular C-terminus. It is expressed on cells of the immune system like lipopolysaccharides (LPS)-activated monocytes and macrophages, IFN-α- or IFN-β-stimulated plasmacytoid dendritic cells (DCs), IFN-γ-stimulated natural killer (NK) cells and also on activated T-cells [159–163].

Among the death ligands, TRAIL is of particular interest in cancer research as it was shown to preferentially induce apoptosis in transformed cells [164]. TRAIL can bind to various DRs but it is only the engagement of two of them that induces apoptosis, namely TRAIL-R1 and -R2 (*figure 1*). These two contain the necessary intracellular death domain (DD) required for apoptosis induction and thus are considered agonistic receptors. Importantly, while TRAIL-R1 can be activated by the binding of both soluble TRAIL and membrane-bound TRAIL, TRAIL-R2 requires a high order of receptor clustering, which is more efficiently induced by the membrane-bound ligand [165,166]. TRAIL-R3 is glycosylphosphatidylinositol (GPI)-anchored protein that lacks an intracellular domain, while TRAIL-R4 contains only a truncated C-terminal cytoplasmic DD and therefore it cannot transmit an apoptotic signal. TRAIL-R3 and TRAIL-R4 are also referred to as antagonistic or decoy receptors, respectively DcR1 and DcR2. According to D. Mérino and co-workers, when TRAIL-R3 is overexpressed, it competes with TRAIL-R1 and TRAIL-R2 for ligand binding. Instead, TRAIL-R4 interacts with DR5 to form heteromeric and apoptosis-incompetent receptor complexes, besides preventing the co-recruitment of DR4 to these sites [167].

Although a captivating principle, the ratio of agonistic *versus* antagonistic receptors is insufficient to explain resistance mechanisms to TRAIL-receptor activation, probably due to complex regulation at the level of receptor signalling and downstream apoptosis signal transduction [168,169]. It also has to be considered that receptor expression is regulated at a transcriptional level as well as post-translationally, with modifications modulating their functionality. In particular, O- or N- glycosylation of TRAIL-R2 and TRAIL-R1 respectively, affect apoptosis signalling in a positive or negative way depending on the specific cell type [170–172]. In general, it is believed that O-glycosylation of DR4 and DR5 and palmitoylation of DR4 increase their membrane stability and prevents endocytosis, thus facilitating their ligand-induced clustering [149,172,173]. Another level of regulation is represented by the transport of the death receptors to the cell surface, a process that has been reported to be impaired in many cancer cells in which it indeed can confer TRAIL resistance [174,175].

The last TRAIL receptor, and the one with the lowest affinity to TRAIL, is the secreted glycoprotein Osteoprotegerin (OPG) [176]. Discovered for its central role in the regulation of bone turnover through the inhibition of osteoclastogenesis, the function of OPG in the TRAIL pathway, although not completely clarified, seems to be that of a decoy receptor [177,178]. Some studies reported indeed that OPG binds to TRAIL and prevents its interaction with the functional death receptors, therefore indirectly promoting cell survival [179].

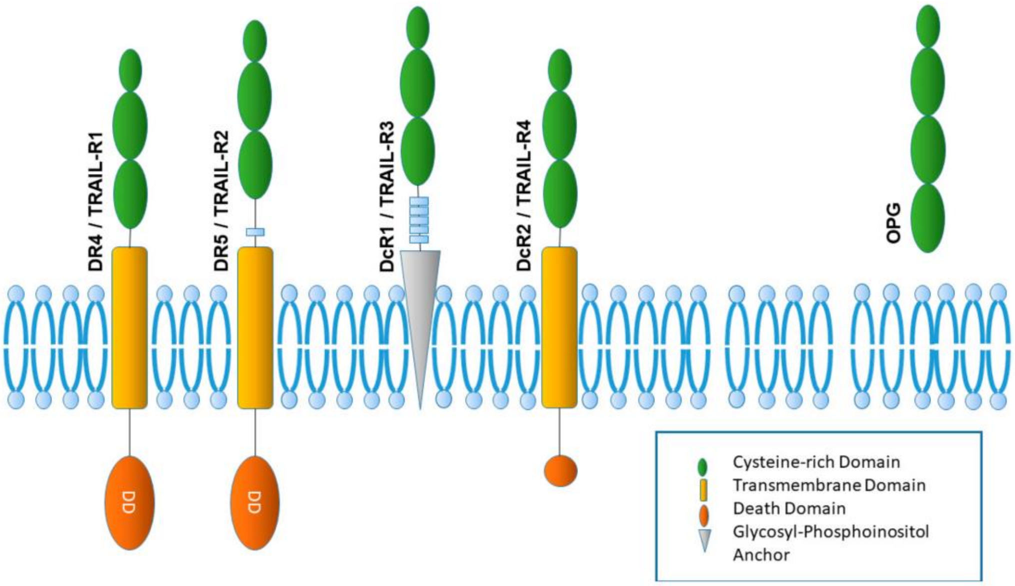

Figure 1: TRAIL receptors

All TRAIL-R contain N-terminal cysteine-rich domain (in green) for ligand binding. TRAIL-R1, TRAIL-R2 and the decoy receptor TRAIL-R4 are transmembrane proteins and indeed contain a transmembrane domain (in yellow). TRAIL-3 is bound to the cell membrane via a glycosylphosphatidylinositol (GPI) anchor while Osteoprotegerin (OPG) is a soluble protein. TRAIL-R3 and OPG no not contain a death domain (DD) while TRAIL-R4 contains a truncated and non-functional DD (tDD). Only the DD of TRAIL-R1 and TRAIL-R2 (in orange) can transmit a signalling cascade. Note that TRAIL-R2 is expressed as a long and a short isoform (not depicted). Adapted from Beyer, K. et al., (2019) [180].

Binding of TRAIL to TRAIL-R1 or TRAIL-R2 induces receptor trimerization and clustering, which results in conformational changes of the cytoplasmic DD. This allows the homotypic interaction with the C-terminal cytosolic DD of the adaptor protein FAS-associated death domain (FADD). Once recruited, FADD can interact through its N-terminal death effector domain (DED) with the DED of procaspase-8 (or FLICE: FADD-like interleukin-1β-converting enzyme); procaspase-10 and cellular FLICE-like inhibitory protein (c-FLIP), forming the death inducing signalling complex (DISC) [181,182].

According to the hierarchical model of the DISC formation, procaspase-8 is required for the recruitment of c-FLIP at the DISC. c-FLIP exists in different isoforms that exert diverse functions. The two short isoforms, c-FLIP$_S$ (short) and c-FLIP$_R$ (raji), completely lack the protease domain and inhibit caspase-8 activation at the DISC, likely by forming inactive heterodimers with procaspase-8 through homotypic interactions of the DED domains. The long isoform of the protein, c-FLIP$_L$ (long), contains an inactive protease domain and at low concentrations can contribute to caspase-8 activation. This is due to the formation of c-FLIP$_L$-procaspase-8 heterodimers that stabilise the catalytic domain of the caspase. At higher concentrations instead, c-FLIPL inhibits apoptosis as it might interfere with the formation of the tertiary DISC structure required for efficient caspase-8 activation [183–185].

When recruited to the DISC, procaspase-8 molecules form filaments that allow a close proximity-driven dimerization of their protease domain, with consequent auto-activation by proteolysis [182]. The first auto-cleavage of procaspase-8 (p55/53) occurs at an aspartate residue and results in the generation of large intermediates (p43/41) that stabilize the formation of catalytically active caspase-8 heterodimers [186]. A further proteolytic cleavage at another aspartate residue generates the activated caspase-8 heterotetramer consisting of two large (p18) and two small (p10) subunits [187]. Active caspase-8 is released from the DISC into the cytosol and in type I cells, the robust caspase-8 activation directly and sufficiently activate the effector caspases-3 and -7 for the execution phase of apoptosis to proceed [188]. Nevertheless, if the mitochondrial apoptosis pathway is not blocked by high expression of anti-apoptotic Bcl-2 family proteins, type I cells preferentially route their signalling through mitochondrial amplification [189].

The apoptosis execution phase depends on the cleavage of the effector procaspases-3 and 7 to activated caspases, a reaction that is catalysed by initiator caspases [190]. The pro-forms of effector caspases differ from that of initiator caspases as they are already pre-assembled as homodimers. Active effector caspases proteolytically activate caspase-activated DNase (CAD). This results in CAD-dependent DNA fragmentation, and effector caspases likewise degrade numerous other proteins, including cytoskeletal structures and the poly (ADP-ribose) polymerase (PARP), which plays a crucial role in DNA repair. Finally, the formation of apoptotic bodies and the expression of ligands recognized by receptors of phagocytic cells, that eventually take up the cell fragments, conclude the clearance phase. During apoptosis, the cell membrane maintains its integrity, preventing the release of damage-associated molecular patterns (DAMPs), such that apoptosis occurs largely in absence of inflammatory responses [191–194].

In cells classified as type II, the amount of active caspase-8 generated at the DISC platform is not sufficient to activate effector caspases. Moreover, high levels of X-linked inhibitor of apoptosis protein (XIAP) can block caspase-3 activation via the type I signalling route. In such cases, a mitochondrial amplification loop that links the extrinsic with the intrinsic apoptosis pathway is required for the full activation of executioner caspases [188]. The link is provided by the proteolytic activity of active caspase-8 that can cleave the protein BH3-interacting domain death agonist (BID) into truncated BID (tBID). BH3-only proteins like tBID can mediate the formation of pores in the outer mitochondrial membrane by interacting with B cell lymphoma-2 (Bcl-2) associated X protein (BAX) and Bcl-2 antagonist/killer (BAK), or by alleviating their repression by anti-apoptotic Bcl-2 family members. While BAK already resides at the mitochondria, BAX is normally located in the cytosol and only due to this interaction it exposes its transmembrane domain for being inserted into the mitochondrial outer membrane [195,196]. Once activated, BAK and BAX form homo-dimers that aggregate into larger homo-oligomers. The minimum oligomerisation required for BAX or BAK to robustly form pores and induce MOMP has not been fully clarified yet. In most scenarios, MOMP proceeds as an all-or-nothing event. However, if the stimulus is not robust enough to trigger apoptosis, MOMP can contribute to carcinogenesis or cancer progression. In such scenarios, only a minority of mitochondria undergo MOMP, followed by sublethal caspase activation and DNA damage, with the latter promoting cellular transformation [197,198].

Besides BAK and BAX, also other proteins of the Bcl-2 family play a role in MOMP regulation. Among them are the anti-apoptotic Bcl-2, Bcl-xL (extra large) and myeloid cell leukemia-1 (Mcl-1), that directly bind BAX and BAK to prevent pore formation. These anti-apoptotic proteins can be sequestered, and therefore their function blocked, by BH3-only proteins. These are pro-apoptotic proteins of the Bcl-2 family and include the aforementioned BID, antagonist of cell death (Bad), Bcl-2 interacting mediator of cell death (Bim), p53 upregulated modulator of apoptosis protein (Puma) and phorbol-12-myristate-13-acetate-induced protein 1, also known as Noxa [199]. The balance between pro- and anti-apoptotic members of the Bcl-2 family dictates the fate of the cell [200,201]. An overview of Bcl-2 proteins and their structural domains is represented in *figure 2*.

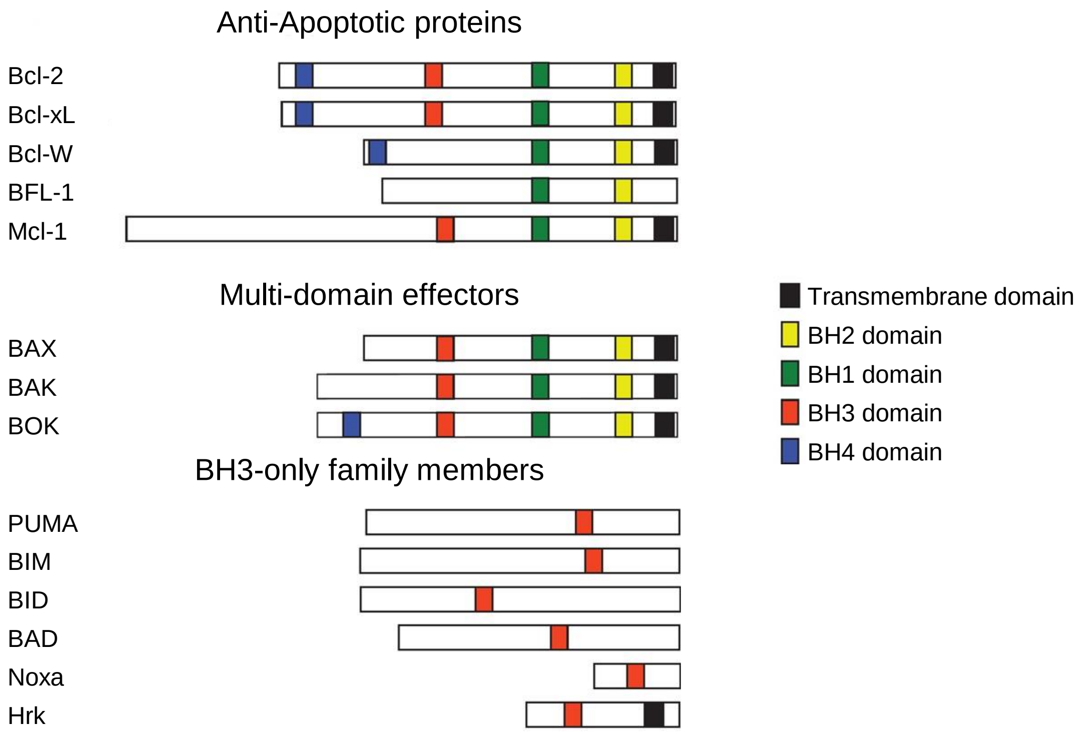

Figure 2: Proteins of the Bcl-2 family and their domains

Bcl-2 family proteins represented with their relative size for comparison. Bcl-2 proteins bear one to four Bcl-2 homology (BH) domains. The anti-apoptotic members have multiple BH3 domains and, apart from BFL-1/A1, they also contain a transmembrane (TM) domain to be anchored on cellular membranes such as the mitochondrial outer membrane, nuclear membrane and endoplasmic reticulum. Pro-apoptotic members include the group of the multi-domain effector molecules, such as BAX, BAK and BOK. These have multiple BH domains and also TM domains that allow their localization to the outer mitochondrial membrane. The other group is represented by BH3-only proteins that only bear the BH3 domain. Not all the BH3-only proteins are represented in this scheme. Modified from Opferman, J. T. et al., (2016) [202].

Following MOMP, cytochrome c translocates from the mitochondrial intermembrane space into the cytosol where it interacts with the cytosolic adaptor protein apoptotic protease-activating factor 1 (APAF-1). APAF-1 undergoes a (deoxy) adenosine triphosphate ((deoxy)ATP)-dependent conformational change and it oligomerizes to form an heptameric complex known as the apoptosome [203,204]. On this platform, the caspase recruitment domains (CARD) of APAF-1 interacts with that of the initiator procaspase-9 [205,206]. On the apoptosome, both the interaction between pro-caspase-9 monomers and the proximity-induced homodimerization of pro-caspase-9 allow for caspase-9 activity to manifest. Caspase-9 then activates effector caspases-3 and -7 as long as it remains bound to the apoptosome [205,207].

In a positive feed-back loop that amplifies apoptosis execution, active caspase-3 can cleave caspase-9. By doing so, it does not activate the initiator caspase but it removes the short peptide motif that allows its interaction with the E3 ubiquitin-protein ligase XIAP (X-linked IAP), therefore alleviating the XIAP inhibition of caspase-9 [208,209]. In addition, caspase-3 can cleave and activate BID, thereby contributing to the robustness of the MOMP decision. Subsequent to BAX/BAK pore formation, caspase-3 additionally proteolytically inactivates mitochondrial respiration and thereby aggravate the bioenergetic crisis of cells running into apoptotic cell death [210].

Smac/DIABLO (second mitochondria-derived activator of caspase/direct IAP-binding protein with low PI) is an additional protein released from mitochondria to promote caspase activation [211]. In particular, Smac binds as a homodimer to inhibitor of apoptosis proteins (IAPs), freeing bound caspases and also promoting the assembly of complexes that serve to activate upstream caspase-8 [212].

The IAP family comprises proteins with different domains. XIAP contains three baculovirus IAP repeats (BIR) through which it interacts and inactivates the caspases 3,7 and 9. It also has a ubiquitin-associate domain (UBA) and a really interesting new gene (RING) domain that can target proteins like caspase-3 and Smac for degradation via the ubiquitin system [213,214]. cIAP1/2 similarly bear three BIR domains and a RING domain and they function in accelerating the degradation of caspase-3, 7 and 9 [214]. Therefore, the anti-apoptotic role of IAP proteins is exerted not only via caspases inhibition but also via the targeting of pro-apoptotic Smac/DIABLO molecule for proteasomal degradation.

Smac exposes an IAP-binding motif (IBM) and it dimerises to bind an IAP molecule with its BIR domains. As the same BIR domain of IAP is also used to bind the small subunit of caspase-9, this allows Smac to displace caspase-9 from XIAP [215,216].

The complexity of the apoptosis pathway is represented as a simplified scheme in *figure 3*.

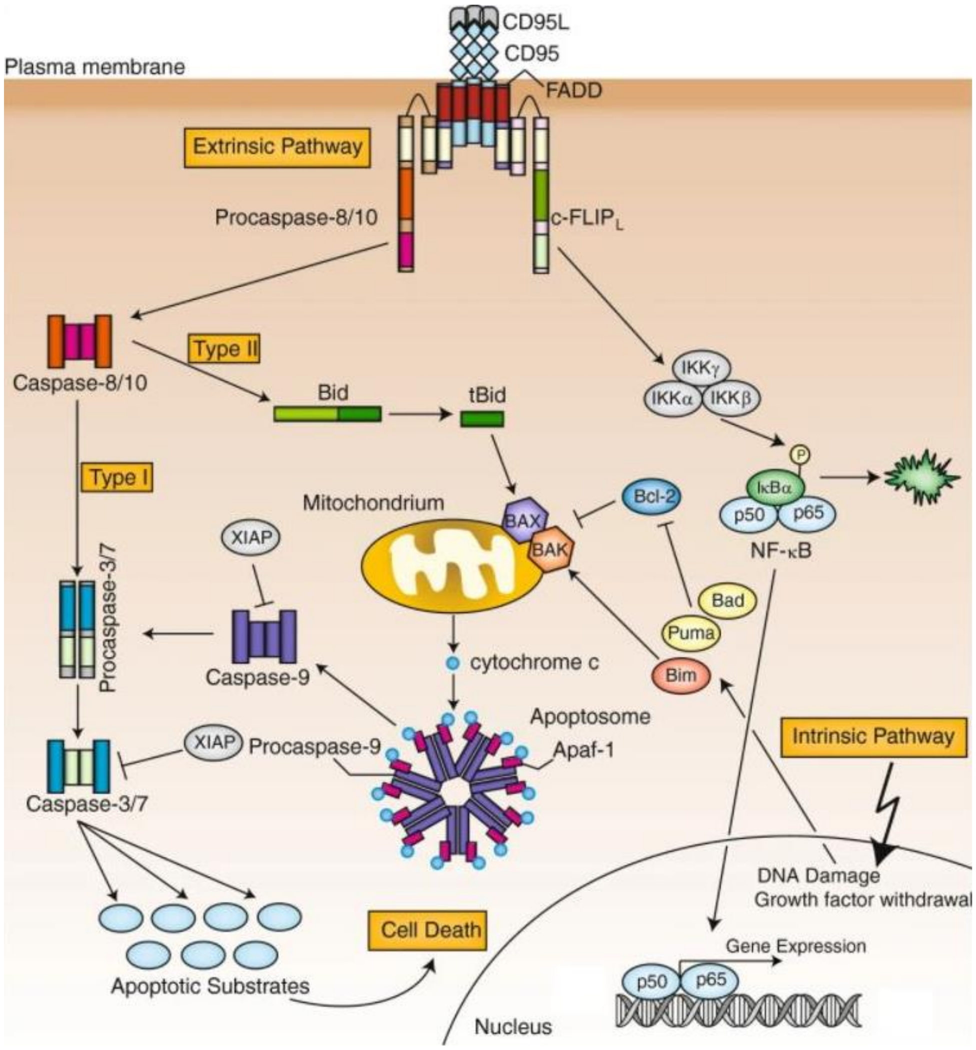

Figure 3: Simplified scheme of the apoptosis signalling pathways

Apoptosis activation can proceed through the extrinsic or the intrinsic pathway. The extrinsic pathway is initiated via stimulation of surface death receptors such as CD95 or TRAIL-R. The binding of homotrimeric Apo2L/TRAIL ligand to DR4 and DR5 drives the clustering of the receptors into complexes of higher molecular weight. In particular, this results in the recruitment of the adaptor molecule FADD, procaspase-8, procaspase-10 and c-FLIP proteins, all together forming the death-inducing signalling complex (DISC). The activation of procaspase-8 at the DISC is regulated by c-FLIP proteins. Active caspase-8 cleaves and activates effector caspase-3 and caspase-7 but also the Bcl-2 family protein BID. The truncated form of BID (tBID) translocates to the mitochondrial outer membrane where it allows its permeabilization. This leads to the release of the pro-apoptotic protein cytochrome c, that is involved in the formation of a cytosolic complex named apoptosome, where procaspase-9 gets activated. Active caspase-9 then activates procaspases 3 and 7, eventually resulting in cell death. Other pro-apoptotic proteins are also released from the mitochondria, such as Smac/DIABLO (not depicted). The release of Smac augments apoptosis by antagonizing the inhibitory effect of XIAP on effector caspases (not depicted). In cells classified as type I, efficiently activated caspase-8 is sufficient to trigger the execution phase of the apoptosis pathway. In type II cells instead, this signalling is less strong and therefore BID cleavage is necessary for apoptosis to be executed. The intrinsic pathway can be activated by diverse intracellular stimuli, like DNA damage or growth factor withdrawal. The members of the Bc-2 family of proteins tightly control apoptosis at the mitochondria. Of note, CD95 or TRAIL can additionally initiate non-apoptotic pathways, such as those of NF-κB or MAPK, leading to cell survival. Adapted from Schleich, K. & Lavrik, I. N. (2013) [217].

3.2 Non-canonical TRAIL-mediated pathways

Besides classical apoptosis induction, many reports showed that TRAIL can also trigger additional pathways such as receptor-interacting serine/threonine-protein kinase 1 (RIP-1)-dependent apoptosis, necroptosis or even cell survival pathways.

Although less strongly than TNF, TRAIL can promote the association of a cytosolic secondary signalling complex, called complex IIb, subsequent to the assembly of DISC. Complex IIb does not contain death receptors but RIP-1, TNF receptor-associated factor 2 (TRAF2) and the NF-κB essential modulator (NEMO)/IKKγ. Additionally, this complex also comprises FADD and caspase-8 and leads to RIP-1-dependent apoptosis [218]. In certain cell types, it was shown that the clustering of TRAIL receptors outside of lipid rafts was the event responsible for the TRAIL signalling through RIP-1 [219]. According to other reports instead, acidic pH conditions are associated with the occurrence of this RIP1-dependent apoptosis [220]. Finally, reviews by M. Feoktistova and A. Degterev explained how a depletion of cIAP, that would otherwise mediate the proteasomal degradation of RIP-1 and drive pro-survival signalling, allows this type of cell death [221,222].

Interestingly, in conditions of caspase-8 inactivation, RIP-1 becomes a key player of a TRAIL-triggered, caspase-independent mode of cell death termed necroptosis [223]. Identified in mice under conditions of FADD and caspase-8 ablation, necroptosis was then found to be prevented by co-ablation of RIP-1 or receptor-interacting serine/threonine-protein kinase 3 (RIP-3) [224,225]. In necroptotic death, RIP-1 phyosphorylates and interacts with RIP-3 to form a complex termed necrosome (also complex IIc) [226]. Intramolecular auto- and trans-phosphorylation of RIP-1/RIP-3 promote the recruitment of the mixed lineage kinase domain-like protein (MLKL) that is then phosphorylated by RIP-3. Phosphorylated MLKL is transferred from the cytosol to the inner leaflet of the plasma membrane where it oligomerizes and forms pores. This results in the destruction of membrane integrity and eventually leads to necroptotic death [227].

In cells that fail to induce cell death upon TRAIL exposure, survival pathways are activated [228,229]. Y. Lin and colleagues found that the death domain of RIP-1 is essential for TRAIL-induced activation of IκB kinase (IKK) and JUN N-terminal kinase (JNK). IKK phosphorylates IκB leading to its degradation and NF-κB nuclear translocation [230]. Among the target genes of the NF-κB transcription factor there are several anti-apoptotic proteins such as cIAP1/2, c-FLIP and Bcl-xL [231–233]. Importantly, while NF-kB activation prevents apoptosis by the induction of anti-apoptotic proteins, active caspases can block NF-kB signalling by cleaving important components of its pathway such as RIP-1, IκBα, IKK2, TRAF1 and even RelA (p65) itself [234]. Moreover, as reviewed by S. von Karstedt and co-workers, the formation of the secondary intracellular signalling complex following DISC formation can activate not only NF-κB, but also the JUN N-terminal kinase (JNK) and the p38 MAPK pathways, contributing to cell proliferation and pro-survival signalling [218,235,236]. TRAIL can also activate the ERK1/2 kinases without inducing NF-κB activation, a mechanism that has been shown to be important for the proliferation of vascular endothelial cells [149,237].

Finally, the linear ubiquitin chain assembly complex (LUBAC), that is the only known E3 ubiquitin ligase that catalyses the generation of linear ubiquitin linkages *de novo*, was found to be part of both TRAIL-R-associated complex I as well as of the cytoplasmic TRAIL-induced complex II, regulating the balance between different outcomes of the TRAIL-induced signalling. In both of these complexes, the LUBAC catalytic subunit HOIP prevents caspase-8 activation and consequently apoptosis, whilst being itself cleaved by caspase-8 during apoptosis. Another target of LUBAC is RIP-1, which when poly-ubiquitinated fails to form the RIP-1/RIP-3/MLKL complex so that necroptosis is prevented. Moreover, LUBAC promotes the recruitment of the IKK complex to complex I, leading to TRAIL-induced NF-κB activation [238].

Taken together, the signalling pathways engaged by TRAIL appear to be multiple and interrelated, with outcomes as diverse as cell death and cell survival depending on the relative amounts and activities of the various regulators.

3.3 TRAIL-based anti-cancer therapies and their limitations

Initially identified for its sequence homology with CD95L and TNF, TRAIL preferentially kills cancer cells in absence of the systemic toxicities observed for other death ligands [164,239,240]. As the status of the tumour-suppressor p53, which is mutated in many cancer cells and thus limits the efficacy of genotoxic therapies, appears to be mostly irrelevant for apoptosis induction via death receptors engagement, these findings boosted interest in exploiting TRAIL signalling for cancer therapy [241]. However, recombinant TRAIL variants performed poorly in clinical trials. The reasons for such limited efficacy can be summed up in three main points: first, the lack of patient stratification based on reliable signatures or biomarkers that indicate TRAIL susceptibility. Second, the low efficacy of first-generation TRAIL therapeutics. Third, the intrinsic or acquired resistance of many cancer types to TRAIL monotherapy

The absence of patient stratification is a limitation that needs to be addressed within the design of clinical trials. Strategies to identify which specific tumour cells may be most responsive to the targeting of death receptors is indeed urgently needed [242].

Regarding the TRAIL-based therapies, these can substantially be distinguished in two groups: humanised recombinant TRAIL (rhTRAIL) and agonistic antibodies for TRAIL-R1 or TRAIL-R2. rhTRAIL variants target both DR4 and DR5, potentially resulting in a stronger death signal compared to the engagement of a single receptor. A drawback of this strategy is that rhTRAIL can also bind decoy receptors, consuming the TRAIL dose that actually induces apoptosis. Dulanermin was the first recombinant TRAIL variant tested in clinical trials. Unfortunately, with its short serum half-life (30–60 minutes) it achieved no significant improved anti-tumour activity compared to standard therapies [243–246]. A more recent trial for patient with non-small-cell lung carcinoma (NSCLC) treated with Dulanermin in combination with chemotherapy (NCT03083743) showed improved progression-free survival (PFS) but no improvement in overall survival (OS) [247]. The poor efficacy of soluble TRAIL when applied systematically seems to be due to its pharmacokinetic properties, as it gets rapidly cleared from the serum [248]. In contrast, agonistic and fully human TRAIL-R-specific antibodies exhibit longer half-lives and higher stability compared to recombinant forms of TRAIL, and at the same time remain well tolerated. Among the TRAIL-R1-specific agonistic antibodies, mapatumumab has reached phase II clinical trial and has been tested for patients with NSCLC, multiple myeloma, non-Hodgkin's lymphoma and hepatocellular carcinoma, in which it showed a very good safety profile. When administered as a monotherapy in patients with follicular non-Hodgkin's lymphoma it caused complete or partial clinical responses. However, its efficacy was not reproducible in other phase II clinical trials, and phase III clinical trials have not commenced [249]. Conatumumab is a TRAIL-R1-specific agonistic antibody that has entered phase II of clinical testing for pancreatic, breast and lung cancers. Unfortunately, despite encouraging *in vitro* results, also this TRAIL-R agonistic antibody elicited disappointing effects in trials [249]. An explanation for the poor efficacy of TRAIL-R agonists might be found in the mechanism of death receptors engagement. In fact, Bivalent antibodies stimulate only two death receptors molecules, thus that trimerization and higher oligomerisation, as required for proper DISC formation and apoptosis induction, are not achieved [250,251]. In addition to this, the development of TRAIL-R antibodies should take into account the different activation modes required by DR4 and DR5: while DR4 can get activated by both membrane-bound TRAIL and soluble TRAIL, DR5 requires membrane-bound TRAIL or soluble TRAIL secondarily cross-linked by antibodies [251,252]. It also has to be noted that the fragment crystallizable (Fc) part of such antibodies can bind to cells in the blood stream, which contributes to lowering their concentration at the tumour site [236].

In order to overcome the shortcomings of first generation of TRAIL-based therapeutics, several strategies have been adopted to improve their stability, pharmacokinetic, valency and cytotoxicity. In this respect, important contributions came from R.E. Kontermann and his group. In a first instance, they increased the stability of TRAIL molecules by fusing them with short peptide sequences to covalently link three extracellular domains of TRAIL. The resulting single chain TRAIL (scTRAIL) was a stable trimer that was further improved in subsequent studies. In particular, M. Siegemund and co-workers developed scTRAIL variants with rationally designed N- or C-terminal deletions and with specific linker sequences that led to fully bioactive scTRAIL molecules with increased thermal stability, solubility and production rate [253]. In a follow-up project, M. Hutt and colleagues worked on a molecule with improved valency, with the aim of augmenting its potential to induce apoptosis. They found that integrating two scTRAIL units in one molecule, by fusing them to dimerization modules, could achieve this goal. In particular, they fused scTRAIL to the C-terminus of the Fc part (Fragment crystallizable region) of a human IgG1, generating a dimeric protein covalently linked via disulfide bonds in the Fc region (Fc-scTRAIL). The resulting hexavalent molecule was named IZI1551 [254]. The use of the Fc region prolonged the half-life of the protein *in vivo* because it increased its size and it also allowed to exploit the FcRn-mediated recycling process [255]. In this study they also reported the potent anti-tumour activity of their new construct in mice xenograft models. Overall, the development of new-generation TRAIL receptor agonists, such as the hexavalent fusion protein IZI1551 (represented in *figure 4*), provides a promising strategy to exploit the TRAIL potential in cancer therapy. Hexavalent TRAIL variants are currently tested in phase II clinical trials (NCT04570631, NCT03082209).

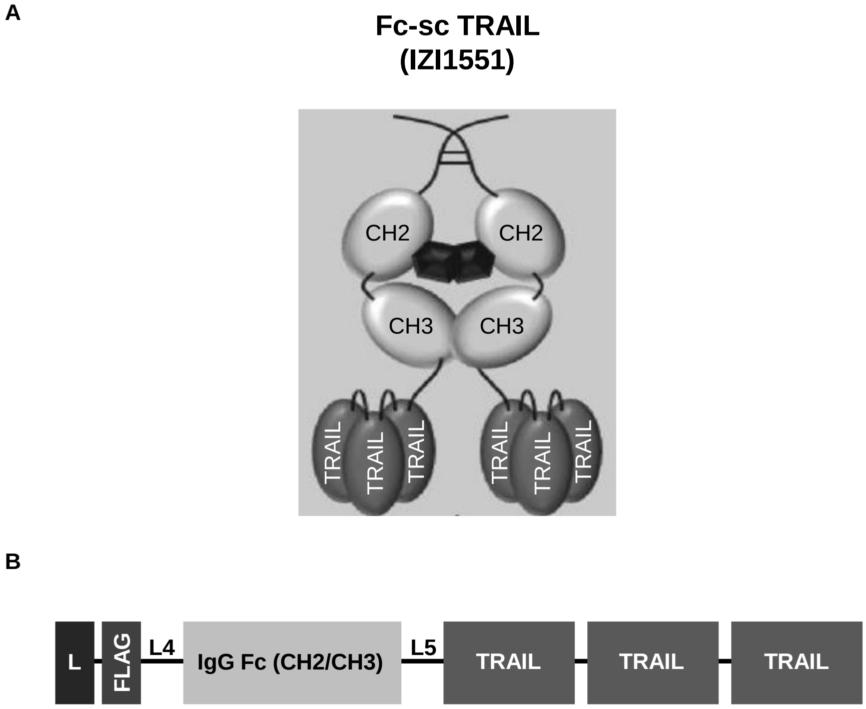

Figure 4: Structure of Fc-scTRAIL (IZI1551)

(A) *Schematic representation of Fc-scTRAIL (IZI1551).* ***(B)*** *Fc-scTRAIL structure. L= Igκ chain leader sequence; L4=GGGGSGT linker; L5=GGSGGGSSGG linker; C =constant domain of the heavy chain. TRAIL subunits are connected by a glycine residue as linker. The Fc fusion protein forms covalently linked dimers due to disulfide bridges in the hinge region of the Fc part. Adapted from Hutt, M. et al., (2017)* [254].

3.4 Need for anti-cancer combination therapies

Many cancer types, and in particular glioblastoma, display an acquired or intrinsic resistance to TRAIL [256–259]. The acquired resistance is due to adaptive mechanisms that arise in response to treatments and they result in the clonal expansion of already existing resistant cells [260]. The intrinsic resistance instead, is due to a deregulation of the expression and/or the function of anti- or pro- apoptotic proteins [261]. Such resistances, together with the limited efficacy that TRAIL-based monotherapy elicited in clinical trials, led to the development of rationally designed multi-drugs combinations that could boost the effect of this drug. Such designs are based on the continuously increasing understanding of signalling triggered by TRAIL receptors and on drug interaction studies conducted to identify TRAIL sensitisers [262,263]. Moreover, as previously described, stimulation with TRAIL does not necessary trigger cell death but can also engage survival pathways and become tumourigenic. For example, in NSCLC and pancreatic ductal adenocarcinoma (PDAC), it was found that the endogenous TRAIL/TRAIL-R-system promotes progression, invasion and metastasis of KRAS-mutated cancers [264]. Hence, the use of TRAIL itself and the design of combination therapies should aim at blocking these unwanted pro-tumourigenic effects.

Administering drugs as part of combination therapies is a very common clinical practice to maximize the therapeutic efficacy of cancer treatments and allows using lower doses of each drug in the cocktail. This would reduce their adverse effects, as well as minimize the induction of drug resistance. Also, a drug combination can trigger a synergistic effect, where the synergy is defined as a combined effect that is greater than the additive effect of each individual drug. Several TRAIL sensitisers have been identified and many combination treatments have entered clinical trials [265]. These are wisely reviewed elsewhere and will not be described extensively here [263,266]. Just as an example of the mechanisms by which TRAIL sensitisers can exert a synergistic effect in combination treatments and overcome the TRAIL resistance, it is interesting to mention the BH3 mimetics. These are small molecules that mimic BH3 proteins by binding to anti-apoptotic Bcl-2 family members, that are frequently overexpressed in solid tumours [267–269]. In glioblastoma, as well as in other cancer types, targeting overexpressed Bcl-2 proteins allowed to restore an apoptosis facilitating balance between pro- and anti- apoptotic proteins, thereby sensitising cancer cells for TRAIL-induced cell death [257,270]. Among the Bcl-2 antagonists developed, some resulted to be highly specific for their target protein and received FDA approval. In particular, ABT-199 (Venetoclax), a specific Bcl-2 inhibitor, was approved in 2016 for the treatment of chronic lymphocytic leukemia (CLL) [271]. Other specific inhibitors include WEHI-539, a selective inhibitor of Bcl-xL, and S63845, that has proven to be a highly selective and potent Mcl-1 inhibitor that was also safe to use in *in vivo* studies [272,273].

Among the most potent TRAIL sensitisers are also proteasome inhibitors, a class of drugs in which various compounds already were approved as monotherapies in myeloma [274,275].
Taken together, these considerations indicate that, thanks to combination treatments, the TRAIL anti-cancer potential can be exploited even in cancer types that appear resistant to TRAIL monotherapies.

4. The Proteasome

The proteasome is a highly sophisticated protease complex that consumes ATP molecules for selectively breaking down most of the intracellular proteins, accounting for 80-90% of the normal protein turn-over of the cell. In contrast to lysosomal degradation, which mostly degrades long-lived and membrane proteins through the autophagy system, the proteasome degrades soluble proteins, especially also short-lived regulatory proteins. Furthermore, proteins damaged by oxidation or that are intrinsically unstructured (also known as natively unfolded proteins) or misfolded are likewise degraded by the proteasome [276–278] Importantly, the vast majority of proteasomal substrates need to be marked with polyubiquitin chains to be degraded. These can also be removed by the action of cellular cysteine-protease and metalloprotease deubiquitylating enzymes (DUBs), which consequently stabilise target proteins and make ubiquitin moieties available for recycling.

The proteasome comprises two sub-complexes: the catalytic core particle (CP) and the regulatory particle (RP). The CP has a sedimentation coefficient of 20S and therefore it is referred to as 20S proteasome. The RPs can be one or two, their sedimentation coefficient is of 19S and they bind to both ends of the 20S proteasome. All together these particles form on holoenzyme of 2.5 MDa that, in density gradient centrifugation analysis, has a sedimentation coefficient of 26S. Hight resolution analysis of the proteasome architecture revealed that this complex has a highly conserved structure from yeast to human [279].

The 20S proteasome has a cylinder-like structure with two outer α-rings and two inner β-rings, which are respectively made up of seven α and seven β subunits. The α subunits have structural functions while the two inner β-rings form the catalytic chamber. Each β-ring contains three catalytically active sites made of threonine residues at their N-termini and show hydrolase activity. These sites differ in their substrate specificity and activity and have been named after enzymes that show similar functions. In particular, β1 provides caspase-like/PGPH (C-L/peptidyl-glutamyl-peptide hydrolysing) activity and cleaves peptide bonds at the C-terminus of acidic residues, β2 provides trypsin-like activity (T-L) and cleaves at basic residues and finally β5 is associated with a chymotrypsin-like (CT-L) activity that recognises hydrophobic amino-acid residues [280]. These three catalytic subunits are threonine proteases and they cleave the substrates in a two-steps process: first, the threonine of the active site attacks the N-terminal of the substrate to form a covalent ester bond and then the intermediate gets hydrolysed for releasing the product and regenerate the active form of the protease.

The centre of the α-ring is almost completely closed. The N-termini of the α subunits form a physical barrier that prevents bulky proteins to enter the inner chamber. Only substrates that are able to pass the opening at the centre of the α-rings can access the active sites. Here, client proteins are degraded into oligopeptides of 3 to 15 amino-acids of length. These are subsequently hydrolysed to single amino acids by oligo-peptidases and/or amino-carboxyl peptidases that associate with the 26S proteasome [281,282].

The RP comprises two sub-complexes, termed the base and the lid. The base contacts the CP directly but loosely and contains both a ring of AAA-ATPases (Rpt1-6) with unfoldase activity and non-ATPase subunits (Rpn1, Rpn2, Rpn10 and Rpn13) that function as ubiquitin-receptors. Of these, Rpn10 recognizes ubiquitin via the ubiquitin-interacting motif (UIM) and Rpn13 via its N-terminal pleckstrin-like receptor for ubiquitin (PRU) domain. The C-terminal domain of this subunit binds to and activates a DUB that releases the ubiquitin moieties from poorly or wrongly ubiquitylated substrates, such that they are allowed to escape the proteasome. The lid is the more peripheral part and it is made up of 10 non-ATPase subunits with various functions, for example enforcing the lid-base contacts. Once client substrates are engaged, the association between CP and RP is enforced and their contact is also visually altered, such that engaged and non-engaged 26S proteasome can be distinguished. The ring of Rpt subunits hydrolyses ATP to unfold protein substrates. An important Rpt is Rpt11 that, together with other loosely associated DUBs, catalyses the release of poly-ubiquitin chains from protein substrates. This allows the subsequent degradation of the substrate, since ubiquitin links make the proteins particularly stable and unable to translocate into the CP [283].

The RP exists in four main states, namely S_A, S_B, S_C, and S_D, that can undergo conformational transitions to subsequently progress from one state to the following one. While the CP remains unchanged, the base and the lid change their relative orientation. S_A represents the ATP-bound proteasomes and it is the conformation at rest, which is ready to bind the substrate. The S_A/S_B transition consists in movements of the lid. S_B/S_C involves rearrangements of the ATPase subunits of the base that allows the opening of a wide central channel. Finally, during the S_C to S_D transition, interactions between the C-terminus of Rpt6 and the CP allow the opening of the gates to the CP, such that the substrate can pass through. These conformational transitions influence the affinity of the proteasome for the ubiquitin chains. They are sensed by the DUBs Usp14, that stimulates the ATPase activity of the Rpt motor [284]. The gating of the RP channel controls not only the entrance of the substrate but also the release of products via the axial channel route out of the CP, a process that is specifically regulated by an ATPase in the base of the RP [285]. A schematic representation of the proteasome is provided in *figure 5*.

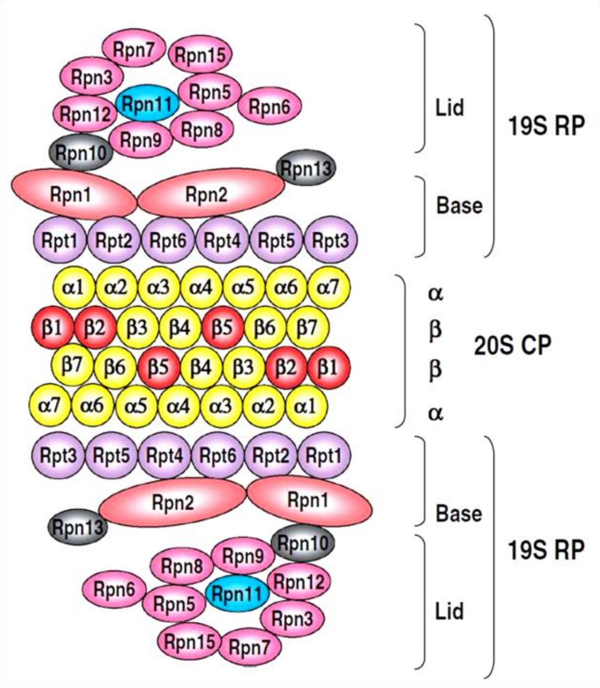

Figure 5: Schematic representation of the proteasome with its subunits

26S proteasome consisting of the CP, core particle (20S proteasome) with its α and β subunits and the RP, regulatory particle (19S) comprising the base and lid subcomplexes. Rpn, RP non-ATPase; Rpt, RP triple-ATPase. Modified from Tanaka, K. et al., (2009) [282].

4.1 The ubiquitin-proteasome system (UPS)

Ubiquitin is a small, ubiquitously expressed protein of 76 amino acids that is highly conserved in the eukaryotic kingdom. Several moieties of ubiquitin form a chain that gets covalently attached to target substrates. This occurs through an iso-peptide linkage between the protruding C-terminal glycine of a ubiquitin molecule and the ε-amino group on the side chain of a lysine residue exposed on the surface of the target protein. Depending on the specific lysine residue that gets ubiquitylated, the substrate is directed to a different fate (*figure 6*). Normally, K48-linked polyubiquitinated proteins are very unstable and are addressed to the 20S proteasome. Responsible for this process are three enzymes that act sequentially to couple ATP hydrolysis with ubiquitin-substrate conjugation. These are: the ubiquitin activating enzyme or E1 enzyme, the ubiquitin conjugating enzyme or E2 enzyme and the ubiquitin ligase or E3 ligase [286]. The number of conjugated ubiquitins needed for the recognition by the proteasome typically was considered to be about four molecules, yet small substrates between 20 and 150 residues can be monoubiquitinated or even multi-monoubiquitinated and recognized by the proteasome [287].

The ubiquitin-proteasome pathway, depicted in *figure 7*, begins with a ubiquitin that needs to be activated. This is achieved by adding it to E1 in an ATP-dependent manner. Thereafter, activated ubiquitin is transferred to the ubiquitin-conjugating enzyme E2. E2 interacts with E3, the enzyme selecting the substrates that are ubiquitylated. From the E2-activated ubiquitin intermediate, the ubiquitin molecule gets conjugated to the target protein on E3. In this way, a ubiquitin chain gets polymerized and acts as a signal that shuttles target proteins to the 26 proteasome[286]. Four main types of E3 enzymes, classified by their mechanisms of action, have been identified: HECT, RING, U-box, and RING-between-RING (RBR). In eukaryotes, there are more than six hundred different E3 ligases with different substrate recognition elements bound to a few common scaffolds. For example, the RING family of E3 ligases comprises the multi-subunit Cullin-RING ligases (CRLs) that exploit one of several Cullin isoforms to scaffold the complex [283]. LUBAC instead, is a multi-subunit member of the RBR family of E3 ligases. Even though lysine attachment is the most frequently observed, in the case of LUBAC the peptide bond is formed between the N-terminal of a methionine residue in a ubiquitin molecule and the C-terminal glycine of the next chain, such that a linear ubiquitin chain is formed [288].

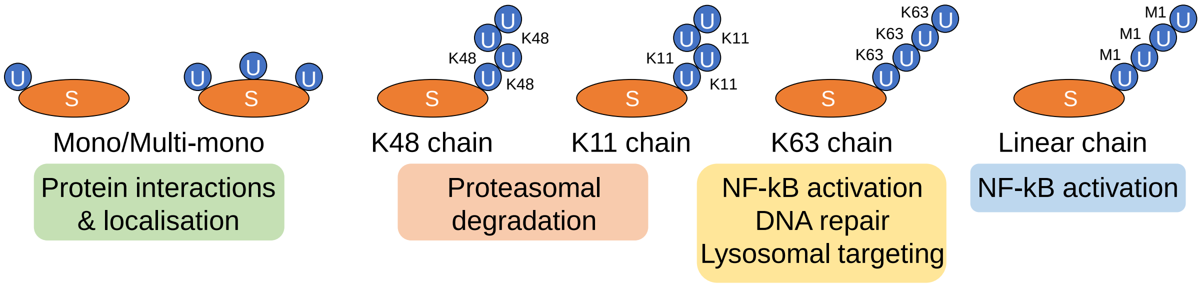

Figure 6: Different ubiquitination modalities and their functions

Several types of ubiquitination with specific roles. Ubiquitin forms iso-peptides linkages between a glycine in its C-terminus and the ε-amino group of a lysine residue in the substrate or in another ubiquitin molecule. Substrates can be monoubiquitinated, multi-monoubiquitinated or polyubiquitinated in different conformations signalling a different fate as indicated in the figure. U: ubiquitin; S: substrate; K= lysine; M: methionine. Modified from Park, C. W. & Ryu, K. Y. (2014) [289].

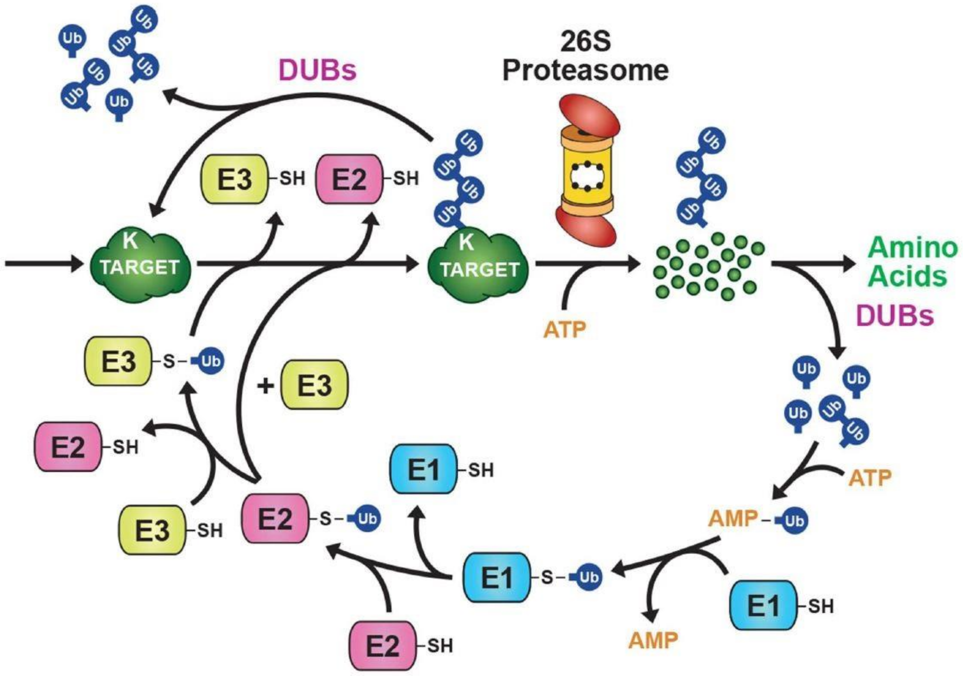

Figure 7: Schematic representation of the ubiquitin-proteasome pathway

The UPS pathway begins with the E1-activating enzyme that activates ubiquitin in an ATP-dependent manner. Activated ubiquitin is then transferred to the E2-conjugating enzyme that attaches it to the E3-ligating enzyme carrying the target protein. This results in a ubiquitin-protein conjugate where a C-terminal glycine of ubiquitin is linked through an iso-peptide bond to an ε-amino group of a lysine residue (K) exposed by the target protein (or another ubiquitin molecule for elongating the ubiquitin chain). Iterations of this process form the poly-ubiquitinated conjugate that can either be disassembled by DUBs or delivered to the 26S proteasome for degradation. In both cases, the ubiquitin molecules are released to be re-used. Modified from Marschall, R. S. & Viestra, R. D. (2019) [283].

4.2 Proteasome inhibition-mediated apoptosis

As most of the cellular proteins are degraded via the UPS, the proteasome carries out a pivotal function in the maintenance of cell homeostasis (proteostasis) and such role can be exploited as a therapeutic target in cancer cells. Indeed, compared to normal tissues, cancer cells generally display a higher rate of protein turnover, meaning that they are more susceptible to proteasome inhibition. That is why, since 2003 when bortezomib (BTZ) gained accelerated FDA-approval as the first proteasome inhibitor (PI) for the treatment of relapsed and refractory multiple myeloma, several other PIs have been investigated as anti-cancer treatments [290]. Additionally, other strategies to target the UPS for cancer therapy are under evaluation. These include inhibitors of the E3 ligase pathway, or alternatively proteolysis-targeting chimeric molecules (Protac) which are compounds that artificially and selectively target cancer-promoting proteins for ubiquitination and degradation [291,292]. PIs exert their function by targeting the β catalytic subunits of the 20S proteasome. The main target is the β5 subunit (CT-L activity), although the other two activities can also be inhibited if PIs are used at higher concentrations [293–295]. Once protein degradation is blocked, the downstream events that lead to cell death can be different, depending on both the specific mode of action of each PI and on the cell type-specific responses [296]. PIs mediate their cytotoxicity by multiple mechanisms, such as the de-activation of survival pathways or the activation of apoptosis via induction of ER stress, accumulation of intrinsic or extrinsic apoptosis proteins or induction of p53-dependent apoptosis.

A well-studied mechanism by which PIs provoke the inactivation of survival pathways is the inhibition of IκBα (NF-κB inhibitor alpha) degradation. In fact, IκBα is an inhibitor of the transcription factor NF-κB and it needs to be degraded to allow its function. If IκBα is not degraded, it sequesters NF-κB such that pro-survival factors and anti-apoptotic genes like those encoding for Bcl-xL and IAPs proteins cannot be transcribed [297]. This has been observed in cutaneous T-cell lymphoma (CTCL), which often displays a constitutive NF-κB activation that confers apoptosis resistance. Such resistance can be overcome upon bortezomib treatment, that induces nuclear translocation and accumulation of IκBα, which in turn associates with NF-κB p65 and p50 in the nucleus and inhibits their binding to the DNA [298,299]. In conclusion, these and other reports proved that PIs can act as indirect inhibitors of the NF-κB survival pathway via stabilisation of its inhibitor IκBα [300,301].

Proteasome inhibition can also promote apoptosis activation, as many apoptosis regulators have been identified as proteasome targets. Indeed, preventing the degradation of pro-apoptotic proteins alters the life/death stimuli balance towards cell death. For example, tBID is an unstable protein that is targeted by the proteasome. Increased tBID stability eases to reach the tBID threshold concentration required for cytochrome c release and apoptosis execution [302].

In many tumour cells, PIs trigger a p53-depend type of apoptosis, for example by inducing the expression of PUMA [303–305]. However, the cytotoxicity of PIs is not necessarily mediated by p53 and even in cancer types that bear a mutated form of this protein, PIs can still induce apoptosis [306]. The cellular levels of p53 are controlled by E3 ligases such as MDM2 that, alone or in concert with MDMX, mediates its ubiquitination and proteasomal degradation [307–309]. Moreover, MDM2 induces a conformational change in p53 that inhibits its binding to the DNA, making MDM2 a master repressor of p53 [310]. Interestingly, not only MDM2 regulates p53 via ubiquitination but MDM2 itself undergoes self-ubiquitination and gets degraded by the proteasome. Therefore, the p53-MDM2 balance, on which the cell fate depends, overall is regulated by proteasomal activities [311]. Among the target genes of p53 is also MDM2 itself such that, in normal cells, p53 induces MDM2 transcription, generating a negative feedback loop between these two proteins that results in low levels p53 [312]. With MDM2 being upregulated in many cancer types, p53 gets degraded and cannot exert its anti-tumour activity, making MDM2 an oncogene [313–315]. Upon PIs treatment, the short-life protein p53 is stabilised and the products of its target genes accumulate. Consequently, although MDM2 remains bound to p53, in the presence of a PI it can no longer prevent its nuclear translocation and activity [316].

Among the important proteins of the apoptotic pathway affected by PIs is also DR5, which at high amounts can facilitate apoptosis execution. Multiple reports utilising different PIs have shown an upregulation of this death receptor on the cell surface, mostly due to ER stress-induced upregulation of ATF4, ATF3 and CHOP that indeed regulate DR5 expression [317–319].

It is also relevant to mention is that PIs can alter cell cycle progression because cyclins, whose balance is tightly and temporally regulated, are proteasome targets. Blocking cyclin D1 degradation can prevent cell division and induces death in mantle cell lymphoma [320,321]. The blockade of cell cycle progression can also be one of the reasons why proliferating cells are more susceptible to PI compared to normal cells [322,323]. Indeed, the cyclin-dependent kinases (cdk) inhibitor p27, that in quiescent cells exhibits a smaller amount of ubiquitination compared to proliferative cells, gets stabilised upon proteasome inhibition, resulting in cell cycle arrest [324]. An extensive review of E3 ligases by I. Gupta and colleagues more comprehensively summarises important apoptotic targets of the UPS and describes the crosstalk between the UPS and apoptosis pathways [325].

In addition to the abovementioned effects occurring upon PI treatment, the most direct and important consequences of blocking the proteasome are the induction of ER stress and the deprivation of amino acids. By preventing the degradation of ubiquitinated targets, PIs lead to the accumulation of misfolded proteins, including those normally translocating out of the ER to be degraded by the proteasome. The resulting ER stress activates the UPR (unfolded proteins response), causing the cell cycle arrest and ultimately apoptosis [326,327]. Moreover, in the absence protein degradation, cells are deprived of their main source of recycled amino acids. A. Suraweera and colleagues showed that this shortage of amino acids, in particular the essential cysteine and asparagine, triggers the integrated stress response (ISR), a pathway that eventually leads to cell death[328].

It is important to note, that the assumption that the cytotoxicity of PIs arises from altered protein turnover is based on studies performed with concentrations and treatment regimens that often exceed those achievable clinically, raising the question which processes induce cancer cell toxicity in patients. For example, in primary human umbilical vein endothelial cells, bortezomib inhibits NF-κB activation with an IC_{50} of approximately 0.5 µM [329]. In patients instead, a subcutaneous administration of bortezomib results in a peak plasma concentration of up to 50 - 100 nM, which is only maintained for around 2 hours [330]. These and other studies highlight that the PI doses required to affect protein levels are actually higher than those necessary for exerting a cytotoxic effect, pointing to mechanism different from an altered protein turnover as the main reason for the clinical efficacy of these drugs. As critically reviewed by L.D. Fricker, an explanation could be that the proteins responsible for cell death upon bortezomib treatment might require only small changes in their turnover to elicit cytotoxicity, so that even moderate perturbance of cellular protein turnover might suffice to induce cell death [331]. In fact, treating mantle cell lymphoma cell lines with a low bortezomib concentration (10 nM) resulted in substantial changes in the levels of the short-lived protein Noxa within the first 8 h, eventually leading to cell death [332]. Still, the quick effects triggered by proteasome inhibition appeared paradoxical if considering the time required for altering the general protein amounts at a detectable level. The same author has interestingly discussed on the possible role of peptides released from the proteasome, which are found in tissue extracts as well as in cultured cells. Quantitative peptidomics analysis revealed an altered level of such peptides upon PI but their biological activity is still elusive and so far, there is only speculation as to whether they mediate the therapeutic or side effects of proteasome inhibition [333,334].

Taken together, the crosstalk between the UPS and the apoptosis pathways is complex but highlight the proteasome as a relevant target in cancer therapy. The development of novel proteasome-targeting therapeutics is described in the following paragraph.

4.3 Marizomib as a second-generation proteasome inhibitor

In the early 90’s, the company MyoGenetics developed a compound named MG-341 for the treatment of muscle-wasting conditions but, unfortunately, its high toxicity prevented its use in patients with such diseases. Over the years, MyoGenetics became ProScript and the drug, renamed PS-341, was tested for its cytotoxic activity in MCF-7 human breast carcinoma cells, yielding an an IC_{90} of 0.05 µM upon 24 hours of exposure [335]. With an optimised formulation, the drug subsequently entered clinical trials in 2002 as bortezomib (Velcade®) and became the first ever PI approved by the FDA [336]. Initially used for the treatment of refractory multiple myeloma, it was later also approved for patients with relapsed or refractory mantle cell lymphoma [337]. In solid tumours, however, bortezomib instead provided disappointing results [338,339]. Reasons for such resistance have been investigated and appeared to be multifactorial. For example, in hepatocellular carcinoma, an increased expression of the β1 and the β5 proteasome subunits, as well as the loss of the ability to stabilize and accumulate pro-apoptotic proteins, were reported to be the among the contributors to the acquired bortezomib-resistance [340].

The limitations of bortezomib-based therapies led to the formulation of second-generation PIs. Second-generation PIs exhibit improved binding and specificity, which increases their potency and reduces their off-target effects, such as the typical peripheral neuropathy induced by bortezomib [341–343].

Natural and synthetic PIs differ in their chemical structure and interaction with the proteasome. A general distinction can be made between those that form a covalent bond with the threonine active site and those that instead form non-covalent bonds, with the latter being considered reversible. In the case of irreversible inhibitors, the recovery of normal cell activities following sublethal proteasome inhibition is slow, probably due to the need for *de novo* proteasome synthesis. Covalent binding is achieved through an electrophilic trap where the threonine of the active site interacts with a peptide moiety. Depending on the nature of the electrophilic traps employed, different classes of PI can be defined.

Peptide boronates are the class of PI to which bortezomib belongs (*figure 8*). Peptide boronates form tetrahedral adducts with the threonine of the active site and these are further stabilized by a hydrogen bond between the N-terminal amino group of the threonine and the N-terminal of the hydroxyl groups of the boronic acid [280] (*figure 9*). Bortezomib primarily inhibits the CT-L activity of the proteasome (at small nanomolar concentrations - below 50 nM - and in very short times - within the first 15 minutes -) and only partially its C-L activity [344]. The drug increases both OS and PFS in patients with relapsed multiple myeloma but side effects have been observed in 30% of cases, including thrombocytopenia and especially the abovementioned peripheral neuropathy [345–347]. Bortezomib preferentially and with higher affinity inhibits the proteasome, but also serine proteases can be inhibited as off-targets, as it was shown for HtrA2, an ATP-dependent serine protease of the mitochondria. Due to the mitochondrial role of HtrA2 in neurons, this is considered to be a possible reason for bortezomib-associated neuropathies [341]. Even though a reversible PI, the dissociation rate of the boronate-proteasome adduct formed by bortezomib is very slow (up to one day), so that bortezomib can be considered to be a slowly reversible inhibitor [348,349]. To allow deeper tissue penetration, second-generation variants with higher off-rates and consequently larger volume of distribution were developed [350].

To overcome the undesirable side-effects of boronic acids, more specific and potent PIs have been developed, such as peptide epoxyketones like carfilzomib (*figure 8*). The potent inhibitory effect of these class of PIs arises from a very specific catalytic mechanism. The catalytic hydroxyl first attacks the carbonyl group of the pharmacophore and then the free α-amino group of the threonine opens up the epoxide to complete the formation of the morpholino adduct [351] (*figure 9*). As catalytic residues of serine and cysteine proteases do not have α-amino groups, they cannot form such adducts, which explains the specificity of the epoxyketone moiety for the proteasome. Therefore, carfilzomib produces less off-target effects compared to bortezomib, which led to its clinical approval in 2012 [352,353]. Carfilzomib irreversibly inhibits the CT-L activity of the proteasome and and appears more potent than bortezomib *in vivo*. At highest dose, it achieved 88% of proteasome inhibition in a phase I trial, whereas the inhibition by bortezomib did not exceed 70% at the maximal tolerated dose [354,355].

Another class of PIs are the β-lactones, which are naturally occurring non-peptide compounds. Compared to epoxyketones, β-lactones are less specific as they can also inhibit some serine proteases, such as the lysosomal cathepsin A and the cytosolic tripeptidyl peptidase II [356,357]. Salinosporamide A, a secondary metabolite produced by the obligate marine actinomycetes bacteria of the genus Salinispora, species *S. tropica*, belongs to this class of PIs. It was discovered in 1989 in near-shore marine sediments of the Bahamas islands during explorations conducted by the Scripps Institution of Oceanography (SIO; University of California, San Diego) [358,359]. Salinosporamide A was then processed by Nereus Pharmaceuticals (San Diego) under the names NPI-0052 and marizomib [359] (*figure 8*). The fact that a prokaryotic organism can generate a proteasome inhibitor raises the question of how this species can survive the effect of its own product. It was found that, although in *S. tropica* the proteasome is essential, the operon responsible for marizomib biosynthesis also encodes different β-subunits. Such variants bear ammino acid substitutions (A49V and M45F) that confer a reduced sensitivity to marizomib compared to the subunits encoded in other parts of the genome [360]. Interestingly, point mutations in the β5 subunit of the 20S proteasome (PSMB5) resembling those in *S. tropica* were found in human cells with an acquired resistance to bortezomib or marizomib, pointing to a common mechanism by which resistance to proteasome inhibitors can arise [361].

Marizomib inactivates the proteasome by a unique mechanism, which consists of the opening of the β-lactone ring followed by formation of a tetrahydrofuran ring as the result of the nucleophilic displacement of the chloride atom of the inhibitor [362] (*figure 9*). Normally, all β-lactone adducts are slowly hydrolysed by water, resulting in the reactivation of the proteasome [363]. However, the tetrahydrofuran ring formed by salinosporamides stabilizes the adduct, resulting in a prolonged inhibition and enhanced potency, due to which marizomib is considered an irreversible PI [364,365]. It seems that it is this irreversibility, rather than differences in cellular uptake, that explains the greater potency of marizomib compared to reversible analogues that do not bear a chlorine chemical-leaving group, such as the PI NPI-0047 [366].

Marizomib is a PI of particular interest for several distinctive characteristics. For example, it inhibits CT-L activity with very low IC_{50}, which in certain cell lines is reported to be as low as 2.5 nM. Additionally, while other PIs almost exclusively target the CT-L activity of the proteasome, marizomib also blocks the β2 subunit with an IC50 = 26 nM and the β1 subunit with IC50 = 330 nM [362,367]. This feature is of particular relevance if considering that resistance to PIs like bortezomib frequently arises from hyperactivation of the β1 and β2 subunits as a compensatory response to the blockade of the β5 proteolytic site, or from mutations of the β5 subunit in the PI binding pocket [368,369]. Studies conducted in patients with solid tumours or haematological malignancies revealed that one cycle of marizomib at therapeutic doses can be sufficient to achieve full inhibition of the CT-L activity, while C-L and T-L activities were initially unaffected or increased, suggesting a compensatory hyperactivation of these other subunits. Importantly, continued marizomib administration allowed, by the end of cycle 2, to overcome these compensatory responses, with up to 80% and 50% inhibition of the T-L and C-L activities respectively [368]. All together, these effects might explain the efficacy of marizomib in patients that are resistant to the treatment with other PIs such as bortezomib [370].

An additional advantage of marizomib compared to bortezomib is that it can be administered orally, as documented in mouse experiments [371]. Although orally available, bortezomib is typically injected intravenously to improve its bioavailability and rapid distribution, and to prolong its half-life [372]. Marizomib instead, even when administered orally, significantly and dose-dependently inhibits the CT-L activity of the proteasomes between 0.025 mg/kg and 0.50 mg/kg. Additionally, under these conditions, marizomib also blocks the other two proteasome activities. All these analyses were conducted on whole blood lysates (WBL) from mice and demonstrated that orally administered marizomib inhibits proteasome activity *in vivo* [371].

Among all the features of marizomib, the most interesting one is that it is a small molecule (317.77 Da) with a lipophilic structure that, despite its very short half-life (<30 minutes), is considered to penetrate the BBB and to block proteasome activity in the brain of cynomolgus monkeys, rats and in orthotopic glioblastoma mice models (0.1 mg/kg or to 0.6 mg/m2; i.v) [373–375]. M.J. Williamson and colleagues have similarly reported that salinosporamide A distributes to the brain of mice and Wistar rats in amounts sufficient to cause substantial proteasome inhibition in this organ [376]. These findings contrast with the results obtained by A.V. Singha and colleagues who suggested that marizomib administered intravenously (0.15 mg/kg) in three doses does not cross the BBB of a Multiple Myeloma MM.1S murine model. Additionally, in this study, non-tumour bearing rats were intravenously injected with radiolabelled marizomib (^{3}H-NPI-0052 at 0.1 mg/kg or 0.6 mg/m^2) to find that radioactivity was barely detectable in the brain of the sacrificed animals, as measured by quantitative whole-body autoradiography (QWBA) [377]. However, it should be considered that evidence of at least regional BBB disruption exists in all gliomas, such that drugs that would not cross a healthy BBB could instead reach the tumour site [378–380]. In support of the BBB-permeability of marizomib, a very recent study was presented by D.A. Bota and colleagues in the 2019 annual meeting of "*Proceedings of the American Association for Cancer Research".* Their study assessed proteasome activity in brain samples of 15 male Swiss Webster mice treated with marizomib or vehicle control (0.3 mg/kg, i.v). In these models, they found that the activity of all 3 proteasome subunits, and especially the CT-L, was significantly reduced in the cerebellum and in the prefrontal cortex samples collected from 3 to 180 minutes post-marizomib administration [381].

Finally, it is noteworthy that marizomib treatment did not induce relevant toxicities *in vivo* when studying mice [377]. Dose limiting toxicities were reported in humans and include transient hallucinations, cognitive changes and loss of balance, probably due to its penetration into the CNS [382,383].

Overall, with its tumour specific toxicity, its potent proteasome inhibition at low nanomolar concentrations and its prolonged activity, marizomib meets the requirements of novel generation PI that could be suitable for the treatment of aggressive and poorly accessible cancers such as glioblastoma.

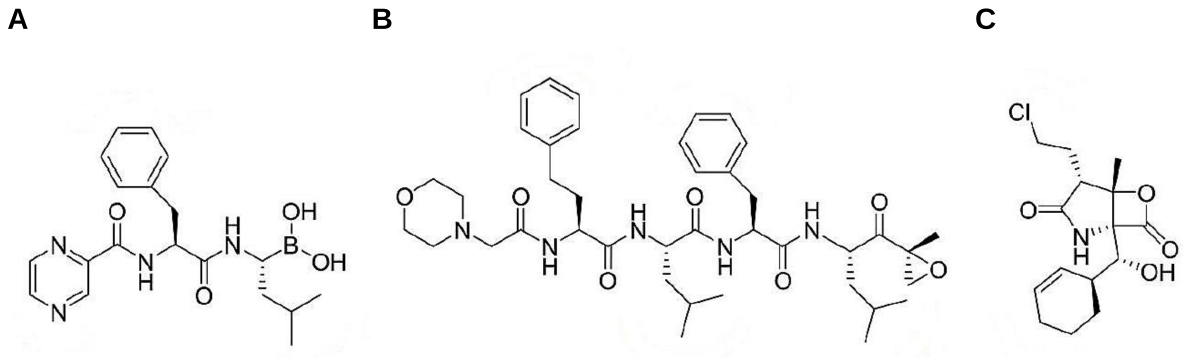

Bortezomib Carfilzomib Marizomib

Figure 8: Chemical representation of three PIs from different structural classes

The chemical structure of three PIs in clinical use is represented. ***(A)*** *Bortezomib is a synthesized peptide boronate that inhibits the proteasome in a slow reversible way.* ***(B)*** *Carfilzomib is a synthesized peptide epoxyketones that inactivates the proteasome in a highly specific and irreversible manner.* ***(C)*** *Marizomib is a naturally occurring β-lactone that irreversibly inhibits the proteasome. Modified from Cromm, P. M & Crew, C. M. (2017)* [384].

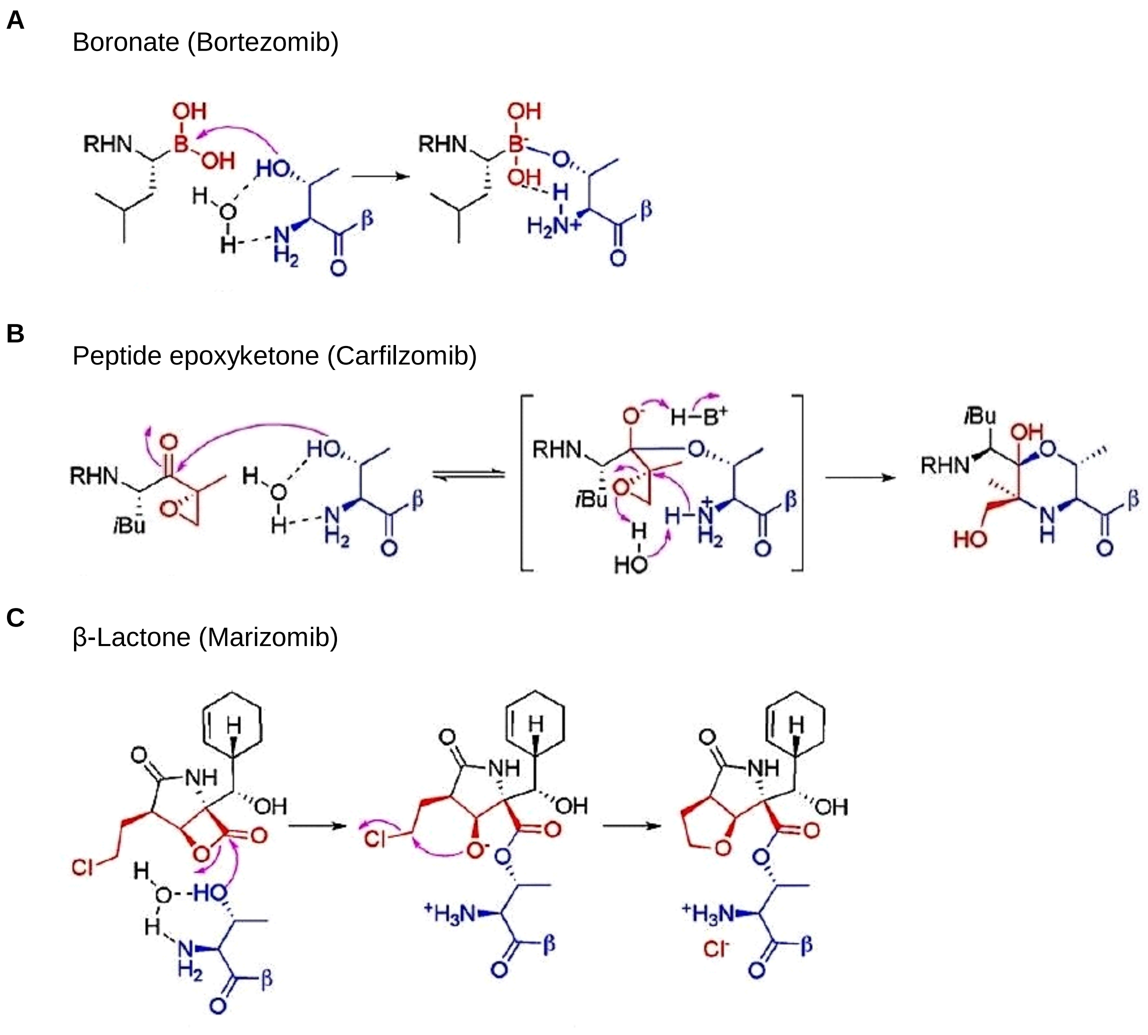

Figure 9: Mechanisms of proteasome inhibition by covalent inhibitors

Mechanism of action of three classes of structurally different PIs. The colours represent: blue for proteasome, black for PIs and red for electrophiles. ***(A)*** *Boronates like bortezomib, form a tetrahedral adduct with the active site threonine. This has a slow dissociate rate, making boronates practically irreversible over several hours.* ***(B)*** *Peptide epoxyketones like the tetrapeptide carfilzomib comprise two components: a peptide portion that binds to the substrate binding pocket of the proteasome and an epoxyketone pharmacophore that interacts with the catalytic amino terminal threonine residue to irreversibly inhibit proteasome activity. More precisely, epoxyketones have two electron deficient carbon atoms that are susceptible to the attack by the proteasome's threonine hydroxyl. Attack at the carbonyl carbon places the proteasome's terminal amino group in close proximity to the highly electrophilic epoxide ring. The subsequent ring opening by the amino group results in the formation of a stable six-membered ring.* ***(C)*** *Marizomib is a β-lactone that inactivates the proteasome by esterifying the catalytic threonine hydroxyl. After the opening of the β-lactone ring, nucleophilic displacement of the chloride atom of the inhibitor allows the formation of a tetrahydrofuran ring that stabilizes the adduct resulting in prolonged proteasome inhibition. Modified from Kissel, A. F. et al., (2011)* [385].

4.4 Proteasome inhibitors and TRAIL-based combination therapies

As introduced in the previous chapter of this thesis (see introduction chapter 3 paragraph 4), cancer patients would benefit from therapies that combine the targeting of multiple tumour-associated alterations that all together contribute to treatment resistance. The design of such combinations even for *in vitro* studies is complex, as multiple factors need to be taken into consideration. For example, the choice of the therapeutics to combine has to be driven by the knowledge of how they interact, such that synergistic cancer cell death can be triggered. Additionally, the duration and schedule of the drug exposure can be optimised if the kinetics by which treatment consequences arise in target cells are known. The rational design of cancer combination therapies that include PIs is challenging, since the inhibition of protein degradation leads to complex consequences. Indeed, as already highlighted in the previous paragraphs, treatments with PIs induce a general imbalance of protein amounts, besides activating the transcription of stress response genes [386]. Targeting the proteasome, and therefore modifying the overall cellular proteome, could sensitise cancer cells to other targeted therapeutics or conventional cytotoxic agents in multiple ways [387]. In fact, numerous examples can be found in the literature that show the synergistic anti-tumour effect of proteasome inhibitors combined with other drugs [388]. In particular, many studies reported the synergistic apoptosis-inducing interaction between PIs and the previously described death ligand TRAIL, which can arise from multiple mechanisms. For example, it was shown that, in lung cancer cells, the PI MG132 stimulates the expression of DR5 via activation of the p53 signalling. Specifically, MG132 stabilizes the transcription factor p53 that can consequently translocate to the nucleus. Here, it binds elements of an intronic region in the DR5 gene, promoting its transcription [389]. In primary chronic lymphocytic leukemia cells, bortezomib induces not only an up-regulation of the TRAIL receptors but surprisingly also a decrease in the levels of anti-apoptotic c-FLIP 228, which contradicts other studies that demonstrate c-FLIP accumulation [390–392]. Importantly, similar sensitising effect of PIs on TRAIL-induced apoptosis have also been observed in highly resistant tumours like glioblastoma. Indeed, K. La Ferla-Brühl and colleagues reported that PIs, but not NF-kB inhibition, could enhance TRAIL-induced apoptosis in glioma cells [393]. Here, PI-induced decreased expression of AKT and XIAP could be some of the reasons why glioma stem cells (GSCs) and TRAIL-resistant glioma cells could be re-sensitised to TRAIL [394]. It is relevant that studies performed on more advanced *in vitro* models of glioblastoma provided similar results. In particular, T. Unterkircher from the group of S. Fulda found that in primary and in patient-derived glioblastoma cells, bortezomib allows the accumulation of tBID, which is required for synergistic cell death upon combining PIs with TRAIL [395]. Finally, R. Koschny and the team of H. Walczak showed that, upon bortezomib-induced down-regulation of c-$FLIP_L$, highly TRAIL-resistant primary glioma cells could be sensitised to execute apoptosis

[396]. A detailed analysis of signal transduction at single cell level demonstrated that treatment with proteasome inhibitors allowed more cells to respond with caspase-8 activation upon TRAIL treatment, whereas in responding cells accumulated cFLIP and Mcl-1 delayed this activation and also elevated the threshold for apoptotic mitochondrial engagement [397].

Although these pre-clinical studies provided evidence that glioblastoma cells are susceptible to PIs, the translation of these findings into clinical trials has been so far rather disappointing. For example, a trial evaluating the intra-tumour penetration of bortezomib in patients with recurrent glioblastoma, found indeed higher drug concentration in the tumour tissue compared to the plasma. However, all patients underwent relapse within six months, which led to the termination of the study [398]. Trials of bortezomib in combination with other drugs, like histone deacetylase, bevacizumab or temozolomide plus bevacizumab, all failed to exert substantial therapeutic benefit [399,400]. A PI like marizomib instead, with its ability to penetrate the BBB and whose safety profile has already been assessed in diverse trials (NCT03345095, NCT04341311, NCT02330562), might succeed where other PIs have failed in the treatment in glioblastoma, especially if appropriate drug partners are combined with it.

5. Ferroptosis

In the landscape of all regulated cell death processes, one of the most recently identified is termed ferroptosis. Even before the definition of the ferroptosis concept, drugs inducing this previously undescribed form of cell death were discovered. Already in 2003, S. Dolma and colleagues from the group of B.R. Stockwell, performed a synthetic lethal high-throughput screening to search for genotype-selective anti-tumour agents that become lethal to tumour cells only in the presence of specific oncoproteins. In this way, they identified erastin (eradicator of RAS and small tumour antigen - ST - expressing cells), a compound that could sensitise BJ primary human foreskin fibroblasts cells overexpressing the mutant RAS oncogene to a form cell death not morphologically recognisable as apoptosis [401]. The mechanism of action of this drug was later on clarified by S.J. Dixon, who found that erastin inhibits system Xc^- and consequently leads to the transcriptional upregulation of genes linked to the ER stress response [402,403]. System Xc^- is a cell-surface cystine/glutamate antiporter composed of a catalytic and a regulatory subunit. The catalytic subunit is represented by the 12-pass transmembrane transporter protein xCT (encoded by the gene SLC7A11: solute carrier family 7 member 11), that constitutes the light chain of the protein. xCT is linked, via a disulfide bridge, to the regulatory subunit that is the single-pass transmembrane protein 4F2hc (solute carrier family 3 member 2, encoded by the SLC3A2 gene), which constitutes the heavy chain [404]. While xCT is responsible for the transport activity and is highly specific for glutamate and cystine, the function of the regulatory subunit is that of a chaperone protein and it is essential for regulating the trafficking of the catalytic subunit to the plasma membrane [405]. System Xc^- exchanges intracellular glutamate with extracellular cystine. Within the cell, cystine gets reduced to cysteine, a biosynthetic precursor of the antioxidant tripeptide glutathione (GSH), which is the necessary cofactor of enzymes such as glutathione peroxidases (GPx) (*figure 10*). GPx-4 in particular, is an enzyme containing eight nucleophilic amino acids (one selenocysteine and seven cysteines) and it is responsible for the elimination of intracellular lipid ROS [406,407]. In fact, this enzyme differs from the other members of the GPx family as it is the only glutathione peroxidase identified in mammals that can scavenge ROS inside biological membranes [408]. ROS are a chemical class that includes hydroxyl radicals ($^{\bullet}OH$), superoxide anions ($^{\bullet}O_2^-$) and non-radical species such as hydrogen peroxide (H_2O_2). These are produced as part of the physiological metabolism of the mitochondria, as well as in the endoplasmic reticulum and in peroxisomes. ROS can arise from reactions catalysed by intracellular enzymes such as NADPH oxidases (NOXs), lipoxygenases (LOXs), cyclooxygenases (COXs), xanthine oxidases (XOs), nitric oxide synthases (NOSs) and cytochrome P450. However, ROS can also be produced in non-enzymatic reactions. In particular, in conditions in which the amount of free iron in the cell exceeds homeostatic levels, the unbound metal may undergo a spontaneous Fenton, Haber-Weiss reaction (*Equations 1*, *2* and *3*). This can happen due to the depletion, or to the autophagic turn-over (ferritinophagy), of the main iron-storage protein of the cell that is ferritin [409]. With its ferroxidase activity, ferritin converts active ferrous cations (Fe^{2+}, reduced state) to unreactive ferric cations (Fe^{3+}, oxidised form) [410–413]. When ferritin reaches its capacity, free Fe^{2+} reacts with the hydrogen peroxide in the Fenton reaction, generating hydroxyl radicals and oxidizing iron to its stable Fe^{3+} form. Fe^{3+} can then be reduced back into Fe^{2+} by molecular oxygen (O_2) (*Equations 1*, *2* and *3*) [414]. The hydroxyl radicals generated in these reactions are very active and can attack not only the DNA in the nucleus and mitochondria, but they can also oxidise polyunsaturated fatty acids (PUFAs) of phospholipid bilayers, causing an altered permeability of the cellular membranes [415,416]. However, it remains to clarify how an uncontrolled PUFAs oxidation process, like that generated by non-enzymatic reactions, can fit into the definition of ferroptosis as a regulated death pathway (Fearnhead et al., 2017; Lei et al., 2019).

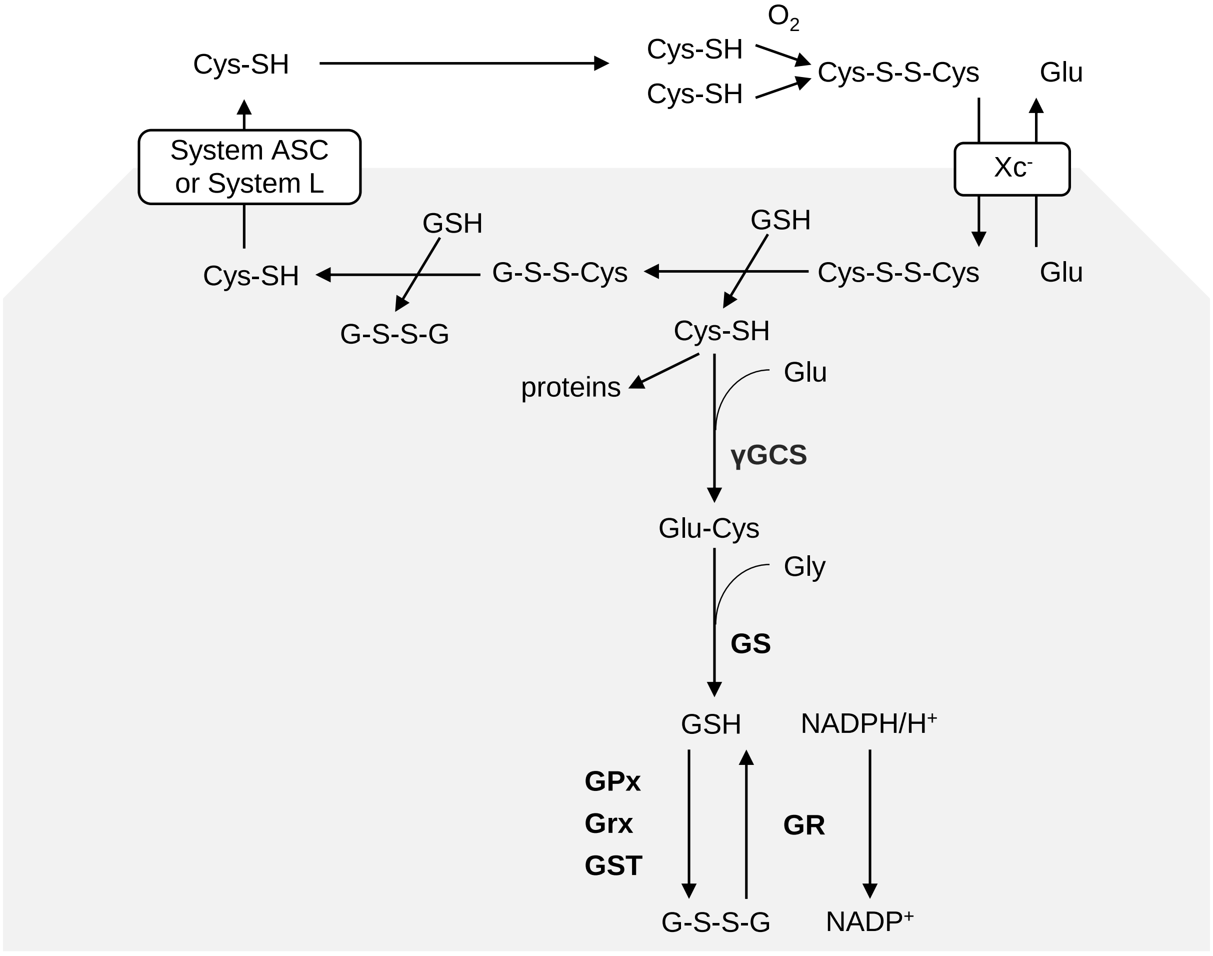

Figure 10: System Xc⁻ cystine/glutamate antiporter

System Xc⁻ exchanges intracellular glutamate for extracellular cystine to drive a cycle of redox reactions: the cystine that is taken up (Cys-S-S-Cys) is reduced to cysteine (Cys-SH), most likely by forming mixed disulfides with glutathione (GSH) (G-S-S-Cys). Cysteine can be again secreted to get oxidised back to cystine in the extracellular space. Intracellular cysteine instead is used for both protein and glutathione synthesis. GSH synthesis is a two-steps reaction catalysed by the subsequent action of two enzymes. First, the rate-limiting enzyme γ-glutamylcysteine synthetase (γ-GCS) conjugate glutamate to cysteine, forming γ-glutamylcysteine (Glu-Cys). Then, glutathione synthetase (GS) adds a glycine (Gly) to form GSH. GSH is the cofactors of enzymes such as glutathione peroxidases (GPx), glutaredoxins (Grx) and glutathione-S-transferases (GST). During the reactions catalysed by these enzymes, GSH gets converted into its oxidised form (G-S–S-G). Oxidised glutathione is recycled back to its reduced form at the expense of NADPH/H+ in a reaction catalysed by the enzyme glutathione reductase (GR). Modified from Conrad, M. & Sato, H. (2012) [406].

Fenton reaction

$$[\mathbf{1}]\ Fe^{2+} + H_2O_2 = Fe^{3+} + OH^- + \cdot OH$$

$$[\mathbf{2}]\ Fe^{3+} + O_2 = Fe^{2+} + O_2^-$$

Nett Haber-Weiss reaction

$$[\mathbf{3}]\ O_2^- + H_2O_2 = O_2 + OH^- + \cdot OH$$

Equation 1: Fenton reaction (1)

*Free Fe^{2+} can react with hydrogen peroxide, generating a hydroxyl radical ($^{\bullet}OH$) and hydroxide ion (OH^-) via the Fenton reaction, in which ferrous iron (Fe^{2+}) is oxidized to ferric iron (Fe^{3+}) **[1]**.*

Equation 2: Fenton reaction (2)

*Fe^{3+} can be reduced back to Fe^{2+} by molecular oxygen (O_2) **[2]**.*

Equation 3: Nett Haber-Weiss reaction

*Nett Haber-Weiss reaction generating hydroxyl radicals ($^{\bullet}OH$) **[3]***

Since the ferroptosis-inducer erastin was identified for the first time, further studies were conducted to elucidate its mechanism of action. In particular, it was N. Yagoda in 2007, who revealed that the mitochondrial voltage-dependent anion channels VDAC2 and VDAC3 are necessary for its lethality and that erastin alters the permeability of the outer mitochondrial membrane. Interestingly, he also observed that erastin induces a RAS-RAF-MEK-dependent oxidative cell death that does not involve cytochrome c release nor caspase-3 or PARP cleavage [417]. Later on, W.S. Yang and B.R. Stockwell published another small molecule screening in which they identified two additional compounds displaying lethality in the presence of oncogenic RAS and they named them RSL5 and RSL3 (RSL: Ras-selective lethal small molecule). Similar to erastin, RSL5 needs VDACs to induce cell death, while RSL3 acts in a VDAC-independent manner. The same group also identified the specific target of RSL3 as the antioxidant enzyme GPx-4 [407]. From these studies, additional features of erastin or RSL3/5 treated-cells emerged. For example, it was observed that, similarly to erastin-induced death, also in the presence of these compounds, BJ fibroblasts die in a caspase-independent manner.

Furthermore, iron chelators like deferoxamine (DFO) and antioxidants such as vitamin E were both effective in inhibiting the lethal effect of these drugs, suggesting the involvement of Fenton chemistry and ROS. Although all of these ferroptosis inducers were discovered in cells harbouring mutant RAS, suggesting that the RAS-RAF-MEK pathway was responsible for their lethality, subsequent studies contradicted this initial assumption [418]. In particular, M. Gao and colleagues showed that inhibition of MEK1/2 with a more selective inhibitor than the one used by the Stockwell's group failed to inhibit ferroptosis [419]. Moreover, also cells that do not express mutant RAS were shown to undergo this kind of cell death [420,421]. In line with these findings, C. Schott and colleagues provided evidence that cells overexpressing mutant RAS can display erastin resistance [422]. Overall, these studies indicated that mutant RAS is actually dispensable for ferroptosis execution.

Despite several findings already clearly pointed to a novel type of cell death, it was not until 2012 that S.J. Dixon and colleagues of the B.R. Stockwell's group formally named this cell death modality ferroptosis, owing to its iron dependency [403]. Since then, other forms of cell death that had erroneously been identified as novel, were re-evaluated to merge them with the concept of ferroptosis [419,423]. Subsequent studies finally helped to elucidate the non-apoptotic nature of ferroptosis, with its distinctive morphological features that include: swelling of the cell, shrinkage of the mitochondria with condensation of the membrane and a reduction of the cristae, rupture of the outer mitochondrial membrane and absence of condensed chromatin [401,403,417,420,424]. Biochemically, ferroptosis is characterised by iron and ROS accumulation, inactivation of GPx-4, overall reduced antioxidant defences and induction of lipid peroxidation [403,407,418,425].

Over the course of almost ten years of investigations on ferroptosis, diverse experimental and clinical compounds have been identified or re-discovered as triggers or inhibitors of this kind of cell death. Lists of both groups of compounds are provided in *table 1* and *table 2*, which have been developed based on the information reviewed by Y. Xie and J. Li and their respective groups (*table 1* and *table 2*) [426,427].

Table 1: Common ferroptosis inducers grouped by mechanism of action

Mechanisms	Compounds	Targets	Ref.
Class 1			
Inhibition of system Xc^- causing GHS depletion	Erastin	System Xc^- and VDAC2/3	402,403,417
	RSL5	System Xc^- and VDAC2/3	418
	Sorafenib	System Xc^- (and VEGFR 1-3; PDGFR-β; FGFR1; RAF)	402,428–430
	Sulfasalazine (SAS)	System Xc^- (and NF-kB; TNF)	431–434
	Extracellular Glutamate	System Xc^-	403,435
Class 2			
Direct inhibition of GPx-4 (covalent binding)	RSL3	GPx-4	407,418
	DPI7, DPI10, DPI12, DPI13, DPI17, DPI18, DPI19	GPx-4	407
Other mechanisms			
Degradation of GPx-4, binding to squalene synthase (SQS) and depletion of antioxidant CoQ10	FIN56	GPx-4 and SQS	436
Direct oxidation of ferrous iron and lipids, indirect inactivation of GPx-4	FINO2	Lipids and labile iron	437,438
Inhibition of GSH synthesis	Buthionine sulfoximine (BSO)	γ-glutamyl cysteine synthetase	407
Induction of ROS, degradation of ferritin	Artesunate (ART)	HEME and V_1 and V_0 domains of lysosomal V-ATPase	439–442

Table 2: Common ferroptosis inhibitors grouped by mechanism of action

Mechanisms	Compounds	Targets	Ref.
Inhibition of lipid peroxidation initiation (specific ferroptosis suppressors)	Ferrostatin-1 (Fer-1)	Ferrous iron from lipid hydroperoxides	403,443,444
	Liproxstatin-1	ROS from lipid peroxidation	420,444
Chelation of iron (membrane impermeable and lipophilic)	Deferoxamine (DFO)	Iron	403,418
	Ciclopirox	Iron	403,445
Protection against lipid peroxidation (reducing agent)	β-Mercaptoethanol	Cystine	403,446
	Vitamin E	ROS (LOX)	447,448
	β-Carotene	ROS	449,450
	Glutathione	ROS	451
Inhibition of protein synthesis	Cycloheximide	System Xc^-	417

5.1 Ferroptosis execution and its study

Each ferroptosis inducer or inhibitor is very different from the others for chemical nature, mode of action and targets (*tables 1* and *2*). This indicates that, likewise apoptotic death, also ferroptosis can be initiated by different pathways that eventually converge on the same execution phase. In particular, the pathways that lead to ferroptosis execution are all characterised by a ROS production that exceed the detoxifying capacity of the cell. Importantly, not all types of ROS, but specifically lipid peroxides are the hallmark of ferroptosis [452]. Indeed, cytosolic ROS formation, induced by other compounds, would trigger different pathways rather than ferroptosis and iron-related toxicities different from ferroptosis are indeed well-known [156,453]. Therefore, a more accurate definition of ferroptosis includes the following three requirements: 1- iron-dependent oxidative stress; 2- generation of oxidised polyunsaturated fatty acid-containing phospholipids (PUFA-PLs); 3- loss of lipid peroxide repair capacity rescuable by lipophilic radical-trapping antioxidants [454]. The accumulation of redox-active iron can be measured experimentally with probes that quantify the relative abundance and the ratio of Fe^{2+} to Fe^{3+} [455]. Lipid peroxidation is detected in ferroptosis studies with fluorescent probes such as C11-BODIPY 581/591 and Liperfluo. C11-BODIPY is a sensor of the production of ROS in a lipophilic environment (like membranes) as it is sensitive to reactive species formed from hydroperoxides, but not to hydroperoxides themselves. Oxidation of the polyunsaturated butadienyl portion of this dye results in a shift of its fluorescence emission peak from ~590 nm to ~510 nm (from red to green), which can be detected by flow cytometry instruments [456]. The other dye sensitive to lipid hydroperoxides is Liperfluo. This probe is soluble in organic solvents and it directly reacts with lipid hydroperoxides to form the fluorescent Liperfluo-OX, which can be detected at long wavelengths [457]. Regarding the loss of lipid peroxide repair capacity instead, this is commonly assessed in assays that measure the enzymatic activity of GPx-4 or the abundance of its substrate glutathione [458]. More recently, in an attempt to specifically stain for ferroptotic cells, H. Feng and colleagues of the Stockwell's lab have also suggested that the human transferrin receptor 1 protein (TfR1) can be used as a specific marker of ferroptosis [459]. Despite all this progress in defining ferroptotic death, many questions still remain. In particular, which lipids undergo peroxidation, what is the source of these ROS, how exactly ferroptosis gets executed downstream of lipid peroxidation and where exactly this phenomenon is localized within the cell are all unclear aspects.

It is known that phospholipids bearing polyunsaturated-fatty-acids (PUFAs), like linoleic or arachidonic acid, are particularly susceptible to peroxidation due to their bis-allylic carbons (carbon atoms that are adjacent to two neighbouring carbon-carbon double bonds) that can be attacked by radicals, LOXs and oxygen [460]. Such oxidants can abstract a hydrogen from the bis-allylic carbon and the insertion of oxygen results in the generation of lipid peroxyl radicals ($L\text{-}O\text{-}O^{\bullet}$) and hydroperoxides (R-O-OH) [461].

Both the ROS generated by LOXs and during the Fenton chemistry are considered responsible for the oxidative damage of PUFA and for triggering ferroptosis. Once ROS are generated, in the case of non-enzymatic reactions the lipid peroxidation process occurs in three phases: in the so-called “initiation” phase, a hydrogen atom of the fatty acid is lost to a ROS to form a lipid radical. In particular, the C–H bonds at the bis-allylic positions are the weakest bonds in the molecules and the hydrogen atoms at these positions are preferentially abstracted by a peroxyl radical. The following can be seen as a cycle phase called “propagation”, as the lipid radical cycles between the fatty acyl radical and the peroxyl radical. The latter is formed when the lipid radical gets oxidized by oxygen, while the oxidation of another lipid generates a lipid hydroperoxide and a new lipid radical, in a vicious circle of continuous increase of lipid radicals. The circle is only terminated when radicals are ‘quenched’ by antioxidants or when they react with another radicals (*figure 11*) [460,462,463].

The role of non-enzymatic Fenton chemistry in the lipid peroxidation process that triggers ferroptosis is underscored by the inhibitory mechanism of the two aromatic amines ferrostatin-

1 (Fer-1) and liproxstatin-1. In fact, these compounds are poor inhibitors of the 15-lipoxygenase enzyme (ALOX15), a LOX isoform that has been implicated in ferroptosis [458]. Instead, they act as potent radical trapping antioxidants (RTA) in lipid bilayers, where they effectively prevent autoxidation of PUFAs [444,464]. However, also the lipid oxidation enzymes LOXs, which are non-heme, iron-containing proteins, can catalyse the dioxygenation of PUFAs [465]. The role of LOXs, and in particular that of the 5-lipoxigenase enzyme (ALOX5), is proven by the fact that, replacing the hydrogen at position seven of arachidonic acid molecules with its heavier isotope deuterium, has a protective effect against ferroptosis [458]. In another study, LOX inhibitors were found to have a cytoprotective effect because they are effective radical-scavenging antioxidants. This suggests that LOX activity may contribute to the cellular pool of lipid hydroperoxides that trigger ferroptosis, but that the cell death process is driven by an auto-amplifying process of lipid autoxidation [466].

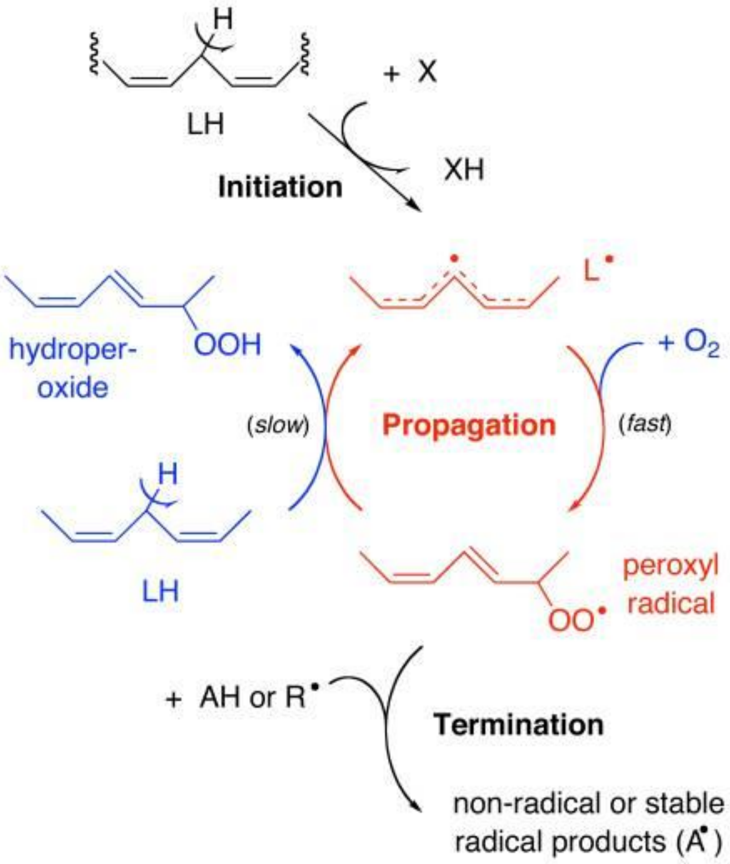

Figure 11: The three steps of non-enzymatic lipid peroxidation

In the initiation phase, a ROS generated in Fenton reactions (hydroxyl radical $^{\bullet}OH$, here represented as X) attacks the weak hydrogen at a bis-allylic carbon of a fatty acid (in black), generating a lipid radical ($L^{\bullet}$ in red). The lipid radical cycles between this form and the peroxyl radical form ($OO^{\bullet}$ in red) generated by the fast oxidation of the lipid radical. The oxidation of another fatty acid (in blue), that transfers a hydrogen atom to the peroxyl radical, converts the latter in a hydroperoxide (OOH in blue) while this new fatty acid generates a new lipid radical ($L^{\bullet}$ in red). The new lipid radical is ready to pick up oxygen and form the next peroxyl radical to repeat the cycle. As the net result of this propagation phase, oxygen and the fatty acid are fed into the cycle to produce a hydroperoxide (blue). Termination of the process occurs when either two radicals ($R^{\bullet}$) react with each other forming a non-radical product, or when an antioxidant (AH) reduces the peroxyl to a hydroperoxide, while being transformed into a stable radical ($A^{\bullet}$). Adapted from Schneider, C. (2009) [463].

It is important to note that, for death to be executed, the free PUFAs need to be incorporated into phospholipids, for which two genes are essential: the acyl-CoA synthetase long-chain family member 4 (ACSL4) and the lysophosphatidylcholine acyltransferase 3 (LPCAT3). ACSL4 is an enzyme that preferentially acylates arachidonic acid, a fatty acid that has a highly unsaturated chain with four double bonds and that is prone to oxidation [467]. LPCAT3 instead, catalyses the insertion of acylated arachidonic acid into membrane phospholipids, as it inserts acyl groups into lysophospholipids (which have one fatty acyl tail) such as phosphatidylcholine (PC) and phosphatidylethanolamine (PE) [468]. Deleting ACSL4 and LPCAT3 suppresses ferroptosis probably due to the consequent reduction of the membrane-resident pool of oxidation-sensitive fatty acids [469]. Indeed, pharmacological targeting of ACSL4 with the antidiabetic class of compounds thiazolidinediones protects cells from ferroptosis [470]. A schematic overview of ferroptosis inducers and inhibitors is provided in *figure 12*.

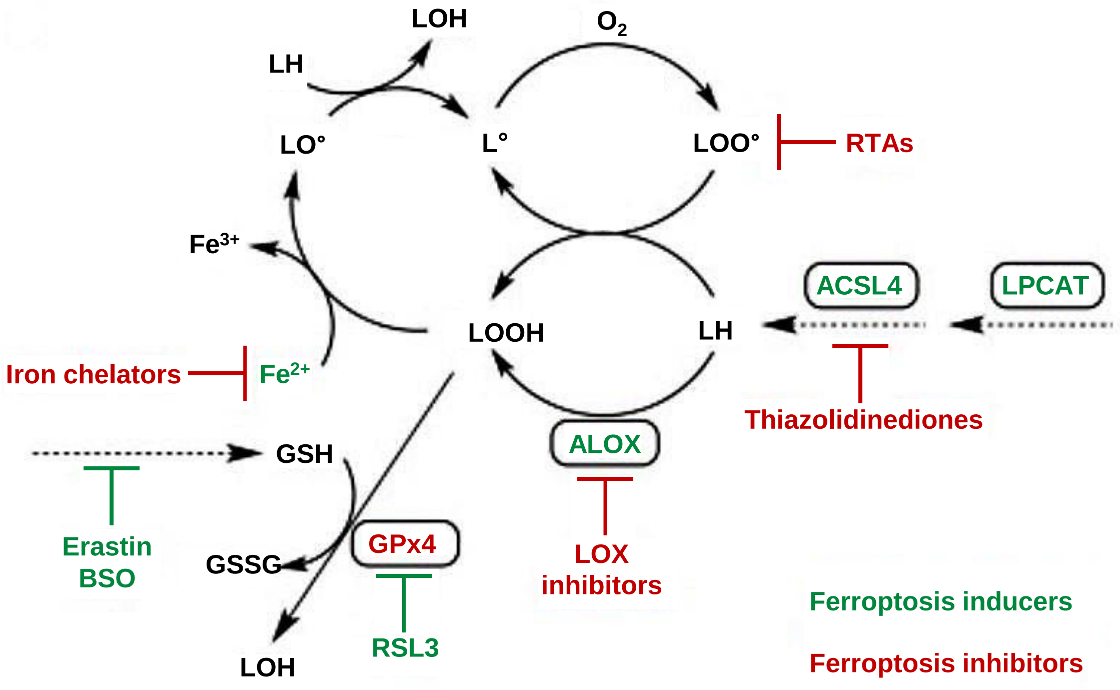

Figure 12: Ferroptosis inducers and inhibitors associated with accumulation of (phospho) lipid hydroperoxides

Schematic representation of the lipid peroxidation reaction with small molecules and enzymes that can induce it (in green) or suppress it (in red). RTAs inhibit auto-peroxidation by quenching lipid radicals. ACSL4 and LPCAT promote the insertion of oxidized lipids into cellular membranes while thiazolidinediones block their enzymatic activity. ALOX catalyses the oxidation of arachidonic acid, a reaction blocked by specific LOX inhibitors. In the absence of iron chelators, Fe^{2+} catalyses the formation of lipid radicals. Erastin and BSO inhibit the biosynthesis of the antioxidant GSH. RSL3 directly inhibits GPx-4 that would otherwise repair the oxidised PUFAs by reducing them to lipid alcohols. Adapted from Shah, R. et al., (2018) [466].

Despite all this knowledge, it is still not clear what is the critical event in ferroptosis that marks the point of no return. The uncontrolled peroxidation of PUFA phospholipids described above is the most downstream step identified. It is possible that the insertion of oxidated lipids into the membranes, which is already known to decrease their fluidity, causes also a change in their shape and curvature, such that the access to oxidants is facilitated [471]. This would increase lipid oxidation in a cycle of further oxidation and membrane curvature, until lipid bilayers are destabilized with micellization and pores formation. The final result would be an irreversible damage of the membrane integrity with consequent cell death [447,472].

A remaining question to answer concerns the cellular localisation of the lipid peroxidation event, as not only the plasma membrane but also the mitochondria, the ER and the lysosomes are candidate sites for this lethal process. Mitochondria are an obvious target, as morphological changes of these organelles have been observed during ferroptotic death [403,473,474]. However, it has been shown that cells depleted of their mitochondria, via the induction of mitophagy, are still able to undergo ferroptosis, although their increase in ROS levels is inferior compared to that of control cells. This indicates that mitochondrial lipid peroxidation occurs but it is dispensable for ferroptosis execution [475]. Another possibility is that the role of mitochondria is context-dependent. For example, in the case of cystine deprivation-induced ferroptosis, mitochondrial metabolism seems to be crucial, while upon GPx-4 inhibition, cells can undergo ferroptosis independently of this organelle [476]. In general, it appears that the exact role of the mitochondria during ferroptosis is still unclear and a comprehensive analysis on this topic is provided in the review by H. Wu and colleagues from the group of W. Gao [477]. Another candidate location of the ferroptotic lipid peroxidation is the ER. Indeed, inhibition of system Xc^- leads to the activation of the ER stress response [402]. However, the exact mechanism that drives lipid peroxidation in the ER until ferroptosis is triggered is not clear. Finally, as ferrostatins are known to accumulate in the lysosomes, also these organelles are being considered as the possible site of the lethal lipid peroxidation, although no prove exists that their involvement is somehow necessary for the ferroptotic process [475].

In conclusion, several cellular locations could be involved in the lipid peroxidation process that leads to ferroptotic death. The specific features of each organelle, in terms of lipid composition and expression level of GSH, LOXs and GPx-4, might contribute to the ferroptosis competence of their membranes [447].

5.2 Ferroptosis in physiology and pathology: perspective for cancer therapy

Ferroptosis has been identified through the discovery of synthetic compounds that induced this novel type of cell death, such as erastin and RSL3 [401,418]. However, natural conditions in which ferroptosis would take place still need to be fully characterised. Only recent studies are providing clearer evidence of the involvement of ferroptosis in diverse pathological situations. For example, accumulation of the excitatory neurotransmitter glutamate in the nervous system is known to exert toxic effects. Consistently with the role of extracellular glutamate in inhibiting the transport of cystine inside the cells, it was found that indeed ferroptosis occurs in neurons upon high concentrations of this neurotransmitter [478]. Another pathological condition in which ferroptosis seems to be involved is the case of ischemia-reperfusion injury (IRI). This provokes a direct and synchronized necrosis of renal tubules that is reported to be suppressed by stable and potent third-generation ferrostatins [479]. Also, inhibition of ferroptosis in neurons protects from intracerebral haemorrhage (ICH) [480]. In general, the number of pathologies with a link to ferroptosis is continuously increasing, comprising conditions as diverse as neurodegenerative diseases and autoimmune disorders [481–483]. Moreover, key ferroptosis regulators appear essential for cell survival. For example, the knockout of GPX4, the gene encoding for the GPx-4 enzyme, results in ferroptosis induction in neurons and renal tubule cells *in vivo*, suggesting that active ferroptosis suppression is needed to maintain cell viability [420,484]. As regulation of lipid peroxidation, antioxidant defences and ferroptosis itself can be found in diverse species, X. Jiang, B.R. Stockwell and M. Conrad speculated that the ferroptosis program is inherent to life and that its counteraction through the development of anti-ferroptotic mechanisms is necessary for cell survival [485,486]. This is also consistent with the hypothesised evolutionary origin of ferroptosis. In fact, the first organisms on Earth that began to use oxygen inevitably also produced potentially toxic ROS and the development of defence mechanisms against lipid peroxidation must have been an early selective event for the life on our planet [452].

Ferroptosis also seems to play a physiological role in tumour suppression. Indeed, an emerging evidence indicates that p53 exerts its tumour suppressor role not only by regulating apoptosis but also other cellular processes such as the anti-oxidant defences and ferroptosis [487]. In particular, SLC7A11, the gene encoding the catalytic subunit of system Xc^-, is a direct target of p53. The binding of p53 to its respective responsive element in the promoter region of SLC7A11 represses the expression of this gene, such that cells are more sensitive to ferroptosis induction [488]. Based on finding of this kind, ferroptosis induction can be seen as a promising novel approach in cancer treatment. In fact, its own discovery is the result of a search for compounds lethal to RAS-mutant cancer cells [401]. The rationale for exploiting ferroptosis susceptibility in cancer therapy relies on the logical assumption that tumour cells have a more active metabolism compared normal cells. This results in a ROS overload that makes them more prone to ferroptotic death. However, cancer cells often adopt compensating strategies to deal with such ROS burden. For example, the transcription factor Nrf-2 (nuclear factor erythroid 2-related factor 2), a master regulator of the cellular antioxidant response, is often upregulated in cancer, hindering ferroptosis susceptibility [489]. In fact, Nrf-2 induces the expression of genes involved in the resistance to oxidants and electrophiles, including SLC7A11 and glutathione peroxidases [490,491]. In the case of glioblastoma cells, it was shown that, compared to non-tumour tissue, they often display higher levels of Nrf-2 and that this condition seems to correlate with a poor clinical outcome [492]. The importance of ferroptosis suppression for cancer cells survival is also suggested by the role that iron plays in their metabolism. In particular, high levels of the transferrin receptor 1 (TFRC1) have frequently been reported. This is a transmembrane glycoprotein that binds transferrin (the protein binding plasma iron) in its diferric form and that is essential for iron uptake [493,494]. As iron fuels the Wnt signalling, cancer cells seem to display an addiction to this metal and they correspondently express decreased levels of the iron efflux pump ferroportin [495,496]. Hence, some of the most aggressive tumours might depend on ferroptosis-suppression for their survival, indicating that targeting this pathway could allow their eradication when other types of therapies are unsuccessful [497,498].

Glioblastoma is one of the cancer types that displays increased levels of both TFRC1 and ferritin. High levels of TFRC1 have been shown to drive sphere formation *in vitro* and tumour growth *in vivo,* while ferritin seems to indirectly regulate cell cycle progression. The mechanism underlying this latter effect is probably the induction of STAT3 that, in turns, regulates the expression of the transcription factor FoxM1. This not only plays a pivotal role in cell cycle signalling but promotes also the nuclear translocation of β-catenin and controls the expression of the Wnt target-genes [499,500]. Besides the elevated iron level and its important role in glioblastoma metabolism, another indication of glioblastoma susceptibility towards ferroptotic death is provided by the reported upregulation of SLC7A11 and its predictive role of glioblastoma patient survival. In particular, S.M. Robert examined 41 glioblastoma patients and found that more than half of them expressed higher levels of SLC7A11 in the tumour samples compared to the matched peritumoural brain tissue. Interestingly, reduced expression of SLC7A11 conferred an improved clinical outcome, with patients living on average 9 months longer [501]. Due to SLC7A11 upregulation, glutamate export is increased and this activates the

Ca^{2+}-permeable AMPA receptor with consequent oscillation of intracellular Ca^{2+} that promotes cell migration. Conversely, decreasing glutamate release, for example via the pharmacological inhibition of system Xc^-, decreases chemotactic invasion and migration of glioblastoma cells [502]. Regarding the importance of SLC7A11 in glioblastoma, it is worth noting that overexpression of this protein results in changes in the distribution of actin in the cytoskeleton, with a morphology resembling epithelial-like cells. Additionally, it also induces the cells to assume a CSC-like phenotype, indicated by the ability to form more numerous and larger (~300 µm in diameter) tumor spheres compared to parental cells [503].

All together, these studies highlight that ferroptosis induction, and in particular system Xc^- targeting, can be a promising approach against highly resistant tumours such as glioblastoma. GPx-4 might be seen as the most obvious target to promote ferroptosis induction, as it is important for the survival of many cancer cells, such as diffuse large B cell lymphomas and renal cell carcinomas [407]. However, it has to be considered that this protein is also essential for healthy cells like kidney tubular cells and spinal motor neurons [420,504]. Therefore, administering GPx-4 inhibitors at a systemic level might result in unacceptable side effects, unless a more specific delivery of these class of drugs is developed. On the other side, system Xc^- knockout mice have been generated without causing major side effects, pointing to the targeting of SLC7A11 as a better option than GPx-4 inhibition [505,506]. Indeed, some drugs inhibiting system Xc^- already received FDA approval and their applicability to glioblastoma has also been tested. Sulfasalazine for example, an FDA-approved drug used for the treatment of Crohn's disease, caused a dose-dependent inhibition of glioma growth [507,508]. Moreover, it appeared not to be toxic to neurons and brain tissue, while it reduced glioma-derived edema and consequently the total volume of tumour burden [509]. These encouraging results should boost ferroptosis research in the direction of its clinical exploitation against cancer.

Aims of the thesis

Glioblastoma patients are notoriously difficult to treat and their prognosis remain poor even when they receive the standard of care treatment. Novel therapies are therefore urgently needed.

TRAIL is a potential anti-cancer treatment that shows a favourable profile of safety and tolerability. However, extensive investigations revealed its poor efficacy in clinical trials. Bioavailability and potency of TRAIL-based therapeutics have since been improved, resulting in second-generation TRAIL receptor agonists such as IZI1551, an antibody-TRAIL fusion protein that was developed at the Institute of Cell Biology and Immunology (IZI) of the University of Stuttgart.

Because TRAIL treatment has proven ineffective as a single agent in most cancers, and monotherapies in general often have limited success, sensitising agents can be strategically combined with it in order to achieve synergistic apoptosis-inducing effects.

A literature review on the effect of proteasome inhibitors in priming cancer cells to TRAIL-induced apoptosis, via up- respectively down-regulation of pro- and anti-apoptotic proteins, provided the rationale to investigate this combination in translationally-relevant glioblastoma models, such as low-passage patient-derived cell lines (PDCLs). In particular, it was hypothesised that the limitations of first-generation drugs could be overcome by combining IZI1551 with marizomib, a proteasome inhibitor that displays the advantageous feature of permeating the BBB.

Alternatively, novel cell death pathways that bypass the intrinsic apoptosis resistance of certain tumour cells have been considered.

Hence, the aims of this thesis were:

- To assess the therapeutic efficacy of IZI1551 and marizomib in a panel of glioblastoma PDCLs and to evaluate their possible synergistic interactions in inducing apoptotic cell death.
- To design an improved treatment schedule based on the kinetic of action of the individual drugs.
- To investigate the mechanism of apoptosis resistance of non-responder cell lines and to identify sensitisation strategies to overcome them.
- To evaluate ferroptosis induction as an alternative cell death pathway to eradicate TRAIL-resistant glioblastoma cells and to characterise the interaction between ferroptosis inducers and BH3 mimetics.

Materials

1. Cell lines and cell culture media

1.1 GMB PDCLs

Table 3: GBM PDCLs and their characteristics

PDCL	**Description**	**Source**
GTCC9	Recurrent. Male patient, 44 years old. EGFR amp. PTEN loss	EMC
GTCC10	Recurrent. Male patient, 50 years old. NA	EMC
N150385	Primary. Male patient, 66 years old. Tp53 mutant	ICM
N150661	Primary. Male patient, 24 years old. EGFR amp, wt	ICM
N151027	Primary. Male patient, 42 years old. EGFR amp, VIII	ICM
N160125	Primary. Female patient, 47 years old. Tp53 mutant	ICM
N160240	Primary. Male patient, 65 years old. IDH mutant	ICM

1.2 Other cell lines

Table 4: Other cell lines and their characteristics

Cell line	**Description**	**Source**
DH5α	E. coli competent cell	IZI
HEK P2	Suspension HEK293 with DR5 KO	Dr. Martin Siegemund
HeLa	Cervical adenocarcinoma	RCSI
HT1080	Fibrosarcoma	IZI
U-87 MG	GBM	RCSI

1.3 Cell culture media and supplements

Table 5: Media and supplements for cell culture

Cell culture media and Supplements	**Manufacturer/Composition**
B27	Thermo Fisher Scientific, Gibco, Waltham, MA, USA
Basic Fibroblast Growth Factor (bFGF)	Peprotech, Hamburg, Germany
Collagen type I, Rat Tail	Thermo Fisher Scientific, Gibco, Waltham, MA, USA
Dulbecco's Modified Eagle Medium (DMEM)	Life Technologies Corporation, Carlsbad, CA, USA

DMEM/Nutrient Mixture F-12 (DMEM/F-12)	Thermo Fisher Scientific, Gibco, Waltham, MA, USA
Endothelial Cell Growth (EGF)	Peprotech, Hamburg, Germany
Endothelial Cell Growth Basal Medium MV 2	Promo cell GmbH, Heidelberg, Germany
F17 Freestyle Expression Medium	Thermo Fischer Scientific Inc., Waltham, USA
Fetal Bovine Serum (FBS)	PAN-Biotech GmbH, Aidenbach, Germany
GlutaMAX	Thermo Fisher Scientific, Inc., Waltham, USA
Heparin	Alfa Aesar, Ward Hill, MA, USA
Koliphor P188	Sigma Aldrich, Merck KGaA, Darmstadt, Germany
LB medium	1% (w/v) peptone, 0.5% (w/v) yeast extract, 0.5% (w/v) NaCl in ddH$_2$O, pH 7
LB amp, glc agar plates	LB medium, 2% (w/v) agar; after autoclaving: 1% (w/v) D-glucose and 100 µg/ml ampicillin
Penicillin-Streptomycin 100x	Thermo Fisher Scientific, Waltham, MA, USA
Reduced Growth Factor Basement Membrane Extract (BME) Cultrex®	Trevigen, Wiesbaden-Nordenstadt, Germany
RPMI 1640 medium	Life Technologies, Gibco, Karlsruhe, Germany

2. Antibodies and drugs

2.1 Antibodies for flow cytometry

Table 6: List of antibodies used in flow cytometry experiments

Antibody	Species	Concentration	Manufacturer
Alexa Fluor 488-conjugated anti-mouse IgG (H+L)	goat	2 mg/ml	Thermo Fisher Scientific Inc., Waltham, USA
Anti-TRAILR1 (MAB347)	mouse IgG1	4 µg/ml	R&D Systems, Wiesbaden-Nordenstadt, Germany
Anti-TRAILR2 (MAB6311)	mouse IgG2b	4 µg/ml	R&D Systems, Wiesbaden-Nordenstadt, Germany
Isotype control	mouse IgG1	4 µg/ml	BD Pharmingen, Heidelberg, Germany
Isotype control	mouse IgG2b	4 µg/ml	BD Pharmingen, Heidelberg, Germany

2.2 Antibodies for western blotting

Table 7: List of antibodies used in western blot experiments

Antibody	Species	Dilution	Manufacturer
Anti-Bcl-2	rabbit	1:1000	Cell Signaling Technology, Danvers, MA, USA
Anti-Bcl-2 (100)	mouse	1:1000	Santa Cruz Biotechnology, Heidelberg, Germany
Anti-Bcl-xL (54H6)	rabbit	1:1000	Cell Signaling Technology, Danvers, MA, USA
Anti-BID (7)	mouse	1:1000	BD Bioscience, Heidelberg, Germany
Anti-BID	rabbit	1:1000	Cell Signaling Technology, Danvers, MA, USA
Anti-caspase-3	mouse	1:1000	Cell Signaling Technology, Danvers, MA, USA
Anti-caspase-8 (1C12)	mouse	1:1000	Cell Signaling Technology, Danvers, MA, USA
Anti-caspase-8 (D35G2)	rabbit	1:1000	Cell Signaling Technology, Danvers, MA, USA
Anti-caspase-8 (B9-2)	mouse	1:1000	BD Bioscience, Heidelberg, Germany
Anti-DR4 (D9S1R)	rabbit	1:1000	Cell Signaling Technology, Danvers, MA, USA

Anti-DR5 (D4E9)	rabbit	1:1000	Cell Signaling Technology, Danvers, MA, USA
Anti-DR5	rabbit	1:1000	Cell Signaling Technology, Danvers, MA, USA
Anti-FADD	rabbit	1:1000	Cell Signaling Technology, Danvers, MA, USA
Anti-FADD (1)	mouse	1:1000	BD Bioscience, Heidelberg, Germany
Anti-c-FLIP (D5J1E)	rabbit	1:1000	Cell Signaling Technology, Danvers, MA, USA
Anti-c-FLIP (D16A8)	rabbit	1:1000	Cell Signaling Technology, Danvers, MA, USA
Anti-GAPDH (D4C6R)	mouse	1:1000	Cell Signaling Technology, Danvers, MA, USA
Anti-GAPDH (6C5)	rabbit	1:1000	Merck Millipore, Darmstadt, Germany
Anti-Mcl1 (D2WE9)	rabbit	1:1000	Cell Signaling Technology, Danvers, MA, USA
Anti-PARP (4C10-5)	mouse	1:1000	BD Bioscience, Heidelberg, Germany
Anti-Vinculin (7F9)	mouse	1:1000	Santa Cruz Biotechnology, Heidelberg, Germany
Anti-XIAP (28/hILP)	mouse	1:1000	BD Bioscience, Heidelberg, Germany
Anti-α-Tubulin	mouse	1:1000	Cell Signaling Technology, Danvers, MA, USA
Horse radish peroxidase (HRP)-conjugated goat anti-mouse IgG+IgM		1:10000	Dianova GmbH, Hamburg, Germany
Horse radish peroxidase (HRP)-conjugated goat anti-rabbit IgG+IgM		1:10000	Dianova GmbH, Hamburg, Germany

2.3 Drugs

Table 8: List of drugs

Drug	**Manufacturer**
ABT-199	Active Biochemicals Co., Limited, Hong Kong, China
Bortezomib	Millenium Pharmaceutical, Cambridge, MA, USA
Erastin	Sigma-Aldrich, Munich, Germany
Ferrostatin-1	Sigma-Aldrich, Munich, Germany
IZI1551	Produced in house, IZI, Stuttgart, Germany
Marizomib	Sigma-Aldrich, Munich, Germany
Q-VD-Oph	Selleckchem, Houston, Texas, USA
RSL3	Sigma-Aldrich, Munich, Germany
S63845	APExBIO Technology LLC, Houston, Texas, USA
WEHI-539	APExBIO Technology LLC, Houston, Texas, USA

3. Buffers and solutions

Table 9: List of buffer and solutions with their composition

Buffer and Solutions	**Composition/Manufacturer**
Accutase®	ThermoFisher Scientific, MA, USA
Annexin V binding buffer 10x	BD Pharmingen, BD Biosciences, San Diego, USA
Anti-Adherence Rinsing Solution	STEMCELL Technologies, Cologne, Germany
Blocking reagent 10x	Roche Diagnostics AG, Basel, Switzerland
Bolt MES SDS Running Buffer 20x	Thermo Fisher Scientific Inc., Waltham, USA
Coomassie staining solution	0.008% (w/v) Coomassie Brilliant Blue G-250, 35 mM HCl
Dulbecco's phosphate-buffered saline (DPBS) 1x	Thermo Fisher Scientific, Waltham, MA, USA
HPLC running buffer	0.1 M Na_2HPO_4/NaH_2PO_4, 0.1 M Na_2SO_4, pH 6.7
Laemmli loading buffer 5x	312.5 nM Tris-HCl pH 6.8, 25% (v/v) glycerine, 10% (w/v) SDS, 500 mM DTT, 0.05% (w/v)
Lysis buffer	27 mM Tris-HCl (pH 6.8), 5% glycerol, 1.6% SDS, 0.83% β-mercaptoethanol, 0.002% bromophenol blue
PBA	PBS, 0.05% (w/v) BSA, 0.02% (w/v) NaN_3 in ddH_20
Phosphate buffered saline (PBS)	2.67 mM KCl, 1.47 mM KH_2PO_4, 137.9 mM NaCl, 8.06 mM Na_2HPO_4, pH 7.4
Ponceau S	0.1% Ponceau S solution, 5% acetic acid
TBS with Tween-20 (TBST)	0.1% (v/v) Tween-20 in TBS
TCM buffer	10 mM Tris-HCl, pH=8, 10 mM CaCl2, 10 mM $MgCl_2$
Tris buffered saline (TBS)	20 mM Tris-HCl, 150 mM NaCl in ddH_20, pH 7.4
Trypsin/EDTA 10x	Life technologies, Gibco, Karlsruhe, Germany

4. Chemicals and reagents

Table 10: List of chemicals and reagents

Chemicals and Reagents	**Manufacturer**
Annexin V-GFP	Produced in-house by Nathalie Peters
Bovine serum albumin (BSA)	Sigma-Aldrich, Munich, Germany
Bovine serum albumin (BSA) standard	Paesel+Lorei GmbH & Co. KG, Rheinberg, Germany
Bradford reagent	Carl Roth GmbH & Co. KG, Karlsruhe, Germany
Calcein AM	Thermo Fisher Scientific, MA, USA
CHAPS	Carl Roth GmbH & Co. KG, Karlsruhe, Germany
Coomassie Brilliant Blue G-250	SERVA Electrophoresis, Heidelberg, Germany
Crystal violet powder	Carl Roth GmbH & Co. KG, Karlsruhe, Germany
Digitonin	SEVA Electrophoresis GmbH, Heidelberg, Germany
Dimethyl sulfoxide (DMSO)	Carl Roth GmbH & Co. KG, Karlsruhe, Germany
Dithiothreitol (DTT)	Carl Roth GmbH & Co. KG, Karlsruhe, Germany
ECL substrate (Pierce™ Plus)	Thermo Fisher Scientific, Ulm, Germany
ECL substrate (SuperSignal™ West Dura)	Thermo Fisher Scientific, Ulm, Germany
EDTA	Carl Roth GmbH & Co. KG, Karlsruhe, Germany
EGTA	Carl Roth GmbH & Co. KG, Karlsruhe, Germany
HEPES	Carl Roth GmbH & Co. KG, Karlsruhe, Germany
Hoechst 33342	Thermo Fisher Scientific, Ulm, Germany
Magnesium chloride ($MgCl_2$)	Carl Roth GmbH & Co. KG, Karlsruhe, Germany
Potassium chloride (KCl)	Carl Roth GmbH & Co. KG, Karlsruhe, Germany
Propidium iodide (PI)	Sigma-Aldrich, St. Louis, Missouri, USA
Protease inhibitor (cOmplete, EDTA free)	Roche Diagnostics AG, Basel, Switzerland
Sodium azide (NaN_3)	Carl Roth GmbH & Co. KG, Karlsruhe, Germany

Sodiumdodecylsulfate (SDS)	Carl Roth GmbH & Co. KG, Karlsruhe, Germany
Suc-LLVY-AMC	Merck Millipore/Calbiochem, Darmstadt, Germany
Tris-(hydroxymethyl)-aminomethane (Tris)	Carl Roth GmbH & Co. KG, Karlsruhe, Germany
Triton® 100x	Carl Roth GmbH & Co. KG, Karlsruhe, Germany
Tryptone N1	Carl Roth GmbH & Co. KG, Karlsruhe, Germany
Tween-20	Carl Roth GmbH & Co. KG, Karlsruhe, Germany
WST-1 cell proliferation reagent	ThermoFisher Scientific, MA, USA
Zinc chloride ($ZnCl_2$)	Carl Roth GmbH & Co. KG, Karlsruhe, Germany

5. Laboratory supply and special implements

Table 11: List of supply materials and special implements

Supply materials and Special Implements	**Distributor**
Anti-FLAG® M2 affinity gel	Sigma-Aldrich, St. Louis, MO, USA
Bottle Top Filter (Low Protein binding, 0.2 µm/0.45 µm)	Corning Incorporated, Tewksbury, MA, USA
Cell Culture Flask (Cell Star®, 25 cm² and 75 cm²)	Greiner Bio-One, Frickenhausen, Germany
Cell Culture Plate (Cell Star®, with lid, 96-well, F and U bottom)	Greiner Bio-One, Frickenhausen, Germany
Centrifuge tubes	Greiner Bio-One, Frickenhausen, Germany
Chromatography columns (Poly-Prep®)	Bio-Rad, Munich, Germany
Cryobox	Thermo Fisher Scientific, Ulm, Germany
Cryovial (Cell Star®)	Greiner Bio-One, Frickenhausen, Germany
Dialysis membrane (MWCO 12.400)	Sigma-Aldrich, St. Louis, MO, USA
Electrophoresis chamber (Bolt™ mini gel tank)	Thermo Fisher Scientific Inc., Waltham, USA
Erlenmeyer flasks	Thermo Fisher Scientific, Ulm, Germany
FLAG peptide	Peptides&Elephants, Potsdam, Germany
FPLC column (Superdex 200 10/300 GL)	GE Healthcare, Little Chalfont, UK
HPLC column (Yarra™ 3 µm SEC-2000/SEC-3000)	Phenomenex, Torrance, CA, USA
NucleoBond® Xtra Midi	Macherey-Nagel, Düren, Germany
Pipettes	Eppendorf AG, Hamburg, Germany
Pre-cast gels (Bolt™ 4-12% Bis-Tris Plus)	Thermo Fisher Scientific Inc., Waltham, USA
Prestained protein ladder (PageRulerTM #26616)	Thermo Fisher Scientific Inc., Waltham, USA
Reaction tubes	Eppendorf AG, Hamburg, Germany
Syringe filter (Acrodisc® 13 mm, 0.2 µm)	Pall Corporation, Port Washington, NY, USA
Transfer Stacks (IBlot®2 NC Mini)	Thermo Fisher Scientific Inc., Waltham, USA
Transwell (PET 6-well ThinCert™, pores of 0.4 µm)	Greiner Bio-One, Frickenhausen, Germany
Ultrafiltration spin columns (Vivaspin™ 500, PES)	Sartorius, Göttingen, Germany

6. Laboratory instruments and software

6.1 Laboratory instruments

Table 12: List of laboratory instruments

Instrument	Distributor
-20 °C freezer	Comfort NoFrost, Liebherr, Bulle, Switzerland
-80 °C freezer	Hettich lab technologies, Tuttlingen, Germany
Cell counter CASY	OLS OMNI Life Science, Bremen, Germany
Centrifuge (Eppendorf centrifuge 5415R)	Hettich lab technologies, Tuttlingen, Germany
Centrifuge (Heraeus Multifuge 3-LR)	Hettich lab technologies, Tuttlingen, Germany
Counting chamber (Neubauer)	Paul Marienfeld, Lauda-Königshofen, Germany
ECL imager (Amersham Imager 600)	GE Healthcare Europe GmbH, Freiburg, Germany
Electrophoresis power supply (EPS 601)	GE Healthcare Europe GmbH, Freiburg, Germany
Electrophoresis power supply (EPS 301)	GE Healthcare Europe GmbH, Freiburg, Germany
Flow cytometer (MACSQuant Analyser 10)	Militneyi Biotec, Bergisch Gladbach, Germany
Flow cytometer (BD LSRII SORP HTS)	BD Biosciences, New York, USA
Heat block (HBT-1-131)	Haep Labor Consult, Bovenden, Germany
Heat block (Eppendorf Thermomixer compact)	Merck KGaA, Darmstadt, Germany
iBlot 2 Dry Blotting System	Thermo Fisher Scientific Inc., Waltham, USA
Incubator (Varocell)	Varolab GmbH, Giesen, Germany
Incubator (Forma Reach-In CO2 Incubator)	Thermo Fisher Scientific Inc., Waltham, USA
IncuCyte® S3	Essen BioScience, Ann Arbor, USA
Inverted digital microscope (EVOS M5000)	ThermoFisher Scientific Waltham, MA, USA
Inverted microscope (Eclipse TE300)	Nikon Europe BV, Amsterdam, Netherlands
Microplate reader (SPARK™)	Tecan, Meannedorf, Switzerland
Microplate reader (GENios)	Tecan, Weymouth, UK
Mini Gel Tank	Thermo Fisher Scientific Inc., Waltham, USA
Scanner (Epson Perfection V200)	Saiko Epson Corporation, Amsterdam, Netherlands

Shaking platform (Sarstedt TPM-2)	Gemini, Nuembrecht, Germany
Spectrophotometer (NanoDrop ND-1000)	Thermo Fisher Scientific, Ulm, Germany
Voltohmmeter (EVOM)	World Precision Instruments, Sarasota, FL, USA
Vortex Mixer VF2	IKA®-Werke GmbH & CO. KG, Staufen, Germany

6.2 Software

Table 13: List of softwares

Software	**Distributor**
Fiji	ImageJ
Flowing software 2.5.1	Cell Imaging Core, Turku Centre for Biotechnology, University of Turku and Åbo Akademi University
GraphPad Prism 9	GraphPad Software Inc., San Diego, CA, USA
IncuCyte® S3 Software	Essen BioScience, Ann Arbor, USA
MACSQuantify	MACS Miltenyi Biotec, Bergisch Gladbach, Germany
Microsoft Excel 2016	Microsoft Corporation, Redmond USA

Methods

1. Production of IZI1551

The vector construct for IZI1551 (Flag/Fc (Q, G)-scTRAIL-pSecTag) was provided by Prof. Dr. Roland Kontermann and its production and purification were performed according to the method developed by M. Hutt and co-workers and optimized by V. Vetma as part of her PhD thesis work [254,510].

1.1 Transformation of DH5α competent bacteria with IZI1551 plasmid DNA and purification

10 ng of IZI1551 plasmid DNA was diluted in 20 µl of H_20 and placed on ice. 40 µl of TCM buffer and 100 µl of DH5α competent bacteria cells were added to the plasmid dilution and incubated on ice for 30 minutes. This was followed by a two minutes heat-shock at 42 °C and an additional one minute on ice. 640 µl of prewarmed LB medium were immediately added to the suspension and this was incubated on a shaker at 250 rpm and at 37 °C for one hour. 50 µl of the transformed bacterial suspension were plated onto LB agar plates containing 25 µg/ml of kanamycin and plates were incubated at 37 °C overnight. The next day a colony was transferred into 1200 ml of LB medium containing 1% (w/v) glucose and 100 µg/ml ampicillin and it was incubated overnight on an orbital shaker at 37 °C. Finally, the plasmid DNA was purified using a NucleoBond® Xtra Midi kit (midi-preparation) according to the manufacturer's protocol. The DNA concentration was determined by measuring the absorbance at 260 nm using the NanoDrop™ ND-1000 spectrophotometer.

1.2 Culturing of the HEK P2 cell line for the production of IZI1551

IZI1551 was produced in the human embryonic kidney (HEK) P2 suspension cell line with a DR5 knockout generated by Dr. Martin Siegemund. The cell line was cultured in F17 Expression Style medium supplemented with 4 mM GlutaMAX, 0.1% Koliphor P188 and with the addition of 4 µg/mL puromycin. Erlenmeyer flasks containing the suspension HEK P2 cells were incubated on an orbital shaker at 37 °C and 5% CO_2. The cell number was counted daily with a CASY cell counter and it was maintained lower than 2×10^6 cells/ml.

1.3 Transient transfection with polyethyleneimine (PEI)

24 hours prior to transfection, 1.2 x 10^6 cells were spun down at 500 g for 10 minutes and the supernatant with antibiotic-containing medium was aspired. The cell pellet was resuspended in 360 ml of F17 Expression Style Medium supplemented with 4 mM GlutaMAX, 0.1% Koliphor P188 and in absence of antibiotics. Transfection was done when the cells were in their exponential growth phase (1.5-2 x 10^6 cells/ml). For that, on the day of transfection, the morphology of the cells was inspected under the microscope and the cells were counted to verify that the viability was higher than 90%. 400 µg of plasmid DNA were prepared with 20 ml of F17 medium. 1mg/mL of PEI was prepared in 20 ml of F17 medium. Both solutions were incubated for five minutes at room temperature (RT). Then, the PEI solution was added to the DNA mixture and the resulting solution was further incubated at RT for 20 minutes. This mixture was then added to 360 ml of HEK P2 cells in their exponential growth phase and the cells were placed back on the orbital shaker at 37 °C and 5% CO_2. 24 hours after the transfection, 0.5% of tryptone N1 (TN1) and 10 µM $ZnCl_2$ were added to the cell suspension. The cells were then incubated for additional four days on the orbital shaker and proteins were finally harvested from the supernatant and further purified.

1.4 Protein harvesting and purification by anti-FLAG chromatography

On the fifth day post-transfection, the transfected cells from the suspension were discarded by spinning them down at 2000 g for 30 minutes at 4 °C and the supernatant containing the proteins was collected to be sterile filtered (using filters with pores of 0.45 µm in diameter). In parallel, an anti-FLAG M2 Affinity Gel was loaded with PBS into a purifying column and it was equilibrated with three washing steps using 100 mM glycine-HCl at pH=3.5. Additional four washing rounds with DPBS were performed. To capture the target protein, the protein solution and the affinity resin (in PBS) were incubated together on a rolling platform at 4 °C overnight. The affinity gel was then collected by centrifugation at 2000 g for 30 minutes and transferred to a chromatography column. DPBS was used in three steps to wash away excess gel. Bound proteins were eluted with DPBS containing 100 µg/ml FLAG peptide. Washing and elution steps were qualitatively analysed with the dye Coomassie brilliant blue G-250. The protein-containing eluate was then dialyzed in 5 litres of PBS overnight at 4 °C. The affinity gel was recovered for future use by repeating the equilibration and it was stored at 4 °C in 50% (v/v) glycerol in PBS containing 0.02% sodium azide.

1.5 Size-exclusion HPLC

The purified protein was analysed by size exclusion high-performance liquid chromatography (HPLC). The protein eluate contained aggregates, fractions with diverse oligomerization status or cleavage products and it was further purified by fast protein liquid chromatography (FPLC). The concentrated protein was applied to a Superdex 200 10/300 GL column using PBS as mobile phase and a flow rate of 0.5 ml/min. Protein was collected in 100 µl to 250 µl fractions. Fractions containing the desired protein configuration were pooled. These steps were all performed by Doris Göttsch. 100 µl aliquots of IZI1551 in PBS were stored at -80 °C.

1.6 Determining the concentration of IZI1551

The concentration of the recombinant IZI1551 was determined for each thawed vial prior to use. For that, 10 µl of highly concentrated protein were diluted in 15 µl of PBS. 5 µl of this mix were used to determine the protein concentration (mg/ml) by measuring the absorption at 280 nm with a NanoDrop™ ND-1000 spectrophotometer. The Beer-Lambert equation was used to calculate the concentration of the protein:

$$[\mathbf{4}]\ C = \frac{A_{280} \times Mw}{\mathcal{E} \times l}$$

Equation 4: Beer-Lambert equation

The Beer-Lambert equation was used to calculate the concentration of IZI1551, given its known molecular weight (Mw = 169.18 kDa) and its extinction coefficient ($\varepsilon = 239.14 \times 10^3\ M^{-1}\ cm^{-1}$).

where:
C = concentration (mg/ml)
A_{280} = absorption at 280 nm
Mw = molecular weight of the protein (mg/µmol)
$\mathcal{E}$ = extinction coefficient (ml/(µmol×cm))
l = optical path length (cm)
Afterwards, the protein concentration (mg/ml) was divided by the molecular weight (mg/mmol) to convert the units from mg/ml to mol/l (molarity).

1.7 Biochemical characterisation and quality control of IZI1551

To confirm the purity of the produced protein, an SDS-PAGE was performed. 5 µg of the protein were resolved in a Bolt 4-12% Bis-Tris Plus Gel under reducing and non-reducing conditions. The gel was boiled in ddH$_2$O and incubated in Coomassie staining solution for one hour at RT and the gel was then visualised with the photo scanner Epson Perfection V200. A band of approximately 170 kDa, corresponding to the size of the full length IZI1551 (dimer of 169.18 kDa), was detected under non-reducing conditions and one band of approximately 85 kDa (reduced disulfate bonds) was detected under reducing conditions (*figure 13*).

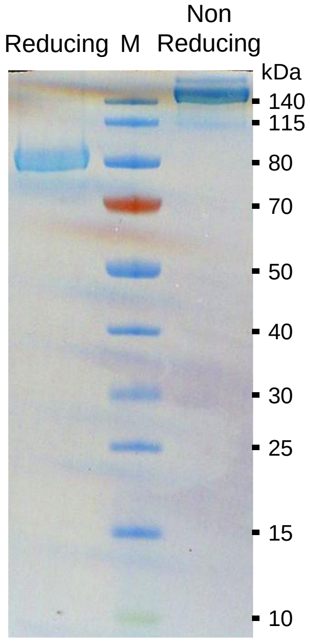

Figure 13: SDS-PAGE of IZI1551 for biochemical characterisation

SDS-PAGE to examine the purity of the produced protein. Full length protein and protein with reduced disulfate bonds were detected, but not degradation products. M: protein ladder. Reducing: with β-mercaptoethanol. Non-Reducing: without β-mercaptoethanol.

To test the efficacy of the protein produced, its ability to reduce the viability of an IZI1551-sensitive cell line such as HeLa was compared to that of a previous batch. For that, serial fold dilutions of the protein, from 10 nM to 10^{-6} nM, were prepared. These were applied in triplicates on HeLa cells seeded at a density of 10^4 cells/well in an F-bottom 96-well plate 24 hours prior to the experiment. A negative control consisting of untreated cells was also included. Following 24 hours of IZI1551 treatment, a 2% Triton solution was added onto three wells as a positive control and the viability of the cells was determined: the treatment was removed and 100 µl of 0.5% Crystal Violet solution were added to each well. Following one hour of incubation at RT, the crystal violet staining was removed, the cells were rinsed with tap water and the plate was left to dry at RT overnight. The next day, 200 µl of methanol were added in each well and the absorption was measured at 570 nm with a SPARK^{TM} microplate reader. The obtained values were normalised to that of the untreated control. The reduced viability of HeLa cells upon treatment with the newly produced IZI1551 was compared to that upon treatment with a previously produced batch.

2. Cell culture

Cell culture of all non-PDCLs was performed according to standard operating procedures in the laboratory of Prof. Dr. Markus Morrison (Rehm).

2.1 2D GBM PDCLs cultures

All glioblastoma PDCLs were cultivated in neurosphere medium (NS) freshly prepared once every two weeks as follows: DMEM/F-12 supplemented with 2% B27; 20 ng/ml of bFGF; 20 ng/ml of EGF; 5 µg/ml of heparin and 1% Pen/Strep. Flasks for the maintenance of 2D cultures were rinsed with PBS for reducing their surface tension and they were freshly coated BME in a ratio 1:100 with NS medium and in a sufficient volume to cover the whole culturing surface (2.5 ml for T75 flasks, 1.5 ml for T25 flasks, 1 ml for 6-well plates and 40 µl for 96-well plates). The coated flasks were incubated for 30 minutes at 5% CO_2, 37 °C and 96% relative humidity in an incubator and cells were seeded onto it. To maintain a proliferative cell culture, dilutions were carried out every four to 20 days depending on the growth rate of each cell line. For this purpose, as well as for harvesting, cells were detached by treating them with an amount of Accutase® sufficient to cover the cell surface for 10 to 20 minutes in the incubator at 5% CO_2, 37 °C and 96% relative humidity. The detachment reaction was stopped by diluting Accutase® with PBS in a ratio 1:5. The cell suspension was spun down for five minutes at 400 rcf and the cell pellet was either diluted as necessary in NS medium and placed back into the flasks or prepared for counting. During the passaging routines, cells were never discarded but a cell suspension of at least 1 million cells in a ratio 1:10 with DMSO was always stored for long term in sterile cryovial at -80 °C. Cell counting was performed using a Neubauer counting chamber (hemocytometer). 10 µl of the cell suspension were mixed with 10 µl of a trypan blue solution to exclude the dead cells from the count. 10 µl of the solution were loaded onto the counting chamber and the cell number was calculated as the mean number of cells counted in the four squares of the chamber. This was then multiplied by the volume of the cell suspension loaded onto the hemocytometer and multiplied by 10^4 as conversion factor to obtain the number of cells per millilitre. A different number of cells was seeded according to the surface area of the cultureware and to the requirements of the experiment. Attachment of the cells to the culturware was allowed to occur overnight in an incubator at 37 °C and 5% CO_2. Medium was changed every two or three days. Cells were only used until passage number 25 (short-term cultures) unless differently stated. All cell lines were regularly tested for mycoplasma infection.

2.2 3D GBM PDCLs cultures

Glioblastoma PDCLs were cultivated in NS medium prepared as described in paragraph 2.1. Flasks for the maintenance of 3D cultures were pre-rinsed with the surfactant solution Anti-Adherence Rinsing Solution that reduces the surface tension and prevents cell adhesion. For splitting or harvesting, glioblastoma spheroids were spun down and thoroughly resuspended in Accutase® for both enzymatic and mechanical dissociation. After 20 minutes, the enzymatic reaction was stopped by diluting the cell suspension in PBS. Passaging and counting of the single cell suspension was carried out as for the 2D glioblastoma PDCLs. An appropriate number of single cells was seeded onto cultureware pre-rinsed with Anti-Adherence Rinsing Solution and spheroids were allowed to form for 24 hours in an incubator at 5% CO_2, 37 °C and 96% relative humidity. For the maintenance of a proliferative spheroids culture, medium was changed every two or three days and splitting was performed every 7 to 10 days depending on the growth rate of the cell lines and always before the formation of a necrotic core could occur. All cell lines were regularly tested for mycoplasma infection.

2.3 hCMEC/D3 cell culture

Blood-brain barrier hCMEC/D3 endothelial cells were cultured in Endothelial Cell Growth Basal Medium MV 2 with the following supplements: 0.05 ml/ml FBS, 0.004 ml/ml Endothelial Cell Growth Supplement, 10 ng/ml Epidermal Growth Factor, 90 µg/ml Heparin, 1 µg/ml Hydrocortisone and 1 ng/ml bFGF. Culturewares were coated with 10 µg/cm^2 Collagen type I, Rat Tail in acetic acid for one hour at 5% CO_2, 37 °C and 96% relative humidity. Flasks were rinsed with PBS before the cell seeding. Cell cultures were maintained until passage number 10 and a 1:5 or 1:10 dilution was prepared every four or five days. For harvesting, cells were washed with PBS and detached from the surface by treating them with 1 x trypsin/EDTA in PBS for 10 minutes in the incubator. Thereafter, the reaction was stopped with the same culturing medium in a volume 10 times higher than that of trypsin. The cell suspension was spun down for five minutes at 400 rcf, the supernatant was discarded and the cell pellet was resuspended in an appropriate amount of medium for either counting the cells as described in paragraph 2.1 or for splitting them. For the long-term storage, around one million cells were pelleted by centrifugation (300 g for five minutes), supernatant was removed and cells were resuspended in freezing medium (10% (v/v) DMSO in FBS) before finally transferring them to sterile cryovials and freezing them at -80 °C.

2.4 U-87 MG; HT1080 and HeLa cell culture

The cell line U-87 MG was cultured in DMEM medium and the cell lines HT1080 and HeLa were cultured in RPMI1640 + L-Glutamine medium, both supplemented with 10% FBS. Culturewares were kept in an incubator at 37 °C with 5% CO_2 and 95% relative humidity. To harvest the cells, the medium was thoroughly removed via aspiration, the cells were washed with PBS and detached using 1x trypsin/EDTA in PBS. After five to 10 minutes in the incubator, the trypsin was inactivated via addition of FBS-containing medium (8 ml of medium every 2 ml of trypsin) and the cells were spun down for five minutes at 400 rcf. The cells were resuspended in an appropriate amount of fresh medium and either counted using a Neubauer chamber as described in paragraph 2.1 or, every three to five days, they were split in a ratio 1:5 or 1:10 for the maintenance of a proliferative culture. Alternatively, the cell pellet was resuspended in freezing medium (10% (v/v) DMSO in FBS) and conserved at -80 °C in cryovials.

3. Cell death measurements

3.1 Cell death measurements by flow cytometry

Flow cytometry-based measurements of cell death were performed according to standard operating procedure of the laboratory of Prof. Dr. Markus Morrison (Rehm). Briefly, 1,5 × 10^4 (glioblastoma PDCLs) or 1,0 × 10^4 (hCMEC/D3, HT1080, U-87 MG) cells per well were seeded in a 96-well F-plate in the respective culturing medium 24 hours prior to experiments. For glioblastoma PDCLs the surface of the well was either coated with 1:100 BME (2D condition) or washed with Anti-Adherence Rinsing Solution (3D condition). Cells were treated in triplicates for 24 hours or 48 h and with the drug concentrations stated in the results section. Pre-treatment conditions consisted of 30 minutes (Q-VD-OPh) or 24 hours (marizomib) incubation prior to the addition of other drugs. Following treatments, dead cells in the supernatant were collected and combined with detached or dissociated living cells or spheroids (40 µl of Accutase® for 10-20 minutes or 40 µl of 1x trypsin/EDTA in PBS for five minutes at 37 °C). All cells were transferred to a 96 U-well plate and spun down at 400 rcf for five minutes. The supernatant was removed and cells were resuspended in 100 µl of Annexin V Binding Buffer with 1:100 Annexin V-GFP and 1 µM Propidium Iodide (PI). Measurements were done on a MacsQuant flow cytometer using a laser with excitation at 488 nm (emission from 655-730 nm; PI) and a laser with excitation at 488 nm (emission from 500-550 nm; GFP). Single staining was used to compensate the spectrum overlap of the two fluorochromes. Gating was performed to exclude cell debris, cell clumps or non-cellular particles. To analyse the data generated by the flow cytometer, the software MACSQuantify and the flowing software 2.5.1 were used.

3.2 Cell death measurements with the IncuCyte system

1,0 × 10^4 cells/well were resuspended in the corresponding cell culturing medium containing 1 µM PI. Cells were seeded in a 96-well F-bottom plate (pre-coated with 40 µl of 1:100 BME/well for 2D-cultured glioblastoma PDCLs) 24 hours prior to the experiment. Plates were placed in the incubator of a IncuCyte S3 device at 37 °C and 5% CO_2 and they were imaged once prior to the first treatment. Then, cells were treated or pre-treated in triplicates as stated in the results section and imaged at regular intervals as indicated. Two images from two fields of view per well were obtained at a magnification of 20x with both transmitted light and at 585 nm wavelength to detect the fluorescence emitted by PI. In the case of glioblastoma PDCLs, 0.1 µg/µl digitonin were added onto the cells at the end of the treatment in order to permeabilize the cell membranes and images were taken for one additional hour at intervals of 10 minutes. The images from all the time points were analysed with the semi-automated IncuCyte S3 software for the percentage of cell-covered area (confluence) and the percentage of PI-covered area in each well and average values from the two captures per well were calculate by the software. For the glioblastoma PDCLs, cell death was calculated as the percentage of PI-covered area normalized to the percentage of cell covered area that was further normalized to the PI-positive cell area in the digitonin-treated wells. In the case of HT1080 and U-87 MG cell lines instead, due to technical difficulties for the software to accurately detect the cell-covered area and to the swift membrane disruption upon digitonin treatment, the ratio between PI-covered area and cell-covered area was calculated and considered as indicator of cell death. Plotting of the data and statistical analysis was conducted with GraphPad Prism 9.

4. Staining methods for live cell imaging

4.1 Hoechst and PI staining for microscopy

Glioblastoma PDCLs were seeded at a density of 1,0 × 10^4 cells/well in an F-bottom 96-well plate pre-coated with 40 µl of 1:100 BME in NS medium and allowed to attach for 24 hours. Seeding medium was then removed and replaced with 100 µl of fresh medium containing the drug concentrations indicated in the results section as well as 1 µM PI and 1 µg/ml Hoechst 33342. Following 24 hours of treatment, cells were imaged at a 10x magnification with an EVOS M5000 digital inverted microscope using the transmitted light as well as the blue light cube (excitation at 357/44 nm and emission at 447/60 nm) to detect the Hoechst signal and the orange light cube (excitation at 531/40 nm and emission at 593/40 nm) to detect the PI signal.

4.2 Calcein AM staining for viability assay

A Calcein AM stock solution (1 mg/ml) was prepared at a working concentration of 4 µM in DMEM-F12 medium (NS medium without supplements) and equilibrated by incubating it for 15 minutes in the dark at 5% CO_2, 37 °C and 96% relative humidity. Following equilibration, the Calcein solution was used to stain the spheroids as described in paragraph 5.2.

5. Cell viability assays

5.1 WST-1 assay

Glioblastoma PDCLs were plated in a number of 3 × 10^3 cells/well in 96-wells F-plates either pre-coated with 40 µl of 1:100 BME in NS medium (2D cultures) or washed with Anti-Adherence Rinsing Solution (3D cultures). Cells were allowed to attach or to form spheroids for 24 hours in an incubator at 5% CO_2, 37 °C and 96% relative humidity. Drugs were added onto the cells as indicate in the results section and after 24 hours the WST-1 (2-(4-Iodophenyl)-3-(4-nitrophenyl)-5-(2,4-disulfophenyl)-2H-tetrazolium sodium salt) reagent was added in a 1:10 final dilution, according to the manufacturer’s instructions. The WST-1 salt is cleaved to a soluble formazan dye by the succinate-tetrazolium reductase system of the respiratory chain of the mitochondria in a reaction requiring NAD(P)H.

Plates were incubated for three hours in the incubator and the absorbance of each sample was measured at wavelengths of 450 and 620 nm using a microplate reader (GENios or SPARK®, Tecan). The background signal (620 nm) was subtracted from the 450 nm reads and the absorbance was expressed relatively to DMSO-treated control cells.

5.2 Calcein AM staining

3 × 10^3 cells/well of the N160125 cell line were seeded in duplicates in a 96-well plate washed with Anti-Adherence Rising Solution. Cells were allowed to form spheroids for 24 hours. Treatments were added for the duration and concentration indicated in the results section. Following treatment, the spheroids were spun down for 10 minutes at 400 rcf and the supernatant was removed. The spheroids were then resuspended in 4 µM of an equilibrated Calcein AM solution prepared as described in paragraph 4.2. 100 µl of a Calcein AM solution were added in each well and incubated for 30 minutes at 37 °C prior to imaging with an Eclipse TE300 inverted microscope using the FITC channel. Fluorescence was recorded using a 490 nm excitation filter and a 520 nm emission filter. Fluorescence intensity is proportional to the number of viable cells and it was expressed as a fold change compared to untreated controls.

6. Calculation of the synergy scores

The synergy scores of drug interactions between IZI1551 and marizomib were assessed based on the calculation of the combination index (CI). The calculation was done on the cell viability data generated by WST-1 assay. The CI was calculated according to the formula:

$$[\mathbf{5}]\ CI = \frac{a+b}{c}$$

Equation 5: Calculation of the combination index (CI)

In the formula of the CI the following is represented: a = Percentage of alive cells after the single treatment with drug a. b = Percentage of alive cells after the single treatment with drug b. c = Percentage of alive cells after the combination treatment with drugs a and b.

The calculated CI values represent:
CI>1.0 indicates an antagonistic effect
CI = 1.0 indicates an additive effect
CI<1.0 indicates a synergistic effect
(The lower the CI value, the stronger is the synergy).
In this thesis, an operational threshold of 0.9 was chosen to discriminate CI values indicative of synergistic apoptosis-inducing effects.

7. Long term survival assay

1,5 × 10^4 cells/well of N160125 or GTCC10 cell lines were seeded in an BME-coated 96-well F-plate 24 hours prior to experiments. Cells were then treated in triplicates with 1 nM of IZI1551, 80 nM of marizomib or the combination thereof. Alternatively, cells were pre-treated with 50 µl of Q-VD-Oph for 30 minutes prior to the addition of the combination treatment. Following 24 hours of treatment, the supernatant with the dead cells was discarded and alive cells were detached using Accutase® as described in paragraph 2.1. Cells were counted and triplicates of 500 survivor cells per each condition were re-seeded in a BME-coated 96 well plate. Cells were placed in an incubator at 5% CO_2, 37 °C and 96% relative humidity for six days. On the sixth day, cells were imaged at 10x magnification using an EVOS M5000 microscope and their viability was assessed with a WST-1 assay as described in paragraph 5.1. Cells were counted in an exact volume of 100 µl per condition using a MACSQuant flow cytometer and proliferation capacity was normalized by relating the numbers of cells in each condition to that of untreated controls.

8. Western blotting

Western blotting was performed according to standard operating procedures in the laboratory of Prof. Dr. Markus Morrison (Rehm).

8.1 Preparation of whole cell extracts for western blotting

The cell monolayers were detached with Accutase® (2D glioblastoma PDCLs) or 1x trypsin (HT1080, HeLa, U-87 MG) and glioblastoma spheroids were dissociated in Accutase®. Cells were harvested as described before, either in untreated condition for quantifying the basal protein expression or treated as indicated in the results section. The cell pellets were washed with 1 ml of PBS and transferred in 1.5 ml reaction tubes to be spun down at 500 g for 5 minutes at 4 °C. Cell pellets were resuspended in an appropriate amount of lysis buffer + protease inhibitor cocktail cOmplete (EDTA free) and incubated for 15 minutes on ice, followed by centrifugation at 1.6×10^4 g for 15 minutes at 4 °C to pellet the crude cell components. The supernatants were then transferred to new 1.5 ml reaction tubes and either frozen at -20 °C or directly used for protein determination and sample preparation. Pellets were discarded.

8.2 Determination of the protein concentration with the Bradford assay

The protein concentration of the generated cell lysates was determined with the Bradford assay. This is based on the dye Coomassie brilliant blue G-250 that forms complexes with proteins in an acidic environment, causing a shift in the absorbance maximum from 465 nm to 595 nm. 10 µl of pre-diluted lysates (1:10 with ddH_2O), a BSA standard (0.0, 0.125, 0.25, 0.5, 0.75, 1.0, 1.5, 2.0 mg/ml BSA diluted in ddH_2O) and a blank (lysis buffer diluted 1:10 and 1:20 with ddH_2O) were transferred in duplicates to a 96-well plate (F-bottom, clear). 200 µl of the Bradford reagent were added in each well and following five minutes of incubation at RT absorbance was measured at a wavelength of 595 nm with a SPARK™ microplate reader. The protein concentration in whole cell lysates was calculated by comparing the absorbance of the samples of a known concentration to that of samples of unknown concentration. The protein samples were either further prepared for Western blotting or stored at -20 °C for later analysis.

8.3 Protein sample preparation and SDS-PAGE

From the previously obtained cell lysates, samples were prepared for the sodium dodecyl sulfate polyacrylamide gel electrophoresis (SDS-PAGE). The protein samples consisted of the required volume of cell lysate containing 20 or 15 µg of protein, 1:5 of Laemmli loading buffer 5x and H_2O. The protein samples were incubated for five minutes at 95 °C on a heat block and finally, either frozen at -20 °C or directly loaded onto the gel.

The protein samples, together with a protein standard, were loaded on a Bolt™ 4-12% Bis-Tris Plus precast gel and separated in a Bolt™ mini gel tank electrophoresis chamber filled with Bolt™ MES SDS running buffer 20x at 150 Volts for 40 minutes following the manufacturer's instructions.

8.4 Semi-dry protein transfer

After the SDS-PAGE, proteins were transferred to a nitrocellulose membrane using the iBlot 2 Dry Blotting System following the manufacturer's instructions (transfer settings: 20 Volts; 7 minutes). Membranes were stained with a Ponceau S solution to examine the quality of the protein transfer. Membranes were then washed with TBS and incubated for one hour at RT with 1:10 blocking reagent in TBS.

8.5 Protein detection

Following blocking, membranes were incubated overnight at 4 °C with a primary antibody diluted in 1:20 blocking reagent in TBST. Afterwards, the membranes were washed three times for 10 minutes with 1x TBST at RT and then incubated with the secondary antibody diluted in TBST with blocking reagent (1:20), for one hour at RT. Following other three washing steps, proteins were detected by incubating the membrane with an HRP substrate and detecting the signals with an ECL imager. In the case of re-probing, membranes were washed three times with TBST before incubating them with additional antibodies. The brightness and contrast of the protein bands were adjusted with the Fiji software.

9. Marizomib permeability assay

9.1 BBB model

0.4×10^6 cells/well of hCMEC/D3 cells were grown in 1.5 ml of supplemented Endothelial Cell Growth Basal Medium MV 2 (see paragraph 2.3) on PET (polyethylene terephthalate) 6-well ThinCert™ Cell Culture Inserts with a 0.4 μm pore size coated with 10 $\mu g/cm^2$ of Gibco™ Collagen type I, Rat Tail as described in paragraph 2.3. The bottom side of chamber was filled with 2 ml of supplemented Endothelial Cell Growth Basal Medium MV 2 and cells on the insert were allowed to grow until forming a confluent layer (additional five days). The resistance in each well, including a control empty well, was measured daily starting 24 hours after initial seeding (day 1) by an EVOM voltohmmeter combined with STX-2 electrodes. Recorded resistance was related to the surface area of the transwell insert ($\Omega \times cm^2$) and the resistance of cell-free inserts was subtracted from the measured values. On day 2, the medium from both the upper and bottom chambers were replaced with 2 ml of fresh medium. Experiments were performed when the transendothelial electrical resistance (TEER) exceeded 80 $\Omega \times cm^2$.

9.2 Assessing Marizomib penetrance

On the fifth day, when a tight barrier was considered to be formed (TEER>80 $\Omega \times cm^2$), medium from both chambers was replaced: 2.5 ml of fresh medium were added in the bottom compartment, and 2.5 ml of medium containing 40 μM of marizomib or DMSO were added in the upper one. Following 24 hours of treatment (day 6), the medium from the bottom chamber was collected and applied onto N160125 cells grown at a density of 1.5×10^4 cells/well of a BME-coated F-bottom 96-well plate. Alternatively, a separately prepared marizomib solution at 40 nM of concentration and in the same volume as the medium collected from the bottom chamber of the transwell, was added onto the N160125 cells. After 24 hours of pre-treatment, 1 nM of IZI1551 was added in both conditions and after additional 24 hours cell death was measured flow cytometrically as described in paragraph 3.1.

10. Proteasome activity assay

The inhibitory activities of marizomib and bortezomib *in vitro* were determined with a fluorescent reporter assay using the peptide suc-LLVY-AMC (N-(3-carboxy-1-oxopropyl)-L-leucyl-L-leucyl-L-valyl-N-(4-methyl-2-oxo-2H-1-benzopyran-7-yl)-L-tyrosinamide) that is a substrate of the CT-L activity of the proteasome, the main target of both marizomib and bortezomib. The tetrapeptide LLVY quenches the fluorescence of AMC when the reporter peptide is intact. Instead, when the tetrapeptide gets cleaved, AMC is released and the fluorescence emission increases proportionally to the activity of the 26S proteasome.
The protocol for assessing proteasomal activity was adapted from the PhD thesis of M. A. Laussman [511].

10.1 Preparation of stock solutions for the proteasome activity assay

- 0.1 M HEPES buffer, pH 7.4: 2.38 g HEPES initially dissolved in 80 ml of ddH_2O. After adjusting the pH to 7.4, ddH_2O was added up to 100 ml of final volume. The HEPES buffer was sterile filtered and kept at 4 °C.
- 1 M KCl buffer: 14.91 g KCl dissolved in 200 ml of ddH_2O and autoclaved.
- 1 M $MgCl_2$ buffer: 10.2 g of magnesium chloride hexahydrate added to 50 ml of ddH_2O and autoclaved.
- 0.25 M EDTA buffer, pH 8: 9.3 g EDTA disodium salt dihydrate dissolved in 80 ml of ddH_2O. After adjusting the pH to 8, ddH_2O was added up to 100 ml of final volume and the buffer was autoclaved.
- 0.25 M EGTA buffer, pH 8: 9.5 g EGTA added to 80 mL ddH_2O. After adjusting the pH to 8, ddH_2O was added up to 100 ml of final volume and the buffer was autoclaved.
- 1 M DTT stock solution: 3.1 g DTT dissolved in 20 ml of ddH_2O under the fume hood. The DTT solution was sterile filtered and 1 ml aliquots were prepared to be stored at -20 °C.
- CHAPS lysis buffer: 10 ml of 0.1 M HEPES, pH 7.4 was mixed with 4.2 ml of 1 M KCl; 0.5 ml of 1 M $MgCl_2$, 40 µl of 0.25 M EDTA, pH 8; 40 µl of 0.25 M EGTA; 0.5 g CHAPS and ddH_2O up to a final volume of 100 ml (85 ml). The lysis buffer was sterile filtered and 10 ml aliquots were kept at -20 °C. For use, an aliquot was thawed and 10 µl of 1 M DTT was added.

- 2x reaction buffer: freshly prepared by mixing 5 ml of 0.1 M HEPES buffer with 40 µl of 0.25 M EDTA, pH 8 and ddH_2O up to 10 ml.

10.2 Measurement of the CT-L activity of the 26S proteasome

4×10^4 cells/well were seeded in 24-well plates coated with 50 µl of BME 1:100 in NS medium. Cells were treated in triplicates for 24 hours with the concentrations of proteasome inhibitors indicated in the results section. At the time of harvesting, the medium was discarded from the cells and 200 µl/well of CHAPS lysis buffer were added. To facilitate the lysis procedure, the cell pellets were incubated for 10 minutes at 37 °C in a heat block shaker at 1000 rpm. Cell lysates were then transferred into pre-cooled 1.5 ml reaction tubes and kept on ice. From each lysate, triplicates were prepared by pipetting 50 µl of lysate per well into a black F-bottom 96-well plate. The remaining lysates were used for determining the protein concentrations via the Bradford assay. The 50 µl of lysate were incubated with 150 µl of a reaction solution containing: 1x reaction buffer (100 µl of the 2x reaction buffer for a total volume of 200 µl); 20 µM suc-LLVY-AMC substrate (final concentration per well, 6.11 µl from the 20 µM stock in DMSO prepared according to manufacturer instruction) and H_2O up to 200 µl (43.89 µl).

An autofluorescence control was included by mixing 50 µl of CHAPS lysis buffer with 150 µl of a reaction solution (100 µl of 2x reaction buffer and 50 µl of H_2O).

After five minutes of incubation in the dark at RT, the plate was placed in a pre-warmed SPARK^{TM} microplate reader at 37 °C and the fluorescence emission at 465 nm was measured every 10 minutes for 20 times upon excitation of 380 nm.

The obtained fluorescence signals were normalised to the protein concentrations determined via the Bradford assay as described in paragraph 8.2. The remaining CT-L activity of the proteasomes after marizomib or bortezomib treatments was analysed as the mean fluorescent emission from each cell lysate triplicate subtracted of the autofluorescence values. The resulting values were plotted over time and slopes of marizomib- or bortezomib-treated samples were normalized to untreated controls whose slope was set to 100% activity.

11. Flow cytometric analysis of death receptor surface expression

The surface expression of death receptors was measured according to standard operating procedures in the laboratory of Prof. Dr. Markus Morrison (Rehm). Briefly, cells were seeded at a density of 1.5 × 10^4 in F-bottom 96-well plates pre-coated with BME 1:100 in NS medium 24 hours prior to the experiments. Cells were then treated in duplicates for the time duration and drug concentrations indicated in the results section. The supernatant with dead cells was transferred into a U-form plate and attached cells were harvest in Accutase® as described in paragraph 2.1. Detached cells were combined with dead cells in the U-plate and spun down for five minutes, at 400 g and at 4 °C. The supernatant was removed and the cells were resuspended in 100 µl of cold PBA containing 4 µg/ml/sample of the primary antibody (anti-human DR4 or DR5) or of the isotype control ($IgG_{1\ k}$ or $IgG_{2b\ k}$). After 30 minutes of incubation on ice, cells were washed with 150 µl of PBA and resuspended in PBA containing 10 µg/ml of the secondary antibody (goat anti-mouse IgG - Alexa Fluor 488). Following 45 minutes of incubation on ice in the dark, cells were spun down for five minutes, at 400 g and at 4 °C. The supernatant was removed and the cells were first washed with PBA, then resuspend in 100 µl PBA and finally transferred to a U-form plate. Measurements were performed on a MACSQuant instrument using a laser with excitation at 488 nm and emission from 500-550 nm (GFP) and analysis was performed using the flowing software 2.5.1. Gating was performed to exclude cell debris, cell clumps or non-cellular particles as well as to select for IgG_1 or IgG_2 positive events. The median of IgG_1 or IgG_2 positive events was calculated and normalised to the DMSO control for determining the marizomib-induced death receptors accumulation. Alternatively, the median of IgG_1 or IgG_2 positive events was normalised to the median values calculated for the N160125 cell line in order to compare the basal expression levels of death receptors among different cell lines.

12. Statistical analysis

Statistical analysis was performed using GraphPad Prism 9. Data are shown as mean values plus or minus the standard deviation (SD), standard error of the mean (SEM) or range as stated in the figure legends. Statistical significance of differences between groups was verified using the stated significance tests. Significance level were denoted with asterisks: *$p \leq 0.05$; **$p \leq 0.01$; ***$p \leq 0.001$; ****$p \leq 0.0001$. Unless otherwise stated, data are from three independent experiments.

Results

1. Chapter One: GBM PDCLs show heterogeneous phenotypes and respond differentially to IZI1551 and marizomib

In this chapter, a panel of seven glioblastoma PDCLs from both primary and recurrent cases have been analysed. In particular, they have been characterised for their morphology and for their responsiveness to the hexavalent TRAIL receptor agonist IZI1551 alone, or in combination with the brain-penetrant proteasome inhibitor marizomib (MRZ). These PDCLs were established according to the methods described by the groups of M.L.M Lamfers and A. Idbaih and they were cultivated according to the most recent protocols that ensure the maintenance of the tumour characteristics [109,112,512]. In particular, the cells were only utilised for short term and they were cultivated in the absence of serum. Under these conditions, phenotypes and growth behaviours were very diverse among the different cell lines, reflecting the expected inter-tumour heterogeneity found in glioblastoma patients. The relevance of limited cultivation times for drug responsiveness studies was proven in experiments in which cells from short- and long- term cultures displayed very different sensitivities to the same dosage of IZI1551.

Dose-combination matrices of IZI1551 and marizomib revealed that the two drugs acted synergistically in inducing apoptosis in the majority of PDCLs, with marizomib also reducing the long-term proliferation capacity of cells surviving the combination treatment. This first screening provided promising results on the efficacy of combination therapies based on TRAIL and proteasome inhibition in glioblastoma.

1.1 GBM PDCLs show heterogeneous phenotypes that are maintained within low passage cultures

The experiments shown in this and in the following paragraphs were performed on PDCLs of which five came from primary glioblastoma cases and two originated from recurrent tumours. These cell lines were established at the Institut du Cerveau et de la Moelle épinière (ICM) or at the Erasmus Medical Center (EMC) and provided to the Institute of Cell Biology and Immunology (IZI) at a passage number below nine. The peculiar morphology of each cell line, cultured both in 2D and 3D, was documented as soon as their cultivation was started at the

IZI. The micrographs shown in *figures 14A* and *14B* should therefore be taken as a reference for the morphology of these cells, that kept on being monitored throughout the project to detect changes and alterations possibly occurring over time.

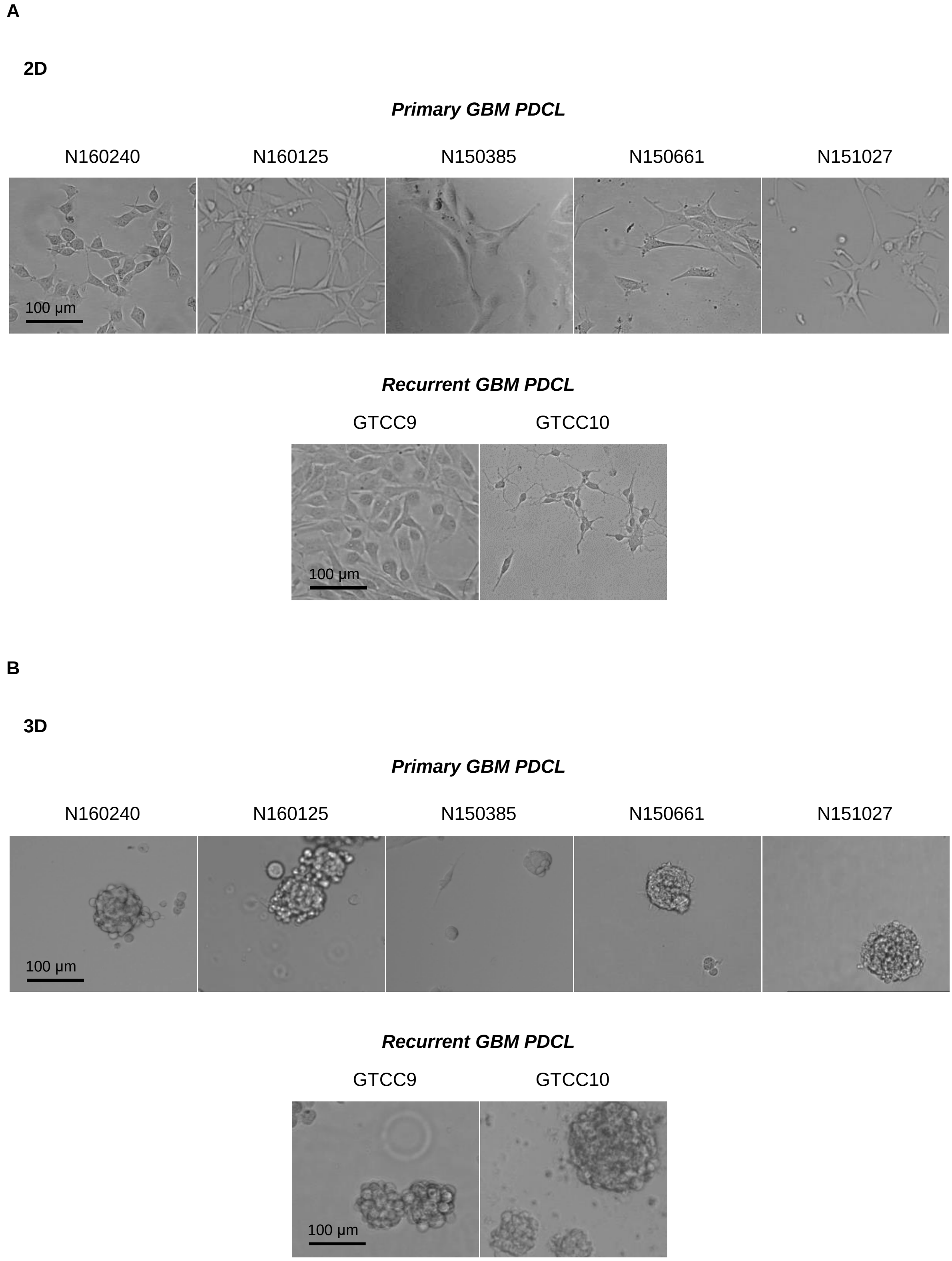

Figure 14: Morphology of 2D and 3D cultures of glioblastoma PDCLs

Transmitted light pictures of primary and recurrent glioblastoma PDCLs at a passage number below nine taken with an inverted digital microscope (EVOS). ***(A)*** *2D cell cultures cultivated on BME-coated flasks.* ***(B)*** *3D cell cultures cultivate on flasks pre-treated with Anti-Adherence Rinsing Solution.*

1.2 Long term cultivation alters the responsiveness of GBM PDCLs to IZI1551

In this project, the cytotoxicity of the translationally relevant second-generation TRAIL receptor agonist IZI1551 against glioblastoma PDCLs was assessed. PDCLs are a superior *in vitro* model for drug responsiveness studies when compared to established cell lines that are routinely passaged an uncountable number of times in most laboratories. To prove that such latter culturing routine can alter cells sensitivity to at least certain drugs, cells of one of the glioblastoma PDCLs of the aforementioned panel were parallelly cultivated for different time durations: in one case cells were only passaged less than 20 times while the other culture was maintained for longer periods until exceeding passage 30. Both cultures were then exposed to increasing concentrations of IZI1551 comprising 10 pM; 100 pM and 1 nM. Next, cells were stained with both Annexin V-GFP and propidium iodide (PI) and cell death was assessed flow cytometrically (*figure 15*). While short term-cultured cells were completely resistant to IZI1551 (*figure 15A*), cells that had been passaged several times (P>30) manifested a dose-dependent response to the drug (f*igure 15B*).

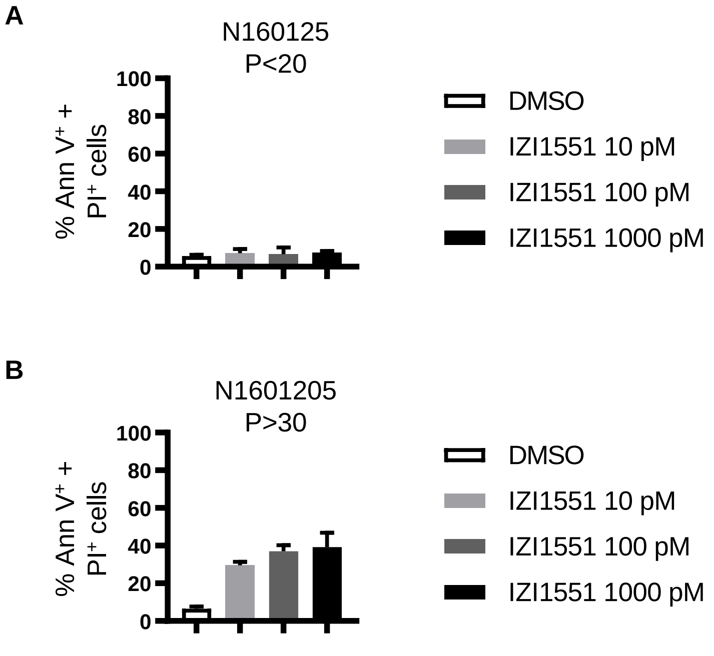

Figure 15: Long term cultivation alters the responsiveness of cells to IZI1551
2D-cultured N160125 cells were seeded at a density of 10^4 cells/well in a 96 well plate 24 h prior to the experiment and then treated for 24 h with the indicated concentrations of IZI1551. Cell death was measured by Annexin V/PI-based flow cytometry. ***(A)*** *Low-passaged N160125 cells (P<20).* ***(B)*** *High passage N160125 cells (P>30). Data represent mean ± range of two independent experiments.*

This experiment showed that prolonged cultivation times altered the characteristics of the cells and determined different responses to the TRAIL receptor agonist. Such different TRAIL sensitivities between short- and long- term cell cultures underlined the need to use patient derived cells only for limited times before their divergence from the tumour of origin would weaken the clinical relevance of drug responsiveness studies. For this reason, all the experiments shown from here on in this thesis have only been performed on cells kept in culture for less than 25 passages.

1.3 PDCLs of a representative GBM panel are mostly sensitive to the combination treatment of IZI1551+MRZ

In order to evaluate the efficacy of IZI1551 and marizomib as possible treatment options for glioblastoma patients, a representative panel of seven glioblastoma PDCLs, comprising both primary and recurrent cases, has been screened for responsiveness to these drugs as single agents and in combination treatments. To this end, the PDCLs were cultured in monolayers and their viability in response to 5x5 dose-combination matrices of IZI1551 and marizomib was assessed by WST-1 assays. Cells were exposed to the different combinations for 24 hours before absorbance was recorded. As shown in *figure 16*, single drug treatments exerted no or very limited efficacy while combination treatments, especially at higher dosages, resulted in a substantially lowered viability in the majority of cell lines tested. This result allowed to distinguish the panel in a group of five responder cell lines and a group of two cell lines classifiable as non-responders. From here on in this thesis, these five responder cell lines, namely GTCC9; N160240; N160125; N150385 and N150661 will be indicated in green while the two non-responder cell lines N151027 and GTCC10 will be indicated in red. Of note, the two cell lines derived from recurrent glioblastoma cases behaved very differently, with GTCC9 being highly sensitive and GTCC10 being strongly resistant to high doses of IZI1551 and marizomib in combination.

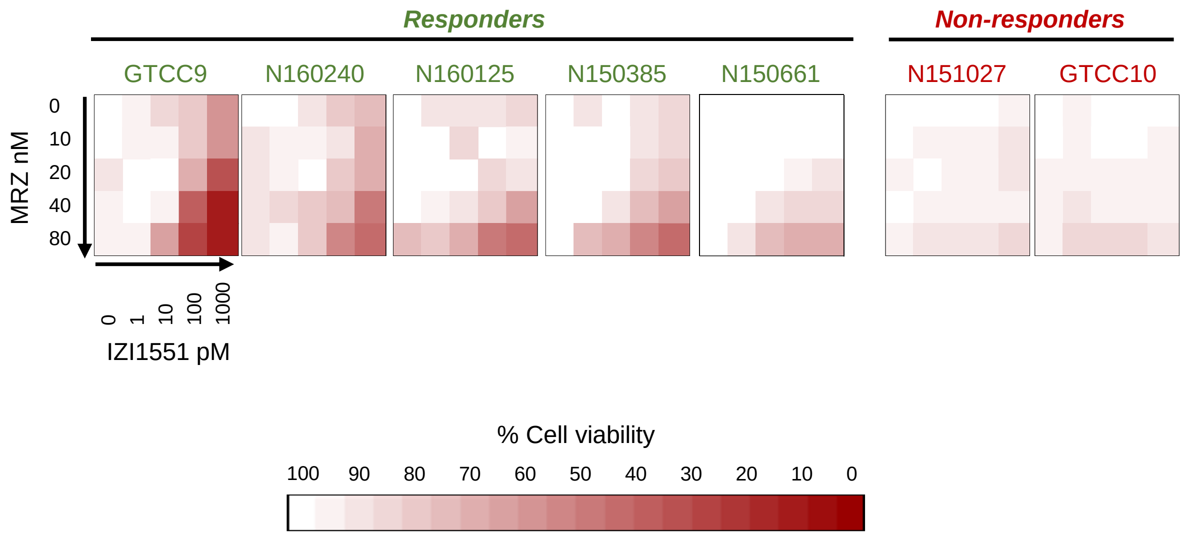

Figure 16: Most GBM PDCLs are sensitive to combination treatments with IZI1551 and MRZ

3 × 10^3 cells/well were cultivated in 2D and stimulated with the indicated concentrations of IZI1551 and MRZ for 24 h. Cell viability was assessed by a WST-1 cell proliferation assay. The percentage of cell viability was plotted in heat maps where the red colour intensity was proportional to the percentage of viability loss. The percentage of cell viability in each condition was normalised to untreated controls. Data are mean values from three independent experiments. SEMs across the repeat experiments and conditions were <20%. Data on N150385; N150661; N151027 and GTCC10 cells were generated by Emily Kolbe under the author's supervision.

Next, drug interactions were analysed by calculating the CI as described in the methods section. The calculation of the synergy scores revealed that for conditions where the combination of IZI1551 and marizomib substantially reduced cell viability, the two drugs acted synergistically, with the highest response corresponding to the highest synergy score (*figure 17*).

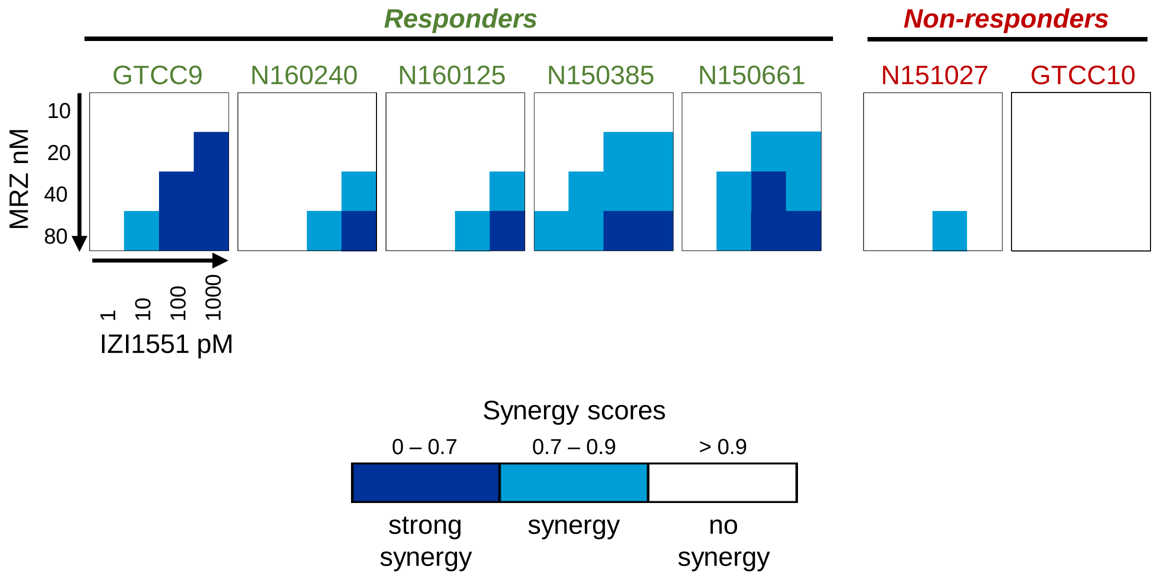

Figure 17: IZI1551/MRZ interactions evoke synergistic responses in sensitive cell lines

Synergy scores of drug interactions were determined by calculating the CI from the data shown in figure 16. The scores were plotted as heat maps in which the deeper blue colours represented stronger synergies.

To prove that loss of viability correlated with actual cell death induction, one of the PDCLs was analysed for Annexin V-GFP and PI positivity following treatment with the 25 drug combinations previously shown. Such measurements were then compared with the results of the WST-1 assay (*figure 18A and 18B*). This comparison indeed showed that the reduced viability induced by IZI1551+MRZ treatments mostly corresponded to cell death represented by phosphatidylserine exposure and PI permeability.

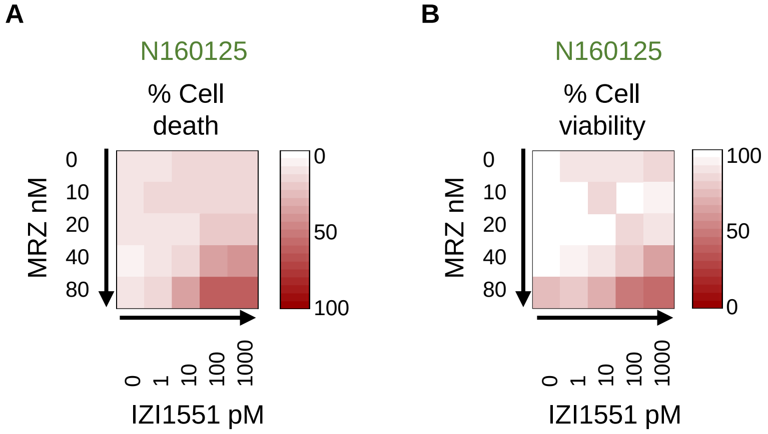

Figure 18: IZI1551+MRZ-induced loss of viability correlates with cell death induction

Comparison between cell viability and cell death measurements of 2D-cultured N160125 cells. ***(A)*** *Cell death was assessed via flow cytometry of cells stained with both Annexin V-GFP and PI.* ***(B)*** *The heat map showing the cell viabilities is from the experiment in figure 16 and is shown here for the purpose of comparison. Cell death data are mean values from three independent experiments. SEMs across the repeat experiments and conditions were <10%.*

All together these findings showed that IZI1551 and marizomib as single agents were too weak to substantially affect the viability of glioblastoma PDCLs and that combination treatments were necessary to evoke robust responses. It was also shown that IZI1551+MRZ treatments lowered the viability of glioblastoma cells in a way that correlated with cell death induction. Moreover, the interaction of these two drugs provoked highly synergistic responses in terms of reduced cell viability.

1.4 IZI1551+MRZ treatment induces apoptosis in GBM PDCLs

To characterise the cell death modalities triggered by the IZI1551+MRZ co-treatment, PDCLs previously classified as responders were exposed to this drug combination in presence or absence of the pan-caspase inhibitor Q-VD-Oph. Following 24 hours of treatment, cells were stained with both Annexin V-GFP and PI and cell death was measured flow cytometrically. As shown in *figure 19,* both IZI1551 and marizomib as single agents failed to trigger cell death at a significant level. The combination of the two drugs instead led to caspase-dependent death, as proven by the addition of Q-VD-Oph that brought cell death amounts back to background levels (*figure 19*).

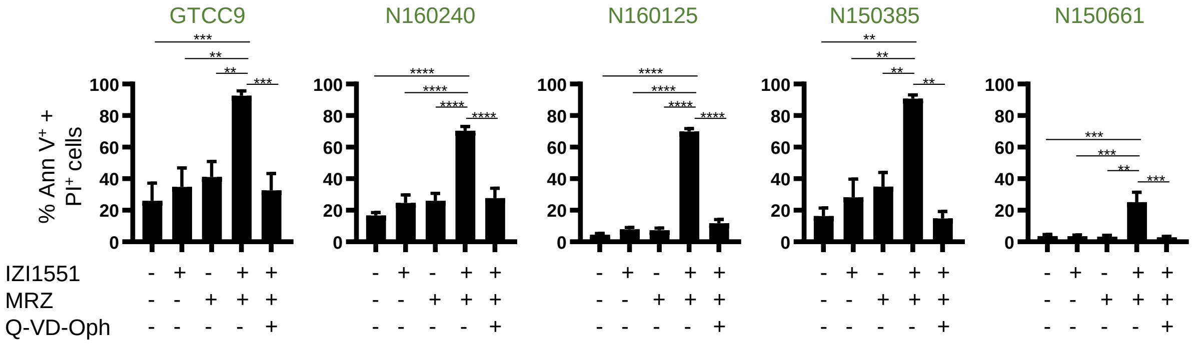

Figure 19: IZI1551+MRZ co-treatment induces caspase-dependent death of GBM PDCLs

*1.5 × 10^4 cells/well were cultivated in 2D and treated for 24 h with IZI1551 (1 nM), MRZ (80 nM) or with the combination thereof in presence or absence of the pan-caspase inhibitor Q-VD-Oph (50 µM, 30 minutes of pre-exposure). Cell death was measured by Annexin V/PI-based flow cytometry. Data represent mean ± SEM from three independent experiments. ** = p ≤ 0.01; *** = p ≤ 0.001 **** = p ≤ 0.0001. When not specified cell death differences were not significant. One-way ANOVA followed by Tukey's post hoc test. Experiments on GTCC9; N150385 and N150661 cells were performed together with Emily Kolbe.*

The co-staining of cell nuclei with both PI and Hoechst 33342 was also indicative of apoptotic death, as the increased PI signal upon combination treatment was reversed by caspase inhibition. Moreover, nuclei condensation and cellular rounding were observed in IZI1551+MRZ-treated cells and both effects were prevented by the addition of Q-VD-Oph (*figure 20*).

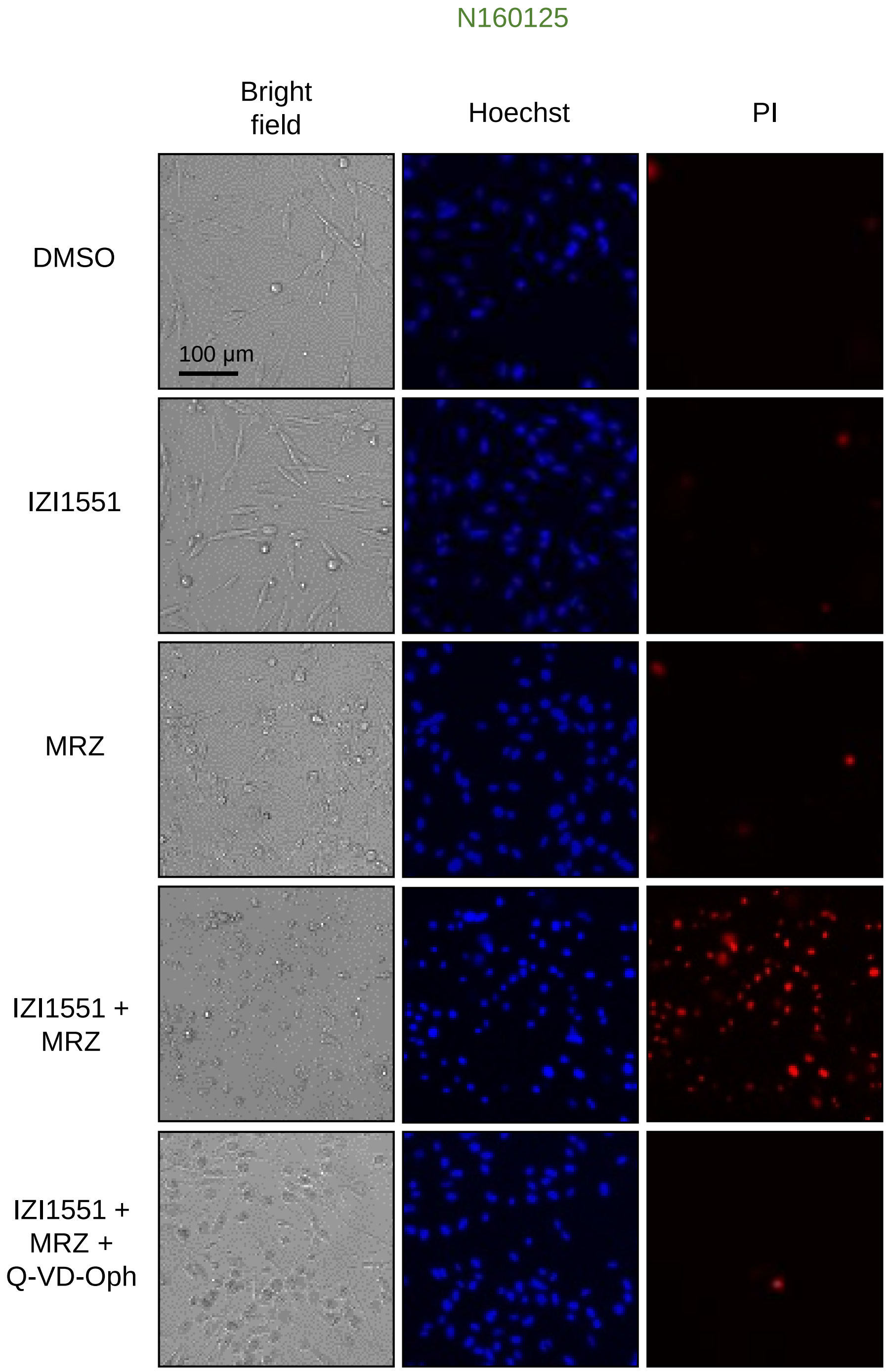

Figure 20: Cellular and nuclear morphologies of N160125 cells upon IZI1551 and MRZ treatments

Representative micrographs of 2D-cultured N160125 cells taken with an inverted digital microscope (EVOS) after 24 h of treatment as in figure 19. Nuclei were stained with Hoechst 33342 and PI. Nuclear condensation and membrane blebbing indicated apoptotic cell death.

All together these experiments indicated that the co-administration of IZI1551 and marizomib on glioblastoma cells evoked a caspase-dependent death that was morphologically recognizable as apoptosis.

1.5 IZI1551+MRZ co-treatment can reduce the long-term proliferation capacity of GBM PDCLs

The results shown in the previous paragraphs provided evidence that co-treatment with IZI1551 and marizomib triggered apoptotic death in most of the glioblastoma PDCLs examined and that such a response was lethal to a significant part of the cell population (above 60% in most of the PDCLs). Next, it was investigated whether the combination treatment could also impair the proliferation capacity of the surviving cells. To study this effect, a representative cell line of the panel, classified as responsive, was examined for its continued proliferation following treatment. In detail, cells were treated with IZI1551, marizomib or their combination in presence or absence of Q-VD-Oph. Following 24 hours of treatment, the exact same number of surviving cells from each condition was re-plated and their viability was assessed after six days by a WST-1 assay. In *figure 21A* the morphology of surviving cells on the sixth day was documented and in *figure 21B* the percentage of cell viability, normalised to cell counts on the sixth day and further to the untreated control, was measured. It appeared evident that upon marizomib as a single agent the long-term proliferation capacity of the surviving cells was reduced by 30% and that the combination treatment even more potently impaired their proliferation on a long term. These effects were all prevented by caspase inhibition (*figure 21*).

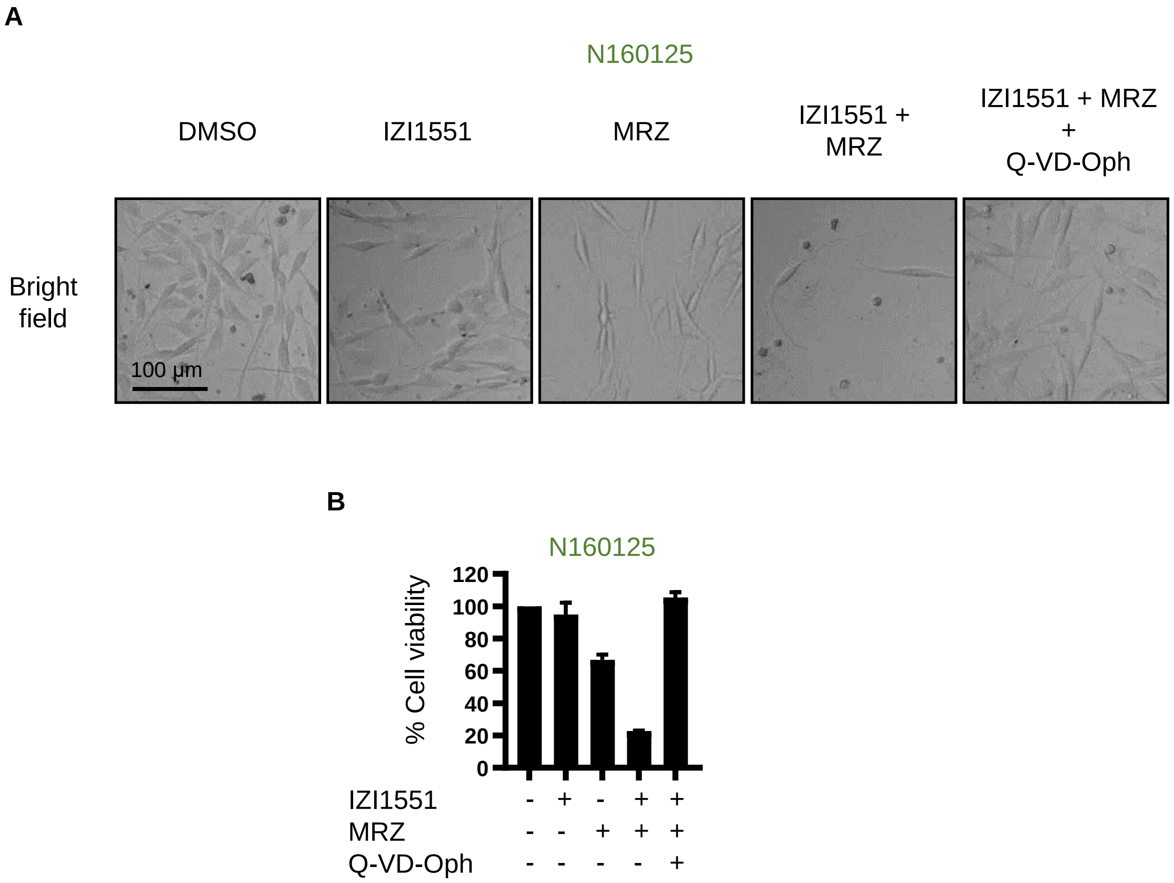

Figure 21: MRZ decreases the long-term proliferation capacity of a responder PDCL both as single agent and in combination with IZI1551

Long term proliferation capacity (six days) of the responder cell line N160125 treated for 24 h with IZI1551 (1 nM), MRZ (80 nM) or with the combination thereof in presence or absence of the pan-caspase inhibitor Q-VD-Oph (50 µM, 30 minutes of pre-exposure). ***(A)*** *Transmitted light pictures of survivor cells taken with an inverted digital microscope (EVOS) on the sixth day of growth.* ***(B)*** *Viability of the surviving cells measured after 6 days of recovery by WST-1 assays and normalised to the cell number on the same day. Viability was further normalised to the untreated control. Bar graphs show mean ± range of two independent experiments.*

Considering the effect that occurred in responsive cells, it was next investigated if the combination of IZI1551+MRZ, although not lethal to GTCC10 cells, could at least impair their long-term proliferation capacity. For that, resistant cells were re-plated in identical numbers following 24 hours of treatment and their viability was measured after six days as described previously. In *figure 22A* it is shown that the proliferation of these cells did not appear to be affected by the combination of IZI1551+MRZ. Indeed, as quantified in *figure 22B*, GTCC10 cells remained equally viable regardless of the treatments.

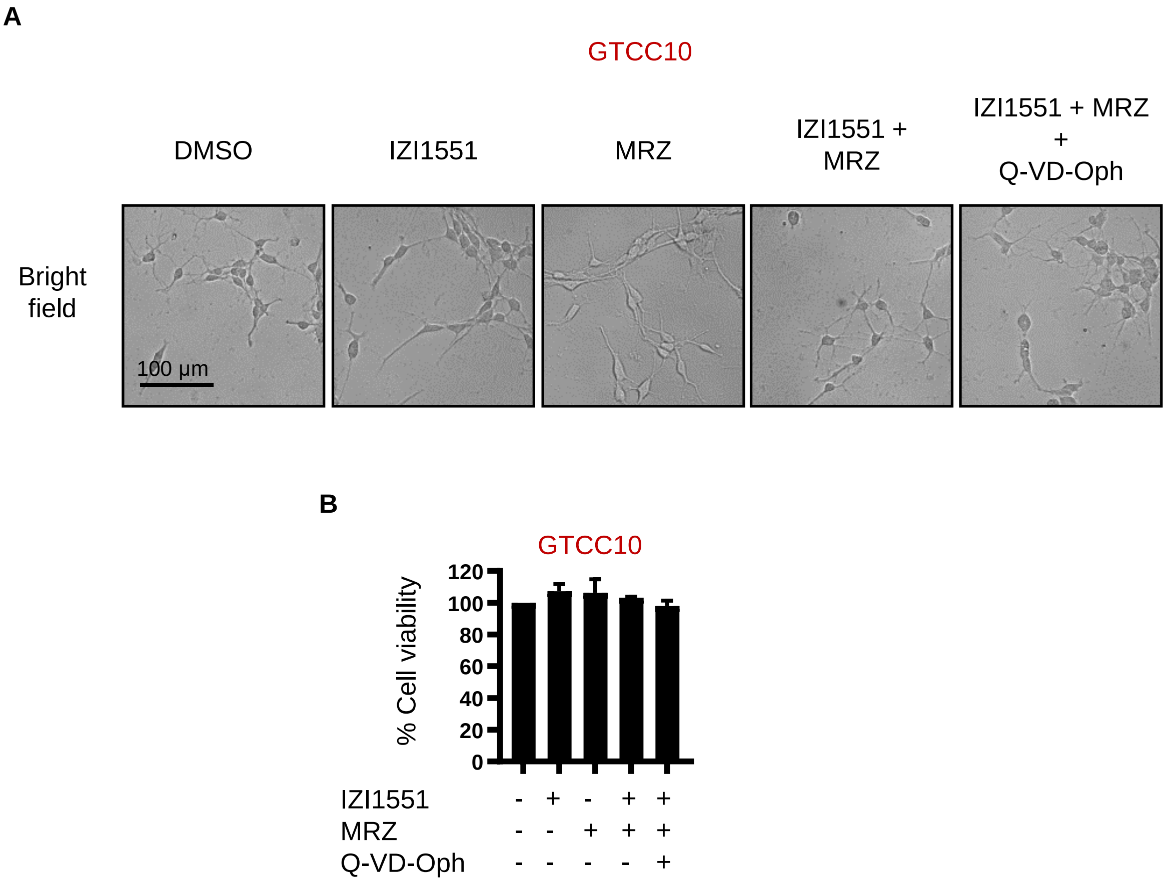

Figure 22: Long-term proliferation capacity of a resistant PDCL is not impaired by IZI1551+MRZ co-treatment

Long term proliferation capacity (six days) of the resistant cell line GTCC10 treated for 24 h with IZI1551 (1 nM), MRZ (80 nM) or with the combination thereof, in presence or absence of the pan-caspase inhibitor Q-VD-Oph (50 µM, 30 minutes of pre-exposure). ***(A)*** *Transmitted light pictures taken with an inverted digital microscope (EVOS) on the sixth day of growth.* ***(B)*** *Viability measured after 6 days of recovery by WST-1 assays and normalised to the cell number on the same day. Viability was further normalised to the untreated control. Bar graphs show mean ± range of two independent experiments. This experiment was performed by Emily Kolbe under the author's supervision.*

Collectively, the results shown in this chapter proved that TRAIL receptor activation together with proteasome inhibition triggered the execution of apoptotic death in most of glioblastoma patient-derived cell lines. Furthermore, it was shown that IZI1551 and marizomib acted synergistically in inducing cell death and that, in a responsive PDCL, they reduced the long-term proliferation capacity of the surviving portion of cells.

2. Chapter Two: IZI1551+MRZ responsiveness profiles of 3D tumour cell spheroids resemble 2D sensitivity

The analysis of 2D-cultured PDCLs provided promising results regarding the potency of the IZI1551+MRZ combination treatment in inducing apoptosis in glioblastoma. On the other hand, monolayers of *in vitro*-cultured cells might oversimplify the complex cell-to-cell contacts and communications that characterise tumours *in vivo*, with the risk of undermining the validity of the findings obtained with such models [123,124]. It was therefore necessary to validate this results in settings that more closely mimic cell interactions within a 3D microenvironment. Hence, 3D tumour spheroids were employed to study the effectiveness of IZI1551+MRZ treatments and their synergistic apoptosis induction in glioblastoma PDCLs. The results gathered in this chapter showed that the drug responsiveness data obtained in 2D conditions were qualitatively reproduced also in more complex 3D settings.

2.1 The combination of IZI1551+MRZ reduces the viability of GBM PDCL 3D tumour spheroids and disrupts their integrity

As mentioned in the introduction of this chapter, drug resistance mechanisms that do not appear in 2D cultures could occur in more complex three-dimensional tumour spheroids. For this reason, preliminary microscopy experiments were conducted to investigate if the combination of IZI155 with marizomib affected the viability of glioblastoma PDCLs also in a 3D setting. Cells of a PDCL that according to 2D data was classified as a responder, namely the N160125, (see chapter 1 paragraph 1.3) were here cultivated as spheroids and then treated with the IZI1551+MRZ combination already tested in 2D conditions. The spheroids were then stained with the cell-permeant fluorescent dye Calcein AM and imaged. The Calcein AM staining is used to determine the cell viability, as this non- fluorescent dye can only be converted into the green-fluorescent Calcein by the cellular esterases of living cells. The phase contrast micrographs in *figure 23A* clearly show the disintegration of N160125 spheroids upon the combination treatment. The decreased fluorescent signal emitted by the cleaved dye in treated spheroids revealed the loss of viability induced by the IZI1551+MRZ combination (*figure 23A*). The fluorescence signals were also quantified: a reduced viability was indeed measured already upon single drug treatment (micrographs not shown) and this effect was even enhanced in the double treatment (*figure 23B*).

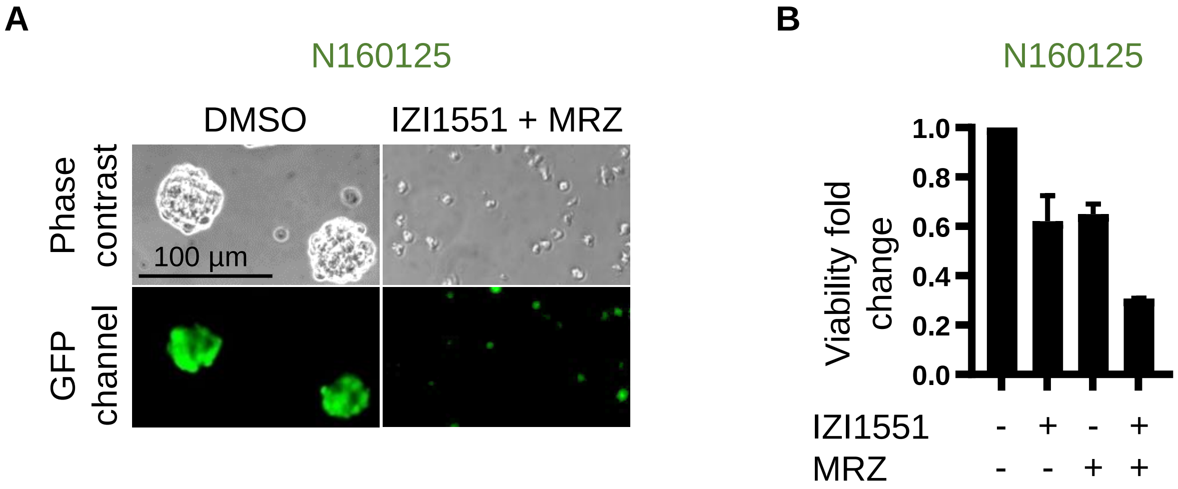

Figure 23: The combination of IZI1551+MRZ induces the disintegration of PDCL spheroids
(A) *Representative micrographs of N160125 spheroids stained with Calcein AM (green; live cells) following 24 h of exposure to 1 nM of IZI1551 and 80 nM of MRZ.* ***(B)*** *Decrease of Calcein AM fluorescence signals normalised to the untreated control. Bar graph represents the mean of two technical repetitions ± range. Representative example of two independent experiments.*

This experiment provided an encouraging result on the reliability of the 2D data already obtained. Hence, the whole panel was analysed in order to fully validate those results. For that, the seven PDCLs of the panel were cultured as tumour spheroids and treated with 5x5 escalating dose combination matrices of IZI1551 and marizomib for 24 hours. The viability of the spheroids was then assessed by WST-1 assays as previously described. In *figure 24* it is shown that spheroids from different PDCLs responded differentially to the treatment. According to such differences, the PDCLs could be distinguished into a group of responders and non-responders, reflecting the exact same separation obtained from 2D data. When looking at the sensitivity of each cell line to a specific treatment dose, only very small discrepancies with 2D data were observed and these were mostly restricted to the N150661 PDCL that was the least responsive cell line of the panel (*figure 16* and *24*).

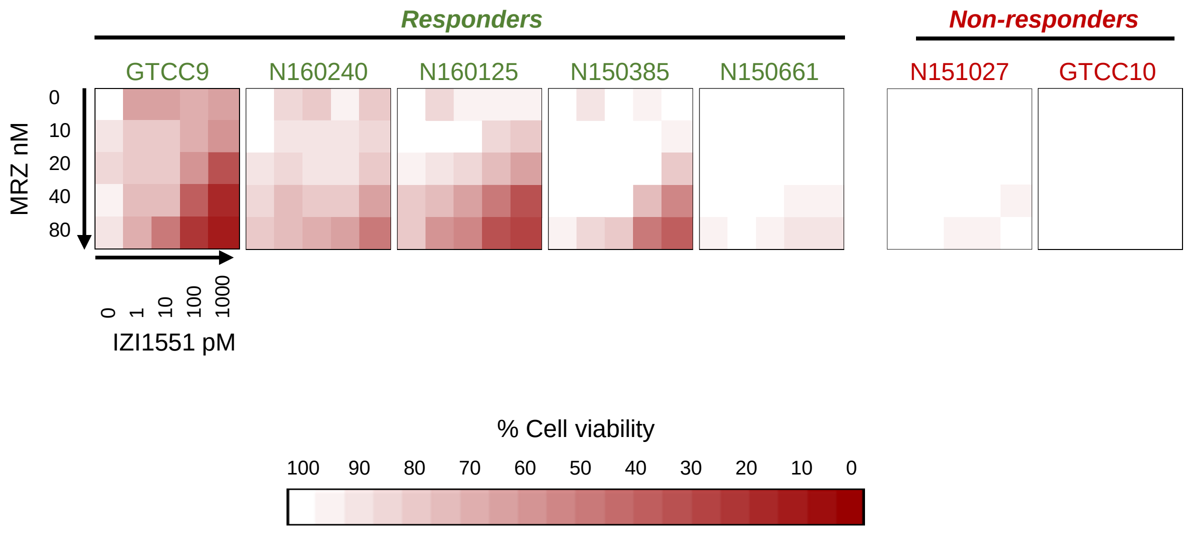

Figure 24: Most PDCL spheroids respond to the combination treatment with IZI1551 and MRZ

One-day-old PDCL spheroids originated from 3 × 10^3 *single cells/well were stimulated with the indicated concentrations of IZI1551 and MRZ for 24 h. Cell viability was assessed by WST-1 cell proliferation assay. The percentage of cell viability was plotted in heat maps where red colour intensity correlated with the percentage of viability loss. The percentage of cell viability in each condition was normalised to untreated controls. Data are mean values from three independent experiments. SEMs across the repeat experiments and conditions were <20%. Data on N150385; N150661; N151027 and GTCC10 cells were generated by Emily Kolbe under the author's supervision.*

2.2 IZI1551+MRZ combinations trigger synergistic responses in 3D tumour spheroids with patterns comparable to those of 2D cultures

In the previous paragraph it was shown that PDCLs cultivated as tumour spheroids responded to IZI1551 and marizomib treatments similarly as they did when cultivated in 2D. It was therefore next studied if the synergistic apoptosis induction that occurred in 2D PDCLs could also be triggered in 3D scenarios. To this purpose, synergy scores for the escalating doses of drug combinations tested in the previous paragraph were calculated for all 3D-cultured PDCLs (*figure 25*). It appeared that IZI1551 and marizomib synergistically reduced the viability of tumour spheroids, with the only exception of N150661 cells in which the two drugs did not trigger any synergistic effect.

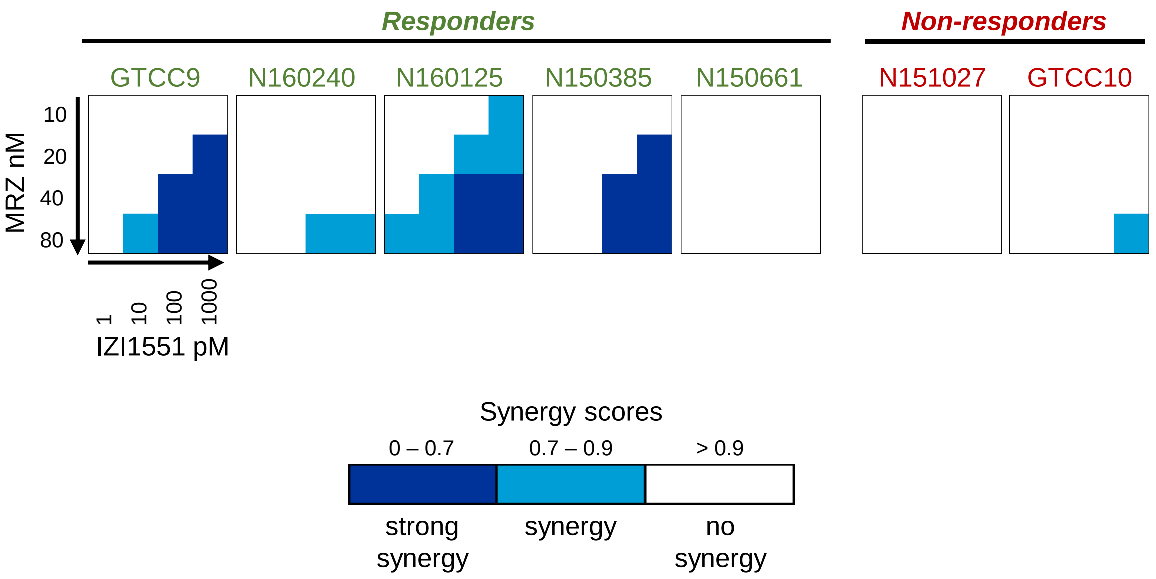

Figure 25: IZI1551/MRZ interactions evoke synergistic responses in most PDCLs spheroids

Synergy scores of drug interactions were determined by calculating the CI from the data shown in figure 24. The scores are plotted as heat maps where the deeper blue colours represented stronger synergies.

2.3 IZI1551+MRZ-induced cell death in 3D tumour spheroids depends on caspase activation

Stimulation with IZI1551 together with marizomib reduced the viability of five out of seven 3D-cultured PDCLs of the panel here considered. It was next investigated whether the lowered viability of the spheroids corresponded to cell death induction. To test that, five PDCLs grown as spheroids were exposed to single drug treatments; to their combination or to IZI1551+MRZ together with the caspase inhibitor Q-VD-Oph. Following 24 hours of treatment, spheroids were dissociated and stained with both Annexin V-GFP and PI for flow cytometry measurements of cell death. The results showed that while single drug treatments were not significantly lethal to any of the PDCLs, their combination induced a cell death type that was completely rescued by caspase inhibition (*figure 26*).

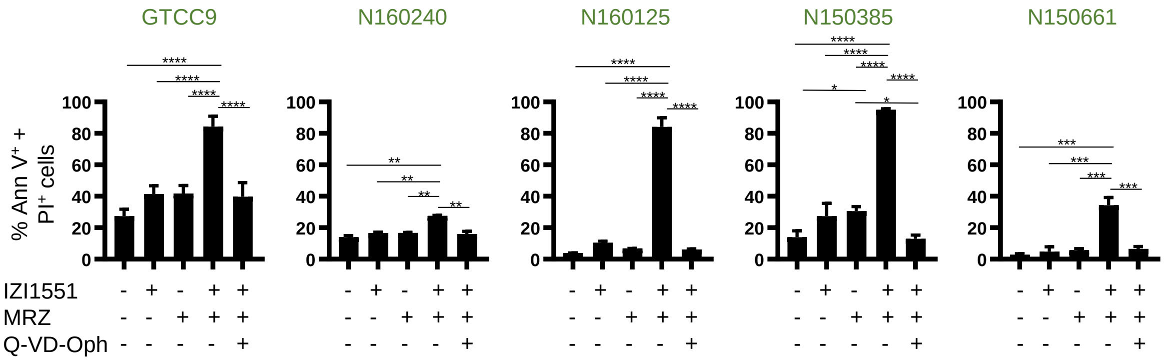

Figure 26: IZI1551+MRZ co-treatment induces caspase-dependent death of PDCL spheroids

*One-day-old PDCL spheroids generated from 1.5 × 10^4 single cells/well were stimulated for 24 h with IZI1551 (1 nM), MRZ (80 nM) or with the combination thereof, in the presence or absence of the pan-caspase inhibitor Q-VD-Oph (50 µM, 30 minutes of pre-exposure). Following spheroids dissociation, cell death was measured by Annexin V/PI-based flow cytometry. Data represent mean ± SEM from three independent experiments. ** = $p \leq 0.01$; *** = $p \leq 0.001$ **** = $p \leq 0.0001$; when not specified cell death differences were not significant. One-way ANOVA followed by Tukey's post hoc test. Experiments on GTCC9; N150385 and N150661 cells were performed by Emily Kolbe under the author's supervision.*

The results of this paragraph indicated that the combination of IZI1551+MRZ, rather than treatment with the single drugs, was necessary to impair the vitality of 3D glioblastoma spheroids grown from PDCLs. In addition, this drug combination led to the disintegration of the spheroids and to a cell death type that, similarly to the situation in 2D, was of caspase-dependent nature. Overall, these findings demonstrated that 3D-grown PDCLs responded to IZI1551/MRZ in the same manner as 2D cultures, making the latter a valid model to further investigate death mechanism in glioblastoma.

3. Chapter Three: Marizomib pre-treatment enhances IZI1551-induced cell death and accelerates its kinetic

The previously reported findings demonstrated the effectiveness of combining TRAIL receptor activation with proteasome inhibition to induce robust caspase-dependent death in glioblastoma PDCLs. These results, together with the knowledge that death receptor engagement and proteasome inhibition trigger apoptosis with differential mechanisms [513–515], provided the rationale to design a treatment schedule that exploits the individual properties of the drugs to further enhance the cytotoxicity of their combination. Such improved efficacy would allow to lower drug doses by still maintaining the lethality of the IZI1551+MRZ combinatorial treatment. In this way, possible drug-induced toxicities that might emerge when translating this study to *in vivo* settings would be minimised. To investigate all these aspects, the death kinetics of different treatment regimens were assessed.

The last part of this chapter tackles the obstacle represented by the blood-brain barrier (BBB) to the treatment of glioblastoma. It was shown that marizomib penetrated a simple *in vitro* model of the human BBB and that a time-shifted exposure to the drugs induced a significant amount of cell death also in the presence of this barrier.

Finally, it has to be noted that all the results shown in this chapter were obtained from 2D cultures, that previously in this thesis were shown to be a reliable model for investigating the behaviour of glioblastoma PDCLs in response to IZI1551 and marizomib.

3.1 IZI1551 induces swift apoptosis responses that precedes the effects of marizomib

To gain a first insight into the different timing of IZI1551 and marizomib actions, cell death responses were here investigated at an early time point. For these studies, two representative glioblastoma PDCLs that were sensitive to the treatment, namely the recurrent cell line GTCC9 and the primary cell line N160125, were considered. At first, a hallmark of apoptosis such as caspase processing was analysed at a time point as early as four hours post-treatment. In particular, the initiator caspase-8, the effector caspase-3 and its substrate PARP, were detected via western blotting both as pro-forms and as cleaved fragments. After four hours, the cleavage of caspase-8; caspase-3 and PARP occurred partially upon IZI1551 single treatment and, in a more pronounced way, upon combination treatment, but not upon exposure to marizomib alone. Importantly, the addition of Q-VD-Oph to the combination treatment totally abolished the cleavage of caspases and that of their substrate, indicating once again the occurrence of apoptotic cell death (*figure 27*).

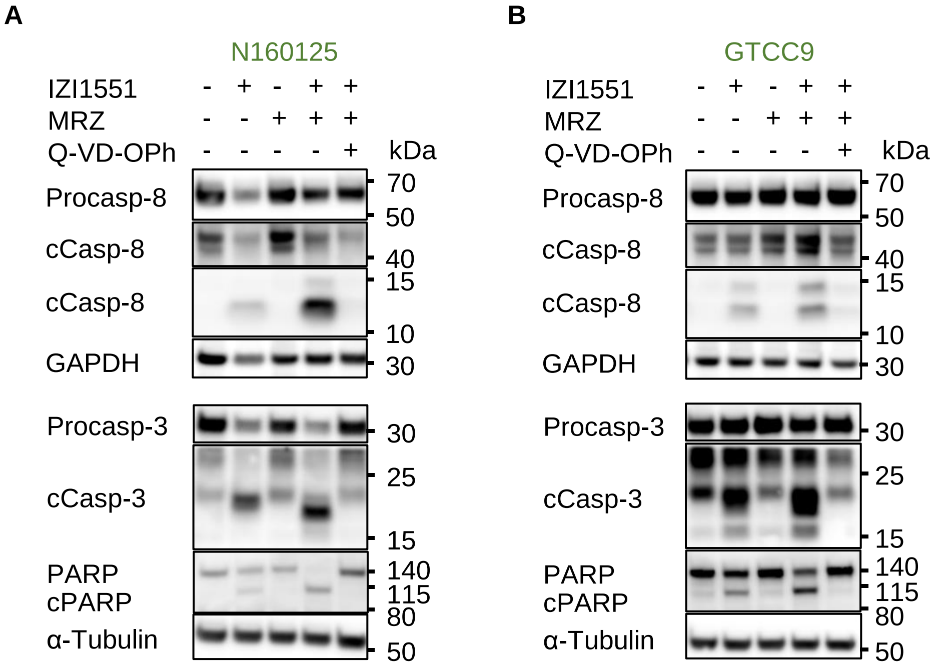

Figure 27: IZI1551 treatment leads to early activation of apoptotic caspases

Responder cell lines N160125 ***(A)*** *and GTCC9* ***(B)*** *were treated for 4 h with IZI1551 (1 nM) or MRZ (80 nM) or a combination of both, in the presence or absence of the pan caspase inhibitor Q-VD-Oph (30 minutes pre-incubation; 50 µM). For each sample, 20 µg of whole-cell lysates were analysed for the indicated proteins by western blotting. GAPDH or α-Tubulin served as loading controls. Similar results were obtained in independent repeat experiments. c=cleaved. Casp=caspase. Procasp=procaspase. GTCC9 data were obtained by Emily Kolbe under the author's supervision.*

Having demonstrated the early cleavage of apoptotic caspases by IZI1551 and by the combination of IZI1551+MRZ, it was next investigated whether this corresponded to actual cell death induction. N160125 and GTCC9 cells were hence treated with single drugs or their combination for four hours before being stained with both Annexin V-GFP and PI for flow cytometry-based cell death measurements. As expected, the stimulation with IZI1551 and the combination treatment exerted a similar effect. Furthermore, at this early time point, a certain portion of cells started to expose phosphatidylserine without taking up PI yet (*figure 28*).

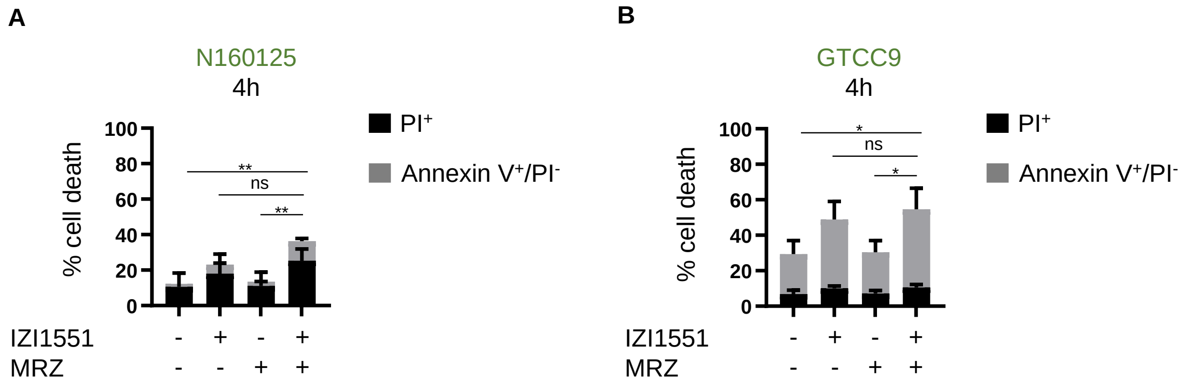

Figure 28: IZI1551+MRZ treatment induces early apoptotic responses

Responder cell lines N160125 ***(A)*** *and GTCC9* ***(B)*** *were treated for 4 h with IZI1551 (1 nM) or MRZ (80 nM) or a combination of both. Cell death was measured by Annexin V/PI-based flow cytometry following 4 h of treatment. Data represent mean ± SEM from three independent experiments. * = p ≤ 0.05; ** = p ≤ 0.01. ns = not significant. Also, wherever not specified cell death differences were not significant. Statistical significance was calculated by one-way ANOVA followed by Tukey's post hoc test on the total amount of cell death (Annexin V⁺ cells + PI⁺ cells). GTCC9 data were obtained by Emily Kolbe under the author's supervision.*

The extremely limited amount of PI positive cells at this early time point was further confirmed by IncuCyte-based live cell imaging of PI-stained cells (*figure 29*).

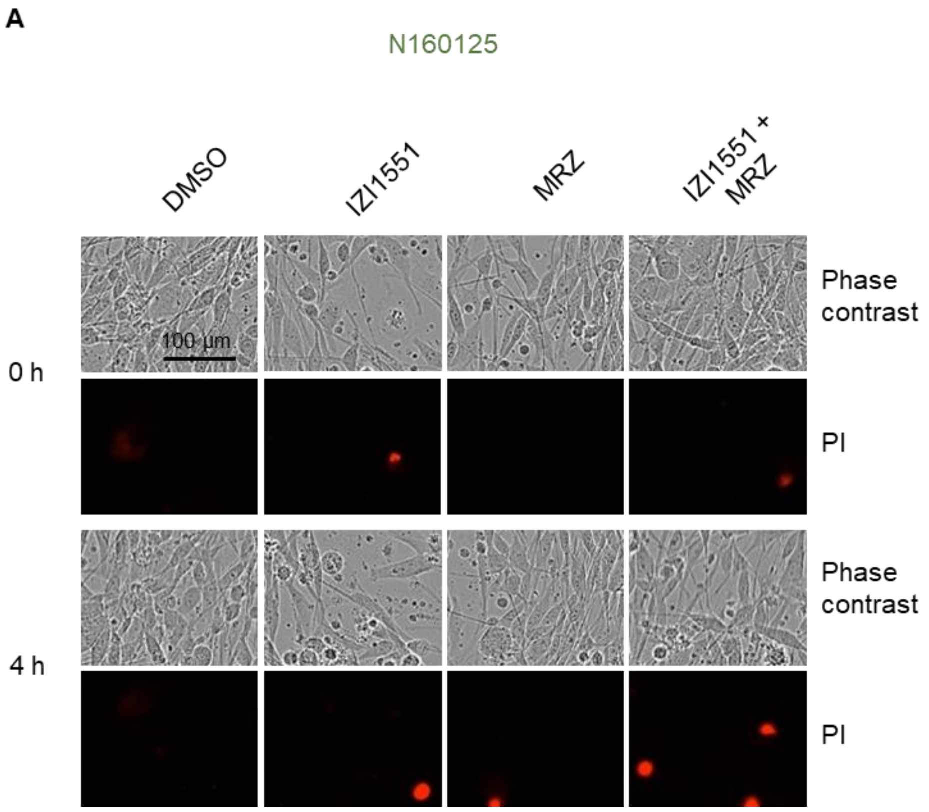

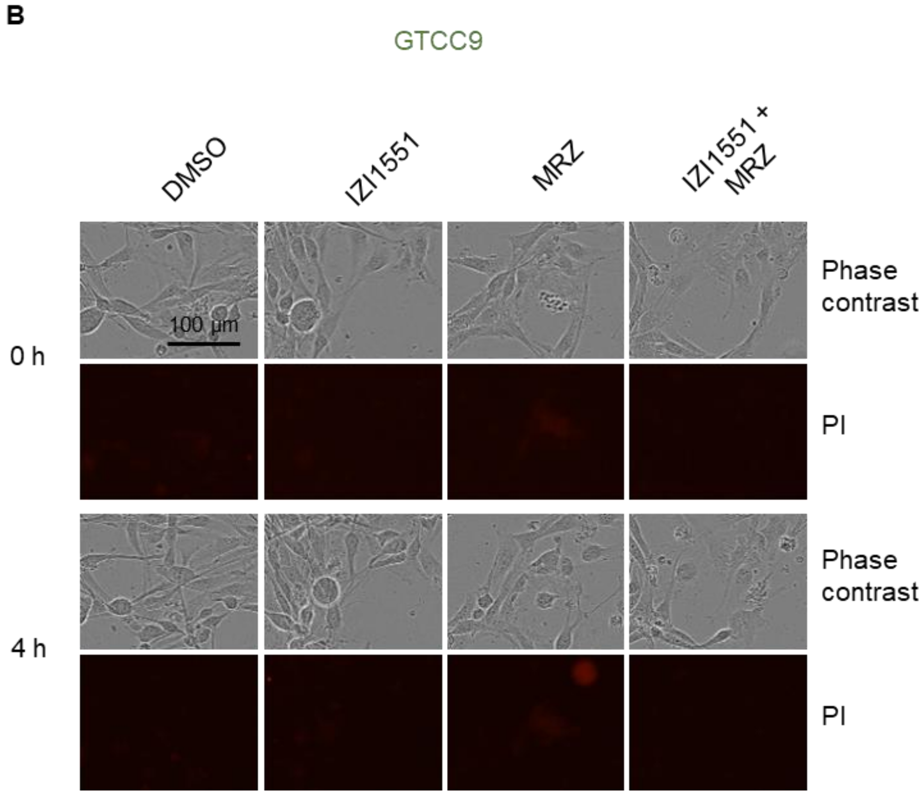

Figure 29: GBM PDCL are mostly PI-impermeable following short treatment periods

Responder cell lines N160125 ***(A)*** *and GTCC9* ***(B)*** *were treated with IZI1551 (1 nM), MRZ (80 nM) or a combination of both in presence of PI and imaged at 0 h and 4 h with an IncuCyte system. Micrographs are representative of three independent experiments. GTCC9 data were obtained by Emily Kolbe under the author's supervision.*

These results showed that IZI1551 as a single agent and the combination treatment exerted a very similar effect at early time points, confirming the assumption that longer exposure to the IZI1551+MRZ combination was required to trigger the synergistic response shown in *figure 17* of chapter one of this thesis. Importantly, the experiments of this paragraph also showed that IZI1551-induced responses are swift and precede that of marizomib. Such data provided the rationale to exploit the different kinetics of IZI1551 and marizomib-induced death in order to improve the cytotoxicity of their combination. This aspect was investigated in the following paragraph.

3.2 MRZ pre-treatment enhances IZI1551-induced apoptosis and accelerates its kinetic

It was shown that IZI1551-induced apoptotic responses manifested faster than that of marizomib. As proteasome inhibition required longer times to exert its effects, it was hypothesised that, within a combination treatment, a pre-exposure to marizomib might increase the responses to IZI1551 stimulation. To study the effect of prolonged marizomib exposure, both as a single agent and in combination with IZI1551, kinetic studies were performed. The purpose was to compare the kinetic and also the efficacy of the simultaneous combination treatment *versus* a combined treatment in which the cells were pre-exposed to marizomib. For that, cells were pre-treated with marizomib for 24 hours before IZI1551 was added. PI was included in the culture medium and its uptake was monitored for the following 24 hours using an IncuCyte system (*figure 30A* and *B*). The percentage of PI-covered area normalised to the cell-covered area (confluence) was calculated and considered as an indicator of cell death, here indicated as “% PI positive area” (*figure 30C* and *D*). The micrographs of *figure 30A* and *B* clearly showed that for both cell lines, marizomib pre-treatment led to increased cell death compared to the condition where drugs were co-administered at the same time. Furthermore, marizomib as a single agent did not appear to augment the number of PI-positive cells compared to the simultaneous treatment with both drugs, even when employed for longer time periods (*figure 30A* and *B)*. The kinetic analysis shown in *figure 30C* and *D* highlighted how, in the combined treatment scenario, marizomib pre-exposure not only enhanced cell death induction but was also effective in speeding up PI uptake as compared to the simultaneous administration of the two drugs (red triangles *versus* blue triangles traces in *figure 30C* and *D*). The quantification of the PI-covered area also allowed to confirm that such improved effect was not achievable upon a prolonged stimulation with marizomib as a single agent (red triangles *versus* green hexagons traces in *figure 30C* and *D*). This indicated that, also under these conditions, both IZI1551 and marizomib are required to trigger strong responses.

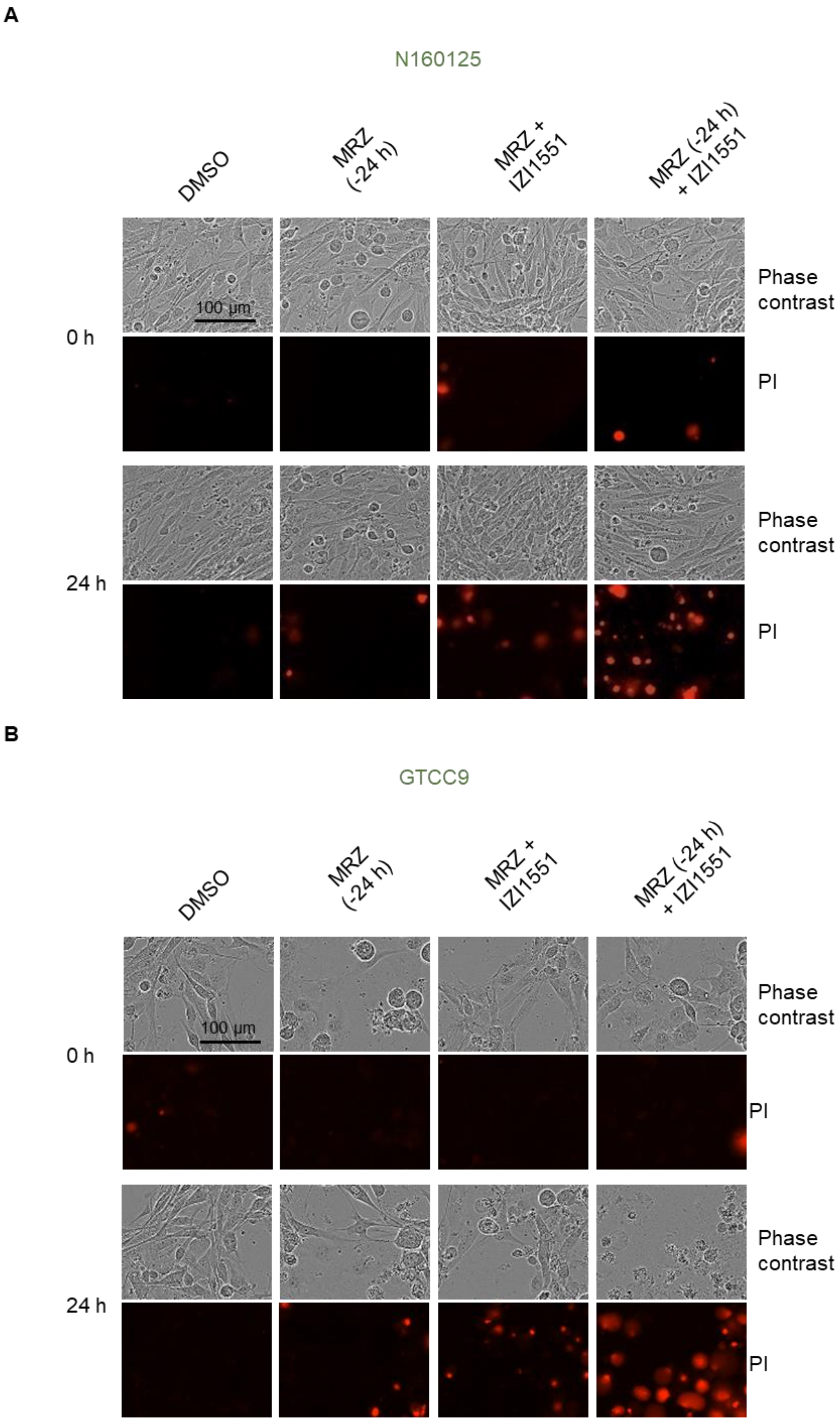
A
N160125
DMSO
MRZ (-24 h)
MRZ + IZI1551
MRZ (-24 h) + IZI1551
100 µm
0 h
24 h
Phase contrast
PI
Phase contrast
PI
B
GTCC9
DMSO
MRZ (-24 h)
MRZ + IZI1551
MRZ (-24 h) + IZI1551
100 µm
0 h
24 h
Phase contrast
PI
Phase contrast
PI

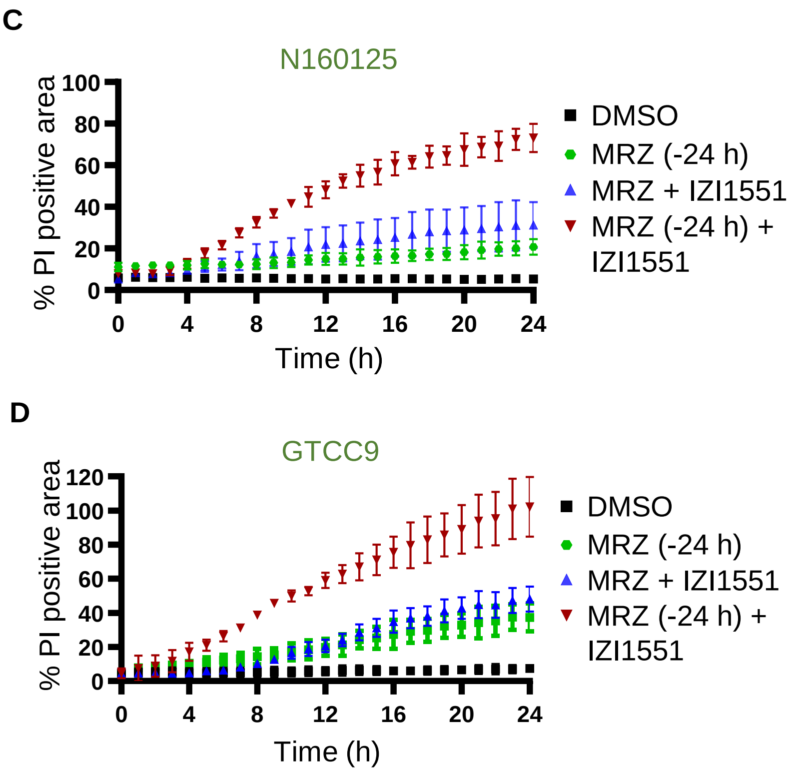

Figure 30: MRZ pre-treatment accelerates and enhances IZI1551-induced cell death

*Responder cell lines N160125 (**A** and **C**) and GTCC9 (**B** and **D**) were co-treated with IZI1551 (1 nM) and MRZ (80 nM) simultaneously or were pre-treated with MRZ for 24 h (MRZ -24 h) in presence of PI. **(A** and **B)** IncuCyte-recorded images at 0 h and 24 h post IZI1551 addition. **(B** and **D)** Quantification of cell death kinetics, calculated as percentage of PI positive cell areas. Representative results from one out of three independent experiments are shown. Error bars represent SD of 3 technical replicates. GTCC9 data were obtained by Emily Kolbe under the author's supervision.*

The increased cell death induction upon combination treatment with marizomib pre-exposure compared to the simultaneous treatment was also confirmed via flow cytometry measurements. For that, the N160125 and GTCC9 cell lines were co-treated with IZI1551 (1 nM) and marizomib (80 nM) simultaneously or pre-treated with marizomib for 24 hours (MRZ -24 h) before stimulation with IZI1551. Cells were collected after four or 24 hours following the addition of IZI1551 and co-stained with Annexin V-GFP and PI for cell death measurements via flow cytometry. Of note, the four hours intermediate time point was considered because, as shown in *figure 28*, this was the point in time when the IZI1551+MRZ simultaneous treatment started to induce apoptosis. Moreover, as shown in *figure* 30, in the co-treatment scenario with the marizomib pre-exposure condition, the cells started to take up PI following four hours of combined stimulation. It was confirmed that pre-treatment with marizomib triggered earlier and enhanced apoptotic responses compared to the simultaneous treatment with IZI1551 and marizomib (*figure 31*) (note that in the recurrent glioblastoma PDCL GTCC9, the pre-treatment strategy did not result in an improved response because the simultaneous addition of the drugs was already almost totally lethal at the concentrations used).

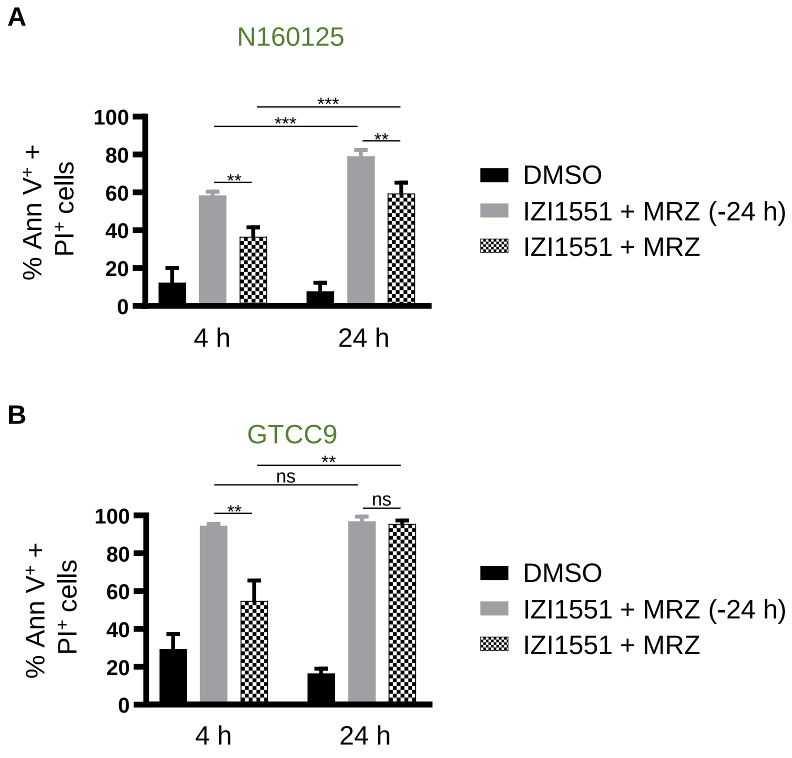

Figure 31: MRZ pre-exposure enhances and accelerates IZI1551-induced apoptosis compared to simultaneous treatment

Annexin V/PI-based flow cytometry of N160125 ***(A)*** *and GTCC9* ***(B)*** *cells co-treated with IZI1551 (1 nM) and MRZ (80 nM) simultaneously or pre-treated with MRZ for 24 h (MRZ -24 h). Data represent mean ± SEM from three independent experiments. ** = $p \leq 0.01$; *** = $p \leq 0.001$ ****. ns = not significant. Two-way ANOVA followed by Tukey's or Sidak's post hoc test. GTCC9 data were obtained by Emily Kolbe under the author's supervision.*

As the time-shifted administration of the drugs resulted in a considerably enhanced apoptosis induction compared to the co-stimulation, it was next important to show that, in the marizomib pre-treatment scenario, lower drug concentrations still led to significant cell death induction. To provide such evidence, cells were stimulated with only 40 nM of marizomib (low) either 24 hours before, or concomitantly with 100 pM of IZI1551 (low) treatment. Following Annexin V-GFP and PI co-staining, apoptosis was quantified from flow cytometry measurements (*figure 32A* and *B*). For both cell lines tested it was shown that, even at low drug concentrations, the pre-treatment strategy was still more effective than the concomitant treatment in inducing apoptosis.

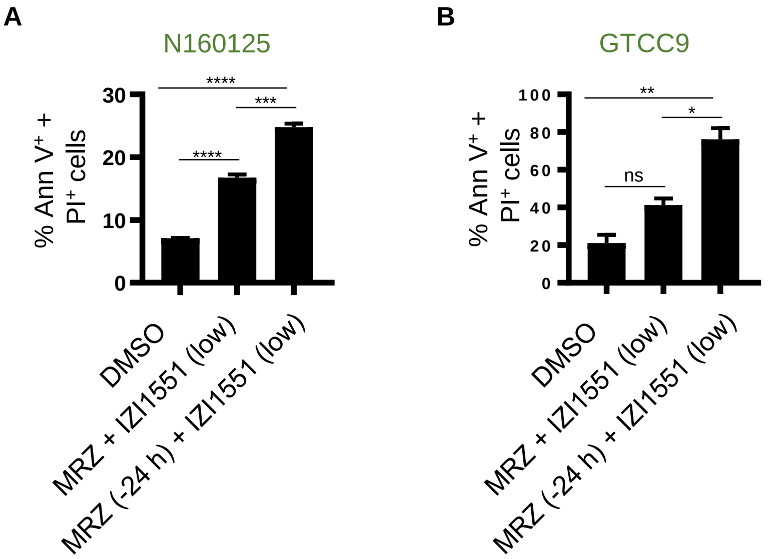

Figure 32: MRZ pre-treatment enhances apoptosis induction even at low drug concentrations

*Annexin V/PI-based flow cytometry of **(A)** N160125 and **(B)** GTCC9 cells co-treated with reduced concentrations of IZI1551 (100 pM) and MRZ (40 nM) simultaneously or pre-treated with a low MRZ concentration (40 nM) for 24 h (MRZ -24 h). Data represent mean ± SEM from three independent experiments. * = $p \leq 0.05$; ** = $p \leq 0.01$; *** = $p \leq 0.001$; **** = $p \leq 0.0001$; ns = not significant. One-way ANOVA followed by Tukey's post hoc test.*

Overall, these results showed that IZI1551 and marizomib display differential death kinetics and that these are exploitable to enhance cell death induction in glioblastoma PDCLs. Furthermore, within a treatment regimen of time-shifted marizomib application, it was possible to reduce the doses of both drugs without losing treatment efficacy.

3.3 MRZ crosses the BBB and primes GBM cells to IZI1551-induced cell death

In the previous paragraph it was shown that pre-stimulating glioblastoma cells with marizomib prior to treatment with IZI1551 optimised apoptotic responses even at low drug doses. Importantly, marizomib is the only proteasome inhibitor so far described to cross the BBB [373,375]. Taking all of this into account, it was here studied if the amount of marizomib that can cross the BBB is sufficient to sensitise glioblastoma PDCLs to IZI1551. To test that, a simple *in vitro* model of the human BBB, grown from hCMEC/D3 human brain endothelial cells, was employed. In order to use this model for studies of marizomib penetrance, it was first necessary to determine whether such treatment was toxic to the cells of the BBB. Hence, flow cytometry-based cell death measurements of hCMEC/D3 cells exposed to marizomib for 24 hours were performed. Importantly, it was shown that marizomib treatment was mostly well tolerated by these cells (*figure 33*).

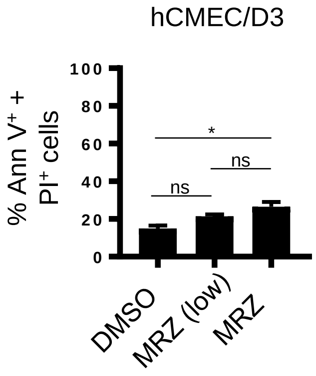

Figure 33:BBB cells are mostly resistant to MRZ treatment

*Human BBB hCMEC/D3 cells were investigated for their sensitivity to 24 h of MRZ treatment (40 nM (low); 80 nM) by Annexin V/PI-based flow cytometry. Data represent mean ± SEM from three independent experiments. * = p ≤ 0.05; ns = not significant. One-way ANOVA followed by Tukey's post hoc test.*

Next, hCMEC/D3 cells, grown on collagen-coated inserts of transwells, were cultured until the formation of a tight cell layer, as verified by the daily monitoring of transendothelial electrical resistance (TEER) (*figure 34* and *figure 35A*). On the fifth day of growth, TEER values were high enough for the BBB to be considered formed (*figure 35A*). At this point, a non-toxic marizomib concentration (40 nM) (see *figure 33*) was added onto the hCMEC/D3 cells from the apical side of the transwells (*figure 34*). Following 24 hours of treatment, it was shown that marizomib did not compromise the integrity of the BBB, as TEER values remained unaltered during such treatment (*figure 35A*). After 24 hours of marizomib treatment, the medium from the basolateral compartment of the transwells was collected and added onto glioblastoma cells for a 24 hours pre-exposure (*figure 35B* "MRZ low BBB (-24 h)") prior to the addition of IZI1551. As a control of the BBB-permeability of marizomib, a condition was also included in which this drug was directly added onto the glioblastoma cells before adding IZI1551 (last condition of *figure 35B*, "MRZ low direct (-24 h)"). In *figure 35B* it is shown that even though the presence of an intact layer of BBB cells partially reduced the efficacy of the IZI1551+MRZ combinatorial treatment, cell death could still be clearly induced under these conditions.

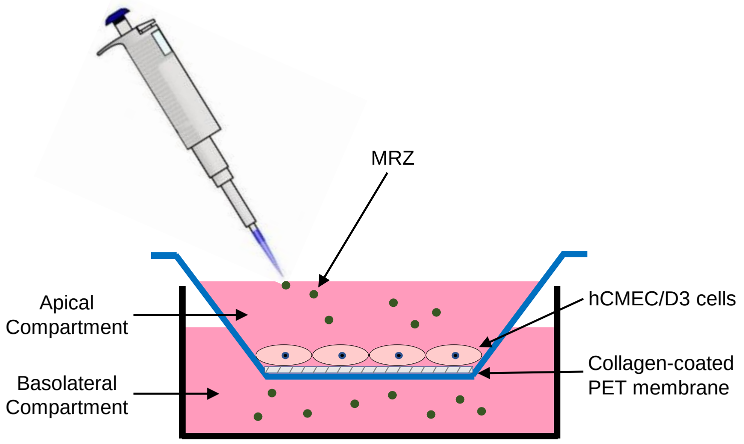

Figure 34: In vitro model of the human BBB

Schematic representation of the BBB model used for MRZ penetration studies. hCMEC/D3 cells were seeded onto collagen pre-coated PET membranes of transwell inserts. The basolateral compartment of the transwell was filled with medium. Cells were grown for five days until a tight barrier was established. On the fifth day, MRZ was added onto the cells from the apical side of the transwell and collected from the basolateral compartment 24 h later (sixth day).

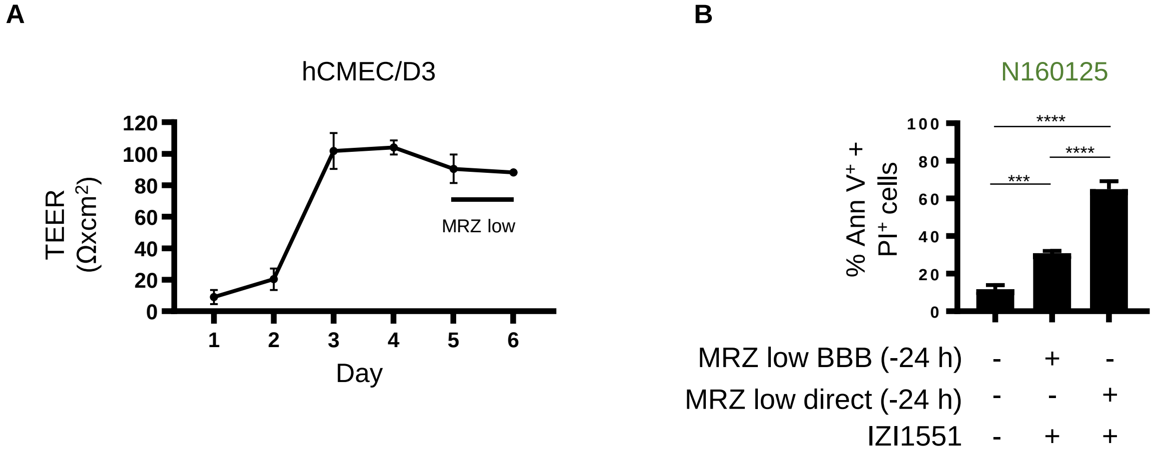

Figure 35: MRZ sufficiently penetrates a human BBB model to sensitise GBM cells to IZI1551-induced apoptosis

***(A)** TEER was measured daily for 5 days following 24 h of growth of hCMEC/D3 on culture inserts. On the fifth day, 40 nM of marizomib (low) were added and the TEER was monitored for an additional 24 h. Data represent mean ± range of n = 2 measurements. **(B)** Cell death in N160125 cells measured by Annexin V/PI-based flow cytometry. Where indicated, cells were pre-treated with marizomib (40 nM) directly or with medium from the basolateral compartment of the hCMEC/D3 BBB model in (A) for 24 h. Data represent mean ± SD of three measurements. *** = $p \leq 0.001$; **** = $p \leq 0.0001$. One-way ANOVA followed by Tukey's post hoc test.*

Taken together, the results shown in this chapter showed that the strategy of pre-stimulating glioblastoma PDCLs with marizomib before IZI1551 treatment allowed to trigger significant apoptotic responses even with low amounts of drugs and in conditions where marizomib needed to penetrate a simple model of the human BBB.

4. Chapter Four: Antagonising Mcl-1 sensitises IZI1551+MRZ resistant cells to apoptosis

In this chapter, the glioblastoma PDCLs that in the beginning of this project (chapter one) were classified as non-responders to the combination treatment of IZI1551 with marizomib were studied. In view of the results of chapter three, where a strategy for optimising treatment responsiveness was identified, it was here tested whether the same approach could sensitise highly resistant glioblastoma cells to IZI1551 and marizomib stimulation. However, even upon marizomib pre-exposure, these cells remained insensitive to the treatment. Thus, possible reasons for their resistance, as well as strategies to reactivate apoptosis induction in such cells, were investigated. In particular, both the efficacy of marizomib in blocking proteasome activity and the competence of these cells in executing TRAIL-induce apoptosis were examined. Expression levels of key proteins of both the extrinsic and intrinsic apoptotic pathway were analysed and compared between responsive and non-responsive cells lines in order to identify differences in the proteins expression patterns that could explain the differential responses. The specific protein expression signature of resistant cells suggested that lowering the threshold for mitochondrial apoptosis could restore treatment susceptibility. Indeed, both in 2D- and 3-cultured PDCLs, the addition of a BH3 mimetic allowed to re-sensitise highly resistant glioblastoma cells to apoptosis induced by the combination of IZI1551+MRZ.

4.1 MRZ pre-treatment does not sensitise highly resistant GBM cells to IZI1551-induced apoptosis

The cell line GTCC10, derived from a recurrent glioblastoma tumour, and the cell line N151027, derived from a primary glioblastoma case, are the two PDCLs of the representative panel examined in this study that showed complete resistance to both IZI1151 and marizomib as single agents and in combination. In chapter three it was shown that marizomib pre-exposure can enhance responsiveness to IZI1551-induced death in sensitive glioblastoma PDCLs. It was therefore hypothesized that the same strategy could allow to restore treatment sensitivity in resistant PDCLs. To test that, a kinetic analysis of marizomib pre-treated N151027 and GTCC10 cells was performed. Cells were treated with marizomib before or concomitantly to IZI1551 in presence of PI and they were then imaged using the IncuCyte system (*figure 36A* and *B*). PI signals were analysed as described in the methods section. The micrographs in *figure 36A* and *B* showed that neither N151027 nor GTCC10 cells died upon treatment. Quantitative analysis of the PI signal correspondently revealed no substantial difference between marizomib pre-treated and simultaneously treated cells over time (*figure 36C* and *D*).

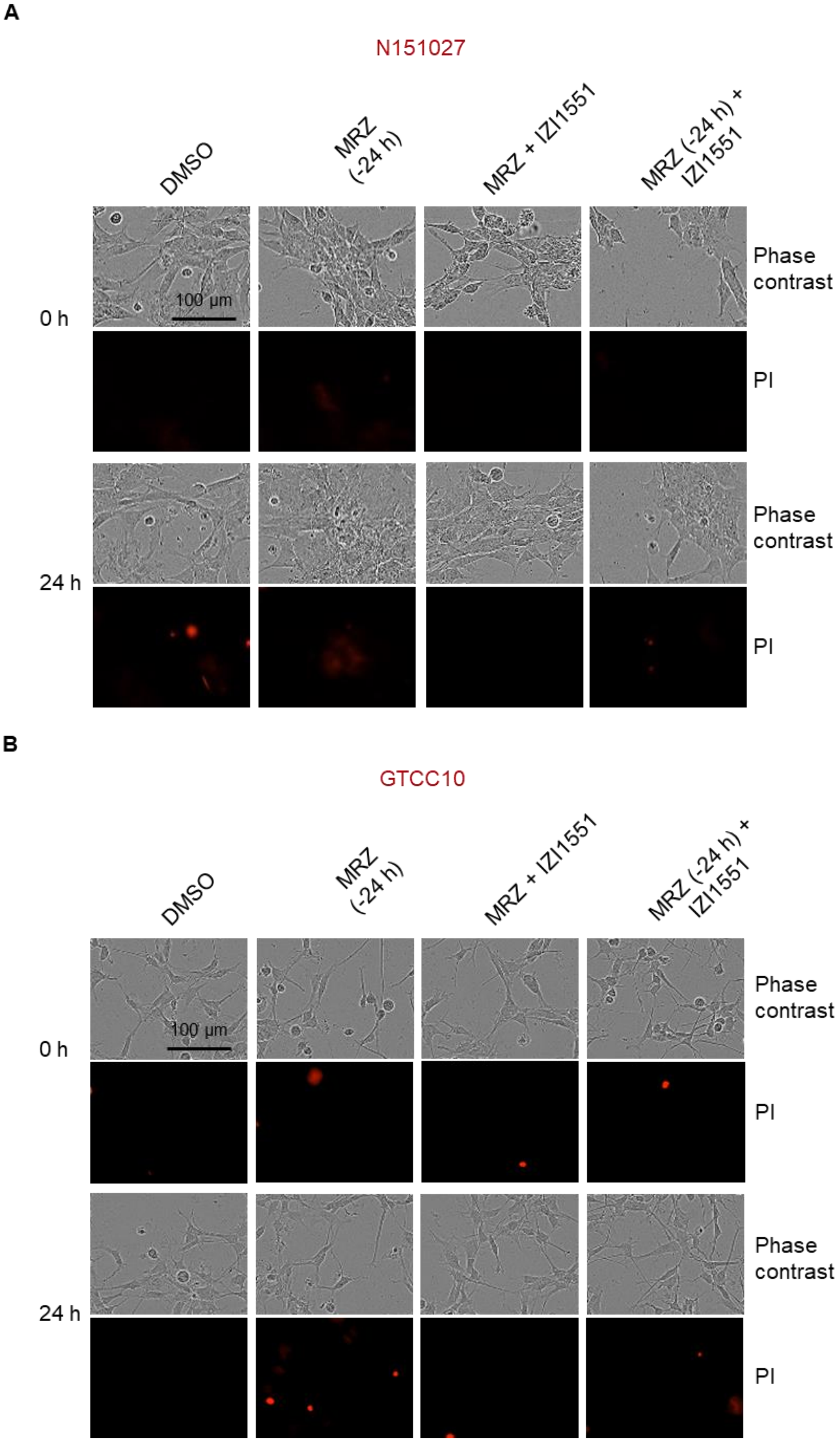
A
N151027
DMSO
MRZ (-24 h)
MRZ + IZI1551
MRZ (-24 h) + IZI1551
0 h
24 h
100 µm
Phase contrast
PI
Phase contrast
PI
B
GTCC10
DMSO
MRZ (-24 h)
MRZ + IZI1551
MRZ (-24 h) + IZI1551
0 h
24 h
100 µm
Phase contrast
PI
Phase contrast
PI

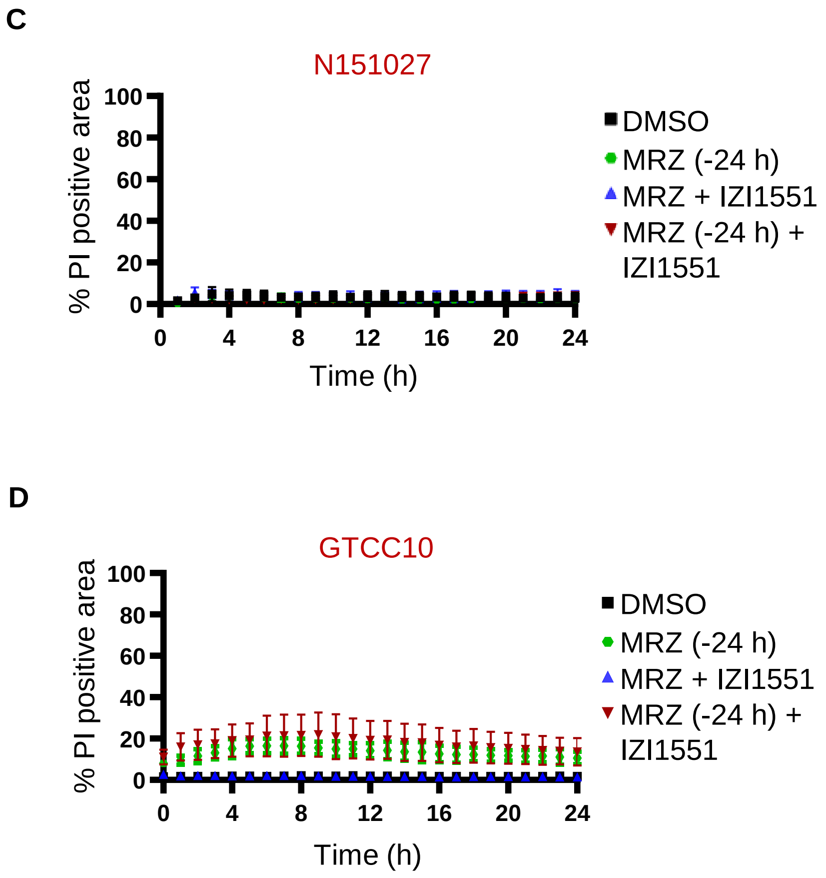

Figure 36: MRZ pre-treatment does not restore IZI1551+MRZ sensitivity in highly resistant GBM cells

*Time lapse monitoring of cell death in N151027 **(A** and **C)** and GTCC10 **(B** and **D)** 2D-cultured PDCLs. Cells were co-treated with IZI1551 (1 nM) and MRZ (80 nM) simultaneously or pre-treated with MRZ for 24 h (MRZ -24 h) before the addition of IZI1551. (**A** and **B)** Representative micrographs of cells imaged at time point 0 h and 24 h in presence of PI. **(C** and **D)** Quantifications of cell death kinetics, calculated as percentage of PI positive cell areas. Representative results from one out of three independent experiments are shown. Error bars represent SD of 3 technical replicates. GTCC10 data were obtained by Emily Kolbe under the author's supervision.*

It was concluded that longer periods of proteasome inhibition do not alter the responsiveness of highly resistant glioblastoma cells to the combinatorial treatment with IZI1551, questioning the very efficacy of marizomib in blocking proteasome activity in these cells. This issue was addressed in the following paragraph.

4.2 MRZ efficiently inhibits proteasome activity in GBM cells

Marizomib has been described as a potent inhibitor of all three enzymatic activities of the proteasome both in pre-clinical and clinical studies [371,377], yet the results presented in the previous parts of this thesis showed that some glioblastoma cells are strongly resistant to it.

To verify that the proteasome is effectively blocked upon marizomib treatment in glioblastoma PDCLs, especially in the resistant ones, its CT-L activity was measured. A representative responsive cell line, namely N160125, and the two resistant cell lines of the panel, namely GTCC10 and N151027, were treated for four hours with marizomib or alternatively with bortezomib for comparison. The fluorescent signal of the cleaved form of the CT-L substrate suc-LLVY-AMC was then analysed (see methods section for details). It appeared that marizomib efficiently blocked proteasome activity both in responder (*figure 37A*) and resistant cells (*figure 37B* and *C*). Of note, the comparison with the inhibition capacity of bortezomib indicated that marizomib had a stronger effect, even at lower concentrations.

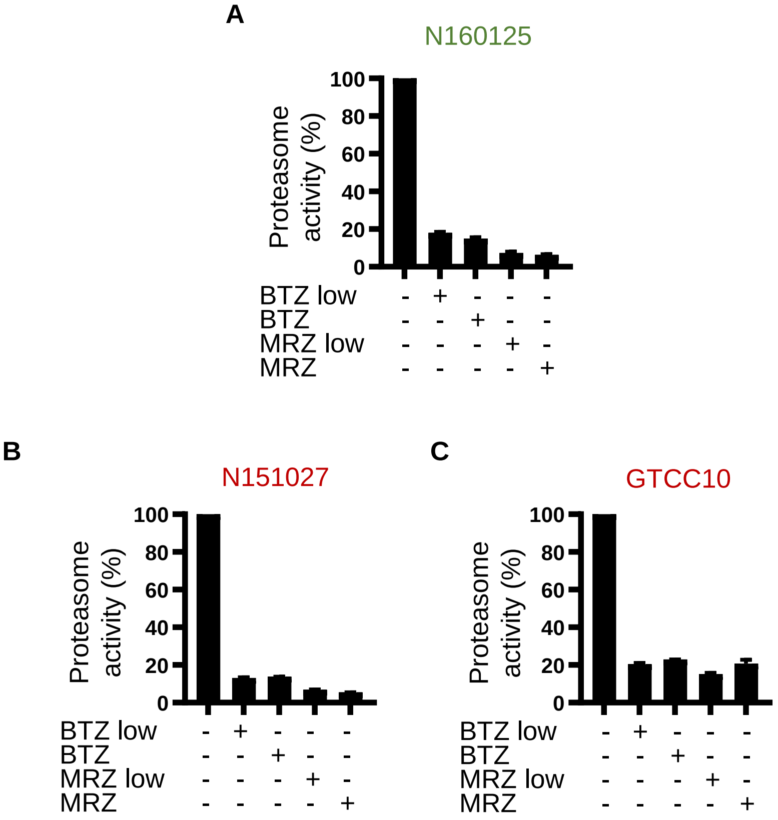

Figure 37: MRZ inhibits proteasome activities both in responder and non-responder cell lines

The 2D-cultured responsive cell line N160125 ***(A)*** *and the resistant cell lines N151027* ***(B)*** *and GTCC10* ***(C)*** *were treated with 40 nM (low) or 80 nM of MRZ or BTZ for 4 h and CT-L activities of the proteasomes were measured from total cell lysates based on the cleavage of Suc-LLVY-AMC. Bars indicate percentage of activity related to untreated controls. Data are shown as mean ± range of n = 2 measurements.*

As the proteasome appeared to be effectively inhibited in the cell lines that did not respond to the combination of IZI1551+MRZ, other reasons for the resistance of N151027 and GTCC10 cells to such treatment were investigated.

4.3 The protein expression signature of highly resistant GBM PDCLs is associated with low competence to induce extrinsic apoptosis

In this section, reasons for the apoptosis incompetence of GTCC10 and N151027 cells upon IZI1551 and marizomib treatment were investigated. As marizomib efficiently blocked proteasome activity in these cells, it was next studied if the pathway of TRAIL-induced apoptosis was impaired. At first, the IZI1551-induced apoptosis initiation phase was studied. In particular, key apoptotic proteins of this part of the pathway were examined for their expression levels in responder *versus* non-responder cell lines. Western blot analysis of total cellular expression of DR4 and DR5, both at basal level and upon marizomib treatment, were conducted. The comparison among two responsive cell lines and one or the other of the resistant ones did not allow to identify a reason for the difference in treatment sensitivity. Indeed, while the responsive cell line GTCC9 expressed high amounts of DR5 and clearly detectable levels of DR4, the second responsive cell line N160125 showed a very different expression pattern, with undetectable DR4 and lower level of DR5. Interestingly, both resistant cell lines, GTCC10 and N151027, shared similar expression levels of death receptors with N160125, indicating that the total amounts of death receptors do not allow to allocate the cell lines to the responder or non-responder group (*figure 38*). It was also interesting to observe that, upon marizomib treatment, no obvious upregulation of total amounts of death receptors was detectable, neither for responsive nor for resistant cells (*figure 38*).

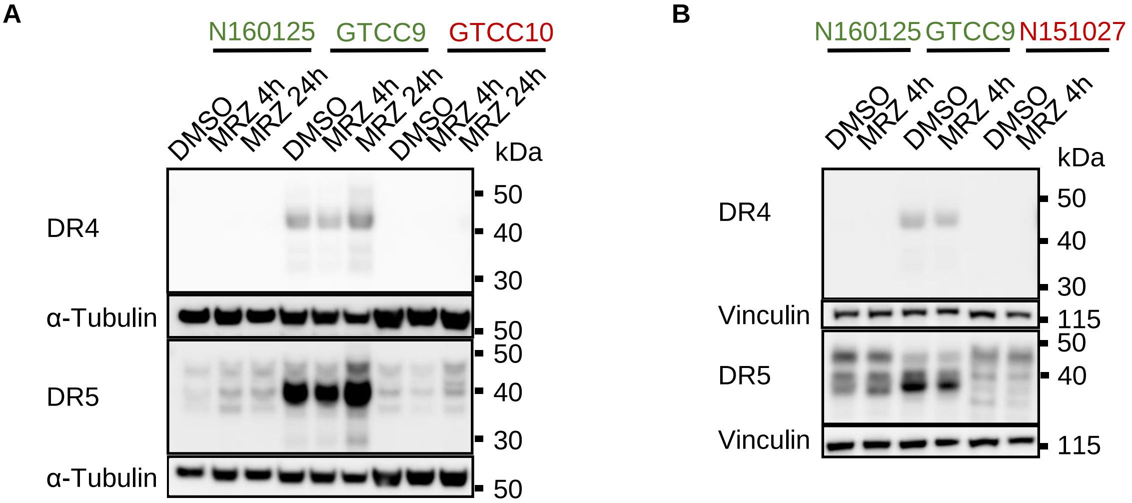

Figure 38: Total amounts of DR4 and DR5 do not correlate with IZI1551+MRZ sensitivity of GBM PDCLs
2D-cultured cells were treated with MRZ (80 nM) for 4 h or 24 h and 15 µg of whole-cell lysates from each sample were analysed for the indicated proteins by western blotting. ***(A)*** *Comparison of death receptors expression*

between responders and GTCC10 cell lines. α-Tubulin served as loading control. ***(B)*** *Comparison of death receptors expression between responders and N151027 cell lines. Vinculin served as loading control. Similar results were obtained in independent repeat experiments.*

However, to accurately conclude on the correlation between the amount of TRAIL receptors and treatment sensitivity, the levels of the formers were further evaluated flow cytometrically with regards to their surface expression. The relative basal expression levels of death receptors in responders *versus* non-responder cell lines, as well as their relative amount upon marizomib treatment, were analysed. It was shown that non-responder cell lines tended to express lower basal amounts of the receptors compared to the responder cell line GTCC9. The comparison with the N160125 responder cells provided similar results as the western blot detections, with non-responder cells expressing indeed low levels of death receptors also on the cell surface (*figure 39*).

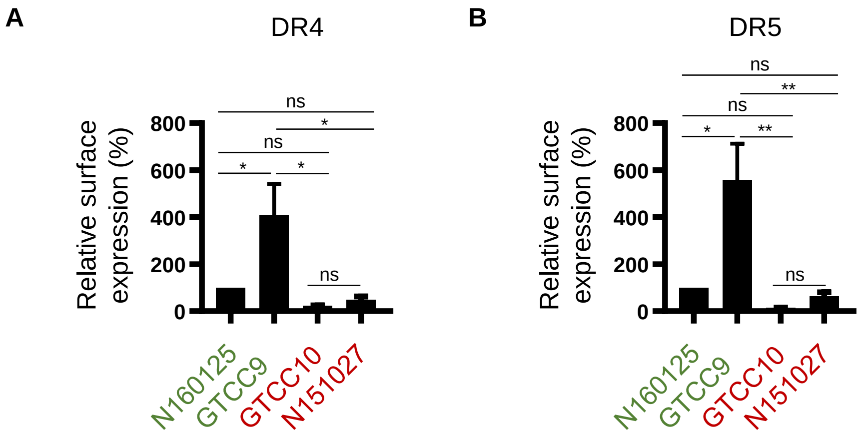

Figure 39: Resistant PDCLs display lower surface expression of death receptors than responsive cells
Surface expression of ***(A)*** *DR4 and* ***(B)*** *DR5. 2D-cultivated cells were analysed by flow cytometry. Population medians, normalized to the median values calculated for N160125 cells, were used to calculate the differences in relative surface expression among responder and non-responder cell lines. Bar graphs show mean values ± SEM of three independent experiments. * = $p \leq 0.05$; ** = $p \leq 0.01$; ns = not significant; one-way ANOVA followed by Tukey's post hoc test. This experiment was conducted by Nathalie Peters. Data analysis was performed by the author.*

Importantly, when examining the effect of proteasome inhibition on the levels of death receptors on the cell surface, it appeared that resistant cells failed or only partially accumulated DR4 and DR5, while marizomib-induced death receptors accumulation was much more enhanced in responsive cells (*figure 40*).

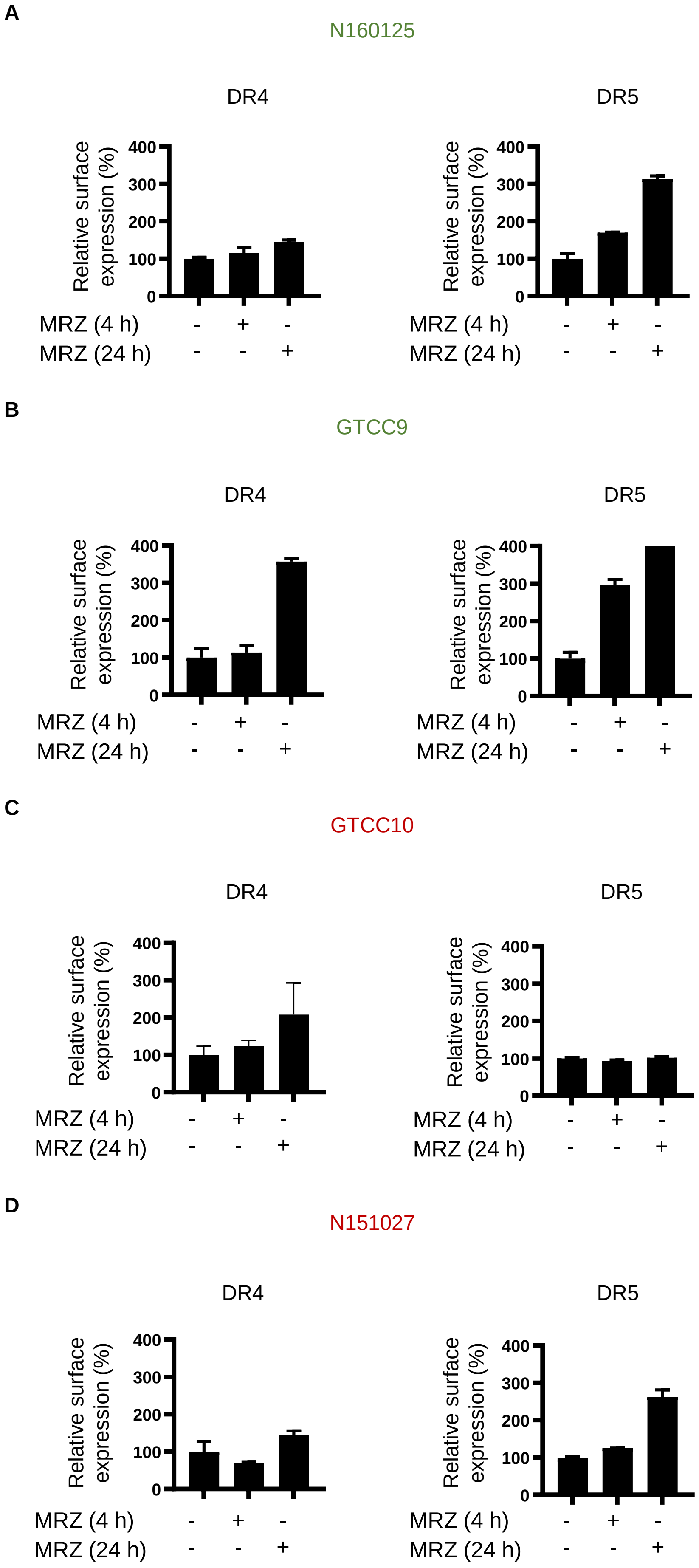
A
N160125
DR4
DR5
Relative surface expression (%)
0
100
200
300
400
MRZ (4 h) - + -
MRZ (24 h) - - +
B
GTCC9
DR4
DR5
Relative surface expression (%)
0
100
200
300
400
MRZ (4 h) - + -
MRZ (24 h) - - +
C
GTCC10
DR4
DR5
Relative surface expression (%)
0
100
200
300
400
MRZ (4 h) - + -
MRZ (24 h) - - +
D
N151027
DR4
DR5
Relative surface expression (%)
0
100
200
300
400
MRZ (4 h) - + -
MRZ (24 h) - - +

Figure 40: Resistant PDCLs mostly fail to accumulate DR4 and DR5 upon marizomib treatment

*Surface expression of DR4 and DR5 in 2D-cultivated responsive (**A** and **B**) and resistant (**C** and **D**) cells analysed by flow cytometry. Population medians, normalized to the median values of untreated controls, were used to calculate the differences in relative surface expression upon MRZ treatment at 4 h and 24 h. Bar graphs show mean values ± SD of three technical repetitions. Similar results were obtained in independent repeat experiments. This experiment was conducted by Nathalie Peters. Data were analysed and plotted by the author.*

Since differences explaining responsiveness and resistance could not be fully identified in the amount of death receptor expressions, other components of the DISC complex, as well as the caspase-8 substrate BID, were compared for their differential expression levels in the sensitive and the resistant cell lines (*figure 41*). Detection of FADD by western blotting showed that its levels were mostly comparable between the responsive cell line N160125 and either GTCC10 or N151027. Instead, the amounts of procaspase-8 and c-FLIP splice variants were consistently lower respectively higher in both resistant cell lines compared to N160125. Moreover, basal levels of BID were lower in the resistant GTCC10 cells than in N160125. When looking at the amounts of these proteins upon marizomib treatment, no notable change was detected, with the exception of the anti-apoptotic and short-lived protein c-FLIP that accumulated upon proteasome inhibition, and of BID levels that decreased only in responsive PDCLs following marizomib treatment (*figure 41*).

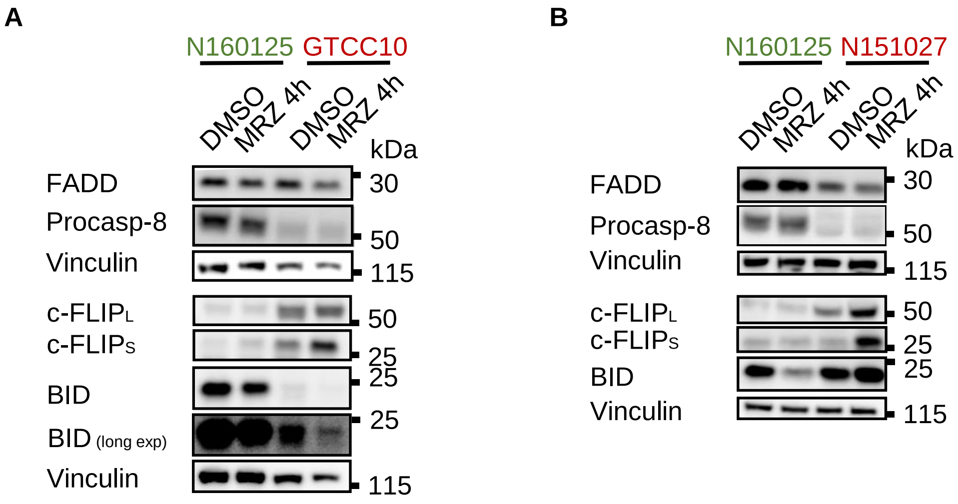

Figure 41: Components of the DISC complex are differentially expressed in responsive and resistant cell lines

2D-cultured cells were treated with 80 nM of MRZ for 4 h and the indicated proteins were detected in whole-cell lysates by western blotting. Vinculin served as loading control. ***(A)*** *Comparison of FADD; procaspase-8; c-FLIP (L/S) and BID expression in the responder N160125 and in the non-responder GTCC10 cell lines.* ***(B)*** *Comparison of protein expression as in (A) between N160125 and N151027 cell lines. Procasp=procaspase. Similar results were obtained in independent repeat experiments.*

Overall, for the proteins here examined, the particular expression signature shared by resistant cell lines distinguished them from the responsive PDCL N160125 and appeared associated with low competence to induce the extrinsic pathway of apoptosis. These observations led to the hypothesis that sensitisation strategies targeting elements downstream of caspase-8 activation could restore apoptosis competence in these highly resistant glioblastoma cells. The following paragraph addresses this possibility.

4.4 Lowering the mitochondrial apoptosis threshold allows apoptosis execution upon IZI1551+MRZ treatment in highly resistant GBM cells

In the representative panel of glioblastoma cell lines examined in this thesis, the two PDCLs N151027 and GTCC10, generated from a primary respectively recurrent tumour, showed high resistance to the combination treatment with the second-generation TRAIL receptor agonist IZI1551 and the proteasome inhibitor marizomib, regardless of the dosage and treatment scheduled tested. Even though the expression level of no specific single protein could be identified as responsible for such resistance, a protein signature that appeared associated with poor apoptosis competence emerged from western blot analysis. Compared to the sensitive PDCLs, the two non-responder cell lines showed lower basal levels of caspase-8 and higher amounts of the anti-apoptotic protein c-FLIP that further accumulated upon marizomib treatment. Based on this protein expression profile, it is conceivable that IZI1551-induced apoptosis initiation was impaired in N151027 and GTCC10 resistant cell lines. In order to compensate for this insufficient apoptosis initiation signal, a sensitisation through the mitochondrial pathway of apoptosis was tested. The threshold for mitochondrial apoptosis execution depends on the balance between pro- and anti- apoptotic proteins of the Bcl-2 family [516]. Hence, the expression of three important anti-apoptotic members of this family, namely Mcl-1; Bcl-xL and Bcl-2, was analysed by western blotting (*figure 42*). Comparing their basal expression levels between two responsive cell lines and the resistant ones did not allow to identify a specific pattern to distinguish the two categories. More precisely, Bcl-xL was equally expressed in all cell lines here examined and Bcl-2 was barely detectable or undetectable in both a sensitive cell line and the two resistant PDCLs. Interestingly, Mcl-1 slightly accumulated upon treatment with marizomib in all three cell lines (*figure 42*).

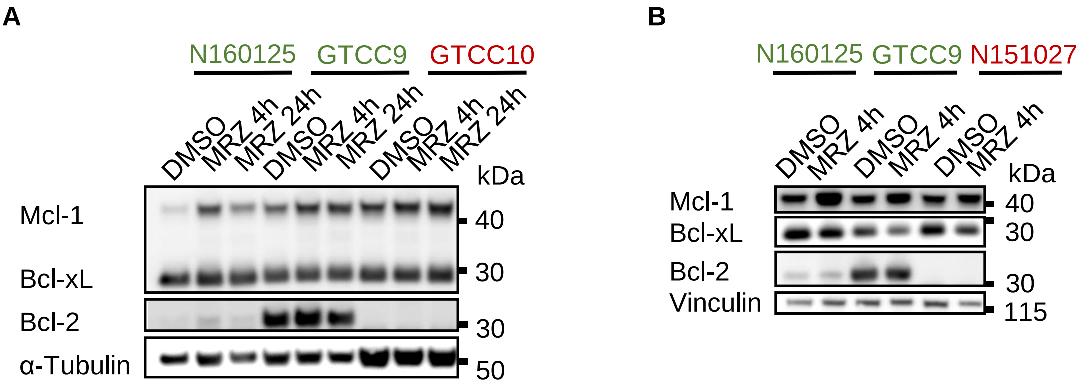

Figure 42: Anti-apoptotic Bcl-2 family proteins were detected in different cell lines

*2D-cultured cells were treated with 80 nM of MRZ for 4 h or 24 h and the indicated proteins were detected in whole-cell lysates by western blotting. Comparison of Mcl-1; Bcl-xL and Bcl-2 expressions between responders and **(A)** GTCC10 or **(B)** N151027 cell lines. α-Tubulin or vinculin served as loading controls. Similar results were obtained in independent repeat experiments.*

The MOMP threshold can be modulated by using targeted therapeutics that have been developed against each of these Bcl-2 family members, namely S63845 for Mcl-1, WEHI-539 for Bcl-xL and ABT-199 for Bcl-2 [517,518]. Therefore, considering the expression levels of these proteins, it was evaluated if their antagonists could sensitise resistant cells to IZI1551+MRZ-induced apoptosis. Bcl-2 was expressed at very low levels in resistant cell lines and indeed, flow cytometric measurements of GTCC10 cells treated with the Bcl-2 specific inhibitor ABT-199 showed that this drug was mostly ineffective in inducing apoptosis, both as a single agent and in a triple combination with IZI1551 and marizomib (*figure 43*).

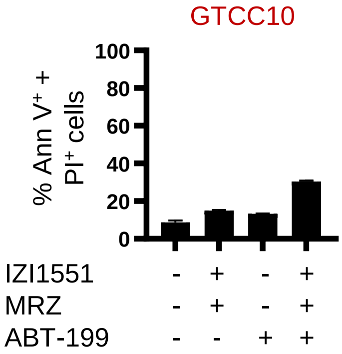

Figure 43: Antagonising Bcl-2 does not restore apoptosis competence in a highly resistant GBM PDCL

Annexin V/PI-based flow cytometry of 2D-cultured GTCC10 cells treated with 10 µM ABT-199; 1 nM IZI1551 plus 80 nM MRZ or the combination thereof for 24 h. Data represent mean ± SD of triplicate samples. Similar results were obtained in an independent repeat experiment.

One other anti-apoptotic protein of the Bcl-2 family, Bcl-xL, was not differentially expressed in responsive *versus* resistant glioblastoma cell lines. Moreover, the clinical applicability of treatments targeting Bcl-xL have been questioned because of their associated effects of platelets toxicity, making this protein an overall non-optimal candidate for specifically and safely restoring apoptosis competence in these highly resistant glioblastoma cells [519].

Mcl-1 is a high-turnover anti-apoptotic protein of the Bcl-2 family that slightly accumulated upon marizomib treatment. Therefore, antagonising this protein could shift the life/death signal balance toward apoptosis execution in cells that are resistant to other treatments. Specifically, it was investigated if lowering the MOMP threshold with the Mcl-1 antagonist S63845 would allow to re-sensitise GTCC10 and N151027 cell lines to apoptosis. Annexin V/PI-based flow cytometry measurements of cells treated with either S63845 alone or with a triple combination of the Mcl-1 inhibitor together with IZI1551 and marizomib provided promising results. Indeed, while S63845 alone only had a limited effect on these cells, the triple treatment with IZI1551+MRZ very effectively induced apoptosis, both in 2D-cultured cells (*figure 44A* and *B*) and in 3D tumour spheroids (*figure 44C*).

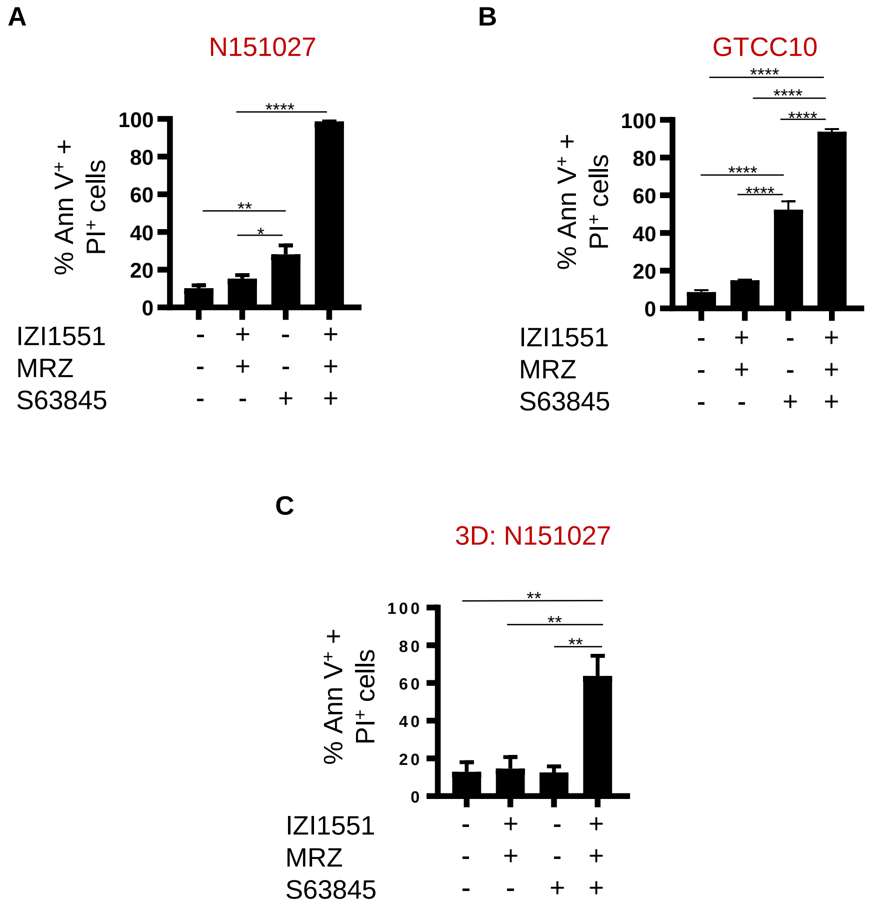

Figure 44: Mcl-1 inhibition restores apoptosis competence in highly resistant GBM PDCL

Annexin V/PI-based flow cytometry of cells treated with 10 µM S63845; 1 nM IZI1551 plus 80 nM MRZ or the combination thereof for 24 h. ***(A)*** *2D-cultured N151027 cells.* ***(B)*** *2D-cultured GTCC10 cells.* ***(C)*** *3D-cultured N151027 cells. Data represent mean ± SEM of three independent experiments. * = p ≤ 0.05; ** = p ≤ 0.01; **** = p ≤ 0.0001; one-way ANOVA followed by Tukey's post hoc test.*

These results proved that lowering the mitochondrial apoptosis threshold is an effective strategy for restoring IZI1551+MRZ sensitivity and allowing apoptosis execution in highly resistant glioblastoma PDCLs.

5. Chapter Five: Ferroptosis as an alternative path to death in GBM

Many cancer types, including glioblastoma, are highly resistant to conventional therapies that are based on the induction of apoptotic cell death [520,521]. For this reason, alternative strategies that can eradicate tumour cells have been explored in the past recent years [522–524]. In this final chapter, a recently identified form of regulated cell death termed ferroptosis was investigated. Ferroptosis is known to present distinctive characteristics compared to other death pathways, such as the lack of caspase activation [417]. Many cancer cells have been described to be ferroptosis-sensitive, with glioblastoma being one of them [525–527]. Here, the characteristics of ferroptosis, including morphological features, death kinetics, and the general cell death mechanism, were studied. The interactions of ferroptosis inducers with inhibitors of Bcl-2 family proteins were also investigated in this chapter, providing a glimpse into the interplay between ferroptosis and other cellular pathways. As ferroptosis is still a relatively poorly characterised form of cell death, its study in this chapter was first performed on a typical ferroptosis model, namely the HT1080 fibrosarcoma cell line, and then extended to U-87 MG, a prototype TRAIL-resistant glioblastoma cell line [528–530]. The findings gathered here comprise the surprising feature of caspase activation induced by the typical ferroptosis inducer RSL3 in HT1080 cells. Importantly, instead of synergising with ferroptosis inducers in triggering cell death, BH3 mimetics rather had a protecting effect on both erastin and RSL3-induced death across different cell lines and Bcl-2 family antagonists.

5.1 Erastin induces death in the HT1080 cell line in a dose-dependent manner and its effect is antagonized by Bcl-2 inhibition

The fibrosarcoma cell line HT1080 is the traditional cell line model in ferroptosis studies [403]. In order to assess HT1080 cells sensitivity to the ferroptosis inducer erastin (Era), cells were treated with concentrations of the drug ranging from 0.125 µM to 1 µM in the presence of PI and imaged for 24 hours at intervals of 1 hour using the IncuCyte system. It was shown that cells died of erastin in a dose-dependent manner, with the lowest drug concentration tested not being toxic to the cells until the latest time point recorded (*figure 45B*). To obtain kinetic data on erastin-induced death, IncuCyte recorded pictures were analysed in terms of increased PI-positive cell area: the percentage of PI-stained area over the percentage of cell-covered area (confluence) in each well was calculated and plotted over time. Considering this ratio as an indicator of cell death, it was shown that death onset was gradually delayed when lowering erastin concentrations (*figure 45A* and *B*). Of note, the morphology of the dying cells was characteristic of ferroptosis, with swelling or "ballooning phenotype" being evident before cell death (*figure 45B*) [424].

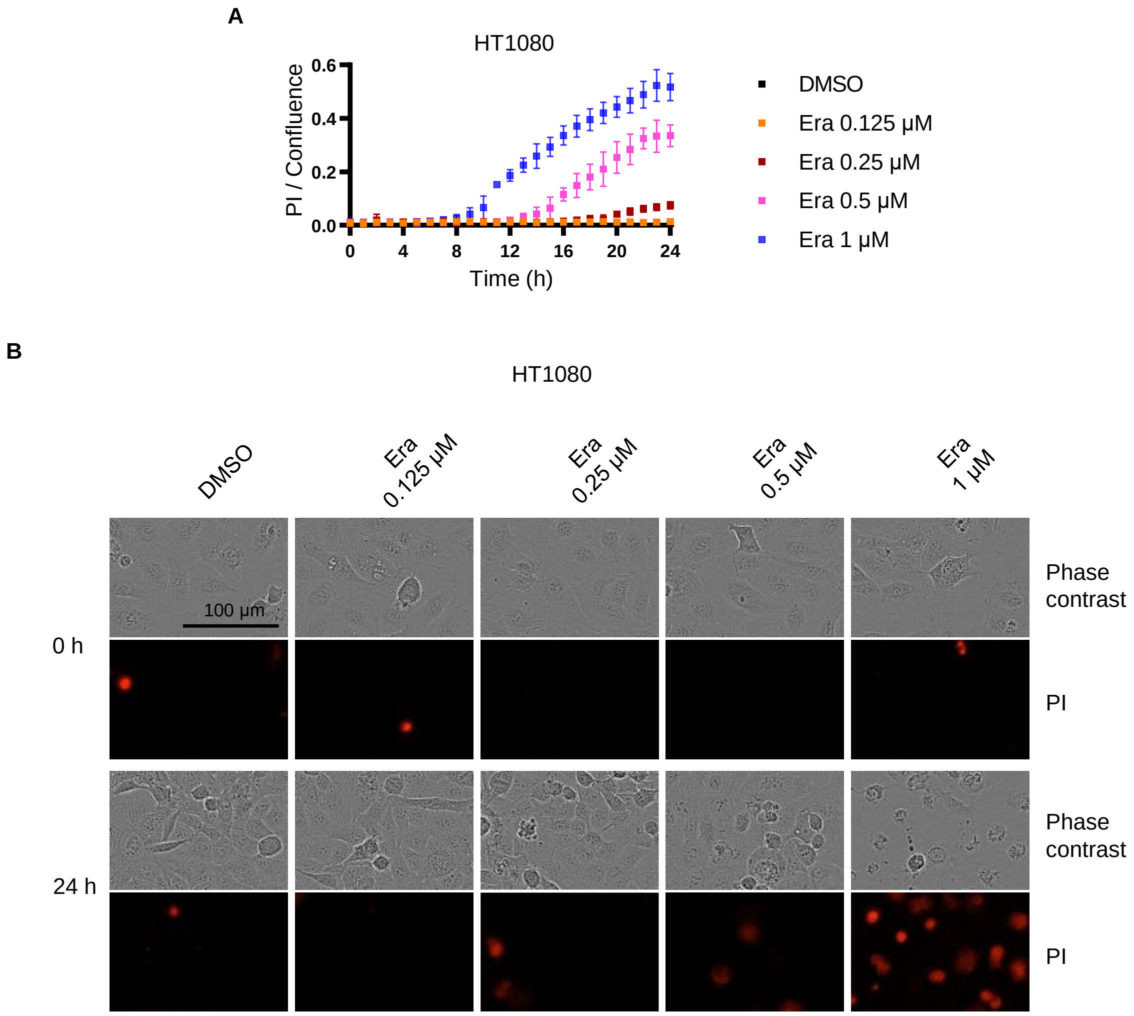

Figure 45: HT1080 cells die of erastin in a dose-dependent manner

HT1080 cells were seeded at a density of 10^4 cells/well in a 96 well plate 24 h prior to the experiment and then treated for 24 h with the indicated concentrations of erastin in presence of PI. ***(A)*** *Quantification of death kinetic calculated as PI positive area over confluence recorded by the IncuCyte system at intervals of 1 h for 24 h.* ***(B)*** *Phase contrast and red fluorescence images taken at time points 0 h and 24 h. Data are presented as mean ± SD of three technical replicates. Similar results were obtained in independent repeat experiments.*

Besides its morphological peculiarity, the ferroptotic nature of erastin-induced death was also characterised in its mechanistic features. For that, HT1080 cells were treated with erastin in presence of the pan-caspase inhibitor Q-VD-Oph or the ROS-scavenger ferrostatin-1 (Fer-1). PI positivity was captured and analysed as described above. While blocking caspases did not prevent erastin-induced death, reducing the amount of ROS with ferrostatin-1 protected all the cells, as indicated by their morphology (*figure 46B*) and by the PI/confluence ratio that was kept at the level of DMSO-treated cells (*figure 46A*).

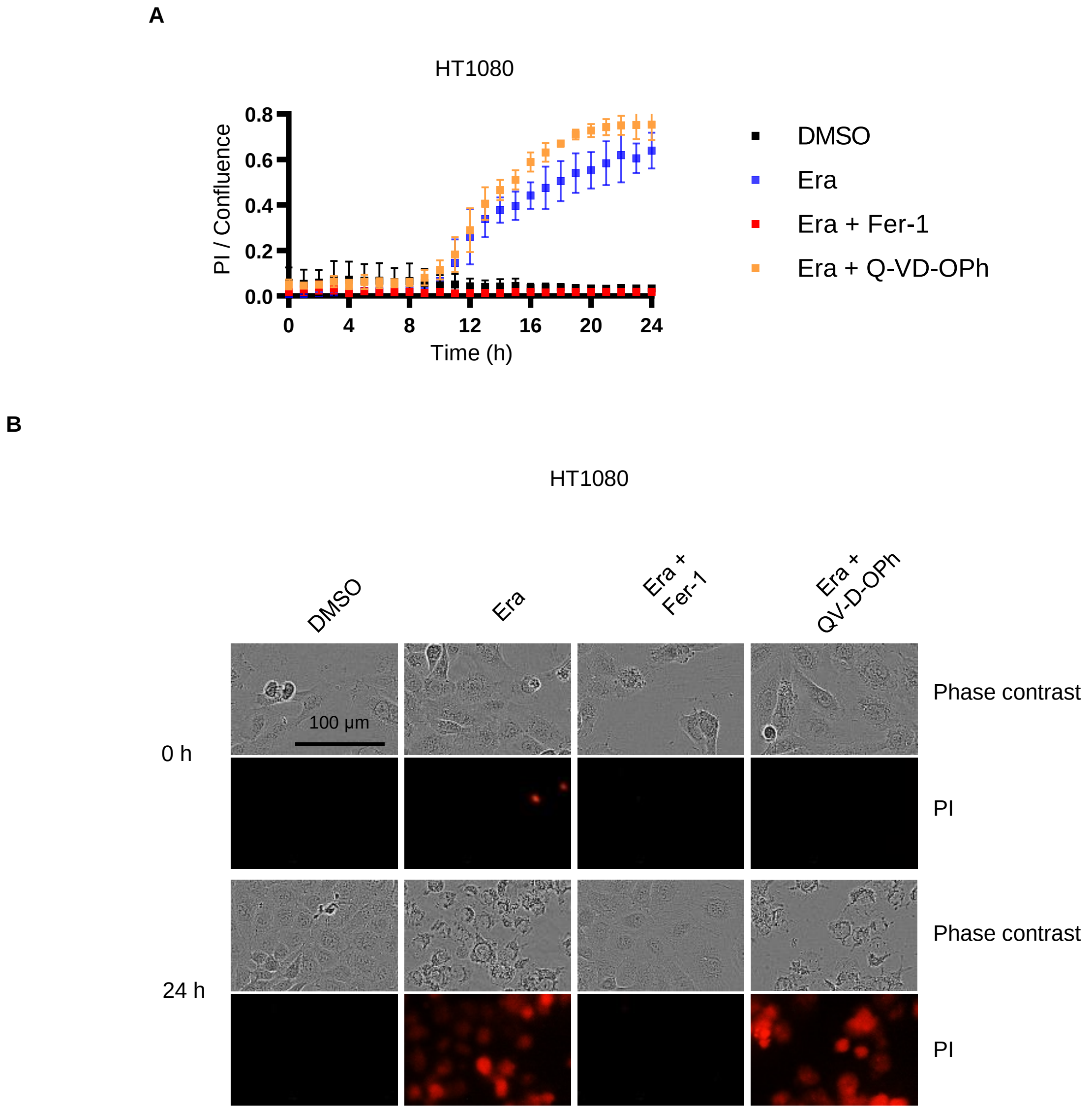

Figure 46: ROS scavenging but not caspase inhibition protects HT1080 cells from erastin-induced death

HT1080 cells were seeded at a density of 10^4 cells/well in a 96 well plate 24 h prior to the experiment and then treated for 24 h in presence of PI. Treatments included 1 µM of erastin alone or in combination with either 2 µM of Fer-1 or 50 µM of Q-VD-Oph (30 minutes pre-exposure). ***(A)*** *Quantification of PI positive area over confluence recorded by the IncuCyte system at intervals of 1 h for 24 h.* ***(B)*** *Phase contrast and red fluorescence images taken at time points 0 h and 24 h. Data are presented as mean ± SD of three technical replicates. Similar results were obtained in independent repeat experiments.*

As a negative control of erastin-induced ferroptosis, the cervical adenocarcinoma cell line HeLa was exposed to the highest erastin concentration tested on HT1080 cells. Consistently with other reports, it was found that 1 µM erastin did not induce death nor changed the morphology of these cells (*figure 47A* and *B*) [531].

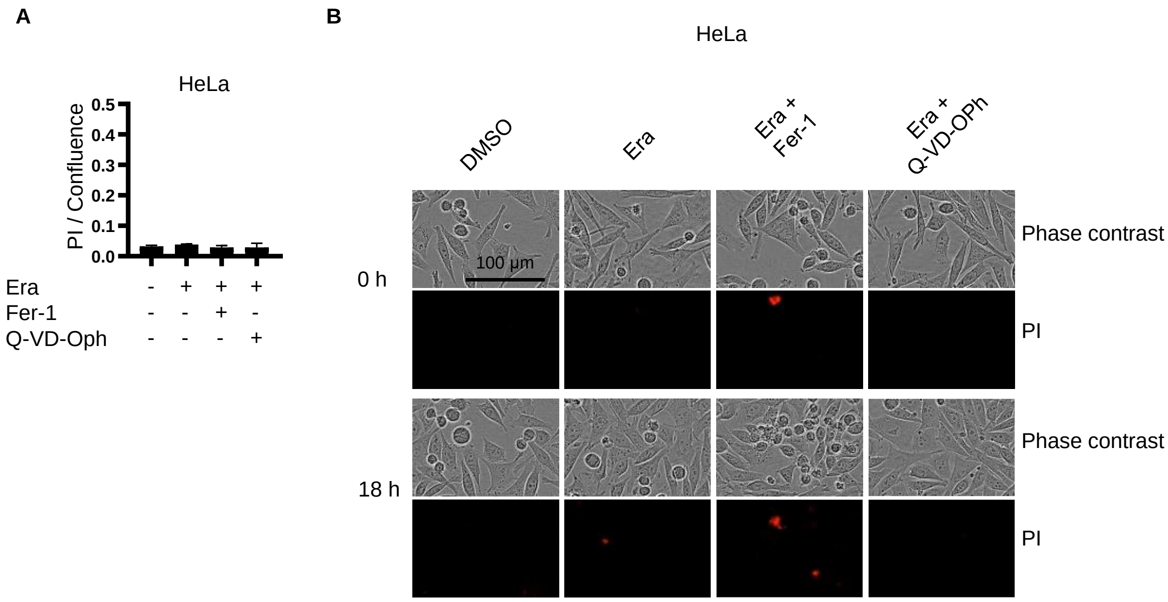

Figure 47: HeLa cells are resistant to erastin treatment

HeLa cells were seeded at a density of 10^4 cells/well in a 96 well plate 24 h prior to the experiment and then treated for 18 h in presence of PI. Treatments included 1 µM of erastin alone or in combination with either 2 µM of Fer-1 or 50 µM of Q-VD-Oph (30 minutes of pre-exposure). ***(A)*** *Quantification of PI positive area over confluence recorded by the IncuCyte system following 18 h of treatment.* ***(B)*** *Phase contrast and red fluorescence images taken at time points 0 h and 18 h. Data are presented as mean ± SD of three technical replicates. Similar results were obtained in independent repeat experiments.*

The data presented so far confirmed HT1080 cells as a reliable model for *in vitro* studies on erastin-induced ferroptosis, with dose-dependent responsiveness to the drug and caspase involvement not being required for death execution. The ROS-scavenger ferrostatin-1 instead provided full protection from the highest erastin concentration tested here.

As it is reported that erastin leads to the accumulation of lipid ROS with consequent mitochondrial damage, a possible convergence with the intrinsic apoptotic pathway was investigated [473,532]. In particular, it was hypothesized that ferroptosis-induced mitochondrial stress might prime the mitochondria to BAK and BAX pore formation, with consequent cytochrome c release and cells eventually dying of apoptosis. Combining ferroptosis inducers with antagonists of anti-apoptotic Bcl-2 family proteins, that would otherwise prevent mitochondrial outer membrane permeabilization, could represent a promising co-treatment strategy to enhance cell death induction, as both pathways converge on the same organelle. As diverse tumour cells depend on anti-apoptotic Bcl-2 family proteins for survival, the sensitivity of HT1080 cells to the Bcl-2 antagonist ABT-199 as a single agent was tested [533,534]. For that, cells were treated with increasing concentrations of ABT-199 in presence of PI. The PI-stained area and the cell-covered area were recorded every hour for 24 hours with an IncuCyte system and cell death analysis was performed as described previously. Even at a concentration as high as 10 µM, ABT-199 did not have any effect on HT1080 cells within the 24 hours here recorded (*figure 48*). However, in combination with erastin, ABT-199 could still be able to provoke a potentiating effect. To test this hypothesis, HT1080 cells were co-stimulated with 1 µM of erastin together with 10 µM of ABT-199 in presence of PI and cell death was assessed using an IncuCyte system from the images recorded during 24 hours of treatment. Surprisingly, such combination did not potentiate cell death induction but rather resulted in a mild protecting effect of ABT-199 on erastin-induced cytotoxicity (*figure 49*).

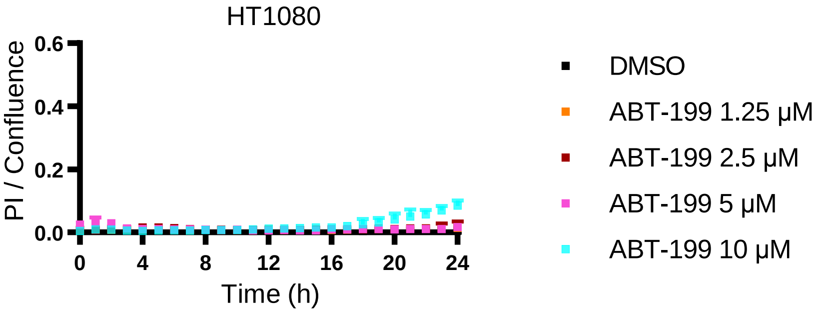

Figure 48: HT1080 cells are resistant to ABT-199 treatment

HT1080 cells were seeded at a density of 10⁴ cells/well in a 96 well plate 24 h prior to the experiment and then treated for 24 h with the indicated concentrations of ABT-199 in presence of PI. Phase contrast and red fluorescence images were recorded with the IncuCyte system at intervals of 1 h for 24 h. Cell death, measured as PI uptake, was analysed with the corresponding software. Data are presented as mean ± SD of three technical replicates. Similar results were obtained in independent repeat experiments.

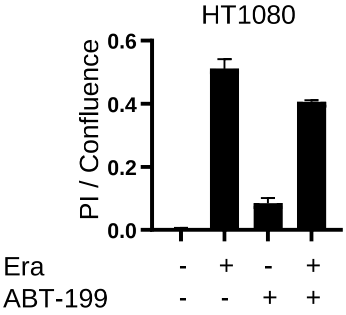

Figure 49: ABT-199 protects HT1080 cells from erastin-induced death

HT1080 cells were seeded at a density of 10^4 cells/well in a 96 well plate 24 h prior to the experiment and then treated for 24 h with 1 µM of erastin; 10 µM of ABT-199 or the combination thereof in presence of PI. Quantification of PI positive area over confluence was recorded by the IncuCyte system after 24 h of treatment. Data are presented as mean ± SD of three technical replicates. Similar results were obtained in independent repeat experiments.

These unexpected results suggested a complex interaction between ferroptosis and apoptosis and required validations with different ferroptosis inducers and apoptosis modulators in both HT1080 cells as well as in other cell lines. Also, the remaining fraction of dead cells after the mitigating effect of ABT-199 on erastin-induced death still had to be characterised in terms of cell death mechanism. These aspects are investigated in the following paragraphs.

5.2 RSL3-induced death can involve caspases activity

Among the various substances that can induce ferroptosis, RSL3 belongs to the group of the direct GPx-4 inhibitors [407,535]. Differently from erastin, that provokes cysteine starvation and also interacts with VDAC2/VDAC3, RSL3-induced ferroptosis does not depend on these factors [536]. Therefore, investigating ferroptosis induced by RSL3 allows to restrict the range of possible other interactions that might occur upstream of GPx-4 inhibition and permits to identify more conserved downstream events that are necessary for ferroptosis execution. In this paragraph, the response to RSL3 of HT1080 cells was analysed and the death mechanism investigated.

To verify a dose-dependent effect of RSL3 in inducing cell death, HT1080 cells were exposed to increasing concentrations of the drug until 4.5 µM in presence of PI. PI uptake and phenotypic changes were captured with an IncuCyte system (*figure 50B*) and the kinetic of PI/confluence ratio was analysed from the 24 micrographs recorded (*figure 50A*). Upon the lower RSL3 concentrations tested, cells started to die following 8 hours of treatment. The lethal effect of 4.5 µM of RSL3 started to manifest after around 5 hours, reaching its maximum at around 14 hours, followed by a plateau phase until the last time point recorded (*figure 50A*). Similar to the morphological changes of erastin-treated cells (see *figure 45B*), swelling was observed also upon RSL3 treatment (*figure 50B*).

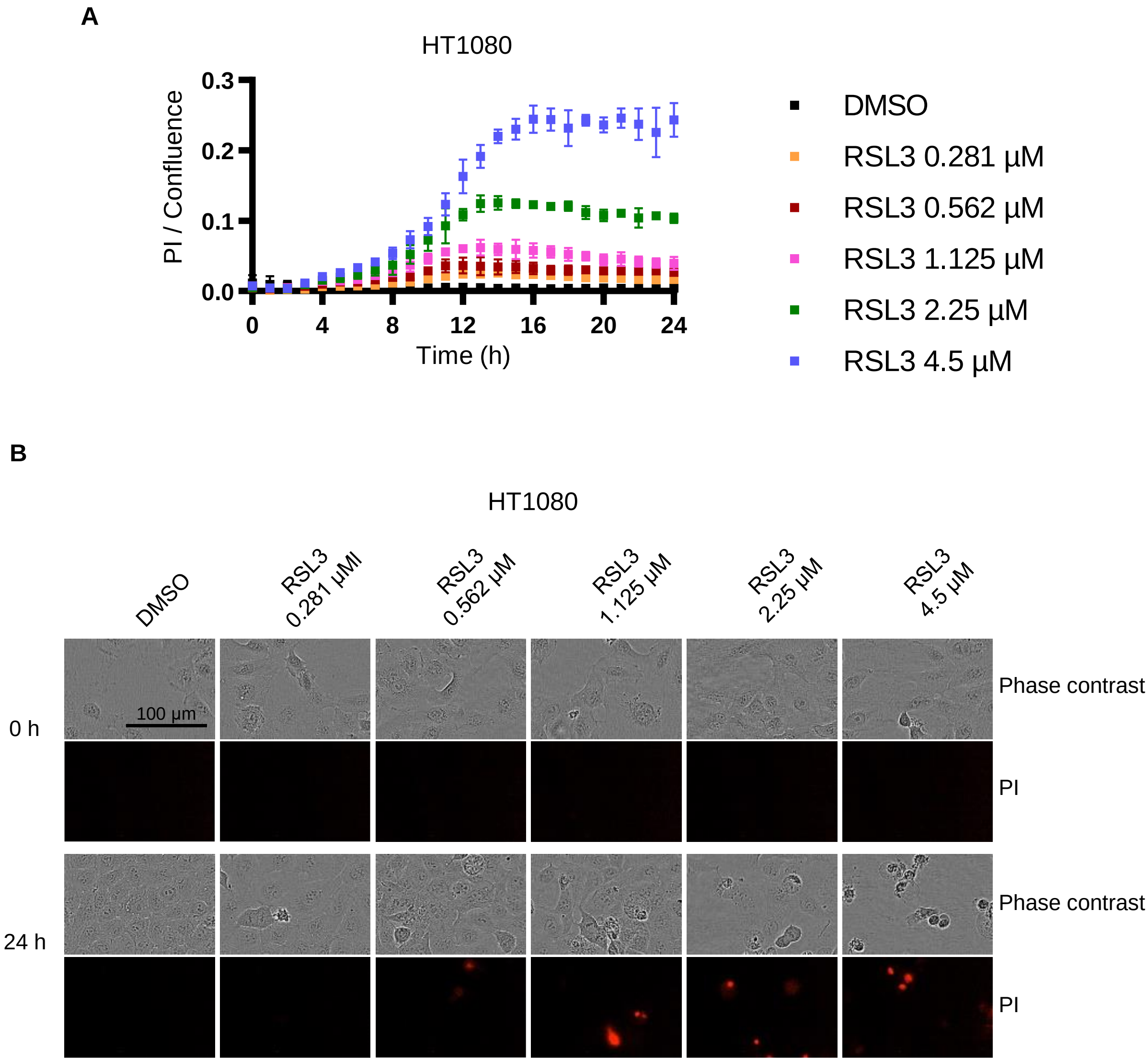

Figure 50: HT1080 cells die of RSL3 in a dose-dependent manner

HT1080 cells were seeded at a density of 10^4 cells/well in a 96 well plate 24 h prior to the experiment and then treated for 24 h with the indicated concentrations of RSL3 in presence of PI. ***(A)*** *The kinetic of cell death was calculated over 24 h as the ratio of PI positive area over confluence from micrographs recorded by the IncuCyte system at intervals of 1 h.* ***(B)*** *Phase contrast and red fluorescence images were taken at time point 0 h and 24 h. Data are presented as mean ± SD of three technical replicates. Similar results were obtained in independent repeat experiments. This experiment was conducted together with Jessica Sieger.*

Next, the caspase inhibitor Q-VD-Oph or the ROS scavenger ferrostatin-1 were added to the RSL3 treatment in order to gain an insight into the mechanism of RSL3-induced death. For that, HT1080 cells treated in presence of PI were imaged by the IncuCyte system for 24 hours and PI positivity was analysed as previously described. The kinetic of ferrostatin-1 action surprisingly revealed that its protecting effect was limited to the first 12 hours of RSL3 treatment and became less efficient after this time point (*figure 51*).

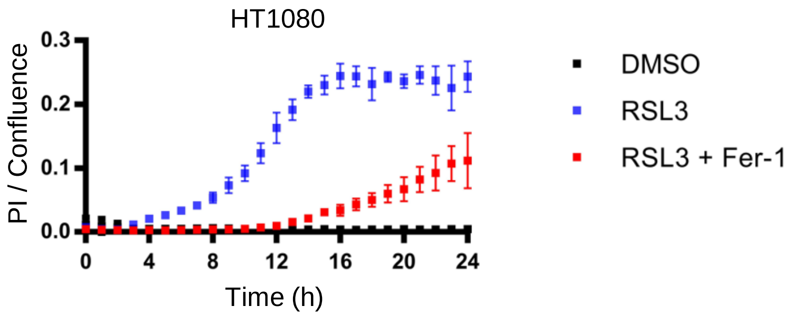

Figure 51: Ferrostatin-1 only partially protects HT1080 cells upon RSL3 treatment

HT1080 cells were seeded at a density of 10^4 cells/well in a 96 well plate 24 h prior to the experiment and then treated for 24 h in PI-containing medium with 4.5 µM of RSL3 in presence or absence of 2 µM of Fer-1. Quantification of PI positive area over confluence was calculated from IncuCyte-recorded images at intervals of 1 h for 24 h. Data are presented as mean ± SD of three technical replicates. Similar results were obtained in independent repeat experiments. This experiment was conducted together with Jessica Sieger.

As the RSL3 concentration used in this experiment (4.5 µM) was higher than what is reported to robustly induce death in HT1080 cells (~0.5 µM), it could be that the continuous ROS production induced by this high dosage of RSL3 led to ferrostatin-1 depletion within the first 12 hours and that radicals generated after this time point could no longer be scavenged [418,537,538]. To investigate this possibility, HT1080 cells were seeded in two 96-well plates 24 hours prior to experiments and then the two plates were treated in parallel with 4.5 µM of RSL3 in presence or absence of 2 µM of ferrostatin-1 (time point 0 h). Following Annexin V-GFP and PI double staining, one plate was analysed via flow cytometry after 5 hours of treatment, which is a time point that preceded the loss of effectiveness of ferrostatin-1 according to the kinetic study performed with the IncuCyte (see *figure 51*). Compared to controls, almost no cell was counted as dead at this early time point (*figure 52A*). The second plate was analysed 24 h following the initial treatment and it included a condition in which cells had been treated with a second dose of ferrostatin-1 after 5 hours from the first one administered at time point 0 hours. It was observed that the addition of extra ferrostatin-1 did not rescue more cells compared to the condition where only one initial dose of the ROS-scavenger was included (*figure 52B*).

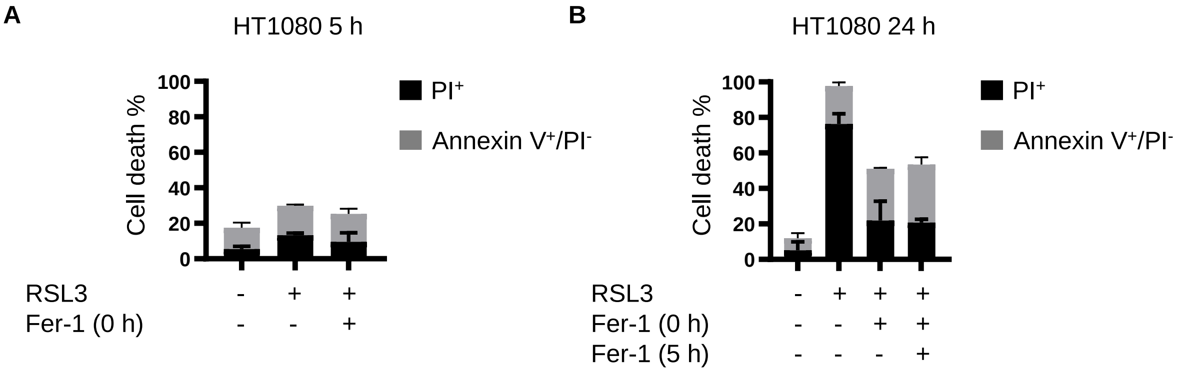

Figure 52: Subsequent ferrostatin-1 treatments do not provide further protection from RSL3 compared to a single dose

HT1080 cells were seeded at a density of 10^4 cells/well in two 96 well plates 24 h prior to the experiment and then treated with 4.5 µM of RSL3 in presence or absence of 2 µM of Fer-1 (Fer-1 0 h). ***(A)*** *Cell death was measured by Annexin V/PI-based flow cytometry following 5 h of treatment.* ***(B)*** *2 µM of freshly prepared Fer-1 (Fer-1 5 h) were added after 5 h from the initial RSL3 + Fer-1 treatment and cell death was measured by Annexin V/PI-based flow cytometry 19 h later. Data are presented as mean ± SD of three technical replicates. Similar results were obtained in independent repeat experiments.*

As RSL3-induced lethality was not fully prevented by ferrostatin-1, this well-known ferroptosis inducer must be responsible for an unreported mechanism of cell death in addition to its documented ferroptosis-inducing production of lipid ROS. To explore if apoptotic death plays a role in RSL3-induced lethality, the pan caspases inhibitor Q-VD-Oph was included in the experiment shown in *figure 51*. Interestingly, while in the first hours Q-VD-Oph exerted no effect, at later time points (from 8 hours onwards) the blocking of caspases partially rescued RSL3-treated cells (*figure 53*).

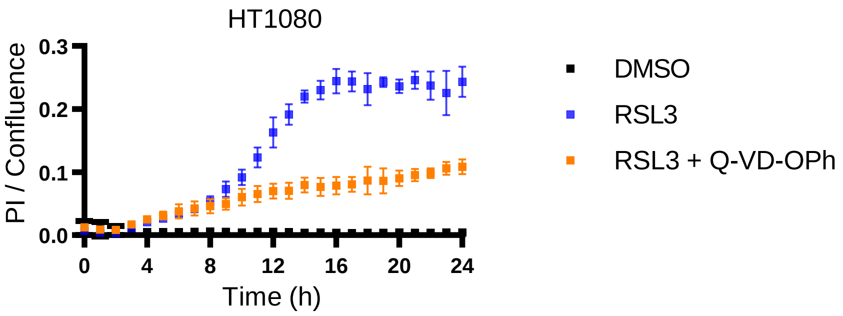

Figure 53: Q-VD-Oph partially protects HT1080 cells from RSL3 treatment

HT1080 cells were seeded at a density of 10^4 cells/well in a 96 well plate 24 h prior to the experiment and then treated in presence of PI for 24 h with 4.5 μM of RSL3 with or without 30 minutes of pre-incubation with 50 μM of Q-VD-Oph. Quantification of PI positive area over confluence was calculated from images recorded by the IncuCyte system at intervals of 1 h for 24 h. Data are presented as mean ± SD of three technical replicates. Data points for DMSO control and RSL3-treated cells are reported from the experiment shown in figure 51. Similar results were obtained in independent repeat experiments. This experiment was conducted together with Jessica Sieger.

In order to better visualize the effect of both ferrostatin-1 and Q-VD-Oph on HT1080 cells treated with 4.5 μM of RSL3, their respective traces from the experiment already shown in *figure 51* and *figure 53* were merged in *figure 54A* and the micrographs captured by the IncuCyte are shown in *figure 54B*.

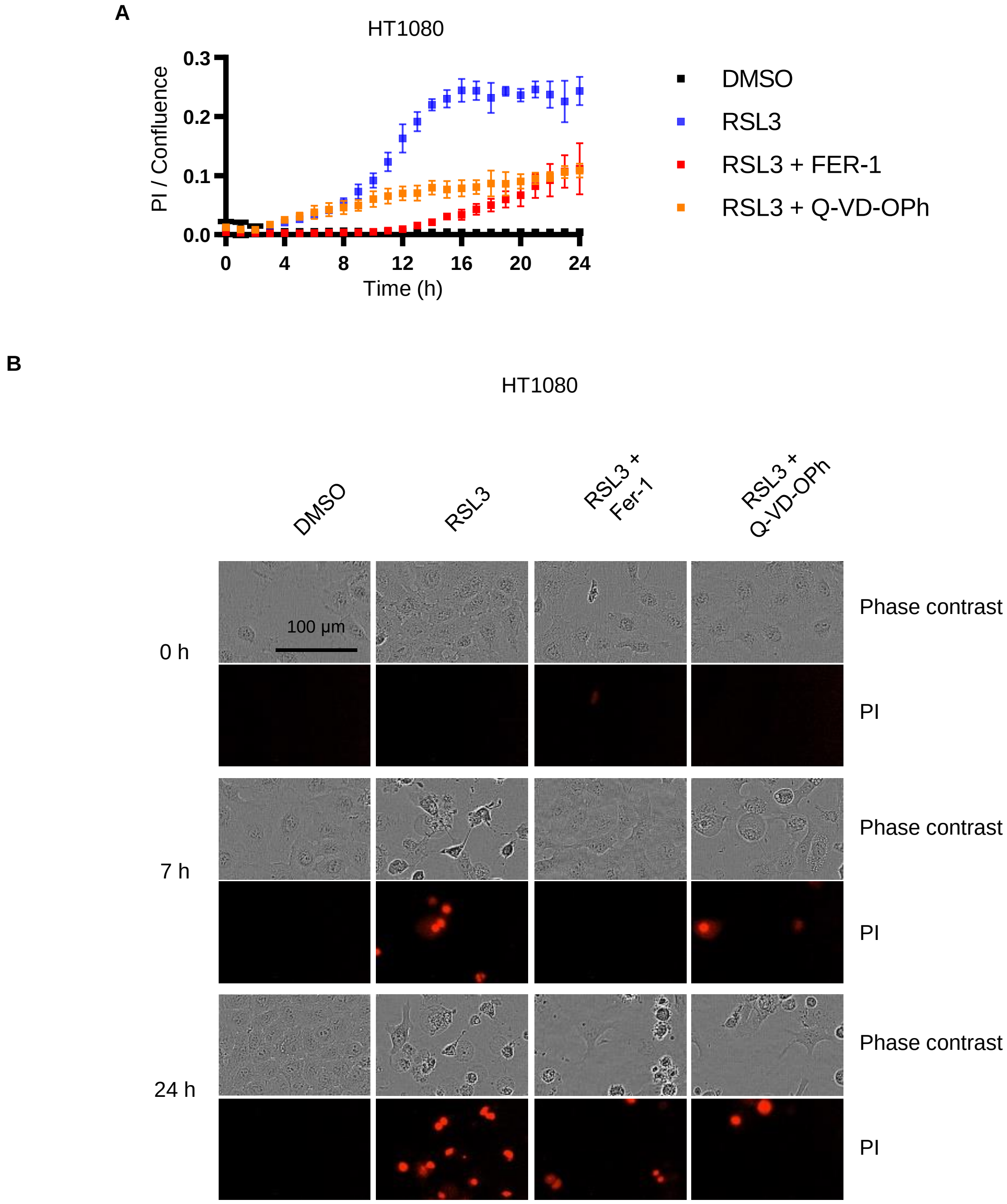

Figure 54: Ferrostatin-1 and Q-VD-Oph partially and sequentially protect HT1080 cells from RSL3 treatment

*(**A**) Merged kinetic traces from the experiment in figure 51 and 53. (**B**) Representative micrographs of phase contrast and red fluorescence images taken with an IncuCyte system at time points 0 h; 7 h and 24 h for the indicated conditions.*

Following the kinetic of ferrostatin-1 treatment it emerged that its protective effect against RSL3-induced death started to decrease approximately when the Q-VD-Oph mitigating effect commenced. The same time point also corresponded to the beginning of the swift cell death increase upon RSL3 single treatment, with a steep curve between 10 and 14 hours before the plateau phase. Therefore, two RSL3-induced death phases could be distinguished: a first slow phase lasting 8 hours that depended on lipid ROS production and that was indeed inhibited by ferrostatin-1. The second one was instead a rapid caspase-depended phase that culminated with maximal cell death at 14-16 h and continued with a plateau in which Q-VD-Oph still exerted its partial protecting effect. While the nature of the first phase seemed clearer, as it could be fully prevented by ferrostatin-1 and no effect was exerted by Q-VD-Oph, pointing to a fully ferroptotic mechanism of death, the second phase remained more elusive as both inhibitors only partially protected the cells from RSL3-induced death. This suggested a mixed mechanism of death that required further investigation. The results of such investigation are not reported in this thesis but in the master thesis by J. Sieger that the author has co-supervised [539]. It is only relevant to highlight here that the biphasic RSL3-induced death is a result obtained with a specific concentration of RSL3 (4.5 µM) and it could not be reproduced at lower concentrations, as shown in *figure 55* where upon 2.25 µM of RSL3 no caspase-dependent death occurred and ferrostatin-1 provided full protection at all the time points tested.

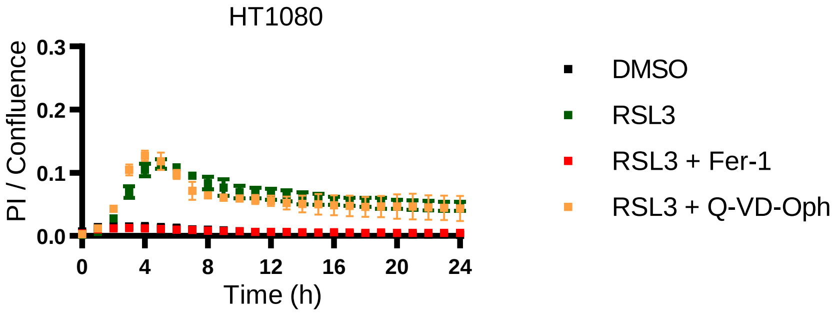

Figure 55: ROS scavenging fully protects HT1080 cells from a low dose of RSL3

HT1080 cells were seeded at a density of 10^4 cells/well in a 96 well plate 24 h prior to the experiment and then treated in presence of PI for 24 h. Treatments included 2.25 µM of RSL3 alone or in combination with either 2 µM of Fer-1 or 50 µM of Q-VD-Oph (30 minutes of pre-exposure). PI positive area over confluence was quantified from micrographs recorded by an IncuCyte system at intervals of 1 h for 24 h. Data are presented as mean ± SD of three technical replicates. Similar results were obtained in independent repeat experiments.

5.3 Ferroptosis induction in the U-87 MG GBM cell line is antagonised by BH3 mimetics

Since its discovery, ferroptosis has always been described as distinct form of death with a different execution pathway compared to that of apoptosis [540]. Still, in this work, a typical apoptosis feature, that is caspase activation, has been found to occur upon a ferroptotic stimulus. Also, the combination of ferroptosis inducers with Bcl-2 family antagonists, had the effect of mitigating cell death induction, indicating a complex interplay between the ferroptosis and the apoptosis pathway. The intricated findings of the previous paragraphs had to be validated in different cell lines in order to formulate a more generalised hypothesis on how ferroptosis can be related to apoptosis and specifically to players of its intrinsic branch. This is of particular importance in the case of glioblastoma, against which very limited approved compounds are available and exploring the role of ferroptosis could pave the way to increase the number of therapeutic options.

Here, the U-87 MG human glioma cell line was used as a model to investigate the sensitivity of glioblastoma cells to ferroptosis induction. In particular, the response of this cell line to the ferroptosis inducer RSL3 was systematically studied. To determine the magnitude of the response to RSL3, U-87 MG cells were exposed to increasing concentrations of the drug up to 4.5 μM. By using the IncuCyte system, pictures of PI-stained cells were captured for 24 hours at intervals of 1 hour and a quantitative analysis of the recorded images was performed as already described in order to obtain kinetic data (*figure 56*). Morphological observations revealed that cell swelling, a typical feature of ferroptotic cell death, occurred already after 4 hours of treatment (*figure 56B*). The dose-response curve plotted in *figure 56A* showed a positive correlation between the amount of drug applied and the increase of PI to confluence ratio. Of note, a plateau phase was reached following 8 hours of treatment and no further increase in cell death was detectable after this time point upon any of the RSL3 concentrations applied (*figure 56A*).

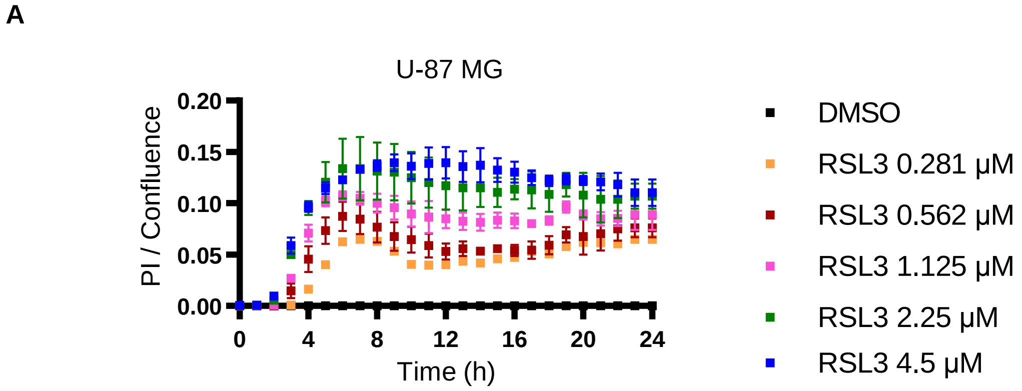

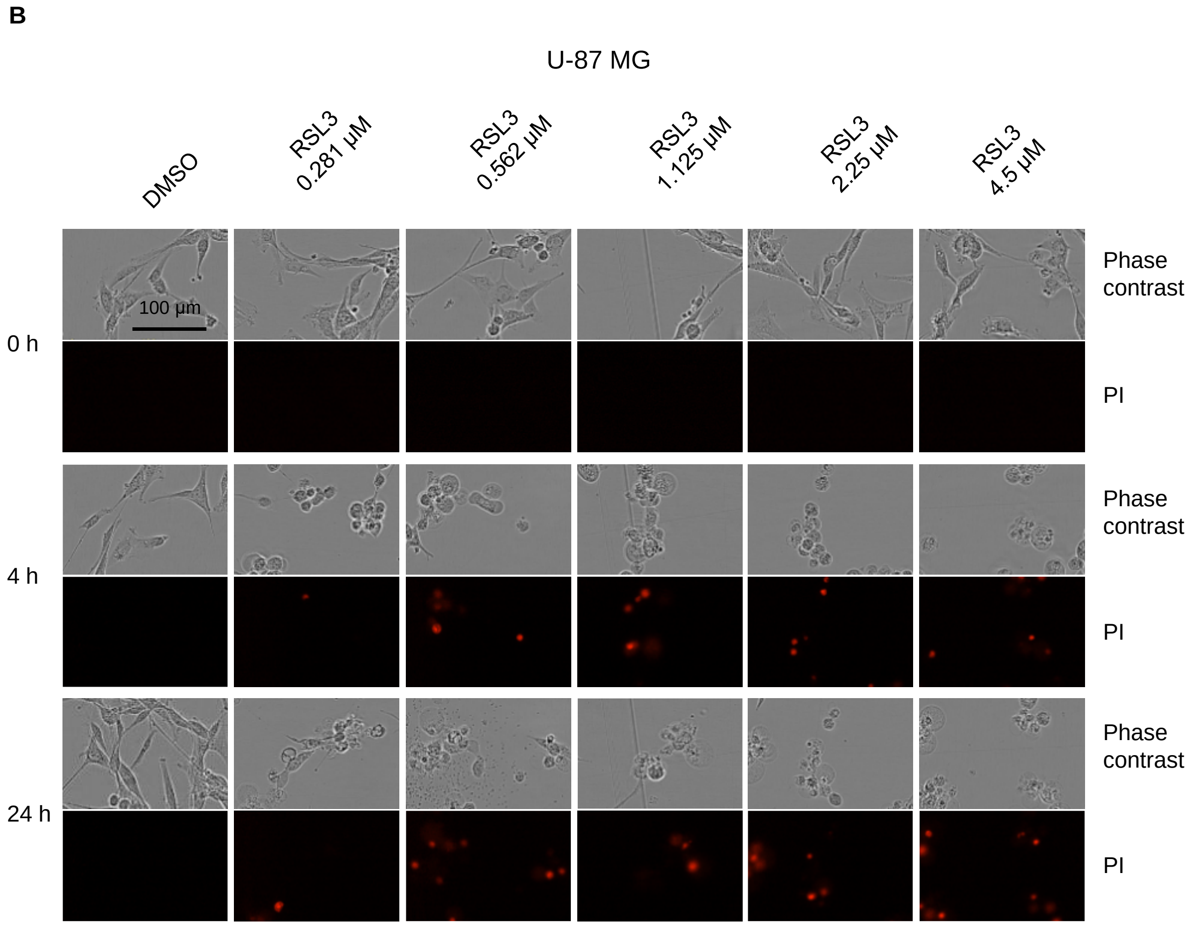

Figure 56: RSL3 induces death in U-87 MG cells in a dose-dependent manner

U-87 MG cells were seeded at a density of 10^4 cells/well in a 96 well plate 24 h prior to the experiment and then treated for 24 h with the indicated concentrations of RSL3 in presence of PI. ***(A)*** *Quantification of death kinetics calculated as PI positive area over confluence based on IncuCyte-recorded images taken at intervals of 1 h for 24 h.* ***(B)*** *Phase contrast and red fluorescence images taken at time point 0 h; 4 h and 24 h. Data are presented as mean ± SD of three technical replicates. Representative example of one out of three independent experiments. This experiment was conducted together with Karen Kresbach.*

Either the ROS-scavenger ferrostatin-1 or the caspases inhibitor Q-VD-Oph were added to RSL3 to determine if a purely and classical ferroptotic death was induced or if caspases were involved in the death mechanism as reported for HT1080 cells in the previous paragraph. To test that, the IncuCyte system was used: it was shown that ferrostatin-1 fully prevented cell death while Q-VD-Oph did not (*figure 57).*

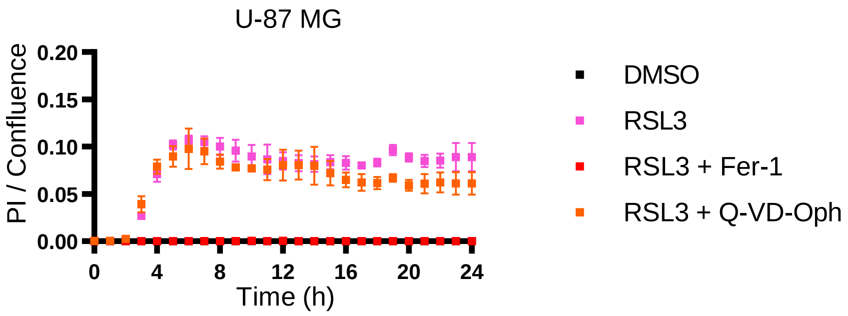

Figure 57: ROS scavenging but not caspases inhibition protects U-87 MG cells from RSL3-induced death

U-87 MG cells were seeded at a density of 10^4 cells/well in a 96 well plate 24 h prior to the experiment and then treated for 24 h in presence of PI. Treatments included 1.125 µM of RSL3 alone or in combination with either 2 µM of Fer-1 or 50 µM of Q-VD-Oph (30 minutes of pre-exposure). The PI positive area over confluence was calculated from images recorded by the IncuCyte system at intervals of 1 h for 24 h. Data are presented as mean ± SD of three technical replicates. Representative example of 1 out of 3 independent experiments. This experiment was conducted by Karen Kresbach under the author's supervision.

To rule out that the lack of caspase activity in response to RSL3 was due to a general incompetence to execute apoptosis, U-87 MG cells were stimulated with typical apoptosis inducers, specifically the combination of IZI1551 (TRAIL) and bortezomib. It was proven that, upon this combination treatment, apoptosis occurred as indeed Q-VD-Oph, but not ferrostatin-1, exerted a protective effect (*figure 58*). These results indicated that, even though U-87 MG cells are able to activate caspases, these are not involved in RSL3-induced death.

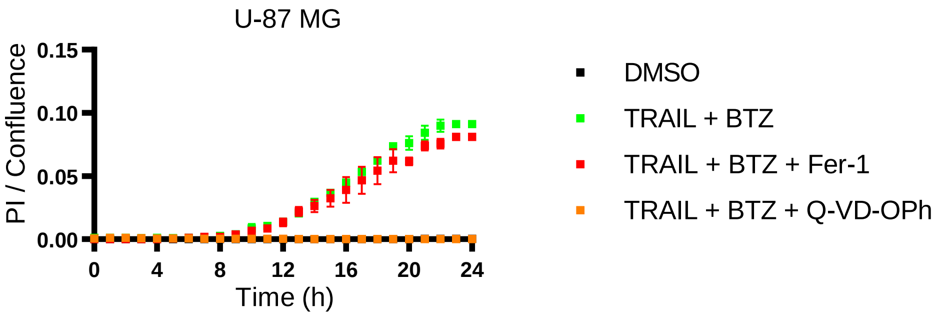

Figure 58: U-87 MG cells are competent to execute apoptosis

U-87 MG cells were seeded at a density of 10^4 cells/well in a 96 well plate 24 h prior to the experiment and then treated for 24 h with the combination of 3 µM of IZI1551 (TRAIL) and 250 ng/ml of BTZ in presence of PI. Either 2 µM of Fer-1 or 50 µM of Q-VD-Oph (30 minutes of pre-treatment) were added to the combination treatment. PI positive area over confluence was quantified from micrographs recorded by the IncuCyte system at intervals of 1 h for 24 h. Data are presented as mean ± SD of three technical replicates. Representative example of one out of three independent experiments is shown. This experiment was conducted by Karen Kresbach under the author's supervision.

With RSL3 inducing ferroptosis in U-87 MG cells, the crosstalk between ferroptotic stress and intrinsic apoptosis was next studied. It was hypothesised that antagonising anti-apoptotic Bcl-

2 family proteins could serve as a tool to fine-tune RSL3-induced death. In view of the preliminary results gathered on HT1080 cells and presented in the beginning of this chapter, it was first investigated how a ferroptosis inducer and BH3 mimetics relate to each other in terms of cell death induction. Following, the nature of the stress induced by this combination treatment was studied in order to gain a better understating of how ferroptosis execution interacts with key players of other death pathways.

Based on micrographs captured by the IncuCyte system, the death kinetic of the combination treatment with RSL3 and increasing doses of the Bcl-2 antagonist ABT-199 was quantified (*figure 59A*) and the changing morphology of U-87 MG cells was documented (*figure 59B*). This analysis revealed that ABT-199, even at high dose (10 µM), was not toxic to U-87 MG cells. Interestingly, the addition of ABT-199 partially protected the cells from RSL3-induced cell death. Death onset for the different combination treatments was the same as for RSL3 single agent and determined to be at 4 hours. After this time point, the increasing ABT-199 doses lowered the toxicity of RSL3 in a dose-dependent manner (*figure 59A*).

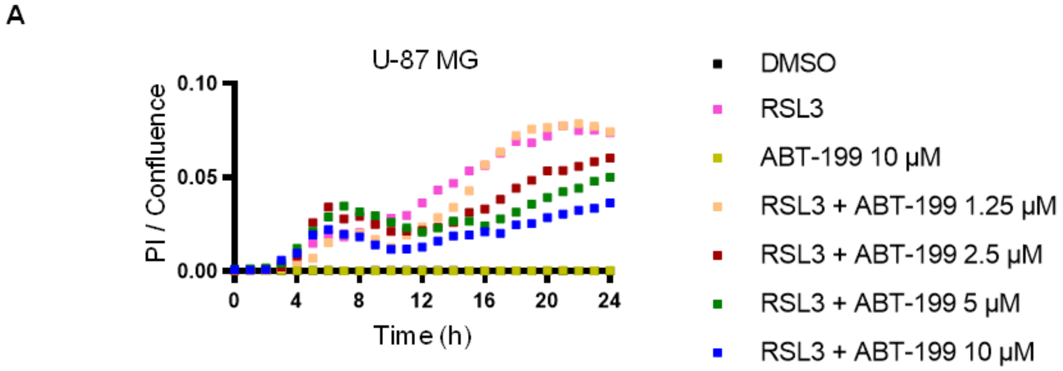

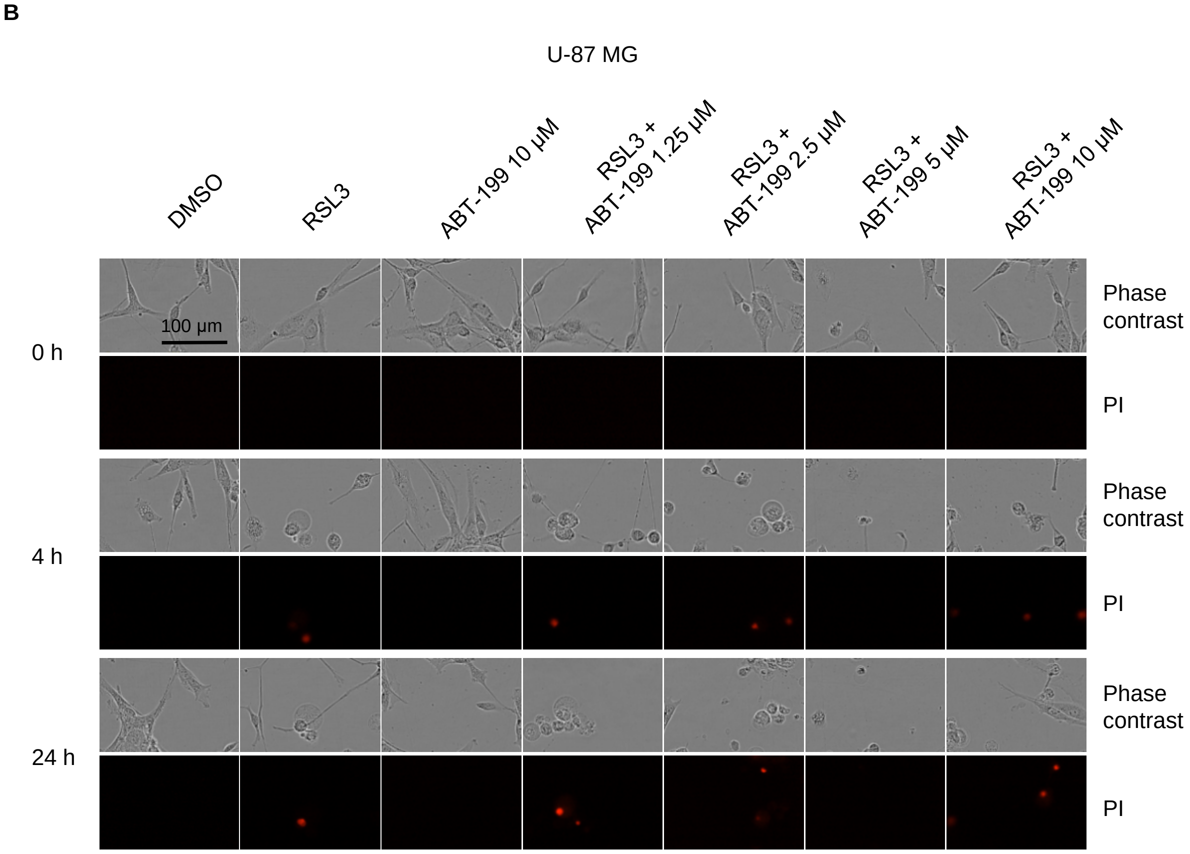

Figure 59: ABT-199 protects U-87 MG cells from RSL3 lethality in a dose-dependent manner

U-87 MG cells were seeded at a density of 10^4 cells/well in a 96 well plate 24 h prior to the experiment and then treated for 24 h in presence of PI with 1.125 µM of RSL3, or 10 µM of ABT-199, or with the combination of 1.125 µM of RSL3 plus 1.25 µM; 2.5 µM; 5 µM or 10 µM of ABT-199. ***(A)*** *Quantification of PI positive area over confluence calculated from images recorded by the IncuCyte system at intervals of 1 h for 24 h.* ***(B)*** *Phase contrast and red fluorescence images were taken at time point 0 h; 4 h and 24 h. Data are presented as mean of three technical replicates. Error bars were omitted for clarity of visualisation. Representative example of one out of three independent experiments. This experiment was conducted by Karen Kresbach under the author's supervision.*

To determine if ABT-199 altered the death mechanism induced by RSL3, either ferrostatin-1 or Q-VD-Oph were added to the combination treatment and the increase of PI covered area was monitored with the IncuCyte system for 24 hours (*figure 60*). It was shown that while ferrostatin-1 rescued all the cells, caspase inhibition did not affect the amount of cell death occurring upon combination treatment with RSL3 and ABT-199. This proved that, even though the inhibition of Bcl-2 partially protected the cells from the cytotoxicity of RSL3, this did not change the mechanism of cell death that remained purely ferroptotic.

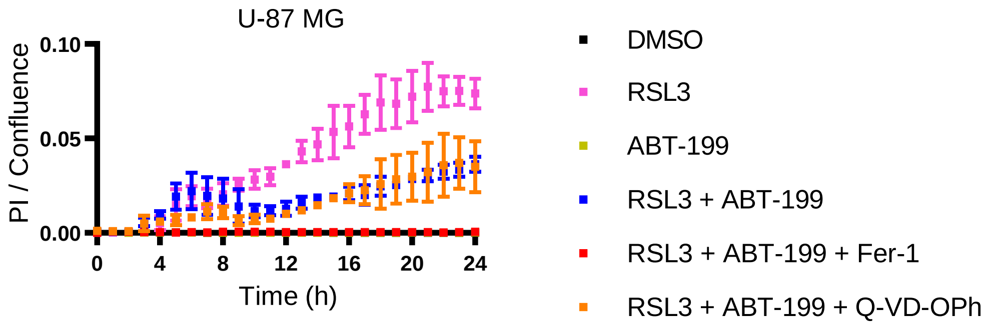

Figure 60: Antagonising Bcl-2 does not alter the ferroptotic nature of RSL3-induced death in U-87 MG cells

U-87 MG cells were seeded at a density of 10^4 cells/well in a 96 well plate 24 h prior to the experiment and then treated for 24 h with 1.125 µM of RSL3, or 10 µM of ABT-199 or the combination thereof in presence of PI. Either 2 µM of Fer-1 or 50 µM of Q-VD-Oph (30 minutes of pre-treatment) were added to the combination treatment. PI positive area over confluence was quantified from micrographs recorded by the IncuCyte system at intervals of 1 h for 24 h. Data are presented as mean ± SD of three technical replicates. Representative example of one out of three independent experiments is shown. This experiment was conducted by Karen Kresbach under the author's supervision.

It was next tested if antagonising Mcl-1 would lead to similar results. Therefore, the same RSL3 dose that was used in the previous experiment was combined with increasing concentrations of the Mcl-1 inhibitor S63845. PI to confluence ratio was calculate from IncuCyte recorded images (*figure 61A*) and representative micrographs are shown in *figure 61B*. A high dose of S63845 (10 µM) had no effect on U-87 MG cells while its combination with RSL3 decreased the amount of cell death compared to the treatment with RSL3 alone. The protective effect was enhanced with higher S63845 concentrations, until reaching full protection at the highest dose tested. This showed that Mcl-1 inhibition, like Bcl-2 inhibition, can mitigate ferroptosis triggered by RSL3.

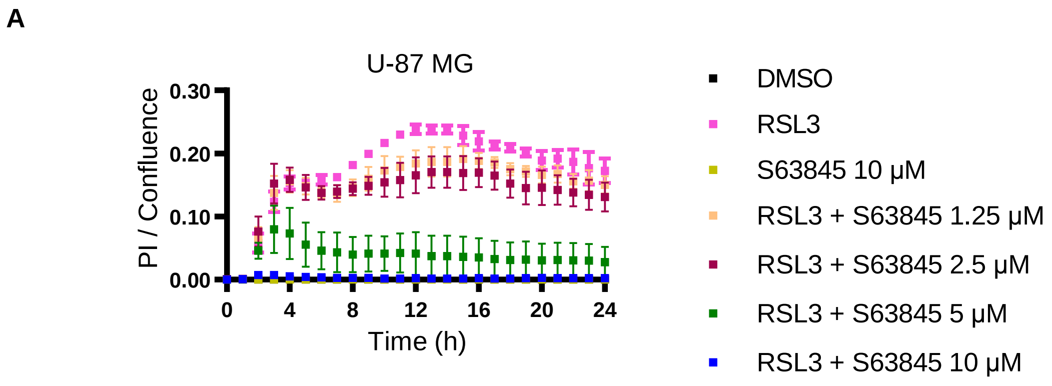

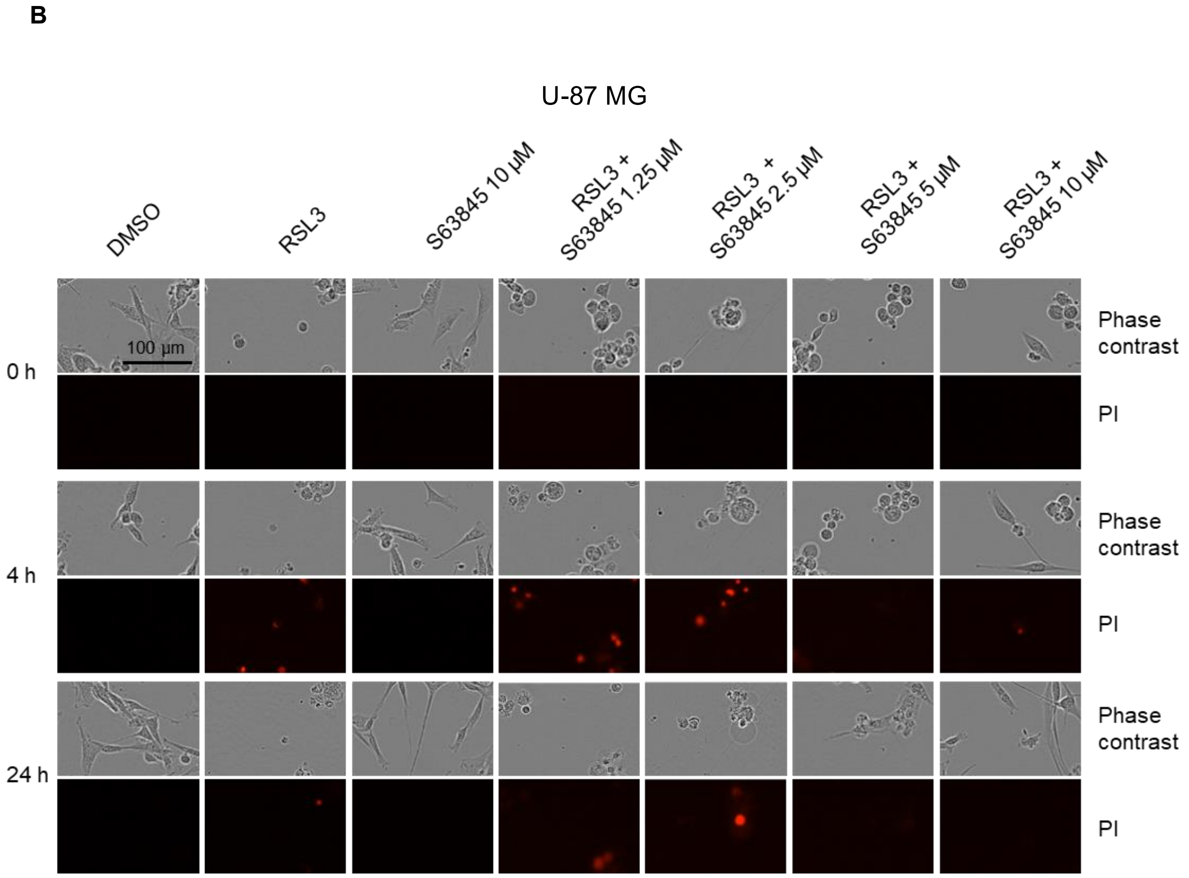

Figure 61: S63845 protects U-87 MG cells from RSL3 lethality in a dose-dependent manner

U-87 MG cells were seeded at a density of 10^4 cells/well in a 96 well plate 24 h prior to the experiment and then treated for 24 h in presence of PI with 1.125 µM of RSL3, or 10 µM of S63845, or with the combination of 1.125 µM of RSL3 plus 1.25 µM; 2.5 µM; 5 µM or 10 µM of S63845. ***(A)*** *Quantification of PI positive area over confluence calculated from images recorded by the IncuCyte system at intervals of 1 h for 24 h.* ***(B)*** *Phase contrast and red fluorescence images were taken at time point 0 h; 4 h and 24 h. Data are presented as mean ± SD of three technical replicates. Representative example of one out of three independent experiments is shown. This experiment was conducted by Karen Kresbach under the author's supervision.*

To find out if the cell death mechanism induced by the combination of RSL3 and S63845 was still that of ferroptosis, an apoptosis or a ferroptosis inhibitor were employed and the cell death kinetic was monitored with the IncuCyte (*figure 62*). Similar to the effect observed in RSL3+ABT-199 co-treated cells, Q-VD-Oph provided no (or barely detectable) protection from RSL3+S63845 treatment, while ferrostatin-1 fully saved the cells.

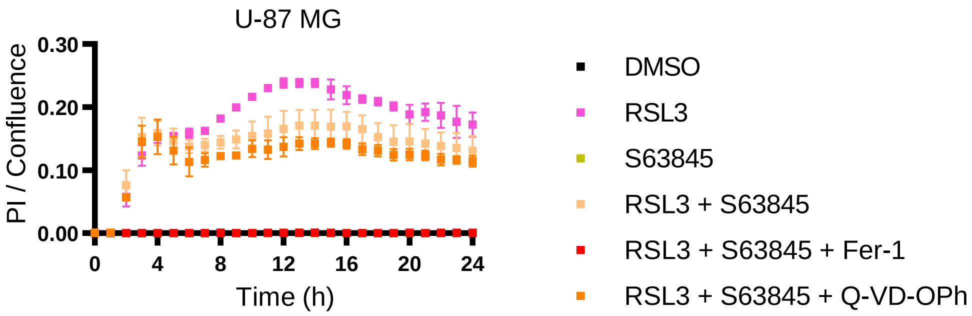

Figure 62: Antagonising Mcl-1 does not alter the ferroptotic nature of RSL3-induced death in U-87 MG cells

U-87 MG cells were seeded at a density of 10^4 *cells/well in a 96 well plate 24 h prior to the experiment and then treated for 24 h with 1.125 µM of RSL3, or 10 µM of S63845 or the combination thereof in presence of PI. Either 2 µM of Fer-1 or 50 µM of Q-VD-Oph (30 minutes of pre-treatment) were added to the combination treatment. PI positive area over confluence was quantified from micrographs recorded by an IncuCyte system at intervals of 1 h for 24 h. Data are presented as mean ± SD of three technical replicates. Representative example of one out of three independent experiments is shown. This experiment was conducted by Karen Kresbach under the author's supervision.*

Finally, also the effect of Bcl-xL inhibition on RSL3-treated cells was tested with the IncuCyte system (*figure 63*). U-87 MG cells appeared to be totally resistant to antagonists of the Bcl-2 family of anti-apoptotic proteins as 10 µM of the Bcl-xL inhibitor WEHI-539, similarly to the inhibitors of Bcl-2 and Mcl-1, induced no cell death (*figure 63B*). When exposing these cells to increasing concentrations of WEHI-539 in presence of a lethal dose of RSL3 (1.125 µM), the calculation of the PI to confluence ratio revealed a dose-dependent decrease of cell death. Furthermore, the addition of WEHI-539 slowed down death onset compared to RSL3 treatment alone (*figure 63A*).

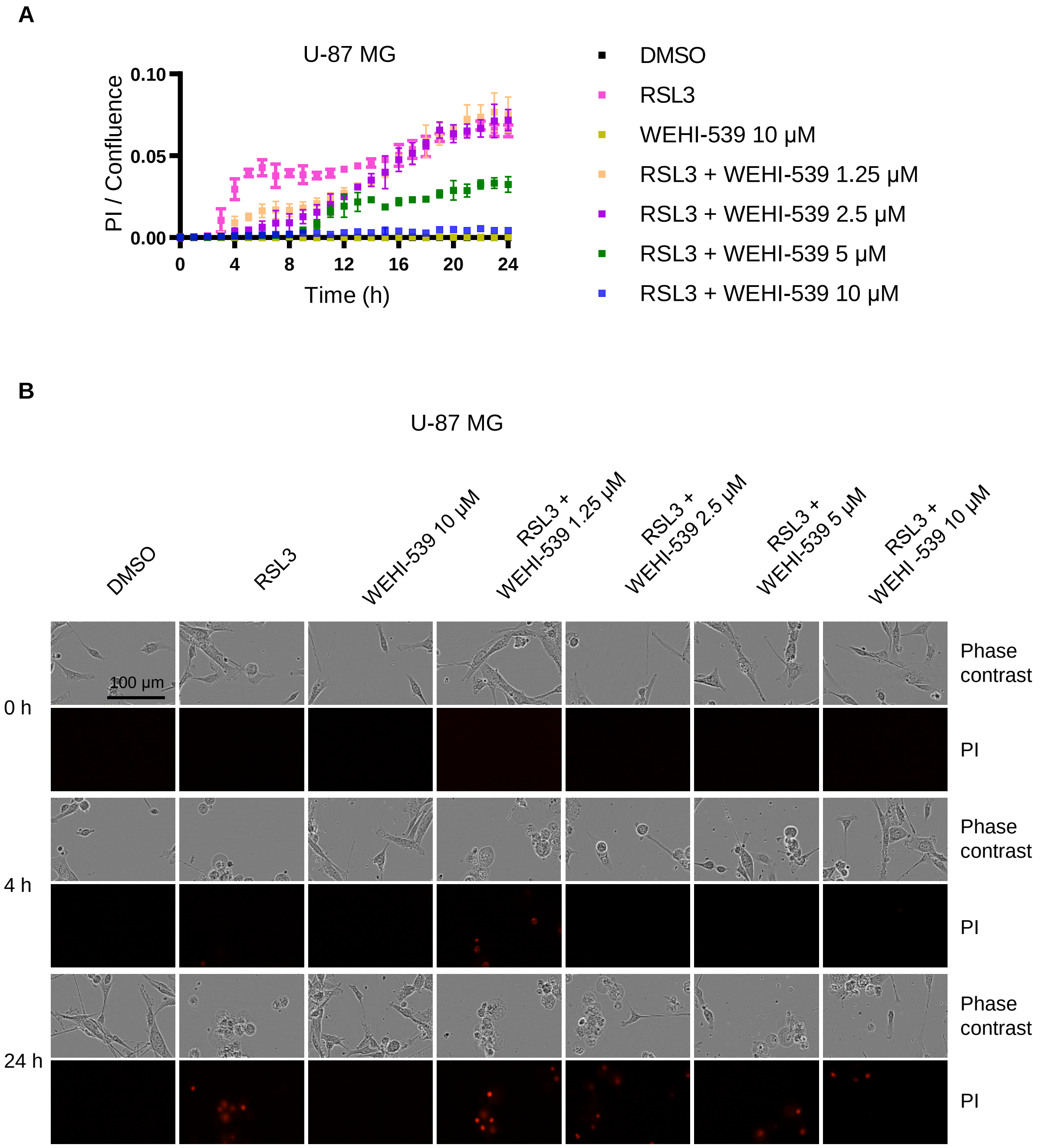

Figure 63: WEHI-539 protects U-87 MG cells from RSL3 lethality in a dose-dependent manner

U-87 MG cells were seeded at a density of 10^4 cells/well in a 96 well plate 24 h prior to the experiment and then treated for 24 h in presence of PI with 1.125 µM of RSL3, or 10 µM of WEHI-539, or with the combination of 1.125 µM of RSL3 plus 1.25 µM; 2.5 µM; 5 µM or 10 µM of WEHI-539. ***(A)*** *Quantification of PI positive area over confluence calculated from images recorded by the IncuCyte system at intervals of 1 h for 24 h****. (B)*** *Phase contrast and red fluorescence images taken at time point 0 h; 4 h and 24 h. Data are presented as mean ± SD of three technical replicates. Representative example of one out of three independent experiments is shown. This experiment was conducted by Karen Kresbach under the author's supervision.*

In presence of ferrostatin-1, the remaining cell death after the mitigating effect of WEHI-539 on RSL3-treated cells was fully abolished until the latest time point recorded (24 hours).

Interestingly, caspase inhibition partially rescued RSL3+WEHI-539-treated cells after approximately 12 hours of combination treatment (*figure 64*).

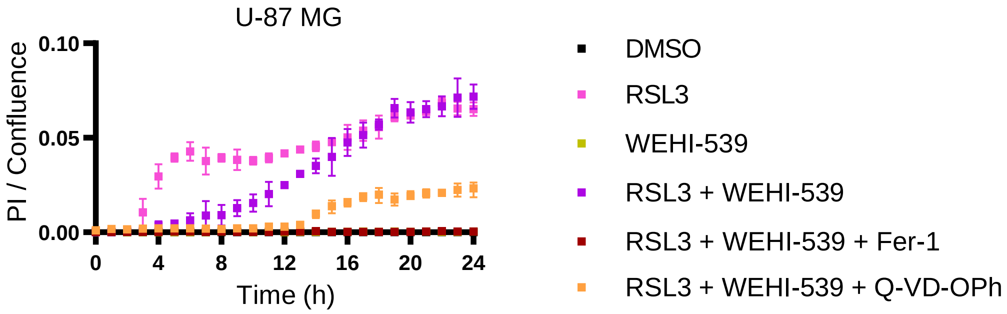

Figure 64: Ferrostatin-1 fully protects and Q-VD-Oph partially rescues RSL3+WEHI-539-induced cell death in U-87 MG cells

U-87 MG cells were seeded at a density of 10^4 *cells/well in a 96 well plate 24 h prior to the experiment and then treated for 24 h with 1.125 µM of RSL3, or 2.5 µM of WEHI-539 or the combination thereof in presence of PI. Either 2 µM of Fer-1 or 50 µM of Q-VD-Oph (30 minutes of pre-treatment) were added to the combination treatment. PI positive area over confluence was quantified from micrographs recorded by an IncuCyte system at intervals of 1 h for 24 h. Data are presented as mean ± SD of three technical replicates. Representative example of one out of three independent experiments is shown. This experiment was conducted by Karen Kresbach under the author's supervision.*

Taken together, the results shown here proved that the U-87 MG cell line is a valid model for studying ferroptosis in glioblastoma. The general antagonistic relationship between ferroptosis inducers and inhibitors of the anti-apoptotic Bcl-2 family proteins reported in HT1080 cells was confirmed also in this cell line. These results highlight the need to further study how ferroptosis induction could be modulated in GBM cells.

Discussion

1. The combination of hexavalent TRAIL-R agonist with a 2nd generation proteasome inhibitor induces apoptosis in optimised GBM pre-clinical models

Pre-clinical research on cancer therapeutics should guarantee a sufficient probability of success in clinical trials. However, although many candidate drugs show great promise at the *in vitro* stage, the majority of them fail in the early phases of clinical studies [541]. One of the reasons for such disappointing results can be found in inappropriate pre-clinical models. In general, long-term *in vitro* culturing of cell lines applies a selective pressure that leads to a genetic drift, with alterations of both genotype and phenotype that undermine the reliability of these cells to model the original tumours [105,106,542]. The inability of over-passaged cell lines to recapitulate the source material of their origin has been documented for several cancer models and led to the establishment of improved culturing routines in the most recent and clinically relevant studies [112,543,544].

Glioblastoma is a highly resistant tumour with very limited treatment options [545]. In order to identify new therapeutic strategies, cell-based models with improved predictive power are particularly urgent in this type of cancer. In this work, three main limitations of glioblastoma *in vitro* models have been addressed. To represent the tumour heterogeneity among different patients that many studies don't account for, here a panel of seven patient samples, from both primary and recurrent glioblastoma cases and comprising the most typical alterations found in this type of cancer, have been analysed (*table 3*) [12]. Secondly, as general evidence exists that limited subculturing better mimics the characteristics of the tumour of origin, the cells used here were of a low passage number (P< 25) [546]. Moreover, their morphologies were documented since the beginning of their cultivation and kept on being monitored throughout the project (*figure 14*). Thirdly, rather than immortalised cell lines maintained in serum-supplemented medium, that is known to have pro-differentiating properties, here primary cultures have been adopted [37,125]. These were kept in serum-free, bFGF and EGF-supplemented medium, in order to preserve their cancer stem-like properties [112,547].

In this work, the inconsistent drug responsiveness between glioblastoma cells at low and high passage numbers has been confirmed. More precisely, upon escalating doses of the hexavalent TRAIL-R agonist IZI1551, glioblastoma cells derived from a primary tumour case that were sub-cultured less than twenty times displayed no response. In contrast, culturing these cells for more than thirty passages resulted in a dose-dependent cell death induction (*figure 15*). Such an altered drug responsiveness of long-term glioma cultures has already been reported by Garcia-Romero and colleagues, who have compared early and late passages of CSC-enriched cultures for their sensitivity to a variety of clinical and pre-clinical drugs [546]. In the case of IZI1551, the reasons for this phenomenon might be multiple, but one hypothesis is that long-term cultures are subjected to a selection that favours high TRAIL receptor-expressing cells and that these are eventually more sensitive to IZI1551-induced apoptosis. Several reports exist on the pro-survival functions engaged by the TRAIL/TRAIL-R signalling, justifying the frequent upregulation of TRAIL receptors in cancer cells [235,548–550]. Importantly, S. Von Karstedt and colleagues have demonstrated a role of TRAIL-R2 in mediating cell migration via its MPD (membrane-proximal domain). They also reported that, blocking the endogenous TRAIL/TRAIL-R interaction, reduced the activation of Rac1 kinase and delayed tumour growth of NSCLC cell lines with an oncogenic KRAS mutation [264]. Therefore, cancer cells might display high amounts of TRAIL receptors to benefit from the pro-proliferative stimulation by endogenous TRAIL. These findings require validations in the settings of the PDCLs panel here examined and could be the subject of a follow-up study.

TRAIL has been identified as a promising cancer therapeutic as it triggers apoptosis independently of the p53 status of a cancer cell and is very well tolerated by healthy tissues [164,239]. To exploit its potential, several TRAIL formats, as well as TRAIL-inducing compounds such as ONC201, have been designed to enter clinical trials [551]. ONC201 is a small molecule that induces the expression of both TRAIL and DR5 and is being tested for the treatment of recurrent glioblastoma (NCT02525692). Among the TRAIL formats, Eftozanermin alfa (ABBV-621) is a hexavalent agonistic fusion protein that recently entered clinical trials for the treatment of hematologic cancers and its structure is very similar to that of IZI1551 [552] (NCT03082209). IZI1551 is a TRAIL-R agonist designed on the scTRAIL format but with the addition of an Fc region as a dimerization module. The resulting fusion protein has an increased size and consequently improved pharmacokinetic properties (14.5 hours of terminal half-life compared to 2.2 hours of scTRAIL), as well as a better stability that augments its capacity to engage and cluster its cognate receptors [254]. Despite these properties, all the glioblastoma PDCLs of the analysed representative panel were largely resistant to IZI1551 as a single agent (*figure 16*), confirming a general trend of glioma cells to poorly respond to TRAIL treatment [257,553]. To overcome such resistance, TRAIL is usually combined with sensitiser drugs that can re-establish the apoptosis susceptibility of cancer cells [257,262].

Among the most promising anti-glioma drugs are proteasome inhibitors [554]. Pharmacological profiling of 100 genetically characterised patient-derived glioblastoma cell cultures established that these cells, that are proven to recapitulate the known molecular heterogeneity of this tumor, are primarily grouped by their sensitivity to proteasome inhibitors, and only secondarily by response to other classes of drugs [555]. Moreover, compared to their differentiated counterparts, glioma stem cells appeared to be particularly sensitive to inhibition of the protein degradation pathway [556,557].

Marizomib is a novel-generation proteasome inhibitor approved by the FDA for the treatment of multiple myeloma, in which it showed higher cytotoxicity compared to the first-generation proteasome inhibitor bortezomib [371]. It has also been shown that marizomib as a single agent effectively reduced the viability of immortalised glioblastoma cell lines at nanomolar doses [375]. In the glioblastoma panel analysed here instead, marizomib exerted no significant effect on the viability of PDCLs, that represent a better model to predict patient's responsiveness (*figure 16*). Mechanisms of resistance to marizomib have been investigated by D. Niewerth and colleagues, who have identified an A49V point mutation in the β-subunit of the 20S proteasome as its major determinant [361]. This indeed, would reduce the affinity of marizomib for the proteasome and it could also explain the lack of responsiveness of the glioblastoma panel examined here. Remarkably, the combination of marizomib and IZI1551 substantially reduced the viability of five out of seven PDCLs, with different escalating doses determining a decreased viability ranging from 15% to 90%. This result highlighted the need for combination therapies that, thanks to the potential of triggering synergistic responses, are now an established strategy to treat glioblastoma [558]. Of note, according to their sensitivity to the combination treatment, the PDCLs of the panel studied here could be sub-grouped into a class of sensitive cells and a class of resistant ones. This is consistent with the knowledge that serum-free PDCLs cultures maintain patient-specific traits and inter-tumour heterogeneity, also in terms of drug sensitivity. Overall, such finding validated this kind of cultures as an improved model for anti-cancer drugs screening [559,560].

Activators of death receptors such as TRAIL are long known to synergize with proteasome inhibitors to induce apoptosis [561]. Here, it was shown that IZI1551 and marizomib interacted synergistically to reduce the viability of the five responsive glioblastoma PDCLs (figure 17). As proteasome inhibitors do not act through a single mechanism but they affect multiple cellular pathways, the synergy between this class of drugs and TRAIL cannot be attributed to the alteration of a single protein or process. Specifically, examples of mechanisms explaining the synergy comprise: suppression of NF-κB pro-survival signalling by IκBα stabilization, accumulation of death receptors, suppression of IAP-mediated degradation of Smac and caspases, stabilisation of otherwise short-lived pro-apoptotic proteins and/or convergence of extrinsic and intrinsic apoptosis branches at the level of mitochondria [256,317,562,563]. The synergistic interactions between these two classes of drugs have been reported in both glioblastoma immortalized cell lines and primary cells. For example, the proteasome inhibitors MG132 and epoxomicin could re-activate apoptosis in TRAIL-resistant U343 and U373 cell lines thanks to an enhanced transcription and surface expression of DR5 [564]. Furthermore, the proteasome inhibitor bortezomib has been shown to be capable of potentiating TRAIL-induced apoptosis in a panel of otherwise TRAIL-resistant glioblastoma cell lines via blocking of the p65-NF-κB DNA-binding activity [565]. Also another boronic acid peptide, namely the proteasome inhibitor PS-341, has been shown to enhance TRAIL-induced apoptosis in glioblastoma cell lines [306]. Importantly, T. Unterkircher and colleagues reported that bortezomib and TRAIL synergistically induced apoptosis in clinically relevant glioblastoma models such as PDCLs, CD133 and Nestin positive cells, as well as in *semi-in vivo* conditions of tumours grown on a chorioallantoic membrane (CAM) model. Moreover, they identified the stabilisation of tBID in the cytosol as a key event responsible for the synergy [395]. In other studies, different mechanisms have been identified to determine the synergy between TRAIL and proteasome inhibitors. In particular, proteasome inhibitors have been reported to block NF-κB activity by stabilising its repressor IκBα. This results in the blockage of pro-survival NF-κB signalling branches that can be triggered by death receptor activation, determining the synergistic lethality between proteasome inhibitors and TRAIL [228,566]. On the contrary, a peculiarity of glioblastoma is that, in these cells, the NF-κB signalling does not seem to have a prominent pro-survival function. In fact, there are studies showing that the DNA-binding activity of NF-κB appeared modest in glioblastoma cell lines compared to other cancer types. Consistently, K. La Ferla-Brühl and colleagues found that inhibiting NF-κB via overexpression of its super-repressor IκBα neither enhanced spontaneous apoptosis nor TRAIL-induced apoptosis of glioblastoma cells [393]. More recently, it was also reported that, in glioblastoma cells, NF-κB might actually have a pro-apoptotic function in TRAIL-induced death. This is seemingly due to its effect in facilitating DISC formation, as proven by a decreased TRAIL-R2 redistribution into lipid rafts upon IκBα overexpression [567]. This concept is not completely new as S. Karl and colleagues from the laboratory of S. Fulda have reported that, in glioblastoma cell lines, a pulse exposure to DNA-damaging anticancer drugs, such as Temozolomide and Doxorubicin, led to NF-κB activation. Importantly, they also showed that, in these settings, NF-κB exerted a pro-apoptotic function during the recovery phase from the initial formation of DNA breaks. The mechanism behind such effect remains obscure but it is attributable to a still unclear role of NF-κB in regulating DNA damage and repair in glioblastoma cells [568]. Overall, it can be concluded that, depending on the specific cell type, NF-κB activation can result in pro- or anti-apoptotic responses. For this reason, in other cancer types, proteasome inhibitor-induced blockage of NF-κB pro-survival activity can account for the synergistic apoptosis induction upon co-treatment with TRAIL. Instead, this might not be the case in glioblastoma, as NF-κB seems to have a pro-death rather than a pro-survival function.

The therapeutic efficacy of a drug can be evaluated based on its effect on cell viability, proliferation, or death. Here, the effect of IZI1551 and marizomib combination treatments has been assessed *via* a cell viability assay based on the NAD(P)H-dependent reduction of the

WST-1 tetrazolium salt into its formazan dye (*figure 16*). As NAD(P)H is generated during the glycolytic reactions occurring in metabolically active cells, the amount of formazan dye produced, quantified with a spectrophotometer, is an indirect indicator of the number of viable cells. As such, the colorimetric assay allowed to easily retrieve high-throughput data like the effectiveness of a 5x5 combination matrix of drug doses. However, viability assays do not distinguish between cytotoxicity, cytostasis and slow growth rates, as a low viability readout can be due to the presence of dead cells, or of healthy but metabolically inactive (or less active) cells [569]. For this reason, it was necessary to verify whether the reduced viability measured *via* the WST-1 assay was due to an actual cytotoxic effect of the treatments. Therefore, in a representative responsive cell line and for the same dose combination matrix, cell death was determined flow cytometrically as number of cells stained with GFP-conjugated Annexin V and with PI. These measurements were then compared with the decreased viability assessed *via* the WST-1 assay. As loss in viability indeed correlated with cell death, it could be concluded that IZI1551+MRZ have a cytotoxic effect at all the concentrations tested (*figure 18*).

While proteasome inhibition is known for inducing mostly intrinsic apoptosis, the engagement of death receptors might result in the induction of extrinsic apoptosis as well as of necroptosis [145,277,303,570]. To characterise the cell death mechanism underlying the toxicity of the IZI1551+MRZ combination, Annexin V-GFP/PI-based flow cytometry measurements were performed on cells treated in presence or absence of Q-VD-Oph. As caspase inhibition entirely rescued the cells, it was concluded that the IZI1551+MRZ combination induced apoptosis with no alternative cell death mechanism being involved (*figure 19*). Consistently, proteasome inhibition is actually known to impair necroptosis competence also in cells with an intact necroptotic machinery and to favour instead apoptosis execution [571,572]. Apoptosis induction was also confirmed in microscopy experiments in which cells were co-stained with Hoechst 33342 and PI: upon combination treatment indeed, not only the fraction of PI-stained cells was considerably increased, but also nuclear and cellular changes characteristic of apoptotic death were observed, such as karyopyknosis, cellular rounding and blebbing. As also in this experiment, Q-VD-Oph reversed all of IZI1551+MRZ-induced effects, it was confirmed that such a combination treatment resulted in caspase-dependent cell death (*figure 20*).

The IZI1551+MRZ combination induced apoptosis in a significant part of the cell population, mostly above 60%. Although not lethal to the remaining fraction of cells, the combination treatment might have impaired their long-term proliferation capacity. To test that, the surviving cells of a representative glioblastoma PDCL classified as responsive, were re-plated in an identical number from each treatment condition and, following six days, their viability was assessed with a WST-1 assay. This revealed that the combination of IZI1551+MRZ substantially reduced the proliferation of the surviving cells. Interestingly, marizomib as single treatment moderately affected their proliferation capacity, while IZI1551 alone did not exert any effect (*figure 21*). This appears consistent with the irreversible nature of the proteasome inhibition carried out by marizomib [368]. In fact, although not lethal as a single agent, marizomib might impair the long-term viability of the cells due to the fact that only newly-produced proteasomes would be active, while those already targeted by this drug would remain inhibited. Considering the slow metabolic rate of the PDCLs, the synthesis of new proteasomes might have not yet occurred in the six days-time of this experiment, such that marizomib-treated cells could not recover until their viability was assessed.

Differently from sensitive PDCLs, cells re-plated from a non-responsive cell line showed no treatment-induced alteration of their proliferation capacity. This revealed that some glioblastoma PDCLs are highly resistant to the combination of IZI1551+MRZ and highlighted the need to employ a different strategy to eradicate them (*figure 22*).

Drug screenings are preferentially performed on 2D-cultured cells because monolayers are easy to maintain and ensure a uniform drug penetration with overall improved experimental reproducibility. However, two-dimensional cell cultures might oversimplify the complexity of cell-to-cell interactions, with the inherent danger of underestimating drug resistance mechanisms that potentially can manifest from more natural 3D microenvironments [123,124]. Hence, drug responsiveness data obtained from 2D-cultured cells required validation under better *in vivo*-mimicking conditions. Glioblastoma PDCLs were therefore grown as tumour spheroids and the panel was interrogated for IZI1551 and marizomib sensitivity also in this setting. Microscopy experiments already revealed that the combination of IZI1551+MRZ caused the disintegration of tumour spheroids (figure 23). Additionally, viability measurements showed that, in 3D-cultured glioblastoma PDCLs, the data already obtained in the 2D model could qualitatively be reproduced. In particular, the PDCLs of the panel were still separable into the same groups of five responsive cell lines and two non-responsive ones. Quantitatively, responses in 3D slightly differed from those of cells monolayers but remarkably, the overall effectiveness of the IZI1551+MRZ combination was confirmed (*figure 24*). This indicated that, although the size and architecture of the spheroids might impede the full penetration of the drugs until their inner core, this aspect did not substantially affect the responses of the PDCLs here examined [573].

Importantly, synergistic apoptosis induction was confirmed in 3D settings and only in the N150661 cell line this kind of interaction between IZI1551 and marizomib was lost (*figure 25*). Moreover, the reduced viability of glioblastoma PDCLs spheroids upon IZI1551+MRZ treatment correlated with apoptosis induction, as determined by Annexin V-GPF/PI-based flow cytometry measurements. As Q-VD-Oph reversed these effects, it was confirmed that, also in the 3D scenario, cell death remained caspase-dependent (*figure 26*). Hence, 3D cultures of glioblastoma PDCLs recapitulated the response pattern of PDCLs monolayers and confirmed that the combination of IZI1551+MRZ induced apoptosis also in more complex cancer cell models.

All together, these data demonstrated that, limited cultivation times of glioblastoma PDCLs maintained as monolayers in serum-free medium, recapitulated responsive and resistant properties of more complex tumour spheroids. For that, they can be considered a valuable model for the pre-clinical assessing of the therapeutic efficacy of cancer drugs. Furthermore, based on this model, treatment with the hexavalent TRAIL receptor agonist IZI1551 and the novel-generation proteasome inhibitor marizomib, resulted in synergistic apoptosis induction in the majority of the glioblastoma PDCLs of a panel that represents the most common genetic alterations found in glioblastoma patients. Additionally, in cell lines classified as responsive, the combination of IZI1551 and marizomib reduced the proliferation capacity of the surviving fraction of cells, while a representative non-responsive cell line remained totally unaffected by this treatment, also on a long term. This last result highlighted the need to identify alternative strategies to treat highly resistant glioblastoma cells. For the responsive cell lines instead, combining IZI1551 and marizomib appeared promising both in terms of efficacy and of safety profile. Indeed, data from the clinical literature indicated that combination of this proteasome inhibitor with the glioblastoma standard of care therapy (TMZ plus radiotherapy) resulted in manageable toxicities, suggesting that a further treatment with IZI1551 could be considered [574].

2. An improved treatment regimen enables MRZ to sufficiently penetrate a BBB model to prime GBM PDCLs to IZI1551-induced apoptosis

The engagement of TRAIL receptors and the inhibition of the proteasome trigger apoptosis through distinct pathways and with diverse kinetics: TRAIL induces primarily extrinsic apoptosis, even if in type 2 cells mitochondrial involvement is required [188]. Proteasome inhibition instead, mostly induces intrinsic apoptosis even though, under certain circumstances, it is also responsible for death ligands-independent activation of caspase-8 within cytoplasmatic platforms [575,576]. While the response to TRAIL receptors engagement is known to be rather quick, requiring only 15 minutes from caspase-8 activation to the permeabilization of the mitochondrial outer membrane, the cellular responses to proteasome inhibitors are complex and employ longer times until death is executed [513,514,577]. These different cell death modalities and kinetics are possibly exploitable to enhance the efficacy of IZI1551+MRZ combination treatments. For that, it was first of all verified that initiation of cell death signalling is indeed kinetically different upon IZI1551 or marizomib stimulation. Western blot analysis of caspase processing showed that, at early time points such as four hours post-treatment, IZI1551 already induced a partial cleavage of initiator caspase-8 and of effector caspase-3, as well as of its substrate PARP. Cleavage of caspase-3 and PARP were further enhanced upon combination treatment and these effects were totally abrogated by co-treatment with Q-VD-Oph, confirming the caspase-dependent nature of IZI1551+MRZ-induced responses. In contrast, at this early stage, marizomib as a single agent failed to induce any caspase processing in both responsive cell lines examined (*figure 27*). Accordingly, following four hours of treatment, also apoptosis induction was kept at control levels upon marizomib alone, as revealed by Annexin-GFP/PI-based flow cytometry (*figure 28*). Instead, both the treatment with IZI1551 alone or in combination with marizomib, caused the exposure of similar amounts of phosphatidylserine in the responsive cell lines N160125 and GTCC9, while PI uptake mostly did not yet occur within the first four hours of treatment (*figure 28*). Overall, these results validated that initiation of apoptosis is slower upon stimulation with marizomib than upon IZI1551 treatment. This provided the rationale to test whether a time-shifted exposure to the drugs, particularly a pre-exposure to marizomib, could enhance the overall induction of apoptosis compared to the simultaneous treatment. Indeed, IncuCyte-based cell death recordings, as well as flow cytometry measurements, showed that cells exposed to marizomib alone for 24 hours before the addition of IZI1551, displayed an increased amount of apoptosis compared to cells simultaneously treated with both drugs (*figure 30* and *31*). Additionally, in the pre-treatment scenario, death kinetic was accelerated as PI uptake was already detected at four hours post IZI1551 addition (*figure 30*). Of note, the enhanced apoptosis induction in the pre-treatment scenario was not solely due to the prolonged exposure to marizomib, as marizomib single treatment, even when applied for longer times, did not augment the number of cells taking up PI at the same level as the combinatorial treatment (*figure 30*). This indicated, once again, that monotherapies are unsuccessful against glioblastoma and that synergistic drug interactions need to be triggered in order to eradicate these cells. Importantly, these experiments also highlighted that the sequence in which drugs are applied greatly affects the efficacy of their combination. Hence, the mechanism and kinetic of action of each therapeutic should be taken into account to design optimal treatment schedules [578]. One example of how a specific regimen significantly altered treatment outcome is the case of NSCLC studied by M.M. Mortenson and colleagues. In particular, they reported that administering bortezomib prior to the standard of care gemcitabine/carboplatin, abrogated the apoptotic effect of the chemotherapy but conversely, a sensitising effect was achieved upon delayed bortezomib addition. Mechanistically, this is due to the different biologic effect of each drug and the specific phase of the cell cycle in which they are functioning. Precisely, bortezomib affects the cell cycle causing a G2/M arrest, while both gemcitabine and carboplatin interfere with correct DNA synthesis. Therefore, if bortezomib is administered first, the consequent G2/M arrest prevents the cells from entering the cell cycle phase in which the chemotherapy would exert its toxicity. Instead, if chemotherapy is given first, it induces a G0 arrest and secondary targets affected by bortezomib can enhance gemcitabine/carboplatin-induced apoptosis [579]. *In vitro* experiments of this kind are important as they provide information on the biochemical and molecular mechanisms of interaction of the drugs used in combination treatments. Clinical studies instead, typically fail to systematically address such questions and also modifications of the relative timing of drug exposure cannot reasonably be integrated into trial designs. Hence, the kinetic study of this work, that proved the enhanced lethality of IZI1551+MRZ treatment upon time-shifted drug administration, is particularly valuable and should guide the design of future trials in glioblastoma.

Given the improved efficacy of the IZI1551+MRZ combination when the proteasome inhibitor was applied first, it was tested if such enhanced toxicity was sufficient to eradicate glioblastoma cells also at lower drug doses, as it is desirable when translating a study into clinical settings. The cell lines N160125 and GTCC9 were treated with concentrations as low as 100 pM of IZI1551 and 40 nM of marizomib, either simultaneously or with the latter drug administered 24 hours earlier. Flow cytometry measurements showed that apoptosis induction was indeed higher in the pre-treatment scenario and that lower drug doses still induced a significant amount of cell death thanks to the altered drug administration sequence (*figure 32*). Having identified a treatment schedule that allowed to lower drug concentrations without losing treatment efficacy is of particular importance for at least two reasons: the first, is the possibility of minimizing the toxicity that might arise from high dosages of a drug when translating pre-clinical studies to clinical settings. The second, is the presence of the BBB that could reduce the amount of a drug that actually reaches glioblastoma tumour cells *in vivo*. Therefore, testing the efficacy of a drug combination in a reduced dosage regiment is a way to mimic a potential *in vivo* scenario.

The BBB is the primary obstacle to the treatment of CNS diseases, as it is impermeable to most drugs. In the case of glioblastoma patients, the BBB is traditionally assumed to be disrupted, although emerging clinical evidence demonstrates that regions of intact barrier are always present [48,379]. Due to this regional integrity, treatments with poor BBB permeability cannot guarantee a therapeutically effective exposure of the drugs to all cancer cells, especially to those within the deeper tissues of the tumour.

Marizomib is a second-generation proteasome inhibitor with improved pharmacodynamic and pharmacokinetic properties [366,580]. Most importantly, there is evidence of its ability to cross the BBB [373,375,376].

Here it was studied if the amount of marizomib that crosses the BBB is sufficient to prime glioblastoma cells to IZI1551-induced apoptosis. As treatments targeting glioblastoma should selectively kill tumor cells and spare that of the BBB, it was first of all verified that marizomib was tolerated by hCMEC/D3 cells (*figure 33*). The cell line hCMEC/D3 is derived from cerebral microvessel endothelial cells and it is the most commonly used model to mimic the human BBB *in vitro* [581,582]*.* It is especially employed in drug transport assays as it expresses a variety of ABC transporters. Moreover, in appropriate growth conditions, it displays the presence of tight junction proteins, such as PECAM-1, JAM-2, VE-cadherin, claudin-3, -5, occludin, beta catenin and zonula occludens proteins, even if claudin-5, occludin and JAM-2 are at lower levels compared to freshly isolated primary human cerebral microvessel endothelial cells [582,583].

A simple model of the human BBB was built by growing hCMEC/D3 cells as a confluent monolayer on collagen-coated polyethylene terephthalate (PET) membranes of a transwell, a scaffold ensuring higher expression of tight junction proteins compared to plastic coverslips [583] (*figure 34*). The cells were grown for five days and the resistance values of the cell monolayer was recorder daily until the calculated TEER was constant and high enough for the barrier to be considered formed (*figure 35A*) [583,584]. At this point, from the apical side of the transwell, a low dose of marizomib was applied on the tight layer of hCMEC/D3 cells (*figure 34*). Importantly, resistance measurements performed 24 hours post-treatment, showed that marizomib did not alter the integrity of the formed barrier (*figure 35A*). The medium recovered from the basolateral side of the transwell, containing marizomib that had crossed the barrier, was applied on glioblastoma cells 24 hours before the addition of IZI1551. Compared to the condition in which marizomib did not have to cross the hCMEC/D3 monolayer and was directly added onto the glioblastoma cells, the presence of the barrier reduced the efficacy of the IZI1551+MRZ co-treatment. However, thanks to the pre-treatment strategy, cell death could still clearly be detected, indicating that the amount of marizomib that crosses a simple BBB model is sufficient to prime glioblastoma cells to IZI1551-induced apoptosis (*figure 35B*). This result is in line with other studies reporting on the ability of marizomib to permeate the BBB and therefore further confirmed this novel proteasome inhibitor as a promising drug against glioblastoma [373,580].

Combination therapies against glioblastoma that include the use of proteasome inhibitors are numerous in the clinical trials. However, many of such studies were stopped because of the poor efficacy of the proteasome inhibitors used. For example, a trial evaluating the use of bortezomib prior to surgery of malignant gliomas and followed by TMZ treatment, was ended as it did not result in an improved progression free survival compared to TMZ alone (NCT00990652). While bortezomib seems to not be effective enough against this tumour, data from this study and from the literature point to the second-generation proteasome inhibitor marizomib as a more promising drug candidate against glioblastoma. In fact, not only it displays a potent inhibiting potential but, as mentioned above, it also has a documented ability to cross the BBB. Marizomib has a peculiar chemical structure, with a chlorine leaving-group that gets rapidly eliminated to form a very stable adduct. The resulting β-lactone ring cannot be regenerated as the C-3O is confined within the cyclic ether ring and produces a steric interference with the protonated N terminus (Thr1NH3+) that does not allow aqueous hydrolysis (*figure 9C*). This structural feature ensures a persistent inhibitory activity and is responsible for the higher cytotoxicity of marizomib compared to analogous compounds with a non-leaving group [366,367,585]. Additionally, studies on its cellular uptake and efflux rate revealed interesting properties. While cellular uptake, occurring by both diffusion and a saturable transport mechanism (carrier-mediated), has a transport efficiency comparable to that of analogous drugs, efflux assays showed that marizomib is mostly retained inside the cells after two hours from the washout, indicating a much slower dissociation rate. Importantly, studies on multiple myeloma and prostate adenocarcinoma cell lines showed that marizomib is not a substrate of any major ABC transporter of the multidrug resistance-associated protein family, making it unlikely that overexpression of these transporters would generate resistance to this compound [366]. Conversely, bortezomib has been shown to be a substrate of the P-glycoprotein efflux pumps and that this is one of the reasons for the resistance to it [586,587]. Overall, it is therefore conceivable that the limitations of several clinical trials on brain tumours would be overcome by replacing other proteasome inhibitors with the more promising brain-penetrating marizomib.

While marizomib can reach the tumour site, biologics of the size of IZI1551, with its 169.18 kDa, are not expected to be BBB-permeant. As the varying extent of BBB destruction in glioblastoma patients cannot guarantee the penetration of most drugs at a therapeutically effective concentration, strategies to circumvent this obstacle must be adopted, especially for drugs of bigger molecular weight [379]. Considering that the first line intervention for glioblastoma cases always involves a maximal safe surgery, implantable carriers appear to be a reasonable solution for the delivery of large biomolecules in these patients. For that, carmustine wafers, commercially available as Gliadel®, have been developed. These are implants soaked with a chemotherapeutic and they can be safely placed in the tumour site during the debulking surgery [96,98]. Technologies to expand this strategy to other compounds are under investigation and also IZI1551 can potentially be accommodated in the tumour cavity following systemic marizomib treatment [99]. In fact, as shown in this study, treatment responsiveness benefits from a marizomib pre-exposure. For that, in the frame of a shifted drug administration, it is important that marizomib can reach the tumor prior to the standard surgery, as this would prime glioblastoma cells to the IZI1551 treatment that can be delivered via the above-mentioned implants.

In addition to these wafers, other strategies to overcome the delivery impediment represented by the presence of the BBB are under development. In particular, upon recurrence, a second surgery is often not recommended because the infiltrating nature of this tumor does not allow its safe removal. In such cases, alternatives to the implantable wafers and that do not require a surgical intervention should be considered. Among the applicable approaches, some are more invasive and consist of the injection, or intraventricular infusion of therapeutics, directly into the cerebrospinal fluid (CSF). The advantage of such solutions is that, as the drugs are given locally, the concentrations to be used are reduced, as are possible side effects that could manifest upon systemic administrations [588,589]. However, in the case of TRAIL receptor agonists like IZI1551, whose safety profile, improved stability and half-life would allow an efficient systemic delivery, the use of such an invasive technique does not appear to be necessary [164,254]. A less invasive approach is represented by the temporary disruption of the integrity of the BBB that, as already mentioned, is at least regionally intact in all glioblastoma cases, hampering more or less severely the delivery of therapeutics to the brain of these patients [379]. The opening of the BBB can be achieved, for example, via an ultrasound-mediated breaking of the tight junctions among the endothelial cells, allowing various molecules to pass through and reach the brain. Technologies of this kind are already being tested for safety and efficacy, with promising initial results [101]. Alternatively, drugs can be specifically modified in order to allow their transport across the BBB. In particular, non-transportable compounds can be coupled to small peptides that are substrates of endogenous receptors, such that the receptor-mediated transcytosis mechanism can be exploited. Examples of such receptors are the human BBB transferrin receptor (TfR) and the LDL-related protein receptor type 1 (LRP1), that can respectively recognize the iron binding protein transferrin (Tf) and the small peptide Angiopep-2 [590,591]. However, the directionality of the transport, as well as the release of the ligand to the brain side, are aspects that required careful consideration. For example, transferrin-mediated transport is reported to occur both from the blood to the brain and *vice-versa* and, in the case of LRP1, endocytosis seems to prevail over transcytosis [592–594]. Hence, engineered molecules should be designed with an affinity that is high enough to allow their uptake from the blood side. At the same time, such affinity should be low to the point that the ligands can be released to the brain tumor. Efforts to tackle this aspect of receptor-mediated transcytosis are currently underway and could provide, in the near future, candidate BBB-permeable versions of TRAIL receptor agonists. In this way, even in the presence of a partially intact BBB, drugs of the size of IZI1551 could be delivered to glioblastoma cells *in vivo*.

Taken together, these data demonstrated that the initiation of cell death signalling is slower upon marizomib than upon IZI1551 treatment. Such differential cell death kinetics should be taken into account to design a treatment schedule that exploits the mechanistic properties of each drug and improves the outcome of their combination. Here it was found that a time-shifted administration of the drugs enhanced the response to the treatment compared to the simultaneous combination. Importantly, such increased cell death responses manifested also when lowering drug concentrations, a desirable condition to minimize possible toxicities emerging in translational settings. Although the bioavailability of marizomib to the tumour site is expected to be decreased due to the presence of the BBB, here it was found that, thanks to the pre-treatment strategy, the amount of marizomib that crossed a simple BBB model was sufficient to prime glioblastoma cells to IZI1551-induced apoptosis. In the case of biologics of the size of IZI1551 instead, strategies for a local administration are under development, with few solutions such as implantable wafers already being approved for clinical use.

3. Lowering the mitochondrial apoptosis threshold re-stores IZI1551+MRZ sensitivity of highly resistant GBM cells

Glioblastoma is a tumor that is highly resistant to conventional therapies, so that alternative therapeutic strategies are urgently needed [595]. In this study, seven glioblastoma PDCLs were analysed for their responsiveness to the combination of IZI1551+MRZ and two of them, namely N151027 and GTCC10, have been identified as non-responders (*figure 16* and *24*). The reasons underlying their resistance might be multiple, including a non-optimal exploitation of the apoptosis-inducing potential of IZI1551 and marizomib, for example due to an inadequate sequence of drug administration. Here, it was shown that a time-shifted exposure to each drug, specifically with marizomib preceding the combination with IZI1551, enhanced the apoptotic response of cell lines classified as sensitive (*figure 30* and *31*). For that, it was hypothesised that the marizomib pre-treatment strategy would be successful also in re-sensitising the N151027 and GTCC10 PDCLs to IZI1551-induced apoptosis. However, IncuCyte-based cell death measurements indicated that, in the pre-treatment scenario, no further increase in the total amount of PI-stained cells occurred in comparison to the simultaneous administration of both drugs (*figure 36*). Hence, the ability of marizomib itself to block proteasomal activity in these cells was questioned. To investigate this further, the CT-L activity of the proteasomes was measured both in the two resistant cell lines and in one of the responsive PDCLs. Upon stimulation with marizomib, both at a low (40 nM) and a high (80 nM) dose, the proteasome was blocked in all the cell lines tested. Of note, marizomib was even slightly more potent than bortezomib in blocking the CT-L activity of the PDCLs, as similarly reported for chronic lymphocytic leukemia and multiple myeloma cells [370,371] (*figure 37*).

Although in the resistant cell lines proteasomal activity was efficiently inhibited by marizomib, this appeared insufficient to sensitise them to TRAIL-induced apoptosis. This suggested that the resistance mechanism lied within the apoptotic signalling network. In fact, many cancer types, especially glioblastoma, display an innate resistance to TRAIL. Reasons for this comprise caspase-8 deficiency, high levels of c-FLIP and altered expression of pro- and/or anti- apoptotic molecules that regulate this pathway, such as proteins of the Bcl-2 family [261,596]. Here, it was studied if the expression of key proteins of the IZI1551-induced initiation phase of apoptosis differed between responsive and non-responsive cell lines. Western blot analysis of total cellular level of TRAIL receptors showed that both non-responder cell lines had low amounts of DR5. Regarding DR4 instead, this was either not expressed or not detectable in these PDCLs. However, such an expression profile of TRAIL receptors was similar to that of the responder cell line N160125 (*figure 38*).

Conclusions about the correlation between the amount of TRAIL receptors and sensitivity to the treatment would be premature without assessing the surface levels of DR4 and DR5 [597]. Precisely, regardless of their total protein expression, TRAIL receptors might be deficient on the plasma membrane due to an accelerated internalisation or to defects in the cargo transport proteins that regulate their trafficking [597–599]. To evaluate if any discrepancy in the cell membrane levels of DR4 and DR5 existed between responsive and non-responsive cell lines, their expression was assessed flow cytometrically. This analysis revealed that both resistant cell lines displayed overall lower surface receptor amounts compared to the sensitive cell lines, confirming the trend already reported in the western blot data (*figure 39*). To further investigate why N151027 and GTCC10 PDCLs did not respond to the combination treatment, it was studied if marizomib could altered the expression of DR4 and DR5 in these cell lines as well as in the responsive ones. In fact, proteasome inhibitors are known to upregulate the expression of death receptors as a mechanism that enables their synergistic interaction with TRAIL in inducing apoptotic death [318,600,601]. Indeed, the responsive PDCLs displayed increased surface amounts of both DR4 and DR5 after stimulation with marizomib, even though this effect was less pronounced for DR4 in the cell line N160125 (*figure 40*), which already showed a low baseline level of this receptor (*figure 39*). Instead, the accumulation of DR4 and DR5 in response to proteasome inhibition was only modest in the resistant PDCLs (*figure 40*), which could be one of the reasons why IZI1551 and marizomib did not synergistically induce apoptosis in these cell lines.

Western blot detection of additional components of the DISC complex revealed also other proteins to be differently expressed in responsive and non-responsive cell lines, with the exception of FADD levels that were comparable in all the PDCLs tested (*figure 41*). Instead, the amounts of procaspase-8 and c-FLIP isoforms were respectively lower and higher in the resistant cell lines, with marizomib further up-regulating c-FLIP in GTCC10 and N151027 (*figure 41*). Of note, the basal expression of BID, a substrate of caspase-8, was lower in the PDCL GTCC10 than in N160125. Also, marizomib treatment decreased the level of full-length BID exclusively in the responsive cell line N160125, possibly indicating its cleavage into tBID (not shown).

Caspase-8 is essential for initiating TRAIL-induced apoptosis and consistently with this role, its deficiency is frequent in many tumour cells [602–604]. In the case of marizomib-induced cell death, caspase-8 seems to play a prominent role. In fact, it was reported that its biochemical inhibition, but not that of caspase-9, significantly reduced marizomib cytotoxicity in multiple myeloma cell lines [371]. Similar results using peptide inhibitors of either caspase-8 or caspase-9 were obtained also in human leukemia cell lines by C.P Miller and colleagues. They additionally showed that, upon marizomib treatment, BID cleavage and the accompanied drop of mitochondrial membrane potential occurred in responsive Jurkat cells. Instead, marizomib stimulation did not result in MOMP induction in cells depleted of caspase-8 and FADD. Importantly, in wild-type cells, marizomib-induced BID cleavage was also followed by an increased caspase-3 activity, all together supporting a model in which this proteasome inhibitor exerts its cytotoxicity through the caspase-8-tBID-mitochondrial axes. [605].

The activation of procaspase-8 is regulated by the ratio of c-FLIP$_{L/S}$ that is bound to it. In fact, c-FLIP$_S$ lacks the protease domain and antagonises caspase-8 activity, probably by forming inactive heterodimers with it [606]. c-FLIP$_L$ instead, has a dual role: at low physiological concentrations it stabilises the catalytic domain of the caspase by forming with it highly active heterodimers and indeed, procaspase-8 seems to have higher affinity for c-FLIP$_L$ than for itself [607]. On the contrary, overexpressing c-FLIP$_L$ can block procaspase-8 activation, as c-FLIP$_L$ would form homodimers that saturate FADD molecules [183,608].

Overall, in the cell lines here examined, the low procaspase-8 level and the high expression of both c-FLIP$_S$ and c-FLIP$_L$ in resistant *versus* responsive PDCLs, constitute a signature of impaired competence to execute extrinsic apoptosis. Thus, it was examined whether targeting elements downstream of caspase-8 activation would compensate for the insufficient apoptosis initiation signal of IZI1551+MRZ. The engagement of the intrinsic apoptotic pathway depends on a balance between pro- and anti- apoptotic proteins. In particular, decreased levels of three main anti-apoptotic members of the Bcl-2 family, namely Bcl-2, Bcl-xL and Mcl-1, can lower the threshold for MOMP execution. The expression of these proteins is frequently altered in cancer cells and overexpressing anti-apoptotic Bcl-2 family proteins confers resistance against apoptosis-inducing therapies [609]. In order to shift this balance toward apoptosis induction, pharmacological inhibitors for each of these three proteins have been developed [517,518].

Here, the expression levels of Bcl-2, Bcl-xL and Mcl-1 were determined *via* western blotting and were compared between the responsive and non-responsive cell lines (*figure 42*). It was found that both resistant PDCLs displayed very low levels of Bcl-2 (*figure 42*). Consistently, treatment with the FDA-approved Bcl-2 inhibitor ABT-199 did not induce apoptosis in these cells, neither as a single agent nor in a triple combination with IZI1551 and marizomib (*figure 43*) [610]. Bcl-xL instead, was equally expressed in all the cell lines tested, which did not point to the levels of this protein as a reason for the differential sensitivity between responsive and resistant PDCLs. Additionally, Bcl-xL is essential for platelet survival and the systemic administration of drugs targeting this protein has been shown to induce thrombocytopenia, making Bcl-xL a non-optimal target to specifically and safely restore apoptosis competence in highly resistant glioblastoma cells [519,611,612]. The last anti-apoptotic member of the Bcl-2 family examined here was Mcl-1, a short-lived anti-apoptotic protein that is reported to accumulate upon proteasome inhibition, further contributing to apoptosis resistance [613,614]. Also, the MCL1 gene is one of the most commonly amplified genes in cancer, for which the targeting of the Mcl-1 protein is a frequently used strategy to allow apoptosis induction in Mcl-1-dependent tumour cells [615]. Here, Mcl-1 expression was detected in both the resistant cell lines and it was also shown that it tended to accumulate upon stimulation with marizomib (*figure 42*). This provided the rationale to test an anti-Mcl-1 approach to lower the threshold for MOMP and re-sensitise these cells to apoptosis. S63845 is a highly selective and potent inhibitor of the Mcl-1 protein. By binding to its BH3 binding groove, this small molecule inhibits the activity of Mcl-1 as it displaces the BH3 proteins bound to it. Importantly, S63845 has been proven to be well tolerated in *in vivo* studies [272]. The treatment of both resistant PDCLs with S63845 as a single agent exerted a modest effect, while the triple combination of the Mcl-1 antagonist with IZI1551 and marizomib potently induced apoptosis in these highly resistant glioblastoma cells (*figure 44A* and *B*). Remarkably, the effectiveness of the Mcl-1 targeting strategy was confirmed in more complex 3D settings (*figure 44C*).

Overall, these data highlighted once again the general ineffectiveness of monotherapies in eradicating glioblastoma cells. Mechanisms of resistance to IZI1551 or to marizomib have been discussed in chapter 1 of this section while the poor efficacy of BH3 mimetics as single agents might depend on different factors. For example, in some cases, mutations in the BH3 binding domain of the Bcl-2 protein have been reported to be responsible for the resistance to ABT-199 [616]. However, such mutations are generally uncommon, with the exception of specific cancer types, such as diffuse large B-cell lymphoma [617,618]. Another possible reason for the resistance to BH3 mimetics as single agents might be found in the redundant function that diverse anti-apoptotic proteins, specifically Mcl-1, Bcl-2 and Bcl-xL, collaborate to exert. Due to that, antagonising only one of the anti-apoptotic proteins of the Bcl-2 family might not result in a lethal effect, as its inactivity can be compensated by the functionality of the other members [619]. Here, the responses to the treatment with ABT-199 or with S63845 as single agents were indeed poor in the PDCLs examined. For that, a triple treatment including IZI1551, marizomib and S63845 was found to be necessary to effectively induce apoptosis in these cells. Although these agents are overall considered safe as monotherapies, with the clinical derivate of S63845 (MIK665/S64315) being tested in clinical trials for AML (NCT03672695, NCT02979366), the risk of administering them as part of a triple combinatorial treatment should be evaluated.

Taken together, the results reported in this work demonstrated that inhibition of the proteasome activity is not, *per se*, an effective apoptosis-inducing stimulus in the PDCLs of the panel here examined. Nevertheless, the combination of the proteasome inhibitor marizomib with IZI1551, synergistically induced apoptosis in the majority of glioblastoma PDCLs.

Considering the crucial role that caspase-8 activation is reported to have in both marizomib- and TRAIL- induced apoptosis, the particular protein expression profile of the resistant PDCLs, and in particular the low levels of procaspase-8 and the high amounts of c-FLIP, might account for the differential responsiveness between these cell lines and the responsive ones.

Studies aiming at specifically enhancing caspase-8 activation and/or inhibiting anti-apoptotic c-FLIP have not yet translated into the design of drugs for clinical use, as it happened instead for therapeutics that can directly trigger the mitochondrial pathway of apoptosis, such as BH3 mimetics [268,620–622]. Remarkably, the data presented here demonstrated that the specific Mcl-1 inhibitor S63845, although mostly not efficacious as a single agent, allowed to sensitise both 2D and 3D-cultured resistant glioblastoma PDCLs to apoptosis induced by the combination of IZI1551+MRZ. This indicated that lowering the MOMP threshold is a promising approach to re-store apoptosis competence of highly resistant glioblastoma cells.

4. Bcl-2 antagonists counteract ferroptosis induction in U-87 malignant glioblastoma cells

Cancer cells often exhibit a dysfunctional regulation of the apoptotic pathway, such that therapies based on the reactivation of this cell death modality are somtimes unsuccessful [520,521]. Strategies that can bypass the obstacle of such apoptosis resistance represent an alternative to target otherwise highly refractory tumour cells.

Ferroptosis is a form of regulated death that has been identified through a synthetic lethal high-throughput screening of small molecules selectively targeting cells that express oncogenic RAS [403]. Importantly, many cancer types that are resistant to conventional therapies have been found to be sensitive to this novel cell death modality [525–527]. This has boosted the pre-clinical research on ferroptosis, with studies aiming at elucidating its molecular mechanisms to possibly exploit them for cancer treatment.

The fibrosarcoma cell line HT1080 is one of the most common ferroptosis models and it is reported to be resistant to TRAIL-induced apoptosis [623]. U-87 MG is a widely used glioblastoma cell line that, likewise HT1080, displays the TRAIL-resistance that characterises many tumour cells [103,528,529]. Because of these features, U-87 MG has been considered here as a prototype to study the susceptibility to ferroptotic death of glioblastoma cells that do not respond to TRAIL.

Here it was shown that, similarly to the cell line HT1080 that responded dose-dependently to erastin or RSL3 treatment, also U-87 MG is a ferroptosis-competent cell line (*figure 45*, *50* and *56*). The morphological features of the dying cells, here recorded with an IncuCyte device, recalled the peculiar “ballooning” phenotype that has also been documented elsewhere and that distinguishes ferroptotic cells from the shrinking apoptotic ones [424] (*figure 45B*, *50B* and *56B*). Mechanistically, RSL3- and erastin- induced death were ROS-depend in both HT1080 and U-87 MG cell lines, as proven by the cytoprotective effect of the ROS-scavenger ferrostatin-1 (*figure 46*, *55* and *57*). Conversely, the pan-caspase inhibitor QVD-Oph, typically used to block apoptotic death, had no effect on HT1080 and U-87 MG cells treated with erastin or with doses of RSL3 up to 2.25 µM (*figure 46*, *55* and *57*).

Intriguingly, upon a dose as high as 4.5 µM of RSL3, HT1080 cells displayed an unexpected behaviour revealed by a cell death kinetic analysis performed with an IncuCyte device: the inhibitory effect of ferrostatin-1 on RSL3-treated cells only manifested during the first 8 hours and appeared attenuated at following time points (*figure 51*). QVD-Oph instead, a drug supposedly unrelated to the ferroptotic death pathway, exerted a partial protective effect on these cells (*figure 53*), remarkably starting at the same time point when the effect of ferrostatin-1 ceased [403] (*figure 54*). Therefore, two phases of cell death were distinguishable when HT1080 cells were treated with high doses of RSL3: a first phase that solely depended on ROS and that could be considered purely ferroptotic and a second phase in which both ROS-related stress and caspase activation were involved (*figure 54A*). Consistently, only the cells dying during the first phase (t<8 h) were all morphologically recognizable as ferroptotic, while in the second phase distinct phenotypes were observed (*figure 54B*). RSL3 is a typical ferroptosis inducer and caspase activation is not expected to occur in this cell death modality [407,418]. In a first instance, it was hypothesised that the decreased protective effect of ferrostatin-1 during the second phase was due to its depletion during the first phase. Hence, it was tested whether a second dose of ferrostatin-1, prior to the end of so-called phase one, would rescue the cells in the following phase. However, flow cytometry-based cell death measurements performed 24 hours post-RSL3 treatment, revealed no difference between the single administration of ferrostatin-1 and the condition in which two subsequent doses, at time point 0 h and 5 h, were applied onto HT1080 cells (*figure 52*). As a double administration of ferrostatin-1 did not result in an increased cytoprotective effect, the consumption of ferrostain-1 could not be identified as the reason for the reported effects. Consistently, recent insights into the mechanism of action of ferrostatin-1 revealed that this does not get consumed while inhibiting iron-dependent lipid peroxidation [443]. Moreover, if the only reason for the lower protective capacity of ferrostatin-1 was its partial depletion, then the remaining amount of cell death in the second phase would have been expected to be purely ferroptotic. Instead, the inhibitory effect of QVD-Oph clearly pointed to a “conversion” into a different cell death modality that involved caspases. These results suggested that RSL3 might interfere with pathways distinct from ferroptosis. Besides that, off-targets effects might arise when applying RSL3 at specific concentrations or in specific cells. Additional experiments on a broader panel of cell lines are required in order to validate these findings. Most importantly, the cellular role of GPx-4 needs to be further investigated to clarify whether the effects reported in this work are specific to RSL3 or if they can be extended to GPx-4 inhibition in general. This could be done both by directly targeting the GPX4 gene, with knockout or silencing experiments, or by utilising compounds, different from RSL3, that inhibit the enzymatic activity of this protein. An interesting work in this direction that partially confirms the findings reported here, is the one by the group of Q. Zhang on triple negative breast cancer (TNBC) cells lines. They have identified DMOCPTL, a parthenolide analogue in clinical study for the treatment of acute myeloid leukemia (AML), as an inducer of both apoptosis and ferroptosis [624]. Precisely, they found that both the caspase inhibitor Z-VAD-FMK and ferroptosis inhibitors, like deferoxamine (DFO) and ferrostatin-1, partially protected TNBC cells treated with DMOCPTL. Apoptosis induction was confirmed by exposure of phosphatidylserine and cleavage of caspase 9, caspase 3 and

PARP. The occurrence of ferroptosis instead, appeared evident because DMOCPTL treatment determined a time- and dose-dependent increase of lipid ROS, detected by flow cytometric measurements of BODIPY 581/591 C11 oxidation [456,624]. However, their study had some limitations that did not allow to fully clarify how apoptosis and ferroptosis relate to each other upon GPx-4 inhibition. In fact, no kinetic analysis but only end-point measurements were performed at a late time point (48 hours), so that no information was provided as to whether the two cell death modalities occurred subsequently or concomitantly. To verify if apoptosis takes place during the first hours following GPx-4 inhibition, it would be necessary to prove that both phosphatidylserine exposure and caspase processing occur in this early phase and that both events are rescuable by caspase inhibition. In fact, PS exposure alone should neither be considered a real “early” event during apoptosis nor an exclusive feature of this cell death modality [625]. In fact, PS exposure was reported to occur also prior to the loss of plasma membrane integrity during necroptosis and, most importantly, upon RSL3 treatment in Jurkat cells [626–628]. Similarly, the results reported in this thesis showed that, upon stimulation with a hight dose of RSL3 (4.5 μM), a portion of HT1080 cells were stained with Annexin V-GFP (*figure 52*). However, also in this case, the absence of a co-treatment with a caspase inhibitor does not allow to rule out the possibility that the flipping of PS was independent of apoptosis. Another important point of the study by the group of Q. Zhang was that neither Z-VAD-FMK nor ferrostatin-1 fully rescued the cells treated with DMOCPTL. This effect recalled the partial protection that both ferrostatin-1 and Q-VD-Oph provided to HT1080 cells upon prolonged (> 10/12 hours) treatment with RSL3 (*figure 54*). However, the two inhibitors should be used in combination to verify that this would save the complete cells population. Only by including such a control it could be concluded that both apoptosis and ferroptosis are responsible for the reported cell death induction, without any other mechanism being involved. Finally, it is relevant to highlight that DMOCPTL-induced ferroptosis mechanistically differed from that triggered by RSL3, as this novel compound directly binds and ubiquitinate GPx-4, thereby leading to its degradation [624]. This indicated that not only RSL3 treatment, but in general targeting GPx-4 could activate death pathways distinct from ferroptosis. Interestingly, the apoptosis-inducing effects of typical ferroptotic drugs are not limited to direct GPx-4 inhibitors but were reported to occur also upon erastin treatment. In particular, a recent study on gastric cancer cell lines by Y. Sun and colleagues, showed that the amount of ROS accumulated upon a specific dose of erastin, corresponding to the 30% of its inhibitory concentration, did not cause ferroptosis but an arrest of the cell cycle in G1/G0 phase. Additionally, this also led to an increased proportion of Annexin V^+/PI^- and Annexin V^+/PI^+ cells, as detected in flow cytometry experiments. Importantly, these effects were rescued by co-treatment with the caspase inhibitor Z-VAD-FMK but not by co-treatment with the ferroptosis inhibitor ferrostatin-1. Detections of hallmarks of apoptosis such as cleaved PARP and cleaved caspase-3 confirmed the evidence of apoptotic death [532]. Similarly, an earlier study by H. Huo and co-workers already showed that erastin has a pro-apoptotic effect in colorectal cancer cells. This was demonstrated by Annexin V-based flow cytometric analysis and by caspase activity assays, interestingly showing an increased activity of caspase-3 and caspase-9 but not of caspase-8 [629].

Overall, the findings of this thesis support recent data from the literature and indicate that the same stress-inducing signal can result in different types of cell death that even share the same initiation steps. Conceptually, this is a well-known notion if considering that, for example, TRAIL can trigger both apoptosis and necroptosis depending on the specific cellular context [223]. It is conceivable that, the ROS-related stress induced by a high concentration of RSL3 specifically in HT1080 cells overcomes, or lies outside, the protective capacity of ferrostatin-1 and that cells already committed to dye find their way through the engagement of an alternative caspase-dependent cell death modality. However, the “switch” regulating the shift between ferroptosis and other cell death pathways is unclear and also the cellular role of GPx-4 requires further elucidations.

In this work, features of apoptotic death induced by typical ferroptosis inducers were only observed upon RSL3 doses that exceeded the concentrations typically used in other studies. [418,537,538]. Importantly, these results could not be reproduced in the glioblastoma cell line U-87 MG. Hence, no further investigations on the role of GPx-4 during apoptotic death was conducted in the frame of this work.

Ferroptotic cell death is known to induce morphological and functional alterations of the mitochondria, with an accumulation of ROS that points to the involvement of such organelles in this cell death modality [477,630]. This is consistent with the role of the mitochondria as the main cellular source of ROS and as the central hub of iron metabolism [631,632]. At the same time, mitochondria are also important in the apoptosis pathway, during which their membrane integrity gets corrupted due to BAX/BAK-depend pore formation [633]. This process is regulated by proteins of the Bcl-2 family and can be modulated by BH3 mimetics, small molecules that antagonise the anti-apoptotic members thereby facilitating MOMP execution [268]. While apoptosis is a relatively well characterised cell death pathway, with identified key players and drugs to target them, ferroptosis remains still elusive and strategies to modulate its execution are less defined. Indeed, besides experimental drugs, only very few clinically approved compounds exist that can induce this type of cell death, such as sorafenib, sulfasalazine, artemisinin and, indirectly, also statins [430,431,498,634]. As ferroptosis is emerging as an alternative cell death modality to target apoptosis-resistant tumour cells, understanding its connections with other cell death pathways is crucial to possibly exploit it for cancer therapy. Indeed, combinatorial treatments are being explored through the integration of ferroptosis induction into conventional cancer therapies, in order to identify synergistic sensitisation strategies and/or drug-resistance reversal effects [635].

Given the convergence of both the ferroptotic and the apoptotic cell death pathways on the same organelle, namely the mitochondria, it was here investigated how modulators of the BAX/BAK-dependent mitochondrial pore formation, such as BH3 mimetics, relate to ferroptosis inducers and whether they can be exploited to enhance ferroptosis execution.

As mentioned before in this thesis, diverse tumour cells depend on anti-apoptotic proteins of the Bcl-2 family for their survival [533,534]. Hence, the sensitivity to Bcl-2 antagonists of the ferroptosis cell line model HT1080 and that of the ferroptosis-competent glioblastoma cell line U-87 MG was evaluated. None of the BH3 mimetic used, namely ABT-199; S63845 and WEHI-539 that antagonise Bcl-2; Mcl-1 and Bcl-xL respectively, was lethal to HT1080 or U-87 MG cells when applied as single agents (*figure 48, 59, 61,* and *63*). Intriguingly, when combined with ferroptosis inducers such as erastin or RSL3, BH3 mimetics attenuated cell death induction (*figure 49, 59, 61* and *63*). Remarkably, in U-87 MG cells, this protective effect was enhanced when progressively increasing the concentrations of the BH3 mimetic drug (*figure 59, 61* and *63*). This finding is in stark contrast with the assumption that combining diverse cell death-inducing stimuli would result in higher toxicity. In particular, other reports indicated that the combination of ferroptosis inducers and BH3 mimetics synergistically triggered cell death [636,637]. However, the study by K.H. Lin and colleagues refers to Bcl-2-dependent AML cell lines in which ABT-199 treatment already induced MOMP-dependent apoptosis and GPx-4 dysfunction further contributed to the mitochondrial stress [637]. Instead, in the cell lines analysed here, BH3 mimetics did not provoke a lethal effect and also the extent of the mitochondrial damage was not assessed under these conditions. For that, besides their role in inducing MOMP, other functions of anti-apoptotic Bcl-2 proteins should be considered. For example, a plausible explanation for the reversal proportionality between BH3 mimetic doses and cell death upon a constant ferroptosis stimulus, might be found in the role that Bcl-2, Mcl-1 and Bcl-xL play in autophagy induction. In particular, these proteins are interaction partners of Beclin-1, a key protein in autophagy [638,639]. The use of BH3 mimetics might therefore free Beclin-1, with consequent pro-survival autophagic responses that attenuate the pro-death function of ferroptosis inducers. Although yet to be tested, this hypothesis is supported by findings such as the identification of a natural BH3 mimetic compound, named gossypol ((-)-enantiomer), that functions as a pan-inhibitor of the anti-apoptotic members of the Bcl-2 family. Gossypol indeed, induced autophagy in prostate cancers, an effect attributable to the interruption of the interaction between these proteins and Beclin-1 [640,641]. Similarly, also the BH3-mimetic ABT-737 was reported to induce autophagy, as it competes with Bcl-2 or Bcl-xL for the binding to Beclin-1 [642].

To mechanistically characterise the cell death modality triggered by the addition of a BH3 mimetic to a ferroptosis inducer, the caspase inhibitor Q-VD-Oph or the ferroptosis suppressor ferrostatin-1 were added to the combinatorial treatments. In the case of the glioblastoma cell line U-87 MG, ferrostatin-1 completely rescued the cells, while Q-VD-Oph did not (*figure 60, 62* and *64*). This indicated that the cytotoxic effect of the combination treatment was independent of caspase activity, meaning that cell death remained purely ferroptotic. An exception to that, was the partial protective effect of Q-VD-Oph on the WEHI-539+RSL3-induced death in the same cell line (*figure 64*). However, how exacly a purely ferroptotic cell death would switch into a caspase-dependent one upon the addition of a Bcl-xL antagonist remained unclear.

Overall, the finding that BH3 mimetics exert a protective effect on ferroptosis induction, although inconvenient in the treatment of glioblastoma, can be of high relevance for all of those conditions whose pathogenesis is linked to this kind of cell death. For example, the brain in general with its high metabolic activity, and especially neuronal membranes which are rich in PUFA, are particularly prone to oxidative stress. To counteract such condition, the production of antioxidants is tightly balanced in this organ [643]. Consistently, ferroptotic cell death is now emerging to be involved in different types of brain injuries, such as those caused by cerebral stroke or by neurodegenerative diseases [504,644–646]. In particular, in animal models of the Alzheimer's disease and of both ischemic and hemorrhagic stroke, it has been shown that anti-ferroptotic approaches can reduce neuronal death [480,647–651]. Because this study demonstrated that BH3 mimetics can counteract ferroptotic death, drugs such as ABT-199, which has been shown to be safe and is already used in the clinic, could be re-purposed as an anti-ferroptosis therapy in the treatment of neurological diseases.

Taken all together, these results showed that, similarly to the HT1080 cells line, the U-87 MG is also a valid model for ferroptosis studies and therefore it can be used as a prototype to investigate this cell death modality in glioblastoma cells. The scarcity of clinically relevant ferroptosis-inducing compounds and the dose-limiting toxicities of the available ones pushes towards the design of combinatorial treatments with already approved drugs [652,653]. In this way ferroptosis execution could be modulated via exploitation of other cellular pathways. However, the data shown here revealed an antagonistic interaction between ferroptosis inducers and inhibitors of Mcl-1, Bcl-2 and Bcl-xL. This indicated that further elucidations on how ferroptosis inducers relate to other cellular pathways are required for the knowledge-driven design of therapies that rationally combine, or rather exclude, drugs that would promote cell survival instead of cell death. Nevertheless, the observed protection from ferroptosis execution suggested that BH3 mimetics could be employed to attenuate the damages caused by pathological conditions in which this cell death modality is involved. A more profound understanding of these interactions is anyways necessary in order to balance combinatorial treatments for clinical use.

Summary and conclusion

The current study provided evidence that, in agreement with data from the literature, the long-term cultivation of glioblastoma cell lines alters their responsiveness to cancer therapeutics.

In contrast, in clinically relevant *in vitro* models, such as low-passage glioblastoma PDCLs maintained under stemness-preserving conditions, the combination of the hexavalent TRAIL receptor agonist IZI1551 with the proteasome inhibitor marizomib resulted in synergistic apoptosis induction in most of the cell lines tested. The IZI1551-induced responses expectedly manifested earlier than the more complex ones exerted by marizomib, as revealed by the earlier processing of caspases. The differential apoptosis-initiation kinetics of the two drugs could be exploited to enhance the responsiveness to their combination, with marizomib pre-treatment priming glioblastoma PDCLs to IZI1551-induced apoptosis. The improved cytotoxicity achieved with the time-shifted drug exposure also allowed to reduce the doses of each agent by still maintaining treatment efficacy. This is of particular relevance in a clinical setting as it would minimize the possible toxicity induced by high concentrations of the individual drugs.

Marizomib is reported to be a blood-brain barrier (BBB) permeant compound. Here it was shown that, in a representative sensitive glioblastoma PDCL, the amount of marizomib that was able to cross a simple model of the human BBB, was sufficient to confer sensitisation to IZI1551-induced cell death when the pre-treatment strategy was applied.

Among the seven glioblastoma PDCLs examined, two emerged as highly resistant to the IZI1551+MRZ treatment, although marizomib efficiently inhibited their proteasomal activity. One reason for such resistance was found in a protein expression signature associated with poor competence to initiate extrinsic apoptosis. Specifically, compared to responsive cell lines, these PDCLs expressed lower basal amounts of TRAIL receptors that even failed to accumulate upon marizomib exposure. In addition to that, the reduced expression of procaspase-8 and the higher amount of anti-apoptotic c-FLIP, contributed to define a protein profile that underlies the need to sensitise resistant PDCLs through an alternative pathway. Indeed, increasing the mitochondrial apoptosis sensitivity with S63845, a BH3 mimetic antagonising the anti-apoptotic Mcl-1, allowed to restore IZI1551+MRZ responsiveness of otherwise highly resistant glioblastoma PDCLs. Importantly, both the response patterns to the IZI1551+MRZ combinatorial treatments as well as the effectiveness of sensitising resistant PDCLs thought a reduction of the mitochondrial apoptosis threshold, were confirmed in the more complex 3D glioma spheroids model, validating all the key findings of this study.

The safety of marizomib has already been clinically tested in both multiple myeloma and glioblastoma. In the latter case, toxicities were manageable also when combining it with temozolomide-based radiochemotherapy, suggesting that further combinations could be considered. In this preclinical study, it was shown that the addition of the hexavalent TRAIL receptor agonist IZI1551 to marizomib treatment is a promising approach to treat glioblastoma.

The safety of TRAIL as an anti-cancer agent has long been established and the limitations of its clinical use lie primarily in its low efficacy. Remarkably, IZI1551 is an improved TRAIL format similar to Eftozanermin alfa (ABBV-621), a compound that, both alone and in combination with bortezomib, is currently in phase II clinical trial for the treatment of relapsed or refractory multiple myeloma patients. However, in the case of glioblastoma, the presence of the BBB represents a further obstacle for the successful application of anti-cancer drugs. While marizomib was reported to cross this barrier, big biologics, such as TRAIL fusion proteins, are not expected to permeate it. To overcome this limitation, attempts to engineer TRAIL variants that exploit the receptor-mediated transport mechanisms of endothelial cells should be considered. Additionally, technologies using injectable or implantable hydrogels are under development for the delivery of large drugs to the brain, with carmustin wafers already been tested at a clinical level.

It remains to verify, how the combination of IZI1551 with marizomib and the treatment regimen tested here, could be integrated into, or even replace, the current standard of care for glioblastoma patients. Ideally, following marizomib treatment, IZI1551 implants could be placed in the tumour site at the moment of the debulking surgery.

Overall, the results shown in this thesis demonstrated that, an appropriate drug combination and an optimised treatment schedule, allow the anti-cancer potential of TRAIL to be exploited even against highly resistant tumours, such as glioblastoma. All of this, lays the basis to forward this study to *in vivo* settings.

The treatment of glioblastoma patients is currently almost exclusively limited to the use of TMZ. At the moment, the most commonly studied therapeutic interventions to eradicate this tumor are based on the induction of apoptotic death. However, glioblastoma cells manifest a high degree of resistance to apoptosis, in particular to that induced by TRAIL. Hence, besides investigating combinatorial treatments with compounds that can sensitise cells to TRAIL-induced apoptosis, alternative cell death modalities should be explored in order to expand the landscape of glioblastoma treatment options. A possible strategy is represented by ferroptosis, one of the most recently identified forms of regulated death that differs from apoptosis for the cellular components involved in its execution. Here it was hypothesized that, in order to eliminate TRAIL-resistant glioblastoma cells, ferroptotic death could be exploited as a substitute, or as an adjuvant, of apoptosis induction. It was shown that a bona-fide glioblastoma cell line, namely U-87 MG, died dose-dependently upon treatment with the ferroptosis inducer RSL3, setting the basis to further investigate the applicability of this cell death-inducing strategy against glioblastoma. However, the side effects of the few clinically approved compounds that have been shown to trigger ferroptosis require to carefully dose their use. Hence, it was studied how ferroptosis inducers related to treatments targeting other death pathways, such that their combination could allow to reduce the dosage of ferroptotic drugs by still maintaining, or even enhancing, cell death. As ferroptotic death is driven by lipid peroxidation, with consequent damage of cellular membranes such as those of the mitochondria, it was hypothesised that the stress on this organelle could have been further augmented upon exposure to BH3 mimetics. Intriguingly, it was found that BH3 mimetics reduced, rather than enhanced, the ferroptosis susceptibility of U-87 MG cells, making this combination unsuitable as an anti-cancer therapy. However, considering the emerging role of ferroptosis in the pathogenesis of neurological diseases, these findings open up the possibility of re-purposing BH3 mimetics for the treatment of ferroptosis-induced brain injuries. In general, a deeper understating of how ferroptosis integrates into other cellular pathways is necessary to advance its exploitation at a clinical level.

Bibliography

Bibliography

1. Virchow, R. Die Krankhaften Geschwülste: Dreissig Vorlesungen gehalten während des Wintersemesters 1862-1863 an der Universität zu Berlin. (A. Hirschwald, 1863).
2. Ostrom, Q. T., Cioffi, G., Waite, K., Kruchko, C. & Barnholtz-Sloan, J. S. CBTRUS Statistical Report: Primary Brain and Other Central Nervous System Tumors Diagnosed in the United States in 2014-2018. Neuro Oncol **23**, iii1–iii105 (2021).
3. Nakada, M. et al. Aberrant signaling pathways in glioma. Cancers (Basel) **3**, 3242–3278 (2011).
4. Dandy, W. E. Removal of right cerebral hemisphere for certain tumors with hemiplegia: preliminary report. Journal of the American Medical Association **90**, 823–825 (1928).
5. Alexander, B. M. & Cloughesy, T. F. Adult Glioblastoma. J Clin Oncol **35**, 2402–2409 (2017).
6. Bondy, M. L. et al. Brain tumor epidemiology: consensus from the Brain Tumor Epidemiology Consortium. Cancer **113**, 1953–1968 (2008).
7. Farrell, C. J. & Plotkin, S. R. Genetic causes of brain tumors: neurofibromatosis, tuberous sclerosis, von Hippel-Lindau, and other syndromes. Neurol Clin **25**, 925–946, viii (2007).
8. Hochberg, F., Toniolo, P., Cole, P. & Salcman, M. Nonoccupational risk indicators of glioblastoma in adults. J Neurooncol **8**, 55–60 (1990).
9. Ohgaki, H. Epidemiology of brain tumors. Methods Mol Biol **472**, 323–342 (2009).
10. Bailey, P. & Cushing, H. A classification of the tumors of the glioma group on a histogenetic basis: with a correlated study of prognosis. (Lippincott, 1926).
11. Louis, D. N. et al. The 2021 WHO Classification of Tumors of the Central Nervous System: a summary. Neuro Oncol **23**, 1231–1251 (2021).
12. Louis, D. N. et al. The 2016 World Health Organization Classification of Tumors of the Central Nervous System: a summary. Acta Neuropathol **131**, 803–820 (2016).
13. Hou, L. C., Veeravagu, A., Hsu, A. R. & Tse, V. C. K. Recurrent glioblastoma multiforme: a review of natural history and management options. Neurosurg Focus **20**, E5 (2006).
14. Sherriff, J. et al. Patterns of relapse in glioblastoma multiforme following concomitant chemoradiotherapy with temozolomide. Br J Radiol **86**, 20120414 (2013).
15. Mughal, A. A. et al. Patterns of Invasive Growth in Malignant Gliomas-The Hippocampus Emerges as an Invasion-Spared Brain Region. Neoplasia **20**, 643–656 (2018).
16. Velásquez, C. et al. Molecular and Clinical Insights into the Invasive Capacity of Glioblastoma Cells. J Oncol **2019**, 1740763 (2019).
17. Brennan, C. W. et al. The somatic genomic landscape of glioblastoma. Cell **155**, 462–477 (2013).
18. Ceccarelli, M. et al. Molecular Profiling Reveals Biologically Discrete Subsets and Pathways of Progression in Diffuse Glioma. Cell **164**, 550–563 (2016).
19. Noushmehr, H. et al. Identification of a CpG island methylator phenotype that defines a distinct subgroup of glioma. Cancer Cell **17**, 510–522 (2010).
20. Phillips, H. S. et al. Molecular subclasses of high-grade glioma predict prognosis, delineate a pattern of disease progression, and resemble stages in neurogenesis. Cancer Cell **9**, 157–173 (2006).
21. Verhaak, R. G. W. et al. Integrated genomic analysis identifies clinically relevant subtypes of glioblastoma characterized by abnormalities in PDGFRA, IDH1, EGFR, and NF1. Cancer Cell **17**, 98–110 (2010).
22. Wang, Q. et al. Tumor Evolution of Glioma-Intrinsic Gene Expression Subtypes Associates with Immunological Changes in the Microenvironment. Cancer Cell **32**, 42-56.e6 (2017).
23. Aubry, M. et al. From the core to beyond the margin: a genomic picture of glioblastoma intratumor heterogeneity. Oncotarget **6**, 12094–12109 (2015).
24. Sottoriva, A. et al. Intratumor heterogeneity in human glioblastoma reflects cancer evolutionary dynamics. Proc Natl Acad Sci U S A **110**, 4009–4014 (2013).
25. Neftel, C. et al. An Integrative Model of Cellular States, Plasticity, and Genetics for Glioblastoma. Cell **178**, 835-849.e21 (2019).
26. Patel, A. P. et al. Single-cell RNA-seq highlights intratumoral heterogeneity in primary glioblastoma. Science **344**, 1396–1401 (2014).
27. Jin, X. et al. Targeting glioma stem cells through combined BMI1 and EZH2 inhibition. Nat Med **23**, 1352–1361 (2017).
28. Puchalski, R. B. et al. An anatomic transcriptional atlas of human glioblastoma. Science **360**, 660–663 (2018).
29. Becker, A. P., Sells, B. E., Haque, S. J. & Chakravarti, A. Tumor Heterogeneity in Glioblastomas: From Light Microscopy to Molecular Pathology. Cancers (Basel) **13**, 761 (2021).
30. Bergmann, N. et al. The Intratumoral Heterogeneity Reflects the Intertumoral Subtypes of Glioblastoma Multiforme: A Regional Immunohistochemistry Analysis. Front Oncol **10**, 494 (2020).
31. Bao, B., Ahmad, A., Azmi, A. S., Ali, S. & Sarkar, F. H. Overview of cancer stem cells (CSCs) and mechanisms of their regulation: implications for cancer therapy. Curr Protoc Pharmacol **Chapter 14**, Unit 14.25 (2013).
32. Lathia, J. D. et al. Distribution of CD133 reveals glioma stem cells self-renew through symmetric and asymmetric cell divisions. Cell Death Dis **2**, e200 (2011).
33. Beier, D. et al. CD133(+) and CD133(-) glioblastoma-derived cancer stem cells show differential growth characteristics and molecular profiles. Cancer Res **67**, 4010–4015 (2007).
34. Galli, R. et al. Isolation and characterization of tumorigenic, stem-like neural precursors from human glioblastoma. Cancer Res **64**, 7011–7021 (2004).

35. Heddleston, J. M., Li, Z., McLendon, R. E., Hjelmeland, A. B. & Rich, J. N. The hypoxic microenvironment maintains glioblastoma stem cells and promotes reprogramming towards a cancer stem cell phenotype. Cell Cycle **8**, 3274–3284 (2009).
36. Neradil, J. & Veselska, R. Nestin as a marker of cancer stem cells. Cancer Sci **106**, 803–811 (2015).
37. Singh, S. K. et al. Identification of a cancer stem cell in human brain tumors. Cancer Res **63**, 5821–5828 (2003).
38. Bhaduri, A. et al. Outer Radial Glia-like Cancer Stem Cells Contribute to Heterogeneity of Glioblastoma. Cell Stem Cell **26**, 48-63.e6 (2020).
39. Rich, J. N. Cancer stem cells: understanding tumor hierarchy and heterogeneity. Medicine (Baltimore) **95**, S2–S7 (2016).
40. Gupta, P. B., Pastushenko, I., Skibinski, A., Blanpain, C. & Kuperwasser, C. Phenotypic Plasticity: Driver of Cancer Initiation, Progression, and Therapy Resistance. Cell Stem Cell **24**, 65–78 (2019).
41. Iwadate, Y. Plasticity in Glioma Stem Cell Phenotype and Its Therapeutic Implication. Neurol Med Chir (Tokyo) **58**, 61–70 (2018).
42. Safa, A. R., Saadatzadeh, M. R., Cohen-Gadol, A. A., Pollok, K. E. & Bijangi-Vishehsaraei, K. Glioblastoma stem cells (GSCs) epigenetic plasticity and interconversion between differentiated non-GSCs and GSCs. Genes Dis **2**, 152–163 (2015).
43. Dahan, P. et al. Ionizing radiations sustain glioblastoma cell dedifferentiation to a stem-like phenotype through survivin: possible involvement in radioresistance. Cell Death Dis **5**, e1543 (2014).
44. Lee, G. et al. Dedifferentiation of Glioma Cells to Glioma Stem-like Cells By Therapeutic Stress-induced HIF Signaling in the Recurrent GBM Model. Mol Cancer Ther **15**, 3064–3076 (2016).
45. Soeda, A. et al. Hypoxia promotes expansion of the CD133-positive glioma stem cells through activation of HIF-1alpha. Oncogene **28**, 3949–3959 (2009).
46. Dirkse, A. et al. Stem cell-associated heterogeneity in Glioblastoma results from intrinsic tumor plasticity shaped by the microenvironment. Nat Commun **10**, 1787 (2019).
47. Bocci, F. et al. Toward understanding cancer stem cell heterogeneity in the tumor microenvironment. Proc Natl Acad Sci U S A **116**, 148–157 (2019).
48. Abbott, N. J., Patabendige, A. A. K., Dolman, D. E. M., Yusof, S. R. & Begley, D. J. Structure and function of the blood-brain barrier. Neurobiol Dis **37**, 13–25 (2010).
49. Iorio, A. L. et al. Blood-Brain Barrier and Breast Cancer Resistance Protein: A Limit to the Therapy of CNS Tumors and Neurodegenerative Diseases. Anticancer Agents Med Chem **16**, 810–815 (2016).
50. Nies, A. T. et al. Expression and immunolocalization of the multidrug resistance proteins, MRP1-MRP6 (ABCC1-ABCC6), in human brain. Neuroscience **129**, 349–360 (2004).
51. Wijaya, J., Fukuda, Y. & Schuetz, J. D. Obstacles to Brain Tumor Therapy: Key ABC Transporters. Int J Mol Sci **18**, E2544 (2017).
52. Calatozzolo, C. et al. Expression of drug resistance proteins Pgp, MRP1, MRP3, MRP5 and GST-pi in human glioma. J Neurooncol **74**, 113–121 (2005).
53. Declèves, X. et al. Molecular and functional MDR1-Pgp and MRPs expression in human glioblastoma multiforme cell lines. Int J Cancer **98**, 173–180 (2002).
54. Declèves, X., Amiel, A., Delattre, J.-Y. & Scherrmann, J.-M. Role of ABC transporters in the chemoresistance of human gliomas. Curr Cancer Drug Targets **6**, 433–445 (2006).
55. Goldwirt, L., Beccaria, K., Carpentier, A., Farinotti, R. & Fernandez, C. Irinotecan and temozolomide brain distribution: a focus on ABCB1. Cancer Chemother Pharmacol **74**, 185–193 (2014).
56. Huang, L. et al. Significance and Mechanisms of P-glycoprotein in Central Nervous System Diseases. Curr Drug Targets **20**, 1141–1155 (2019).
57. Robey, R. W., Ierano, C., Zhan, Z. & Bates, S. E. The challenge of exploiting ABCG2 in the clinic. Curr Pharm Biotechnol **12**, 595–608 (2011).
58. Stacy, A. E., Jansson, P. J. & Richardson, D. R. Molecular pharmacology of ABCG2 and its role in chemoresistance. Mol Pharmacol **84**, 655–669 (2013).
59. Stupp, R. et al. Radiotherapy plus concomitant and adjuvant temozolomide for glioblastoma. N Engl J Med **352**, 987–996 (2005).
60. Lee, S. Y. Temozolomide resistance in glioblastoma multiforme. Genes Dis **3**, 198–210 (2016).
61. Stupp, R. et al. Effects of radiotherapy with concomitant and adjuvant temozolomide versus radiotherapy alone on survival in glioblastoma in a randomised phase III study: 5-year analysis of the EORTC-NCIC trial. Lancet Oncol **10**, 459–466 (2009).
62. Weller, M. et al. MGMT Promoter Methylation Is a Strong Prognostic Biomarker for Benefit from Dose-Intensified Temozolomide Rechallenge in Progressive Glioblastoma: The DIRECTOR Trial. Clin Cancer Res **21**, 2057–2064 (2015).
63. Jiang, G. et al. A novel approach to overcome temozolomide resistance in glioma and melanoma: Inactivation of MGMT by gene therapy. Biochem Biophys Res Commun **406**, 311–314 (2011).
64. Liu, L. & Gerson, S. L. Targeted modulation of MGMT: clinical implications. Clin Cancer Res **12**, 328–331 (2006).
65. Hegi, M. E. et al. Correlation of O6-methylguanine methyltransferase (MGMT) promoter methylation with clinical outcomes in glioblastoma and clinical strategies to modulate MGMT activity. J Clin Oncol **26**, 4189–4199 (2008).
66. Kitange, G. J. et al. Evaluation of MGMT promoter methylation status and correlation with temozolomide response in orthotopic glioblastoma xenograft model. J Neurooncol **92**, 23–31 (2009).

67. Feldheim, J. et al. Changes of O6-Methylguanine DNA Methyltransferase (MGMT) Promoter Methylation in Glioblastoma Relapse-A Meta-Analysis Type Literature Review. Cancers (Basel) **11**, E1837 (2019).
68. Park, C.-K. et al. The Changes in MGMT Promoter Methylation Status in Initial and Recurrent Glioblastomas. Transl Oncol **5**, 393–397 (2012).
69. Ren, X., Ai, D., Li, T., Xia, L. & Sun, L. Effectiveness of Lomustine Combined With Bevacizumab in Glioblastoma: A Meta-Analysis. Front Neurol **11**, 603947 (2020).
70. Taal, W. et al. Single-agent bevacizumab or lomustine versus a combination of bevacizumab plus lomustine in patients with recurrent glioblastoma (BELOB trial): a randomised controlled phase 2 trial. Lancet Oncol **15**, 943–953 (2014).
71. Weller, M. & Le Rhun, E. How did lomustine become standard of care in recurrent glioblastoma? Cancer Treat Rev **87**, 102029 (2020).
72. Wick, W. et al. Lomustine and Bevacizumab in Progressive Glioblastoma. N Engl J Med **377**, 1954–1963 (2017).
73. Batchelor, T. T. et al. Phase III randomized trial comparing the efficacy of cediranib as monotherapy, and in combination with lomustine, versus lomustine alone in patients with recurrent glioblastoma. J Clin Oncol **31**, 3212–3218 (2013).
74. Shih, T. & Lindley, C. Bevacizumab: an angiogenesis inhibitor for the treatment of solid malignancies. Clin Ther **28**, 1779–1802 (2006).
75. Weathers, S.-P. & de Groot, J. VEGF Manipulation in Glioblastoma. Oncology (Williston Park) **29**, 720–727 (2015).
76. Cohen, M. H., Gootenberg, J., Keegan, P. & Pazdur, R. FDA drug approval summary: bevacizumab plus FOLFOX4 as second-line treatment of colorectal cancer. Oncologist **12**, 356–361 (2007).
77. Moustakas, A. & Kreisl, T. N. New treatment options in the management of glioblastoma multiforme: a focus on bevacizumab. Onco Targets Ther **3**, 27–38 (2010).
78. Wirsching, H.-G. et al. Bevacizumab plus hypofractionated radiotherapy versus radiotherapy alone in elderly patients with glioblastoma: the randomized, open-label, phase II ARTE trial. Ann Oncol **29**, 1423–1430 (2018).
79. Neyns, B. et al. Stratified phase II trial of cetuximab in patients with recurrent high-grade glioma. Ann Oncol **20**, 1596–1603 (2009).
80. Detti, B. et al. Regorafenib in glioblastoma recurrence: A case report. Cancer Treat Res Commun **26**, 100263 (2021).
81. Cocco, E., Scaltriti, M. & Drilon, A. NTRK fusion-positive cancers and TRK inhibitor therapy. Nat Rev Clin Oncol **15**, 731–747 (2018).
82. Wang, Y., Long, P., Wang, Y. & Ma, W. NTRK Fusions and TRK Inhibitors: Potential Targeted Therapies for Adult Glioblastoma. Front Oncol **10**, 593578 (2020).
83. Zhang, S. & Rabkin, S. D. The discovery and development of oncolytic viruses: are they the future of cancer immunotherapy? Expert Opin Drug Discov **16**, 391–410 (2021).
84. Kaufman, H. L., Kohlhapp, F. J. & Zloza, A. Oncolytic viruses: a new class of immunotherapy drugs. Nat Rev Drug Discov **14**, 642–662 (2015).
85. Martuza, R. L., Malick, A., Markert, J. M., Ruffner, K. L. & Coen, D. M. Experimental therapy of human glioma by means of a genetically engineered virus mutant. Science **252**, 854–856 (1991).
86. Andtbacka, R. H. I. et al. Talimogene Laherparepvec Improves Durable Response Rate in Patients With Advanced Melanoma. J Clin Oncol **33**, 2780–2788 (2015).
87. Kelly, E. & Russell, S. J. History of oncolytic viruses: genesis to genetic engineering. Mol Ther **15**, 651–659 (2007).
88. Stavrakaki, E., Dirven, C. M. F. & Lamfers, M. L. M. Personalizing Oncolytic Virotherapy for Glioblastoma: In Search of Biomarkers for Response. Cancers (Basel) **13**, 614 (2021).
89. Goetz, C. & Gromeier, M. Preparing an oncolytic poliovirus recombinant for clinical application against glioblastoma multiforme. Cytokine Growth Factor Rev **21**, 197–203 (2010).
90. Merrill, M. K. et al. Poliovirus receptor CD155-targeted oncolysis of glioma. Neuro Oncol **6**, 208–217 (2004).
91. Desjardins, A. et al. Recurrent Glioblastoma Treated with Recombinant Poliovirus. N Engl J Med **379**, 150–161 (2018).
92. Carrieri, F. A., Smack, C., Siddiqui, I., Kleinberg, L. R. & Tran, P. T. Tumor Treating Fields: At the Crossroads Between Physics and Biology for Cancer Treatment. Front Oncol **10**, 575992 (2020).
93. Bähr, O., Tabatabai, G., Fietkau, R., Goldbrunner, R. & Glas, M. ACTR-31. The use of ttfields for newly diagnosed GBM patients in Germany in routine clinical care (tiger: ttfields in Germany in routine clinical care). Neuro Oncol **21**, vi20 (2019).
94. Fabian, D. et al. Treatment of Glioblastoma (GBM) with the Addition of Tumor-Treating Fields (TTF): A Review. Cancers (Basel) **11**, E174 (2019).
95. Stupp, R. et al. Effect of Tumor-Treating Fields Plus Maintenance Temozolomide vs Maintenance Temozolomide Alone on Survival in Patients With Glioblastoma: A Randomized Clinical Trial. JAMA **318**, 2306–2316 (2017).
96. Chowdhary, S. A., Ryken, T. & Newton, H. B. Survival outcomes and safety of carmustine wafers in the treatment of high-grade gliomas: a meta-analysis. J Neurooncol **122**, 367–382 (2015).
97. Gururangan, S. et al. Phase I study of Gliadel wafers plus temozolomide in adults with recurrent supratentorial high-grade gliomas. Neuro Oncol **3**, 246–250 (2001).

98. Gutenberg, A. et al. The combination of carmustine wafers and temozolomide for the treatment of malignant gliomas. A comprehensive review of the rationale and clinical experience. J Neurooncol **113**, 163–174 (2013).
99. Basso, J. et al. Hydrogel-Based Drug Delivery Nanosystems for the Treatment of Brain Tumors. Gels **4**, E62 (2018).
100. O'Reilly, M. A. & Hynynen, K. Blood-brain barrier: real-time feedback-controlled focused ultrasound disruption by using an acoustic emissions-based controller. Radiology **263**, 96–106 (2012).
101. Park, S. H. et al. One-Year Outcome of Multiple Blood–Brain Barrier Disruptions With Temozolomide for the Treatment of Glioblastoma. Front Oncol **10**, 1663 (2020).
102. Hong, X., Chedid, K. & Kalkanis, S. N. Glioblastoma cell line-derived spheres in serum-containing medium versus serum-free medium: a comparison of cancer stem cell properties. Int J Oncol **41**, 1693–1700 (2012).
103. Allen, M., Bjerke, M., Edlund, H., Nelander, S. & Westermark, B. Origin of the U87MG glioma cell line: Good news and bad news. Sci Transl Med **8**, 354re3 (2016).
104. Dolgin, E. Venerable brain-cancer cell line faces identity crisis. Nature **537**, 149–150 (2016).
105. Li, A. et al. Genomic changes and gene expression profiles reveal that established glioma cell lines are poorly representative of primary human gliomas. Mol Cancer Res **6**, 21–30 (2008).
106. Torsvik, A. et al. U-251 revisited: genetic drift and phenotypic consequences of long-term cultures of glioblastoma cells. Cancer Med **3**, 812–824 (2014).
107. Frenster, J. D. & Placantonakis, D. G. Establishing Primary Human Glioblastoma Tumorsphere Cultures from Operative Specimens. Methods Mol Biol **1741**, 63–69 (2018).
108. Seidel, S., Garvalov, B. K. & Acker, T. Isolation and culture of primary glioblastoma cells from human tumor specimens. Methods Mol Biol **1235**, 263–275 (2015).
109. Balvers, R. K. et al. Serum-free culture success of glial tumors is related to specific molecular profiles and expression of extracellular matrix-associated gene modules. Neuro Oncol **15**, 1684–1695 (2013).
110. Davis, B. et al. Comparative genomic and genetic analysis of glioblastoma-derived brain tumor-initiating cells and their parent tumors. Neuro Oncol **18**, 350–360 (2016).
111. Ledur, P. F., Onzi, G. R., Zong, H. & Lenz, G. Culture conditions defining glioblastoma cells behavior: what is the impact for novel discoveries? Oncotarget **8**, 69185–69197 (2017).
112. Lee, J. et al. Tumor stem cells derived from glioblastomas cultured in bFGF and EGF more closely mirror the phenotype and genotype of primary tumors than do serum-cultured cell lines. Cancer Cell **9**, 391–403 (2006).
113. Spinelli, C. et al. Molecular subtypes and differentiation programmes of glioma stem cells as determinants of extracellular vesicle profiles and endothelial cell-stimulating activities. J Extracell Vesicles **7**, 1490144 (2018).
114. Taïb, B. et al. Lipid accumulation and oxidation in glioblastoma multiforme. Sci Rep **9**, 19593 (2019).
115. Baskaran, S. et al. Primary glioblastoma cells for precision medicine: a quantitative portrait of genomic (in)stability during the first 30 passages. Neuro Oncol **20**, 1080–1091 (2018).
116. Gomez-Roman, N., Stevenson, K., Gilmour, L., Hamilton, G. & Chalmers, A. J. A novel 3D human glioblastoma cell culture system for modeling drug and radiation responses. Neuro Oncol **19**, 229–241 (2017).
117. Pollard, S. M. et al. Glioma stem cell lines expanded in adherent culture have tumor-specific phenotypes and are suitable for chemical and genetic screens. Cell Stem Cell **4**, 568–580 (2009).
118. Rahman, M. et al. Neurosphere and adherent culture conditions are equivalent for malignant glioma stem cell lines. Anat Cell Biol **48**, 25–35 (2015).
119. Chen, J.-W. E., Pedron, S. & Harley, B. A. C. The Combined Influence of Hydrogel Stiffness and Matrix-Bound Hyaluronic Acid Content on Glioblastoma Invasion. Macromol Biosci **17**, (2017).
120. Grundy, T. J. et al. Differential response of patient-derived primary glioblastoma cells to environmental stiffness. Sci Rep **6**, 23353 (2016).
121. Hughes, C. S., Postovit, L. M. & Lajoie, G. A. Matrigel: a complex protein mixture required for optimal growth of cell culture. Proteomics **10**, 1886–1890 (2010).
122. Calabrese, C. et al. A perivascular niche for brain tumor stem cells. Cancer Cell **11**, 69–82 (2007).
123. Musah-Eroje, A. & Watson, S. A novel 3D in vitro model of glioblastoma reveals resistance to temozolomide which was potentiated by hypoxia. J Neurooncol **142**, 231–240 (2019).
124. Stöhr, D. et al. Stress-induced TRAILR2 expression overcomes TRAIL resistance in cancer cell spheroids. Cell Death Differ **27**, 3037–3052 (2020).
125. Joseph, J. V. et al. Serum-Induced Differentiation of Glioblastoma Neurospheres Leads to Enhanced Migration/Invasion Capacity That Is Associated with Increased MMP9. PLoS One **10**, e0145393 (2015).
126. Ladiwala, U., Basu, H. & Mathur, D. Assembling neurospheres: dynamics of neural progenitor/stem cell aggregation probed using an optical trap. PLoS One **7**, e38613 (2012).
127. Agro, L. & O'Brien, C. In vitro and in vivo Limiting Dilution Assay for Colorectal Cancer. Bio Protoc **5**, 1–11 (2015).
128. Hu, Y. & Smyth, G. K. ELDA: extreme limiting dilution analysis for comparing depleted and enriched populations in stem cell and other assays. J Immunol Methods **347**, 70–78 (2009).
129. De Witt Hamer, P. C. et al. The genomic profile of human malignant glioma is altered early in primary cell culture and preserved in spheroids. Oncogene **27**, 2091–2096 (2008).
130. Merz, F. et al. Organotypic slice cultures of human glioblastoma reveal different susceptibilities to treatments. Neuro Oncol **15**, 670–681 (2013).
131. Heffernan, J. M., Overstreet, D. J., Le, L. D., Vernon, B. L. & Sirianni, R. W. Bioengineered Scaffolds for 3D Analysis of Glioblastoma Proliferation and Invasion. Ann Biomed Eng **43**, 1965–1977 (2015).

132. Li, Q. et al. Scalable Culturing of Primary Human Glioblastoma Tumor-Initiating Cells with a Cell-Friendly Culture System. Sci Rep **8**, 3531 (2018).
133. Lancaster, M. A. & Knoblich, J. A. Generation of cerebral organoids from human pluripotent stem cells. Nat Protoc **9**, 2329–2340 (2014).
134. Lancaster, M. A. et al. Cerebral organoids model human brain development and microcephaly. Nature **501**, 373–379 (2013).
135. Hubert, C. G. et al. A Three-Dimensional Organoid Culture System Derived from Human Glioblastomas Recapitulates the Hypoxic Gradients and Cancer Stem Cell Heterogeneity of Tumors Found In Vivo. Cancer Res **76**, 2465–2477 (2016).
136. Jacob, F. et al. A Patient-Derived Glioblastoma Organoid Model and Biobank Recapitulates Inter- and Intra-tumoral Heterogeneity. Cell **180**, 188-204.e22 (2020).
137. Ananthanarayanan, B., Kim, Y. & Kumar, S. Elucidating the mechanobiology of malignant brain tumors using a brain matrix-mimetic hyaluronic acid hydrogel platform. Biomaterials **32**, 7913–7923 (2011).
138. Fischbach, C. et al. Engineering tumors with 3D scaffolds. Nat Methods **4**, 855–860 (2007).
139. Kievit, F. M. et al. Chitosan-alginate 3D scaffolds as a mimic of the glioma tumor microenvironment. Biomaterials **31**, 5903–5910 (2010).
140. Derakhshanfar, S. et al. 3D bioprinting for biomedical devices and tissue engineering: A review of recent trends and advances. Bioact Mater **3**, 144–156 (2018).
141. Heinrich, M. A. et al. 3D-Bioprinted Mini-Brain: A Glioblastoma Model to Study Cellular Interactions and Therapeutics. Adv Mater **31**, e1806590 (2019).
142. Hermida, M. A. et al. Three dimensional in vitro models of cancer: Bioprinting multilineage glioblastoma models. Adv Biol Regul **75**, 100658 (2020).
143. Fuchs, Y. & Steller, H. Programmed cell death in animal development and disease. Cell **147**, 742–758 (2011).
144. Büttner, S. et al. Why yeast cells can undergo apoptosis: death in times of peace, love, and war. J Cell Biol **175**, 521–525 (2006).
145. Galluzzi, L. et al. Molecular mechanisms of cell death: recommendations of the Nomenclature Committee on Cell Death 2018. Cell Death Differ **25**, 486–541 (2018).
146. Kerr, J. F., Wyllie, A. H. & Currie, A. R. Apoptosis: a basic biological phenomenon with wide-ranging implications in tissue kinetics. Br J Cancer **26**, 239–257 (1972).
147. Saraste, A. & Pulkki, K. Morphologic and biochemical hallmarks of apoptosis. Cardiovasc Res **45**, 528–537 (2000).
148. Locksley, R. M., Killeen, N. & Lenardo, M. J. The TNF and TNF receptor superfamilies: integrating mammalian biology. Cell **104**, 487–501 (2001).
149. Gonzalvez, F. & Ashkenazi, A. New insights into apoptosis signaling by Apo2L/TRAIL. Oncogene **29**, 4752–4765 (2010).
150. Walczak, H. Death receptor-ligand systems in cancer, cell death, and inflammation. Cold Spring Harb Perspect Biol **5**, a008698 (2013).
151. Guicciardi, M. E. & Gores, G. J. Life and death by death receptors. FASEB J **23**, 1625–1637 (2009).
152. Dhuriya, Y. K. & Sharma, D. Necroptosis: a regulated inflammatory mode of cell death. J Neuroinflammation **15**, 199 (2018).
153. Grootjans, S., Vanden Berghe, T. & Vandenabeele, P. Initiation and execution mechanisms of necroptosis: an overview. Cell Death Differ **24**, 1184–1195 (2017).
154. Galluzzi, L., Brenner, C., Morselli, E., Touat, Z. & Kroemer, G. Viral control of mitochondrial apoptosis. PLoS Pathog **4**, e1000018 (2008).
155. Jendrossek, V. The intrinsic apoptosis pathways as a target in anticancer therapy. Curr Pharm Biotechnol **13**, 1426–1438 (2012).
156. Redza-Dutordoir, M. & Averill-Bates, D. A. Activation of apoptosis signalling pathways by reactive oxygen species. Biochim Biophys Acta **1863**, 2977–2992 (2016).
157. Zhou, L., Yuan, R. & Lanata, S. Molecular mechanisms of irradiation-induced apoptosis. Front Biosci **8**, d9-19 (2003).
158. Chipuk, J. E., Bouchier-Hayes, L. & Green, D. R. Mitochondrial outer membrane permeabilization during apoptosis: the innocent bystander scenario. Cell Death Differ **13**, 1396–1402 (2006).
159. Ehrlich, S., Infante-Duarte, C., Seeger, B. & Zipp, F. Regulation of soluble and surface-bound TRAIL in human T cells, B cells, and monocytes. Cytokine **24**, 244–253 (2003).
160. Falschlehner, C., Schaefer, U. & Walczak, H. Following TRAIL's path in the immune system. Immunology **127**, 145–154 (2009).
161. Kemp, T. J., Elzey, B. D. & Griffith, T. S. Plasmacytoid dendritic cell-derived IFN-alpha induces TNF-related apoptosis-inducing ligand/Apo-2L-mediated antitumor activity by human monocytes following CpG oligodeoxynucleotide stimulation. J Immunol **171**, 212–218 (2003).
162. Liu, S., Yu, Y., Zhang, M., Wang, W. & Cao, X. The involvement of TNF-alpha-related apoptosis-inducing ligand in the enhanced cytotoxicity of IFN-beta-stimulated human dendritic cells to tumor cells. J Immunol **166**, 5407–5415 (2001).
163. Takeda, K. et al. Involvement of tumor necrosis factor-related apoptosis-inducing ligand in NK cell-mediated and IFN-gamma-dependent suppression of subcutaneous tumor growth. Cell Immunol **214**, 194–200 (2001).
164. Walczak, H. et al. Tumoricidal activity of tumor necrosis factor-related apoptosis-inducing ligand in vivo. Nat Med **5**, 157–163 (1999).

165. Mühlenbeck, F. et al. The tumor necrosis factor-related apoptosis-inducing ligand receptors TRAIL-R1 and TRAIL-R2 have distinct cross-linking requirements for initiation of apoptosis and are non-redundant in JNK activation. J Biol Chem **275**, 32208–32213 (2000).
166. Truneh, A. et al. Temperature-sensitive differential affinity of TRAIL for its receptors. DR5 is the highest affinity receptor. J Biol Chem **275**, 23319–23325 (2000).
167. Mérino, D. et al. Differential inhibition of TRAIL-mediated DR5-DISC formation by decoy receptors 1 and 2. Mol Cell Biol **26**, 7046–7055 (2006).
168. Kim, K., Fisher, M. J., Xu, S. Q. & el-Deiry, W. S. Molecular determinants of response to TRAIL in killing of normal and cancer cells. Clin Cancer Res **6**, 335–346 (2000).
169. Thorburn, A., Behbakht, K. & Ford, H. TRAIL receptor-targeted therapeutics: resistance mechanisms and strategies to avoid them. Drug Resist Updat **11**, 17–24 (2008).
170. Micheau, O. Regulation of TNF-Related Apoptosis-Inducing Ligand Signaling by Glycosylation. Int J Mol Sci **19**, E715 (2018).
171. Seyrek, K., Richter, M. & Lavrik, I. N. Decoding the sweet regulation of apoptosis: the role of glycosylation and galectins in apoptotic signaling pathways. Cell Death Differ **26**, 981–993 (2019).
172. Wagner, K. W. et al. Death-receptor O-glycosylation controls tumor-cell sensitivity to the proapoptotic ligand Apo2L/TRAIL. Nat Med **13**, 1070–1077 (2007).
173. Wu, Y.-H., Yang, C.-Y., Chien, W.-L., Lin, K.-I. & Lai, M.-Z. Removal of syndecan-1 promotes TRAIL-induced apoptosis in myeloma cells. J Immunol **188**, 2914–2921 (2012).
174. Jin, Z., McDonald, E. R., Dicker, D. T. & El-Deiry, W. S. Deficient tumor necrosis factor-related apoptosis-inducing ligand (TRAIL) death receptor transport to the cell surface in human colon cancer cells selected for resistance to TRAIL-induced apoptosis. J Biol Chem **279**, 35829–35839 (2004).
175. Reis, C. R., Chen, P.-H., Bendris, N. & Schmid, S. L. TRAIL-death receptor endocytosis and apoptosis are selectively regulated by dynamin-1 activation. Proc Natl Acad Sci U S A **114**, 504–509 (2017).
176. Emery, J. G. et al. Osteoprotegerin is a receptor for the cytotoxic ligand TRAIL. J Biol Chem **273**, 14363–14367 (1998).
177. Simonet, W. S. et al. Osteoprotegerin: a novel secreted protein involved in the regulation of bone density. Cell **89**, 309–319 (1997).
178. Tsuda, E. et al. Isolation of a novel cytokine from human fibroblasts that specifically inhibits osteoclastogenesis. Biochem Biophys Res Commun **234**, 137–142 (1997).
179. Reid, P. & Holen, I. Pathophysiological roles of osteoprotegerin (OPG). Eur J Cell Biol **88**, 1–17 (2009).
180. Beyer, K. et al. Interactions of Tumor Necrosis Factor-Related Apoptosis-Inducing Ligand (TRAIL) with the Immune System: Implications for Inflammation and Cancer. Cancers (Basel) **11**, E1161 (2019).
181. Fu, T.-M. et al. Cryo-EM Structure of Caspase-8 Tandem DED Filament Reveals Assembly and Regulation Mechanisms of the Death-Inducing Signaling Complex. Mol Cell **64**, 236–250 (2016).
182. Schleich, K. et al. Molecular architecture of the DED chains at the DISC: regulation of procaspase-8 activation by short DED proteins c-FLIP and procaspase-8 prodomain. Cell Death Differ **23**, 681–694 (2016).
183. Hughes, M. A. et al. Co-operative and Hierarchical Binding of c-FLIP and Caspase-8: A Unified Model Defines How c-FLIP Isoforms Differentially Control Cell Fate. Mol Cell **61**, 834–849 (2016).
184. Humphreys, L. M. et al. A revised model of TRAIL-R2 DISC assembly explains how FLIP(L) can inhibit or promote apoptosis. EMBO Rep **21**, e49254 (2020).
185. Fox, J. L. et al. Cryo-EM structural analysis of FADD:Caspase-8 complexes defines the catalytic dimer architecture for co-ordinated control of cell fate. Nat Commun **12**, 819 (2021).
186. Chang, D. W., Xing, Z., Capacio, V. L., Peter, M. E. & Yang, X. Interdimer processing mechanism of procaspase-8 activation. EMBO J **22**, 4132–4142 (2003).
187. Keller, N., Mares, J., Zerbe, O. & Grütter, M. G. Structural and biochemical studies on procaspase-8: new insights on initiator caspase activation. Structure **17**, 438–448 (2009).
188. Scaffidi, C. et al. Two CD95 (APO-1/Fas) signaling pathways. EMBO J **17**, 1675–1687 (1998).
189. Aldridge, B. B., Gaudet, S., Lauffenburger, D. A. & Sorger, P. K. Lyapunov exponents and phase diagrams reveal multi-factorial control over TRAIL-induced apoptosis. Mol Syst Biol **7**, 553 (2011).
190. Logue, S. E. & Martin, S. J. Caspase activation cascades in apoptosis. Biochem Soc Trans **36**, 1–9 (2008).
191. Elmore, S. Apoptosis: a review of programmed cell death. Toxicol Pathol **35**, 495–516 (2007).
192. Krysko, D. V., D'Herde, K. & Vandenabeele, P. Clearance of apoptotic and necrotic cells and its immunological consequences. Apoptosis **11**, 1709–1726 (2006).
193. Mills, J. C., Stone, N. L. & Pittman, R. N. Extranuclear apoptosis. The role of the cytoplasm in the execution phase. J Cell Biol **146**, 703–708 (1999).
194. Ndozangue-Touriguine, O., Hamelin, J. & Bréard, J. Cytoskeleton and apoptosis. Biochem Pharmacol **76**, 11–18 (2008).
195. Kale, J., Osterlund, E. J. & Andrews, D. W. BCL-2 family proteins: changing partners in the dance towards death. Cell Death Differ **25**, 65–80 (2018).
196. Reyna, D. E. & Gavathiotis, E. Self-regulation of BAX-induced cell death. Oncotarget **7**, 66326–66327 (2016).
197. Ichim, G. et al. Limited mitochondrial permeabilization causes DNA damage and genomic instability in the absence of cell death. Mol Cell **57**, 860–872 (2015).
198. Xu, Y., Surman, D. R. & Ripley, R. T. Minority MOMP: a toxic, slow demise. Oncotarget **11**, 3559–3561 (2020).
199. Martinou, J.-C. & Youle, R. J. Mitochondria in apoptosis: Bcl-2 family members and mitochondrial dynamics. Dev Cell **21**, 92–101 (2011).

200. Knight, T., Luedtke, D., Edwards, H., Taub, J. W. & Ge, Y. A delicate balance - The BCL-2 family and its role in apoptosis, oncogenesis, and cancer therapeutics. Biochem Pharmacol **162**, 250–261 (2019).
201. Singh, R., Letai, A. & Sarosiek, K. Regulation of apoptosis in health and disease: the balancing act of BCL-2 family proteins. Nat Rev Mol Cell Biol **20**, 175–193 (2019).
202. Opferman, J. T. Attacking cancer's Achilles heel: antagonism of anti-apoptotic BCL-2 family members. FEBS J **283**, 2661–2675 (2016).
203. Kim, H.-E., Du, F., Fang, M. & Wang, X. Formation of apoptosome is initiated by cytochrome c-induced dATP hydrolysis and subsequent nucleotide exchange on Apaf-1. Proc Natl Acad Sci U S A **102**, 17545–17550 (2005).
204. Yuan, S. & Akey, C. W. Apoptosome structure, assembly, and procaspase activation. Structure **21**, 501–515 (2013).
205. Bao, Q. & Shi, Y. Apoptosome: a platform for the activation of initiator caspases. Cell Death Differ **14**, 56–65 (2007).
206. Cain, K. et al. Apaf-1 oligomerizes into biologically active approximately 700-kDa and inactive approximately 1.4-MDa apoptosome complexes. J Biol Chem **275**, 6067–6070 (2000).
207. Li, Y. et al. Mechanistic insights into caspase-9 activation by the structure of the apoptosome holoenzyme. Proc Natl Acad Sci U S A **114**, 1542–1547 (2017).
208. Denault, J.-B., Eckelman, B. P., Shin, H., Pop, C. & Salvesen, G. S. Caspase 3 attenuates XIAP (X-linked inhibitor of apoptosis protein)-mediated inhibition of caspase 9. Biochem J **405**, 11–19 (2007).
209. Fujita, E., Egashira, J., Urase, K., Kuida, K. & Momoi, T. Caspase-9 processing by caspase-3 via a feedback amplification loop in vivo. Cell Death Differ **8**, 335–344 (2001).
210. Ricci, J.-E. et al. Disruption of mitochondrial function during apoptosis is mediated by caspase cleavage of the p75 subunit of complex I of the electron transport chain. Cell **117**, 773–786 (2004).
211. Saelens, X. et al. Toxic proteins released from mitochondria in cell death. Oncogene **23**, 2861–2874 (2004).
212. Kiraz, Y., Adan, A., Kartal Yandim, M. & Baran, Y. Major apoptotic mechanisms and genes involved in apoptosis. Tumour Biol **37**, 8471–8486 (2016).
213. MacFarlane, M., Merrison, W., Bratton, S. B. & Cohen, G. M. Proteasome-mediated degradation of Smac during apoptosis: XIAP promotes Smac ubiquitination in vitro. J Biol Chem **277**, 36611–36616 (2002).
214. Yang, Y. L. & Li, X. M. The IAP family: endogenous caspase inhibitors with multiple biological activities. Cell Res **10**, 169–177 (2000).
215. Srinivasula, S. M. et al. A conserved XIAP-interaction motif in caspase-9 and Smac/DIABLO regulates caspase activity and apoptosis. Nature **410**, 112–116 (2001).
216. Vaux, D. L. & Silke, J. Mammalian mitochondrial IAP binding proteins. Biochemical and Biophysical Research Communications **304**, 499–504 (2003).
217. Schleich, K. & Lavrik, I. N. Mathematical modeling of apoptosis. Cell Commun Signal **11**, 44 (2013).
218. Varfolomeev, E. et al. Molecular determinants of kinase pathway activation by Apo2 ligand/tumor necrosis factor-related apoptosis-inducing ligand. J Biol Chem **280**, 40599–40608 (2005).
219. Song, J. H. et al. Lipid rafts and nonrafts mediate tumor necrosis factor related apoptosis-inducing ligand induced apoptotic and nonapoptotic signals in non small cell lung carcinoma cells. Cancer Res **67**, 6946–6955 (2007).
220. Meurette, O. et al. TRAIL induces receptor-interacting protein 1-dependent and caspase-dependent necrosis-like cell death under acidic extracellular conditions. Cancer Res **67**, 218–226 (2007).
221. Degterev, A., Ofengeim, D. & Yuan, J. Targeting RIPK1 for the treatment of human diseases. Proc Natl Acad Sci U S A **116**, 9714–9722 (2019).
222. Feoktistova, M. et al. cIAPs block Ripoptosome formation, a RIP1/caspase-8 containing intracellular cell death complex differentially regulated by cFLIP isoforms. Mol Cell **43**, 449–463 (2011).
223. Jouan-Lanhouet, S. et al. TRAIL induces necroptosis involving RIPK1/RIPK3-dependent PARP-1 activation. Cell Death Differ **19**, 2003–2014 (2012).
224. Dillon, C. P. et al. RIPK1 blocks early postnatal lethality mediated by caspase-8 and RIPK3. Cell **157**, 1189–1202 (2014).
225. Varfolomeev, E. E. et al. Targeted disruption of the mouse Caspase 8 gene ablates cell death induction by the TNF receptors, Fas/Apo1, and DR3 and is lethal prenatally. Immunity **9**, 267–276 (1998).
226. Li, J. et al. The RIP1/RIP3 necrosome forms a functional amyloid signaling complex required for programmed necrosis. Cell **150**, 339–350 (2012).
227. Sun, L. et al. Mixed lineage kinase domain-like protein mediates necrosis signaling downstream of RIP3 kinase. Cell **148**, 213–227 (2012).
228. Degli-Esposti, M. A. et al. The novel receptor TRAIL-R4 induces NF-kappaB and protects against TRAIL-mediated apoptosis, yet retains an incomplete death domain. Immunity **7**, 813–820 (1997).
229. Schneider, P. et al. TRAIL receptors 1 (DR4) and 2 (DR5) signal FADD-dependent apoptosis and activate NF-kappaB. Immunity **7**, 831–836 (1997).
230. Lin, Y. et al. The death domain kinase RIP is essential for TRAIL (Apo2L)-induced activation of IkappaB kinase and c-Jun N-terminal kinase. Mol Cell Biol **20**, 6638–6645 (2000).
231. Lee, H. H., Dadgostar, H., Cheng, Q., Shu, J. & Cheng, G. NF-kappaB-mediated up-regulation of Bcl-x and Bfl-1/A1 is required for CD40 survival signaling in B lymphocytes. Proc Natl Acad Sci U S A **96**, 9136–9141 (1999).
232. Micheau, O., Lens, S., Gaide, O., Alevizopoulos, K. & Tschopp, J. NF-kappaB signals induce the expression of c-FLIP. Mol Cell Biol **21**, 5299–5305 (2001).

233. Wang, C. Y., Mayo, M. W., Korneluk, R. G., Goeddel, D. V. & Baldwin, A. S. NF-kappaB antiapoptosis: induction of TRAF1 and TRAF2 and c-IAP1 and c-IAP2 to suppress caspase-8 activation. Science **281**, 1680–1683 (1998).
234. Wajant, H. TRAIL and NFkappaB signaling--a complex relationship. Vitam Horm **67**, 101–132 (2004).
235. Azijli, K., Weyhenmeyer, B., Peters, G. J., de Jong, S. & Kruyt, F. a. E. Non-canonical kinase signaling by the death ligand TRAIL in cancer cells: discord in the death receptor family. Cell Death Differ **20**, 858–868 (2013).
236. von Karstedt, S., Montinaro, A. & Walczak, H. Exploring the TRAILs less travelled: TRAIL in cancer biology and therapy. Nat Rev Cancer **17**, 352–366 (2017).
237. Secchiero, P. et al. TRAIL promotes the survival and proliferation of primary human vascular endothelial cells by activating the Akt and ERK pathways. Circulation **107**, 2250–2256 (2003).
238. Lafont, E. et al. The linear ubiquitin chain assembly complex regulates TRAIL-induced gene activation and cell death. EMBO J **36**, 1147–1166 (2017).
239. Ashkenazi, A. et al. Safety and antitumor activity of recombinant soluble Apo2 ligand. J Clin Invest **104**, 155–162 (1999).
240. Pitti, R. M. et al. Induction of apoptosis by Apo-2 ligand, a new member of the tumor necrosis factor cytokine family. J Biol Chem **271**, 12687–12690 (1996).
241. O'Connor, L., Harris, A. W. & Strasser, A. CD95 (Fas/APO-1) and p53 signal apoptosis independently in diverse cell types. Cancer Res **60**, 1217–1220 (2000).
242. Yang, A., Wilson, N. S. & Ashkenazi, A. Proapoptotic DR4 and DR5 signaling in cancer cells: toward clinical translation. Curr Opin Cell Biol **22**, 837–844 (2010).
243. Pan, Y. et al. Evaluation of pharmacodynamic biomarkers in a Phase 1a trial of dulanermin (rhApo2L/TRAIL) in patients with advanced tumours. Br J Cancer **105**, 1830–1838 (2011).
244. Quintavalle, C. & Condorelli, G. Dulanermin in cancer therapy: still much to do. Transl Lung Cancer Res **1**, 158–159 (2012).
245. Soria, J.-C. et al. Randomized phase II study of dulanermin in combination with paclitaxel, carboplatin, and bevacizumab in advanced non-small-cell lung cancer. J Clin Oncol **29**, 4442–4451 (2011).
246. Wainberg, Z. A. et al. A phase 1B study of dulanermin in combination with modified FOLFOX6 plus bevacizumab in patients with metastatic colorectal cancer. Clin Colorectal Cancer **12**, 248–254 (2013).
247. Ouyang, X. et al. Phase III study of dulanermin (recombinant human tumor necrosis factor-related apoptosis-inducing ligand/Apo2 ligand) combined with vinorelbine and cisplatin in patients with advanced non-small-cell lung cancer. Invest New Drugs **36**, 315–322 (2018).
248. Lemke, J., von Karstedt, S., Zinngrebe, J. & Walczak, H. Getting TRAIL back on track for cancer therapy. Cell Death Differ **21**, 1350–1364 (2014).
249. Snajdauf, M. et al. The TRAIL in the Treatment of Human Cancer: An Update on Clinical Trials. Front Mol Biosci **8**, 628332 (2021).
250. Dhein, J. et al. Induction of apoptosis by monoclonal antibody anti-APO-1 class switch variants is dependent on cross-linking of APO-1 cell surface antigens. J Immunol **149**, 3166–3173 (1992).
251. Wajant, H. Molecular Mode of Action of TRAIL Receptor Agonists-Common Principles and Their Translational Exploitation. Cancers (Basel) **11**, E954 (2019).
252. Wajant, H. et al. Differential activation of TRAIL-R1 and -2 by soluble and membrane TRAIL allows selective surface antigen-directed activation of TRAIL-R2 by a soluble TRAIL derivative. Oncogene **20**, 4101–4106 (2001).
253. Siegemund, M. et al. An optimized antibody-single-chain TRAIL fusion protein for cancer therapy. MAbs **8**, 879–891 (2016).
254. Hutt, M. et al. Superior Properties of Fc-comprising scTRAIL Fusion Proteins. Mol Cancer Ther **16**, 2792–2802 (2017).
255. Kontermann, R. E. Strategies to extend plasma half-lives of recombinant antibodies. BioDrugs **23**, 93–109 (2009).
256. Fulda, S., Wick, W., Weller, M. & Debatin, K.-M. Smac agonists sensitize for Apo2L/TRAIL- or anticancer drug-induced apoptosis and induce regression of malignant glioma in vivo. Nat Med **8**, 808–815 (2002).
257. Lincoln, F. A. et al. Sensitization of glioblastoma cells to TRAIL-induced apoptosis by IAP- and Bcl-2 antagonism. Cell Death Dis **9**, 1112 (2018).
258. Trivedi, R. & Mishra, D. P. Trailing TRAIL Resistance: Novel Targets for TRAIL Sensitization in Cancer Cells. Front Oncol **5**, 69 (2015).
259. Weyhenmeyer, B. C. et al. Predicting the cell death responsiveness and sensitization of glioma cells to TRAIL and temozolomide. Oncotarget **7**, 61295–61311 (2016).
260. Cingöz, A. et al. Generation of TRAIL-resistant cell line models reveals distinct adaptive mechanisms for acquired resistance and re-sensitization. Oncogene **40**, 3201–3216 (2021).
261. Zhang, L. & Fang, B. Mechanisms of resistance to TRAIL-induced apoptosis in cancer. Cancer Gene Ther **12**, 228–237 (2005).
262. Hellwig, C. T. & Rehm, M. TRAIL signaling and synergy mechanisms used in TRAIL-based combination therapies. Mol Cancer Ther **11**, 3–13 (2012).
263. Refaat, A., Abd-Rabou, A. & Reda, A. TRAIL combinations: The new 'trail' for cancer therapy (Review). Oncol Lett **7**, 1327–1332 (2014).
264. von Karstedt, S. et al. Cancer cell-autonomous TRAIL-R signaling promotes KRAS-driven cancer progression, invasion, and metastasis. Cancer Cell **27**, 561–573 (2015).

265. Booth, N. L. et al. A cell-based high-throughput screen to identify synergistic TRAIL sensitizers. Cancer Immunol Immunother **58**, 1229–1244 (2009).
266. Kretz, A.-L. et al. TRAILblazing Strategies for Cancer Treatment. Cancers (Basel) **11**, E456 (2019).
267. Fels, C. et al. Bcl-2 expression in higher-grade human glioma: a clinical and experimental study. J Neurooncol **48**, 207–216 (2000).
268. Kehr, S. & Vogler, M. It's time to die: BH3 mimetics in solid tumors. Biochim Biophys Acta Mol Cell Res **1868**, 118987 (2021).
269. Villalobos-Ortiz, M., Ryan, J., Mashaka, T. N., Opferman, J. T. & Letai, A. BH3 profiling discriminates on-target small molecule BH3 mimetics from putative mimetics. Cell Death Differ **27**, 999–1007 (2020).
270. Hetschko, H. et al. Pharmacological inhibition of Bcl-2 family members reactivates TRAIL-induced apoptosis in malignant glioma. J Neurooncol **86**, 265–272 (2008).
271. Roberts, A. W. et al. Targeting BCL2 with Venetoclax in Relapsed Chronic Lymphocytic Leukemia. N Engl J Med **374**, 311–322 (2016).
272. Kotschy, A. et al. The MCL1 inhibitor S63845 is tolerable and effective in diverse cancer models. Nature **538**, 477–482 (2016).
273. Lessene, G. et al. Structure-guided design of a selective BCL-X(L) inhibitor. Nat Chem Biol **9**, 390–397 (2013).
274. Ito, S. Proteasome Inhibitors for the Treatment of Multiple Myeloma. Cancers (Basel) **12**, 265 (2020).
275. Moreau, P. et al. Proteasome inhibitors in multiple myeloma: 10 years later. Blood **120**, 947–959 (2012).
276. Dantuma, N. P., Lindsten, K., Glas, R., Jellne, M. & Masucci, M. G. Short-lived green fluorescent proteins for quantifying ubiquitin/proteasome-dependent proteolysis in living cells. Nat Biotechnol **18**, 538–543 (2000).
277. Orlowski, R. Z. The role of the ubiquitin-proteasome pathway in apoptosis. Cell Death Differ **6**, 303–313 (1999).
278. Xu, H. & Ren, D. Lysosomal physiology. Annu Rev Physiol **77**, 57–80 (2015).
279. Schweitzer, A. et al. Structure of the human 26S proteasome at a resolution of 3.9 Å. Proc Natl Acad Sci U S A **113**, 7816–7821 (2016).
280. Groll, M., Koguchi, Y., Huber, R. & Kohno, J. Crystal structure of the 20 S proteasome:TMC-95A complex: a non-covalent proteasome inhibitor. J Mol Biol **311**, 543–548 (2001).
281. Glickman, M. H. & Ciechanover, A. The ubiquitin-proteasome proteolytic pathway: destruction for the sake of construction. Physiol Rev **82**, 373–428 (2002).
282. Tanaka, K. The proteasome: overview of structure and functions. Proc Jpn Acad Ser B Phys Biol Sci **85**, 12–36 (2009).
283. Marshall, R. S. & Vierstra, R. D. Dynamic Regulation of the 26S Proteasome: From Synthesis to Degradation. Front Mol Biosci **6**, 40 (2019).
284. Bard, J. A. M. et al. Structure and Function of the 26S Proteasome. Annu Rev Biochem **87**, 697–724 (2018).
285. Köhler, A. et al. The axial channel of the proteasome core particle is gated by the Rpt2 ATPase and controls both substrate entry and product release. Mol Cell **7**, 1143–1152 (2001).
286. Livneh, I., Cohen-Kaplan, V., Cohen-Rosenzweig, C., Avni, N. & Ciechanover, A. The life cycle of the 26S proteasome: from birth, through regulation and function, and onto its death. Cell Res **26**, 869–885 (2016).
287. Nakagawa, T. & Nakayama, K. Protein monoubiquitylation: targets and diverse functions. Genes Cells **20**, 543–562 (2015).
288. Deol, K. K., Lorenz, S. & Strieter, E. R. Enzymatic Logic of Ubiquitin Chain Assembly. Front Physiol **10**, 835 (2019).
289. Park, C.-W. & Ryu, K.-Y. Cellular ubiquitin pool dynamics and homeostasis. BMB Rep **47**, 475–482 (2014).
290. Kane, R. C., Bross, P. F., Farrell, A. T. & Pazdur, R. Velcade: U.S. FDA approval for the treatment of multiple myeloma progressing on prior therapy. Oncologist **8**, 508–513 (2003).
291. Sakamoto, K. M. et al. Development of Protacs to target cancer-promoting proteins for ubiquitination and degradation. Mol Cell Proteomics **2**, 1350–1358 (2003).
292. Swords, R. T. et al. Pevonedistat (MLN4924), a First-in-Class NEDD8-activating enzyme inhibitor, in patients with acute myeloid leukaemia and myelodysplastic syndromes: a phase 1 study. Br J Haematol **169**, 534–543 (2015).
293. Harer, S. L., Bhatia, M. S. & Bhatia, N. M. Proteasome inhibitors mechanism; source for design of newer therapeutic agents. J Antibiot (Tokyo) **65**, 279–288 (2012).
294. Manasanch, E. E. & Orlowski, R. Z. Proteasome inhibitors in cancer therapy. Nat Rev Clin Oncol **14**, 417–433 (2017).
295. Zhang, X., Adwal, A., Turner, A. G., Callen, D. F. & Abell, A. D. New Peptidomimetic Boronates for Selective Inhibition of the Chymotrypsin-like Activity of the 26S Proteasome. ACS Med Chem Lett **7**, 1039–1043 (2016).
296. Crawford, L. J. A. et al. Comparative selectivity and specificity of the proteasome inhibitors BzLLLCOCHO, PS-341, and MG-132. Cancer Res **66**, 6379–6386 (2006).
297. Luo, J.-L., Kamata, H. & Karin, M. IKK/NF-kappaB signaling: balancing life and death--a new approach to cancer therapy. J Clin Invest **115**, 2625–2632 (2005).
298. Juvekar, A. et al. Bortezomib induces nuclear translocation of IκBα resulting in gene-specific suppression of NF-κB--dependent transcription and induction of apoptosis in CTCL. Mol Cancer Res **9**, 183–194 (2011).
299. Karin, M., Cao, Y., Greten, F. R. & Li, Z.-W. NF-kappaB in cancer: from innocent bystander to major culprit. Nat Rev Cancer **2**, 301–310 (2002).

300. Amiri, K. I., Horton, L. W., LaFleur, B. J., Sosman, J. A. & Richmond, A. Augmenting chemosensitivity of malignant melanoma tumors via proteasome inhibition: implication for bortezomib (VELCADE, PS-341) as a therapeutic agent for malignant melanoma. Cancer Res **64**, 4912–4918 (2004).
301. Karin, M. & Ben-Neriah, Y. Phosphorylation meets ubiquitination: the control of NF-[kappa]B activity. Annu Rev Immunol **18**, 621–663 (2000).
302. Breitschopf, K., Zeiher, A. M. & Dimmeler, S. Ubiquitin-mediated degradation of the proapoptotic active form of bid. A functional consequence on apoptosis induction. J Biol Chem **275**, 21648–21652 (2000).
303. Concannon, C. G. et al. Apoptosis induced by proteasome inhibition in cancer cells: predominant role of the p53/PUMA pathway. Oncogene **26**, 1681–1692 (2007).
304. Hideshima, T. et al. Molecular mechanisms mediating antimyeloma activity of proteasome inhibitor PS-341. Blood **101**, 1530–1534 (2003).
305. Masdehors, P. et al. Deregulation of the ubiquitin system and p53 proteolysis modify the apoptotic response in B-CLL lymphocytes. Blood **96**, 269–274 (2000).
306. Yin, D. et al. Proteasome inhibitor PS-341 causes cell growth arrest and apoptosis in human glioblastoma multiforme (GBM). Oncogene **24**, 344–354 (2005).
307. Momand, J., Zambetti, G. P., Olson, D. C., George, D. & Levine, A. J. The mdm-2 oncogene product forms a complex with the p53 protein and inhibits p53-mediated transactivation. Cell **69**, 1237–1245 (1992).
308. Poyurovsky, M. V. & Prives, C. Unleashing the power of p53: lessons from mice and men. Genes Dev **20**, 125–131 (2006).
309. Shadfan, M., Lopez-Pajares, V. & Yuan, Z.-M. MDM2 and MDMX: Alone and together in regulation of p53. Transl Cancer Res **1**, 88–89 (2012).
310. Cross, B. et al. Inhibition of p53 DNA binding function by the MDM2 protein acidic domain. J Biol Chem **286**, 16018–16029 (2011).
311. Inuzuka, H., Fukushima, H., Shaik, S. & Wei, W. Novel insights into the molecular mechanisms governing Mdm2 ubiquitination and destruction. Oncotarget **1**, 685–690 (2010).
312. Michael, D. & Oren, M. The p53-Mdm2 module and the ubiquitin system. Semin Cancer Biol **13**, 49–58 (2003).
313. Hou, H., Sun, D. & Zhang, X. The role of MDM2 amplification and overexpression in therapeutic resistance of malignant tumors. Cancer Cell Int **19**, 216 (2019).
314. Oliner, J. D., Saiki, A. Y. & Caenepeel, S. The Role of MDM2 Amplification and Overexpression in Tumorigenesis. Cold Spring Harb Perspect Med **6**, a026336 (2016).
315. Shaikh, M. F. et al. Emerging Role of MDM2 as Target for Anti-Cancer Therapy: A Review. Ann Clin Lab Sci **46**, 627–634 (2016).
316. Williams, S. A. & McConkey, D. J. The proteasome inhibitor bortezomib stabilizes a novel active form of p53 in human LNCaP-Pro5 prostate cancer cells. Cancer Res **63**, 7338–7344 (2003).
317. Carlsten, M. et al. Bortezomib sensitizes multiple myeloma to NK cells via ER-stress-induced suppression of HLA-E and upregulation of DR5. Oncoimmunology **8**, e1534664 (2019).
318. Cheong, H.-J., Lee, K. S., Woo, I. S., Won, J.-H. & Byun, J. H. Up-regulation of the DR5 expression by proteasome inhibitor MG132 augments TRAIL-induced apoptosis in soft tissue sarcoma cell lines. Cancer Res Treat **43**, 124–130 (2011).
319. Xu, L., Su, L. & Liu, X. PKCδ regulates death receptor 5 expression induced by PS-341 through ATF4-ATF3/CHOP axis in human lung cancer cells. Mol Cancer Ther **11**, 2174–2182 (2012).
320. Jares, P., Colomer, D. & Campo, E. Molecular pathogenesis of mantle cell lymphoma. J Clin Invest **122**, 3416–3423 (2012).
321. Musgrove, E. A., Caldon, C. E., Barraclough, J., Stone, A. & Sutherland, R. L. Cyclin D as a therapeutic target in cancer. Nat Rev Cancer **11**, 558–572 (2011).
322. Kumeda, S. I., Deguchi, A., Toi, M., Omura, S. & Umezawa, K. Induction of G1 arrest and selective growth inhibition by lactacystin in human umbilical vein endothelial cells. Anticancer Res **19**, 3961–3968 (1999).
323. Machiels, B. M. et al. Detailed analysis of cell cycle kinetics upon proteasome inhibition. Cytometry **28**, 243–252 (1997).
324. Pagano, M. et al. Role of the ubiquitin-proteasome pathway in regulating abundance of the cyclin-dependent kinase inhibitor p27. Science **269**, 682–685 (1995).
325. Gupta, I., Singh, K., Varshney, N. K. & Khan, S. Delineating Crosstalk Mechanisms of the Ubiquitin Proteasome System That Regulate Apoptosis. Front Cell Dev Biol **6**, 11 (2018).
326. Kostova, Z. & Wolf, D. H. For whom the bell tolls: protein quality control of the endoplasmic reticulum and the ubiquitin-proteasome connection. EMBO J **22**, 2309–2317 (2003).
327. Obeng, E. A. et al. Proteasome inhibitors induce a terminal unfolded protein response in multiple myeloma cells. Blood **107**, 4907–4916 (2006).
328. Suraweera, A., Münch, C., Hanssum, A. & Bertolotti, A. Failure of amino acid homeostasis causes cell death following proteasome inhibition. Mol Cell **48**, 242–253 (2012).
329. Palombella, V. J. et al. Role of the proteasome and NF-kappaB in streptococcal cell wall-induced polyarthritis. Proc Natl Acad Sci U S A **95**, 15671–15676 (1998).
330. Moreau, P. et al. Prospective comparison of subcutaneous versus intravenous administration of bortezomib in patients with multiple myeloma. Haematologica **93**, 1908–1911 (2008).
331. Fricker, L. D. Proteasome Inhibitor Drugs. Annu Rev Pharmacol Toxicol **60**, 457–476 (2020).
332. Heine, S. et al. Cyclin D1-CDK4 activity drives sensitivity to bortezomib in mantle cell lymphoma by blocking autophagy-mediated proteolysis of NOXA. J Hematol Oncol **11**, 112 (2018).

333. Dasgupta, S. et al. Proteasome inhibitors alter levels of intracellular peptides in HEK293T and SH-SY5Y cells. PLoS One **9**, e103604 (2014).
334. Gelman, J. S. et al. Alterations of the intracellular peptidome in response to the proteasome inhibitor bortezomib. PLoS One **8**, e53263 (2013).
335. Teicher, B. A., Ara, G., Herbst, R., Palombella, V. J. & Adams, J. The proteasome inhibitor PS-341 in cancer therapy. Clin Cancer Res **5**, 2638–2645 (1999).
336. Orlowski, R. Z. et al. Phase I trial of the proteasome inhibitor PS-341 in patients with refractory hematologic malignancies. J Clin Oncol **20**, 4420–4427 (2002).
337. Teicher, B. A. & Anderson, K. C. CCR 20th anniversary commentary: In the beginning, there was PS-341. Clin Cancer Res **21**, 939–941 (2015).
338. Huang, Z. et al. Efficacy of therapy with bortezomib in solid tumors: a review based on 32 clinical trials. Future Oncol **10**, 1795–1807 (2014).
339. Rolfe, M. The Holy Grail: Solid Tumor Efficacy by Proteasome Inhibition. Cell Chem Biol **24**, 125–126 (2017).
340. Wu, Y.-X., Yang, J.-H. & Saitsu, H. Bortezomib-resistance is associated with increased levels of proteasome subunits and apoptosis-avoidance. Oncotarget **7**, 77622–77634 (2016).
341. Arastu-Kapur, S. et al. Nonproteasomal targets of the proteasome inhibitors bortezomib and carfilzomib: a link to clinical adverse events. Clin Cancer Res **17**, 2734–2743 (2011).
342. Argyriou, A. A., Iconomou, G. & Kalofonos, H. P. Bortezomib-induced peripheral neuropathy in multiple myeloma: a comprehensive review of the literature. Blood **112**, 1593–1599 (2008).
343. Dou, Q. P. & Zonder, J. A. Overview of proteasome inhibitor-based anti-cancer therapies: perspective on bortezomib and second generation proteasome inhibitors versus future generation inhibitors of ubiquitin-proteasome system. Curr Cancer Drug Targets **14**, 517–536 (2014).
344. Berkers, C. R. et al. Activity probe for in vivo profiling of the specificity of proteasome inhibitor bortezomib. Nat Methods **2**, 357–362 (2005).
345. Arnulf, B. et al. Updated survival analysis of a randomized phase III study of subcutaneous versus intravenous bortezomib in patients with relapsed multiple myeloma. Haematologica **97**, 1925–1928 (2012).
346. Meregalli, C. An Overview of Bortezomib-Induced Neurotoxicity. Toxics **3**, 294–303 (2015).
347. Murai, K. et al. Bortezomib induces thrombocytopenia by the inhibition of proplatelet formation of megakaryocytes. Eur J Haematol **93**, 290–296 (2014).
348. Hasinoff, B. B. Progress curve analysis of the kinetics of slow-binding anticancer drug inhibitors of the 20S proteasome. Arch Biochem Biophys **639**, 52–58 (2018).
349. Hasinoff, B. B. & Patel, D. Myocyte-Damaging Effects and Binding Kinetics of Boronic Acid and Epoxyketone Proteasomal-Targeted Drugs. Cardiovasc Toxicol **18**, 557–568 (2018).
350. Kupperman, E. et al. Evaluation of the proteasome inhibitor MLN9708 in preclinical models of human cancer. Cancer Res **70**, 1970–1980 (2010).
351. Demo, S. D. et al. Antitumor activity of PR-171, a novel irreversible inhibitor of the proteasome. Cancer Res **67**, 6383–6391 (2007).
352. Dimopoulos, M. et al. Carfilzomib, dexamethasone, and daratumumab versus carfilzomib and dexamethasone for patients with relapsed or refractory multiple myeloma (CANDOR): results from a randomised, multicentre, open-label, phase 3 study. Lancet **396**, 186–197 (2020).
353. Kuhn, D. J. et al. Potent activity of carfilzomib, a novel, irreversible inhibitor of the ubiquitin-proteasome pathway, against preclinical models of multiple myeloma. Blood **110**, 3281–3290 (2007).
354. Hamilton, A. L. et al. Proteasome inhibition with bortezomib (PS-341): a phase I study with pharmacodynamic end points using a day 1 and day 4 schedule in a 14-day cycle. J Clin Oncol **23**, 6107–6116 (2005).
355. O'Connor, O. A. et al. A phase 1 dose escalation study of the safety and pharmacokinetics of the novel proteasome inhibitor carfilzomib (PR-171) in patients with hematologic malignancies. Clin Cancer Res **15**, 7085–7091 (2009).
356. Geier, E. et al. A giant protease with potential to substitute for some functions of the proteasome. Science **283**, 978–981 (1999).
357. Ostrowska, H., Wojcik, C., Omura, S. & Worowski, K. Lactacystin, a specific inhibitor of the proteasome, inhibits human platelet lysosomal cathepsin A-like enzyme. Biochem Biophys Res Commun **234**, 729–732 (1997).
358. Feling, R. H. et al. Salinosporamide A: a highly cytotoxic proteasome inhibitor from a novel microbial source, a marine bacterium of the new genus salinospora. Angew Chem Int Ed Engl **42**, 355–357 (2003).
359. Fenical, W. et al. Discovery and development of the anticancer agent salinosporamide A (NPI-0052). Bioorg Med Chem **17**, 2175–2180 (2009).
360. Kale, A. J., McGlinchey, R. P., Lechner, A. & Moore, B. S. Bacterial self-resistance to the natural proteasome inhibitor salinosporamide A. ACS Chem Biol **6**, 1257–1264 (2011).
361. Niewerth, D. et al. Antileukemic activity and mechanism of drug resistance to the marine Salinispora tropica proteasome inhibitor salinosporamide A (Marizomib). Mol Pharmacol **86**, 12–19 (2014).
362. Groll, M., Huber, R. & Potts, B. C. M. Crystal structures of Salinosporamide A (NPI-0052) and B (NPI-0047) in complex with the 20S proteasome reveal important consequences of beta-lactone ring opening and a mechanism for irreversible binding. J Am Chem Soc **128**, 5136–5141 (2006).
363. Dick, L. R. et al. Mechanistic studies on the inactivation of the proteasome by lactacystin in cultured cells. J Biol Chem **272**, 182–188 (1997).
364. Denora, N., Potts, B. C. M. & Stella, V. J. A mechanistic and kinetic study of the beta-lactone hydrolysis of Salinosporamide A (NPI-0052), a novel proteasome inhibitor. J Pharm Sci **96**, 2037–2047 (2007).

365. Manam, R. R. et al. Leaving groups prolong the duration of 20S proteasome inhibition and enhance the potency of salinosporamides. J Med Chem **51**, 6711–6724 (2008).
366. Obaidat, A. et al. Proteasome regulator marizomib (NPI-0052) exhibits prolonged inhibition, attenuated efflux, and greater cytotoxicity than its reversible analogs. J Pharmacol Exp Ther **337**, 479–486 (2011).
367. Macherla, V. R. et al. Structure-activity relationship studies of salinosporamide A (NPI-0052), a novel marine derived proteasome inhibitor. J Med Chem **48**, 3684–3687 (2005).
368. Levin, N. et al. Marizomib irreversibly inhibits proteasome to overcome compensatory hyperactivation in multiple myeloma and solid tumour patients. Br J Haematol **174**, 711–720 (2016).
369. Oerlemans, R. et al. Molecular basis of bortezomib resistance: proteasome subunit beta5 (PSMB5) gene mutation and overexpression of PSMB5 protein. Blood **112**, 2489–2499 (2008).
370. Ruiz, S. et al. The proteasome inhibitor NPI-0052 is a more effective inducer of apoptosis than bortezomib in lymphocytes from patients with chronic lymphocytic leukemia. Mol Cancer Ther **5**, 1836–1843 (2006).
371. Chauhan, D. et al. A novel orally active proteasome inhibitor induces apoptosis in multiple myeloma cells with mechanisms distinct from Bortezomib. Cancer Cell **8**, 407–419 (2005).
372. Adams, J. et al. Proteasome inhibitors: a novel class of potent and effective antitumor agents. Cancer Res **59**, 2615–2622 (1999).
373. Di, K. et al. Marizomib activity as a single agent in malignant gliomas: ability to cross the blood-brain barrier. Neuro Oncol **18**, 840–848 (2016).
374. Harrison, S. J. et al. Phase I Clinical Trial of Marizomib (NPI-0052) in Patients with Advanced Malignancies Including Multiple Myeloma: Study NPI-0052-102 Final Results. Clin Cancer Res **22**, 4559–4566 (2016).
375. Manton, C. A. et al. Induction of cell death by the novel proteasome inhibitor marizomib in glioblastoma in vitro and in vivo. Sci Rep **6**, 18953 (2016).
376. Williamson, M. J. et al. Comparison of biochemical and biological effects of ML858 (salinosporamide A) and bortezomib. Mol Cancer Ther **5**, 3052–3061 (2006).
377. Singh, A. V. et al. Pharmacodynamic and efficacy studies of the novel proteasome inhibitor NPI-0052 (marizomib) in a human plasmacytoma xenograft murine model. Br J Haematol **149**, 550–559 (2010).
378. Karmur, B. S. et al. Blood-Brain Barrier Disruption in Neuro-Oncology: Strategies, Failures, and Challenges to Overcome. Front Oncol **10**, 563840 (2020).
379. Sarkaria, J. N. et al. Is the blood-brain barrier really disrupted in all glioblastomas? A critical assessment of existing clinical data. Neuro Oncol **20**, 184–191 (2018).
380. Zünkeler, B. et al. Quantification and pharmacokinetics of blood-brain barrier disruption in humans. J Neurosurg **85**, 1056–1065 (1996).
381. Bota, D. A. et al. Abstract 4733: Human functional brain imaging data support preclinical and clinical evidence that marizomib crosses the blood-brain barrier (BBB) to inhibit proteasome activity in the brain. in Experimental and Molecular Therapeutics 4733–4733 (American Association for Cancer Research, 2019). doi:10.1158/1538-7445.AM2019-4733.
382. Richardson, P. G. et al. Phase 1 study of marizomib in relapsed or relapsed and refractory multiple myeloma: NPI-0052-101 Part 1. Blood **127**, 2693–2700 (2016).
383. Spencer, A. et al. A phase 1 clinical trial evaluating marizomib, pomalidomide and low-dose dexamethasone in relapsed and refractory multiple myeloma (NPI-0052-107): final study results. Br J Haematol **180**, 41–51 (2018).
384. Cromm, P. M. & Crews, C. M. Targeted Protein Degradation: from Chemical Biology to Drug Discovery. Cell Chem Biol **24**, 1181–1190 (2017).
385. Kisselev, A. F., van der Linden, W. A. & Overkleeft, H. S. Proteasome inhibitors: an expanding army attacking a unique target. Chem Biol **19**, 99–115 (2012).
386. Zimmermann, J. et al. Proteasome inhibitor induced gene expression profiles reveal overexpression of transcriptional regulators ATF3, GADD153 and MAD1. Oncogene **19**, 2913–2920 (2000).
387. Sooman, L. et al. Synergistic effects of combining proteasome inhibitors with chemotherapeutic drugs in lung cancer cells. BMC Res Notes **10**, 544 (2017).
388. Gatti, L., Zuco, V., Zaffaroni, N. & Perego, P. Drug combinations with proteasome inhibitors in antitumor therapy. Curr Pharm Des **19**, 4094–4114 (2013).
389. Chen, J.-J., Chou, C.-W., Chang, Y.-F. & Chen, C.-C. Proteasome inhibitors enhance TRAIL-induced apoptosis through the intronic regulation of DR5: involvement of NF-kappa B and reactive oxygen species-mediated p53 activation. J Immunol **180**, 8030–8039 (2008).
390. Kabore, A. F. et al. The TRAIL apoptotic pathway mediates proteasome inhibitor induced apoptosis in primary chronic lymphocytic leukemia cells. Apoptosis **11**, 1175–1193 (2006).
391. Sayers, T. J. et al. The proteasome inhibitor PS-341 sensitizes neoplastic cells to TRAIL-mediated apoptosis by reducing levels of c-FLIP. Blood **102**, 303–310 (2003).
392. Koschny, R. et al. Bortezomib sensitizes primary human astrocytoma cells of WHO grades I to IV for tumor necrosis factor-related apoptosis-inducing ligand-induced apoptosis. Clin Cancer Res **13**, 3403–3412 (2007).
393. La Ferla-Brühl, K. et al. NF-kappaB-independent sensitization of glioblastoma cells for TRAIL-induced apoptosis by proteasome inhibition. Oncogene **26**, 571–582 (2007).
394. Kahana, S. et al. Proteasome inhibitors sensitize glioma cells and glioma stem cells to TRAIL-induced apoptosis by PKCε-dependent downregulation of AKT and XIAP expressions. Cell Signal **23**, 1348–1357 (2011).
395. Unterkircher, T. et al. Bortezomib primes glioblastoma, including glioblastoma stem cells, for TRAIL by increasing tBid stability and mitochondrial apoptosis. Clin Cancer Res **17**, 4019–4030 (2011).

396. Koschny, R. et al. Bortezomib sensitizes primary human astrocytoma cells of WHO grades I to IV for tumor necrosis factor-related apoptosis-inducing ligand-induced apoptosis. Clin Cancer Res **13**, 3403–3412 (2007).
397. Laussmann, M. A. et al. Proteasome inhibition can impair caspase-8 activation upon submaximal stimulation of apoptotic tumor necrosis factor-related apoptosis inducing ligand (TRAIL) signaling. J Biol Chem **287**, 14402–14411 (2012).
398. Raizer, J. J. et al. A phase II trial evaluating the effects and intra-tumoral penetration of bortezomib in patients with recurrent malignant gliomas. J Neurooncol **129**, 139–146 (2016).
399. Friday, B. B. et al. Phase II trial of vorinostat in combination with bortezomib in recurrent glioblastoma: a north central cancer treatment group study. Neuro Oncol **14**, 215–221 (2012).
400. Odia, Y., Kreisl, T. N., Aregawi, D., Innis, E. K. & Fine, H. A. A phase II trial of tamoxifen and bortezomib in patients with recurrent malignant gliomas. J Neurooncol **125**, 191–195 (2015).
401. Dolma, S., Lessnick, S. L., Hahn, W. C. & Stockwell, B. R. Identification of genotype-selective antitumor agents using synthetic lethal chemical screening in engineered human tumor cells. Cancer Cell **3**, 285–296 (2003).
402. Dixon, S. J. et al. Pharmacological inhibition of cystine-glutamate exchange induces endoplasmic reticulum stress and ferroptosis. Elife **3**, e02523 (2014).
403. Dixon, S. J. et al. Ferroptosis: an iron-dependent form of nonapoptotic cell death. Cell **149**, 1060–1072 (2012).
404. Sato, H., Tamba, M., Ishii, T. & Bannai, S. Cloning and expression of a plasma membrane cystine/glutamate exchange transporter composed of two distinct proteins. J Biol Chem **274**, 11455–11458 (1999).
405. Nakamura, E. et al. 4F2 (CD98) heavy chain is associated covalently with an amino acid transporter and controls intracellular trafficking and membrane topology of 4F2 heterodimer. J Biol Chem **274**, 3009–3016 (1999).
406. Conrad, M. & Sato, H. The oxidative stress-inducible cystine/glutamate antiporter, system x (c) (-) : cystine supplier and beyond. Amino Acids **42**, 231–246 (2012).
407. Yang, W. S. et al. Regulation of ferroptotic cancer cell death by GPX4. Cell **156**, 317–331 (2014).
408. Maiorino, M., Conrad, M. & Ursini, F. GPx4, Lipid Peroxidation, and Cell Death: Discoveries, Rediscoveries, and Open Issues. Antioxidants & Redox Signaling **29**, 61–74 (2018).
409. Tang, M., Chen, Z., Wu, D. & Chen, L. Ferritinophagy/ferroptosis: Iron-related newcomers in human diseases. J Cell Physiol **233**, 9179–9190 (2018).
410. Jomova, K. & Valko, M. Advances in metal-induced oxidative stress and human disease. Toxicology **283**, 65–87 (2011).
411. Kajarabille, N. & Latunde-Dada, G. O. Programmed Cell-Death by Ferroptosis: Antioxidants as Mitigators. Int J Mol Sci **20**, E4968 (2019).
412. Muckenthaler, M. U., Galy, B. & Hentze, M. W. Systemic iron homeostasis and the iron-responsive element/iron-regulatory protein (IRE/IRP) regulatory network. Annu Rev Nutr **28**, 197–213 (2008).
413. Park, E. & Chung, S. W. ROS-mediated autophagy increases intracellular iron levels and ferroptosis by ferritin and transferrin receptor regulation. Cell Death Dis **10**, 822 (2019).
414. MacKenzie, E. L., Iwasaki, K. & Tsuji, Y. Intracellular iron transport and storage: from molecular mechanisms to health implications. Antioxid Redox Signal **10**, 997–1030 (2008).
415. Carrier, J., Aghdassi, E., Cullen, J. & Allard, J. P. Iron supplementation increases disease activity and vitamin E ameliorates the effect in rats with dextran sulfate sodium-induced colitis. J Nutr **132**, 3146–3150 (2002).
416. Reizenstein, P. Iron, free radicals and cancer. Med Oncol Tumor Pharmacother **8**, 229–233 (1991).
417. Yagoda, N. et al. RAS-RAF-MEK-dependent oxidative cell death involving voltage-dependent anion channels. Nature **447**, 864–868 (2007).
418. Yang, W. S. & Stockwell, B. R. Synthetic lethal screening identifies compounds activating iron-dependent, nonapoptotic cell death in oncogenic-RAS-harboring cancer cells. Chem Biol **15**, 234–245 (2008).
419. Gao, M., Monian, P., Quadri, N., Ramasamy, R. & Jiang, X. Glutaminolysis and Transferrin Regulate Ferroptosis. Mol Cell **59**, 298–308 (2015).
420. Friedmann Angeli, J. P. et al. Inactivation of the ferroptosis regulator Gpx4 triggers acute renal failure in mice. Nat Cell Biol **16**, 1180–1191 (2014).
421. Yu, Y. et al. The ferroptosis inducer erastin enhances sensitivity of acute myeloid leukemia cells to chemotherapeutic agents. Mol Cell Oncol **2**, e1054549 (2015).
422. Schott, C., Graab, U., Cuvelier, N., Hahn, H. & Fulda, S. Oncogenic RAS Mutants Confer Resistance of RMS13 Rhabdomyosarcoma Cells to Oxidative Stress-Induced Ferroptotic Cell Death. Front Oncol **5**, 131 (2015).
423. Lewerenz, J., Ates, G., Methner, A., Conrad, M. & Maher, P. Oxytosis/Ferroptosis-(Re-) Emerging Roles for Oxidative Stress-Dependent Non-apoptotic Cell Death in Diseases of the Central Nervous System. Front Neurosci **12**, 214 (2018).
424. Battaglia, A. M. et al. Ferroptosis and Cancer: Mitochondria Meet the ‘Iron Maiden’ Cell Death. Cells **9**, E1505 (2020).
425. Kuang, F., Liu, J., Tang, D. & Kang, R. Oxidative Damage and Antioxidant Defense in Ferroptosis. Front Cell Dev Biol **8**, 586578 (2020).
426. Li, J. et al. Ferroptosis: past, present and future. Cell Death Dis **11**, 88 (2020).
427. Xie, Y. et al. Ferroptosis: process and function. Cell Death Differ **23**, 369–379 (2016).
428. Hasskarl, J. Sorafenib: targeting multiple tyrosine kinases in cancer. Recent Results Cancer Res **201**, 145–164 (2014).

429. Lachaier, E. et al. Sorafenib induces ferroptosis in human cancer cell lines originating from different solid tumors. Anticancer Res **34**, 6417–6422 (2014).
430. Louandre, C. et al. Iron-dependent cell death of hepatocellular carcinoma cells exposed to sorafenib. Int J Cancer **133**, 1732–1742 (2013).
431. Gout, P. W., Buckley, A. R., Simms, C. R. & Bruchovsky, N. Sulfasalazine, a potent suppressor of lymphoma growth by inhibition of the x(c)- cystine transporter: a new action for an old drug. Leukemia **15**, 1633–1640 (2001).
432. Rodenburg, R. J., Ganga, A., van Lent, P. L., van de Putte, L. B. & van Venrooij, W. J. The antiinflammatory drug sulfasalazine inhibits tumor necrosis factor alpha expression in macrophages by inducing apoptosis. Arthritis Rheum **43**, 1941–1950 (2000).
433. Shukla, K. et al. Inhibition of xc^- transporter-mediated cystine uptake by sulfasalazine analogs. Bioorg Med Chem Lett **21**, 6184–6187 (2011).
434. Wahl, C., Liptay, S., Adler, G. & Schmid, R. M. Sulfasalazine: a potent and specific inhibitor of nuclear factor kappa B. J Clin Invest **101**, 1163–1174 (1998).
435. Tang, H. M. & Tang, H. L. Cell recovery by reversal of ferroptosis. Biol Open **8**, bio043182 (2019).
436. Shimada, K. et al. Global survey of cell death mechanisms reveals metabolic regulation of ferroptosis. Nat Chem Biol **12**, 497–503 (2016).
437. Abrams, R. P., Carroll, W. L. & Woerpel, K. A. Five-Membered Ring Peroxide Selectively Initiates Ferroptosis in Cancer Cells. ACS Chem Biol **11**, 1305–1312 (2016).
438. Gaschler, M. M. et al. FINO2 initiates ferroptosis through GPX4 inactivation and iron oxidation. Nat Chem Biol **14**, 507–515 (2018).
439. Eling, N., Reuter, L., Hazin, J., Hamacher-Brady, A. & Brady, N. R. Identification of artesunate as a specific activator of ferroptosis in pancreatic cancer cells. Oncoscience **2**, 517–532 (2015).
440. Singh, N. P. & Lai, H. Selective toxicity of dihydroartemisinin and holotransferrin toward human breast cancer cells. Life Sci **70**, 49–56 (2001).
441. Yang, N.-D. et al. Artesunate induces cell death in human cancer cells via enhancing lysosomal function and lysosomal degradation of ferritin. J Biol Chem **289**, 33425–33441 (2014).
442. Zhang, S. & Gerhard, G. S. Heme mediates cytotoxicity from artemisinin and serves as a general anti-proliferation target. PLoS One **4**, e7472 (2009).
443. Miotto, G. et al. Insight into the mechanism of ferroptosis inhibition by ferrostatin-1. Redox Biol **28**, 101328 (2020).
444. Zilka, O. et al. On the Mechanism of Cytoprotection by Ferrostatin-1 and Liproxstatin-1 and the Role of Lipid Peroxidation in Ferroptotic Cell Death. ACS Cent Sci **3**, 232–243 (2017).
445. Hao, S. et al. Metabolic networks in ferroptosis. Oncol Lett **15**, 5405–5411 (2018).
446. Ishii, T., Bannai, S. & Sugita, Y. Mechanism of growth stimulation of L1210 cells by 2-mercaptoethanol in vitro. Role of the mixed disulfide of 2-mercaptoethanol and cysteine. J Biol Chem **256**, 12387–12392 (1981).
447. Feng, H. & Stockwell, B. R. Unsolved mysteries: How does lipid peroxidation cause ferroptosis? PLoS Biol **16**, e2006203 (2018).
448. Stachowska, E. et al. Conjugated linoleic acid increases intracellular ROS synthesis and oxygenation of arachidonic acid in macrophages. Nutrition **24**, 187–199 (2008).
449. Chisté, R. C., Freitas, M., Mercadante, A. Z. & Fernandes, E. Carotenoids inhibit lipid peroxidation and hemoglobin oxidation, but not the depletion of glutathione induced by ROS in human erythrocytes. Life Sci **99**, 52–60 (2014).
450. Fiedor, J. & Burda, K. Potential role of carotenoids as antioxidants in human health and disease. Nutrients **6**, 466–488 (2014).
451. Sun, Y., Zheng, Y., Wang, C. & Liu, Y. Glutathione depletion induces ferroptosis, autophagy, and premature cell senescence in retinal pigment epithelial cells. Cell Death Dis **9**, 753 (2018).
452. Yang, W. S. & Stockwell, B. R. Ferroptosis: Death by Lipid Peroxidation. Trends Cell Biol **26**, 165–176 (2016).
453. Mai, T. T. et al. Salinomycin kills cancer stem cells by sequestering iron in lysosomes. Nat Chem **9**, 1025–1033 (2017).
454. Dixon, S. J. & Stockwell, B. R. The Hallmarks of Ferroptosis. Annu. Rev. Cancer Biol. **3**, 35–54 (2019).
455. Hirayama, T. & Nagasawa, H. Chemical tools for detecting Fe ions. J Clin Biochem Nutr **60**, 39–48 (2017).
456. Drummen, G. P. C., van Liebergen, L. C. M., Op den Kamp, J. A. F. & Post, J. A. C11-BODIPY(581/591), an oxidation-sensitive fluorescent lipid peroxidation probe: (micro)spectroscopic characterization and validation of methodology. Free Radic Biol Med **33**, 473–490 (2002).
457. Yamanaka, K. et al. A novel fluorescent probe with high sensitivity and selective detection of lipid hydroperoxides in cells. RSC Adv. **2**, 7894–7900 (2012).
458. Yang, W. S. et al. Peroxidation of polyunsaturated fatty acids by lipoxygenases drives ferroptosis. Proc Natl Acad Sci U S A **113**, E4966-4975 (2016).
459. Feng, H. et al. Transferrin Receptor Is a Specific Ferroptosis Marker. Cell Rep **30**, 3411-3423.e7 (2020).
460. Yin, H., Xu, L. & Porter, N. A. Free radical lipid peroxidation: mechanisms and analysis. Chem Rev **111**, 5944–5972 (2011).
461. Ayala, A., Muñoz, M. F. & Argüelles, S. Lipid peroxidation: production, metabolism, and signaling mechanisms of malondialdehyde and 4-hydroxy-2-nonenal. Oxid Med Cell Longev **2014**, 360438 (2014).
462. Gaschler, M. M. & Stockwell, B. R. Lipid peroxidation in cell death. Biochem Biophys Res Commun **482**, 419–425 (2017).

463. Schneider, C. An update on products and mechanisms of lipid peroxidation. Mol Nutr Food Res **53**, 315–321 (2009).
464. Shah, R., Margison, K. & Pratt, D. A. The Potency of Diarylamine Radical-Trapping Antioxidants as Inhibitors of Ferroptosis Underscores the Role of Autoxidation in the Mechanism of Cell Death. ACS Chem Biol **12**, 2538–2545 (2017).
465. Haeggström, J. Z. & Funk, C. D. Lipoxygenase and leukotriene pathways: biochemistry, biology, and roles in disease. Chem Rev **111**, 5866–5898 (2011).
466. Shah, R., Shchepinov, M. S. & Pratt, D. A. Resolving the Role of Lipoxygenases in the Initiation and Execution of Ferroptosis. ACS Cent Sci **4**, 387–396 (2018).
467. Soupene, E. & Kuypers, F. A. Mammalian long-chain acyl-CoA synthetases. Exp Biol Med (Maywood) **233**, 507–521 (2008).
468. Kagan, V. E. et al. Oxidized arachidonic and adrenic PEs navigate cells to ferroptosis. Nat Chem Biol **13**, 81–90 (2017).
469. Dixon, S. J. et al. Human Haploid Cell Genetics Reveals Roles for Lipid Metabolism Genes in Nonapoptotic Cell Death. ACS Chem Biol **10**, 1604–1609 (2015).
470. Doll, S. et al. ACSL4 dictates ferroptosis sensitivity by shaping cellular lipid composition. Nat Chem Biol **13**, 91–98 (2017).
471. Borst, J. W., Visser, N. V., Kouptsova, O. & Visser, A. J. Oxidation of unsaturated phospholipids in membrane bilayer mixtures is accompanied by membrane fluidity changes. Biochim Biophys Acta **1487**, 61–73 (2000).
472. Agmon, E., Solon, J., Bassereau, P. & Stockwell, B. R. Modeling the effects of lipid peroxidation during ferroptosis on membrane properties. Sci Rep **8**, 5155 (2018).
473. DeHart, D. N. et al. Opening of voltage dependent anion channels promotes reactive oxygen species generation, mitochondrial dysfunction and cell death in cancer cells. Biochem Pharmacol **148**, 155–162 (2018).
474. Yu, H., Guo, P., Xie, X., Wang, Y. & Chen, G. Ferroptosis, a new form of cell death, and its relationships with tumourous diseases. J Cell Mol Med **21**, 648–657 (2017).
475. Gaschler, M. M. et al. Determination of the Subcellular Localization and Mechanism of Action of Ferrostatins in Suppressing Ferroptosis. ACS Chem Biol **13**, 1013–1020 (2018).
476. Gao, M. et al. Role of Mitochondria in Ferroptosis. Mol Cell **73**, 354-363.e3 (2019).
477. Wu, H., Wang, F., Ta, N., Zhang, T. & Gao, W. The Multifaceted Regulation of Mitochondria in Ferroptosis. Life (Basel) **11**, 222 (2021).
478. Stockwell, B. R. et al. Ferroptosis: A Regulated Cell Death Nexus Linking Metabolism, Redox Biology, and Disease. Cell **171**, 273–285 (2017).
479. Linkermann, A. et al. Synchronized renal tubular cell death involves ferroptosis. Proc Natl Acad Sci U S A **111**, 16836–16841 (2014).
480. Li, Q. et al. Inhibition of neuronal ferroptosis protects hemorrhagic brain. JCI Insight **2**, e90777 (2017).
481. Belaidi, A. A. & Bush, A. I. Iron neurochemistry in Alzheimer’s disease and Parkinson’s disease: targets for therapeutics. J Neurochem **139 Suppl 1**, 179–197 (2016).
482. Hambright, W. S., Fonseca, R. S., Chen, L., Na, R. & Ran, Q. Ablation of ferroptosis regulator glutathione peroxidase 4 in forebrain neurons promotes cognitive impairment and neurodegeneration. Redox Biol **12**, 8–17 (2017).
483. Hu, C.-L. et al. Reduced expression of the ferroptosis inhibitor glutathione peroxidase-4 in multiple sclerosis and experimental autoimmune encephalomyelitis. J Neurochem **148**, 426–439 (2019).
484. Yoo, S.-E. et al. Gpx4 ablation in adult mice results in a lethal phenotype accompanied by neuronal loss in brain. Free Radic Biol Med **52**, 1820–1827 (2012).
485. Conrad, M. et al. Regulation of lipid peroxidation and ferroptosis in diverse species. Genes Dev **32**, 602–619 (2018).
486. Jiang, X., Stockwell, B. R. & Conrad, M. Ferroptosis: mechanisms, biology and role in disease. Nat Rev Mol Cell Biol **22**, 266–282 (2021).
487. Gnanapradeepan, K. et al. The p53 Tumor Suppressor in the Control of Metabolism and Ferroptosis. Front Endocrinol (Lausanne) **9**, 124 (2018).
488. Jiang, L. et al. Ferroptosis as a p53-mediated activity during tumour suppression. Nature **520**, 57–62 (2015).
489. Rojo de la Vega, M., Chapman, E. & Zhang, D. D. NRF2 and the Hallmarks of Cancer. Cancer Cell **34**, 21–43 (2018).
490. Habib, E., Linher-Melville, K., Lin, H.-X. & Singh, G. Expression of xCT and activity of system xc(-) are regulated by NRF2 in human breast cancer cells in response to oxidative stress. Redox Biol **5**, 33–42 (2015).
491. Sasaki, H. et al. Electrophile response element-mediated induction of the cystine/glutamate exchange transporter gene expression. J Biol Chem **277**, 44765–44771 (2002).
492. Fan, Z. et al. Nrf2-Keap1 pathway promotes cell proliferation and diminishes ferroptosis. Oncogenesis **6**, e371 (2017).
493. Daniels, T. R., Delgado, T., Rodriguez, J. A., Helguera, G. & Penichet, M. L. The transferrin receptor part I: Biology and targeting with cytotoxic antibodies for the treatment of cancer. Clin Immunol **121**, 144–158 (2006).
494. Jeong, S. M., Hwang, S. & Seong, R. H. Transferrin receptor regulates pancreatic cancer growth by modulating mitochondrial respiration and ROS generation. Biochem Biophys Res Commun **471**, 373–379 (2016).

495. Gu, Z. et al. Decreased ferroportin promotes myeloma cell growth and osteoclast differentiation. Cancer Res **75**, 2211–2221 (2015).
496. Radulescu, S. et al. Luminal iron levels govern intestinal tumorigenesis after Apc loss in vivo. Cell Rep **2**, 270–282 (2012).
497. Hangauer, M. J. et al. Drug-tolerant persister cancer cells are vulnerable to GPX4 inhibition. Nature **551**, 247–250 (2017).
498. Viswanathan, V. S. et al. Dependency of a therapy-resistant state of cancer cells on a lipid peroxidase pathway. Nature **547**, 453–457 (2017).
499. Schonberg, D. L. et al. Preferential Iron Trafficking Characterizes Glioblastoma Stem-like Cells. Cancer Cell **28**, 441–455 (2015).
500. Zhang, N. et al. FoxM1 promotes β-catenin nuclear localization and controls Wnt target-gene expression and glioma tumorigenesis. Cancer Cell **20**, 427–442 (2011).
501. Robert, S. M. et al. SLC7A11 expression is associated with seizures and predicts poor survival in patients with malignant glioma. Sci Transl Med **7**, 289ra86 (2015).
502. Lyons, S. A., Chung, W. J., Weaver, A. K., Ogunrinu, T. & Sontheimer, H. Autocrine glutamate signaling promotes glioma cell invasion. Cancer Res **67**, 9463–9471 (2007).
503. Polewski, M. D., Reveron-Thornton, R. F., Cherryholmes, G. A., Marinov, G. K. & Aboody, K. S. SLC7A11 Overexpression in Glioblastoma Is Associated with Increased Cancer Stem Cell-Like Properties. Stem Cells Dev **26**, 1236–1246 (2017).
504. Chen, L., Hambright, W. S., Na, R. & Ran, Q. Ablation of the Ferroptosis Inhibitor Glutathione Peroxidase 4 in Neurons Results in Rapid Motor Neuron Degeneration and Paralysis. J Biol Chem **290**, 28097–28106 (2015).
505. Arensman, M. D. et al. Cystine-glutamate antiporter xCT deficiency suppresses tumor growth while preserving antitumor immunity. Proc Natl Acad Sci U S A **116**, 9533–9542 (2019).
506. Sato, H. et al. Redox imbalance in cystine/glutamate transporter-deficient mice. J Biol Chem **280**, 37423–37429 (2005).
507. Chande, N., Tsoulis, D. J. & MacDonald, J. K. Azathioprine or 6-mercaptopurine for induction of remission in Crohn’s disease. Cochrane Database Syst Rev CD000545 (2013) doi:10.1002/14651858.CD000545.pub4.
508. Chung, W. J. & Sontheimer, H. Sulfasalazine inhibits the growth of primary brain tumors independent of nuclear factor-kappaB. J Neurochem **110**, 182–193 (2009).
509. Sehm, T. et al. Sulfasalazine impacts on ferroptotic cell death and alleviates the tumor microenvironment and glioma-induced brain edema. Oncotarget **7**, 36021–36033 (2016).
510. Vetma, V. Assessment of TRAIL sensitisation by IAP antagonist TL32711 in malignant melanoma and development of a framework for response prediction [PhD Thesis]. (University of Stuttgart, 2019).
511. Laussman, M. A. Modulation of apoptosis signalling by proteasome inhibition: a single cell analysis [PhD Thesis]. (Royal College of Surgeons in Ireland, 2011).
512. Rosenberg, S. et al. Multi-omics analysis of primary glioblastoma cell lines shows recapitulation of pivotal molecular features of parental tumors. Neuro Oncol **19**, 219–228 (2017).
513. Ciechanover, A. Intracellular protein degradation: from a vague idea, through the lysosome and the ubiquitin-proteasome system, and onto human diseases and drug targeting (Nobel lecture). Angew Chem Int Ed Engl **44**, 5944–5967 (2005).
514. Hellwig, C. T. et al. Real time analysis of tumor necrosis factor-related apoptosis-inducing ligand/cycloheximide-induced caspase activities during apoptosis initiation. J Biol Chem **283**, 21676–21685 (2008).
515. Snell, V. et al. Activity of TNF-related apoptosis-inducing ligand (TRAIL) in haematological malignancies. Br J Haematol **99**, 618–624 (1997).
516. Gilmore, A. & King, L. Emerging approaches to target mitochondrial apoptosis in cancer cells. F1000Res **8**, F1000 Faculty Rev-1793 (2019).
517. Ashkenazi, A., Fairbrother, W. J., Leverson, J. D. & Souers, A. J. From basic apoptosis discoveries to advanced selective BCL-2 family inhibitors. Nat Rev Drug Discov **16**, 273–284 (2017).
518. Campbell, K. J. & Tait, S. W. G. Targeting BCL-2 regulated apoptosis in cancer. Open Biol **8**, 180002 (2018).
519. Zhang, H. et al. Bcl-2 family proteins are essential for platelet survival. Cell Death Differ **14**, 943–951 (2007).
520. Krakstad, C. & Chekenya, M. Survival signalling and apoptosis resistance in glioblastomas: opportunities for targeted therapeutics. Mol Cancer **9**, 135 (2010).
521. Valdés-Rives, S. A., Casique-Aguirre, D., Germán-Castelán, L., Velasco-Velázquez, M. A. & González-Arenas, A. Apoptotic Signaling Pathways in Glioblastoma and Therapeutic Implications. Biomed Res Int **2017**, 7403747 (2017).
522. Arif, T., Krelin, Y. & Shoshan-Barmatz, V. Reducing VDAC1 expression induces a non-apoptotic role for pro-apoptotic proteins in cancer cell differentiation. Biochim Biophys Acta **1857**, 1228–1242 (2016).
523. Li, Z. et al. The JNK signaling pathway plays a key role in methuosis (non-apoptotic cell death) induced by MOMIPP in glioblastoma. BMC Cancer **19**, 77 (2019).
524. Maltese, W. A. & Overmeyer, J. H. Non-apoptotic cell death associated with perturbations of macropinocytosis. Front Physiol **6**, 38 (2015).
525. Chen, D. et al. ATF4 promotes angiogenesis and neuronal cell death and confers ferroptosis in a xCT-dependent manner. Oncogene **36**, 5593–5608 (2017).
526. Cheng, J. et al. ACSL4 suppresses glioma cells proliferation via activating ferroptosis. Oncol Rep **43**, 147–158 (2020).

527. Li, B. et al. Emerging mechanisms and applications of ferroptosis in the treatment of resistant cancers. Biomed Pharmacother **130**, 110710 (2020).
528. Cao, Y. et al. Lestaurtinib potentiates TRAIL-induced apoptosis in glioma via CHOP-dependent DR5 induction. J Cell Mol Med **24**, 7829–7840 (2020).
529. Knight, M. J., Riffkin, C. D., Muscat, A. M., Ashley, D. M. & Hawkins, C. J. Analysis of FasL and TRAIL induced apoptosis pathways in glioma cells. Oncogene **20**, 5789–5798 (2001).
530. Zhu, Z.-C. et al. Targeting KPNB1 overcomes TRAIL resistance by regulating DR5, Mcl-1 and FLIP in glioblastoma cells. Cell Death Dis **10**, 118 (2019).
531. Shibata, Y., Yasui, H., Higashikawa, K., Miyamoto, N. & Kuge, Y. Erastin, a ferroptosis-inducing agent, sensitized cancer cells to X-ray irradiation via glutathione starvation in vitro and in vivo. PLoS One **14**, e0225931 (2019).
532. Sun, Y., Deng, R. & Zhang, C. Erastin induces apoptotic and ferroptotic cell death by inducing ROS accumulation by causing mitochondrial dysfunction in gastric cancer cell HGC-27. Mol Med Rep **22**, 2826–2832 (2020).
533. Anderson, M. A. et al. The BCL2 selective inhibitor venetoclax induces rapid onset apoptosis of CLL cells in patients via a TP53-independent mechanism. Blood **127**, 3215–3224 (2016).
534. Lee, E. F. et al. BCL-XL and MCL-1 are the key BCL-2 family proteins in melanoma cell survival. Cell Death Dis **10**, 342 (2019).
535. Sui, X. et al. RSL3 Drives Ferroptosis Through GPX4 Inactivation and ROS Production in Colorectal Cancer. Front Pharmacol **9**, 1371 (2018).
536. Zuo, S., Yu, J., Pan, H. & Lu, L. Novel insights on targeting ferroptosis in cancer therapy. Biomark Res **8**, 50 (2020).
537. Belavgeni, A. et al. Exquisite sensitivity of adrenocortical carcinomas to induction of ferroptosis. Proc Natl Acad Sci U S A **116**, 22269–22274 (2019).
538. Yang, M. et al. Clockophagy is a novel selective autophagy process favoring ferroptosis. Sci Adv **5**, eaaw2238 (2019).
539. Sieger, J. Investigating molecular pathways of RSL3-induced cell death: Linking ferroptosis to apoptosis [Master Thesis]. (University of Stuttgart, 2019).
540. Lei, P., Bai, T. & Sun, Y. Mechanisms of Ferroptosis and Relations With Regulated Cell Death: A Review. Front Physiol **10**, 139 (2019).
541. Wong, C. H., Siah, K. W. & Lo, A. W. Estimation of clinical trial success rates and related parameters. Biostatistics **20**, 273–286 (2019).
542. Hughes, P., Marshall, D., Reid, Y., Parkes, H. & Gelber, C. The costs of using unauthenticated, over-passaged cell lines: how much more data do we need? Biotechniques **43**, 575, 577–578, 581-582 passim (2007).
543. Arul, M., Roslani, A. C., Ng, C. L. L. & Cheah, S. H. Culture of low passage colorectal cancer cells and demonstration of variation in selected tumour marker expression. Cytotechnology **66**, 481–491 (2014).
544. Mouriaux, F. et al. Effects of Long-term Serial Passaging on the Characteristics and Properties of Cell Lines Derived From Uveal Melanoma Primary Tumors. Invest Ophthalmol Vis Sci **57**, 5288–5301 (2016).
545. Davis, M. E. Glioblastoma: Overview of Disease and Treatment. Clin J Oncol Nurs **20**, S2-8 (2016).
546. García-Romero, N. et al. Cancer stem cells from human glioblastoma resemble but do not mimic original tumors after in vitro passaging in serum-free media. Oncotarget **7**, 65888–65901 (2016).
547. Stockhausen, M.-T., Kristoffersen, K., Stobbe, L. & Poulsen, H. S. Differentiation of glioblastoma multiforme stem-like cells leads to downregulation of EGFR and EGFRvIII and decreased tumorigenic and stem-like cell potential. Cancer Biol Ther **15**, 216–224 (2014).
548. Daniels, R. A. et al. Expression of TRAIL and TRAIL receptors in normal and malignant tissues. Cell Res **15**, 430–438 (2005).
549. Elrod, H. A. et al. Analysis of death receptor 5 and caspase-8 expression in primary and metastatic head and neck squamous cell carcinoma and their prognostic impact. PLoS One **5**, e12178 (2010).
550. Ganten, T. M. et al. Prognostic significance of tumour necrosis factor-related apoptosis-inducing ligand (TRAIL) receptor expression in patients with breast cancer. J Mol Med (Berl) **87**, 995–1007 (2009).
551. Allen, J. E. et al. Identification of TRAIL-inducing compounds highlights small molecule ONC201/TIC10 as a unique anti-cancer agent that activates the TRAIL pathway. Mol Cancer **14**, 99 (2015).
552. Phillips, D. C. et al. Hexavalent TRAIL Fusion Protein Eftozanermin Alfa Optimally Clusters Apoptosis-Inducing TRAIL Receptors to Induce On-Target Antitumor Activity in Solid Tumors. Cancer Res **81**, 3402–3414 (2021).
553. Capper, D. et al. Stem-cell-like glioma cells are resistant to TRAIL/Apo2L and exhibit down-regulation of caspase-8 by promoter methylation. Acta Neuropathol **117**, 445–456 (2009).
554. Roth, P., Mason, W. P., Richardson, P. G. & Weller, M. Proteasome inhibition for the treatment of glioblastoma. Expert Opin Investig Drugs **29**, 1133–1141 (2020).
555. Johansson, P. et al. A Patient-Derived Cell Atlas Informs Precision Targeting of Glioblastoma. Cell Rep **32**, 107897 (2020).
556. Bota, D. A. et al. Proteasome inhibition with bortezomib induces cell death in GBM stem-like cells and temozolomide-resistant glioma cell lines, but stimulates GBM stem-like cells' VEGF production and angiogenesis. J Neurosurg **119**, 1415–1423 (2013).
557. Yoo, Y. D. et al. Glioma-derived cancer stem cells are hypersensitive to proteasomal inhibition. EMBO Rep **18**, 150–168 (2017).

558. Ghosh, D., Nandi, S. & Bhattacharjee, S. Combination therapy to checkmate Glioblastoma: clinical challenges and advances. Clin Transl Med **7**, 33 (2018).
559. He, C. et al. Patient-derived models recapitulate heterogeneity of molecular signatures and drug response in pediatric high-grade glioma. Nat Commun **12**, 4089 (2021).
560. Skaga, E. et al. Intertumoral heterogeneity in patient-specific drug sensitivities in treatment-naïve glioblastoma. BMC Cancer **19**, 628 (2019).
561. Fujita, E. et al. Enhancement of CPP32-like activity in the TNF-treated U937 cells by the proteasome inhibitors. Biochem Biophys Res Commun **224**, 74–79 (1996).
562. Fulda, S. Novel insights into the synergistic interaction of Bortezomib and TRAIL: tBid provides the link. Oncotarget **2**, 418–421 (2011).
563. Yoshida, T. et al. Proteasome inhibitor MG132 induces death receptor 5 through CCAAT/enhancer-binding protein homologous protein. Cancer Res **65**, 5662–5667 (2005).
564. Hetschko, H., Voss, V., Seifert, V., Prehn, J. H. M. & Kögel, D. Upregulation of DR5 by proteasome inhibitors potently sensitizes glioma cells to TRAIL-induced apoptosis. FEBS J **275**, 1925–1936 (2008).
565. Jane, E. P., Premkumar, D. R. & Pollack, I. F. Bortezomib sensitizes malignant human glioma cells to TRAIL, mediated by inhibition of the NF-{kappa}B signaling pathway. Mol Cancer Ther **10**, 198–208 (2011).
566. de Wilt, L. H. a. M. et al. Bortezomib and TRAIL: a perfect match for apoptotic elimination of tumour cells? Crit Rev Oncol Hematol **85**, 363–372 (2013).
567. Jennewein, C. et al. Identification of a novel pro-apoptotic role of NF-κB in the regulation of TRAIL- and CD95-mediated apoptosis of glioblastoma cells. Oncogene **31**, 1468–1474 (2012).
568. Karl, S. et al. Identification of a novel pro-apopotic function of NF-kappaB in the DNA damage response. J Cell Mol Med **13**, 4239–4256 (2009).
569. Gordon, J. L., Brown, M. A. & Reynolds, M. M. Cell-Based Methods for Determination of Efficacy for Candidate Therapeutics in the Clinical Management of Cancer. Diseases **6**, E85 (2018).
570. Weinlich, R., Oberst, A., Beere, H. M. & Green, D. R. Necroptosis in development, inflammation and disease. Nat Rev Mol Cell Biol **18**, 127–136 (2017).
571. Ali, M. & Mocarski, E. S. Proteasome inhibition blocks necroptosis by attenuating death complex aggregation. Cell Death Dis **9**, 346 (2018).
572. Zhang, Y. et al. Proteasome inhibitor PS-341 limits macrophage necroptosis by promoting cIAPs-mediated inhibition of RIP1 and RIP3 activation. Biochem Biophys Res Commun **477**, 761–767 (2016).
573. Heo, C. E. et al. Probing drug delivery and mechanisms of action in 3D spheroid cells by quantitative analysis. Analyst **145**, 7687–7694 (2020).
574. Mason, W. P. et al. Full enrollment results from an extended phase I, multicenter, open label study of marizomib (MRZ) with temozolomide (TMZ) and radiotherapy (RT) in newly diagnosed glioblastoma (GBM). JCO **37**, 2021–2021 (2019).
575. Hellwig, C. T. et al. Proteasome inhibition triggers the formation of TRAIL receptor 2 platforms for caspase-8 activation that accumulate in the cytosol. Cell Death Differ (2021) doi:10.1038/s41418-021-00843-7.
576. Laussmann, M. A. et al. Proteasome inhibition can induce an autophagy-dependent apical activation of caspase-8. Cell Death Differ **18**, 1584–1597 (2011).
577. Imajoh-Ohmi, S. et al. Lactacystin, a specific inhibitor of the proteasome, induces apoptosis in human monoblast U937 cells. Biochem Biophys Res Commun **217**, 1070–1077 (1995).
578. Zoli, W., Ricotti, L., Tesei, A., Barzanti, F. & Amadori, D. In vitro preclinical models for a rational design of chemotherapy combinations in human tumors. Crit Rev Oncol Hematol **37**, 69–82 (2001).
579. Mortenson, M. M., Schlieman, M. G., Virudachalam, S. & Bold, R. J. Effects of the proteasome inhibitor bortezomib alone and in combination with chemotherapy in the A549 non-small-cell lung cancer cell line. Cancer Chemother Pharmacol **54**, 343–353 (2004).
580. Potts, B. C. et al. Marizomib, a proteasome inhibitor for all seasons: preclinical profile and a framework for clinical trials. Curr Cancer Drug Targets **11**, 254–284 (2011).
581. Eigenmann, D. E. et al. Comparative study of four immortalized human brain capillary endothelial cell lines, hCMEC/D3, hBMEC, TY10, and BB19, and optimization of culture conditions, for an in vitro blood-brain barrier model for drug permeability studies. Fluids Barriers CNS **10**, 33 (2013).
582. Poller, B. et al. The human brain endothelial cell line hCMEC/D3 as a human blood-brain barrier model for drug transport studies. J Neurochem **107**, 1358–1368 (2008).
583. Weksler, B., Romero, I. A. & Couraud, P.-O. The hCMEC/D3 cell line as a model of the human blood brain barrier. Fluids Barriers CNS **10**, 16 (2013).
584. Daniels, B. P. et al. Immortalized human cerebral microvascular endothelial cells maintain the properties of primary cells in an in vitro model of immune migration across the blood brain barrier. J Neurosci Methods **212**, 173–179 (2013).
585. Williams, P. G. et al. New cytotoxic salinosporamides from the marine Actinomycete Salinispora tropica. J Org Chem **70**, 6196–6203 (2005).
586. Chong, K. Y. et al. Wnt pathway activation and ABCB1 expression account for attenuation of Proteasome inhibitor-mediated apoptosis in multidrug-resistant cancer cells. Cancer Biol Ther **16**, 149–159 (2015).
587. O'Connor, R. et al. The interaction of bortezomib with multidrug transporters: implications for therapeutic applications in advanced multiple myeloma and other neoplasias. Cancer Chemother Pharmacol **71**, 1357–1368 (2013).
588. Blaney, S. M. et al. Phase I clinical trial of intrathecal topotecan in patients with neoplastic meningitis. J Clin Oncol **21**, 143–147 (2003).

589. Fleischhack, G. et al. Feasibility of intraventricular administration of etoposide in patients with metastatic brain tumours. Br J Cancer **84**, 1453–1459 (2001).
590. Demeule, M. et al. Involvement of the low-density lipoprotein receptor-related protein in the transcytosis of the brain delivery vector angiopep-2. J Neurochem **106**, 1534–1544 (2008).
591. Pardridge, W. M., Eisenberg, J. & Yang, J. Human blood-brain barrier transferrin receptor. Metabolism **36**, 892–895 (1987).
592. Nazer, B., Hong, S. & Selkoe, D. J. LRP promotes endocytosis and degradation, but not transcytosis, of the amyloid-beta peptide in a blood-brain barrier in vitro model. Neurobiol Dis **30**, 94–102 (2008).
593. Skarlatos, S., Yoshikawa, T. & Pardridge, W. M. Transport of [125I]transferrin through the rat blood-brain barrier. Brain Res **683**, 164–171 (1995).
594. Zhang, Y. & Pardridge, W. M. Rapid transferrin efflux from brain to blood across the blood-brain barrier. J Neurochem **76**, 1597–1600 (2001).
595. Noch, E. K., Ramakrishna, R. & Magge, R. Challenges in the Treatment of Glioblastoma: Multisystem Mechanisms of Therapeutic Resistance. World Neurosurg **116**, 505–517 (2018).
596. Deng, L., Zhai, X., Liang, P. & Cui, H. Overcoming TRAIL Resistance for Glioblastoma Treatment. Biomolecules **11**, 572 (2021).
597. Twomey, J. D., Kim, S.-R., Zhao, L., Bozza, W. P. & Zhang, B. Spatial dynamics of TRAIL death receptors in cancer cells. Drug Resist Updat **19**, 13–21 (2015).
598. Símová, S., Klíma, M., Cermak, L., Sourková, V. & Andera, L. Arf and Rho GAP adapter protein ARAP1 participates in the mobilization of TRAIL-R1/DR4 to the plasma membrane. Apoptosis **13**, 423–436 (2008).
599. Zhang, Y. & Zhang, B. TRAIL resistance of breast cancer cells is associated with constitutive endocytosis of death receptors 4 and 5. Mol Cancer Res **6**, 1861–1871 (2008).
600. Baritaki, S., Huerta-Yepez, S., Sakai, T., Spandidos, D. A. & Bonavida, B. Chemotherapeutic drugs sensitize cancer cells to TRAIL-mediated apoptosis: up-regulation of DR5 and inhibition of Yin Yang 1. Mol Cancer Ther **6**, 1387–1399 (2007).
601. Liu, X. et al. The proteasome inhibitor PS-341 (bortezomib) up-regulates DR5 expression leading to induction of apoptosis and enhancement of TRAIL-induced apoptosis despite up-regulation of c-FLIP and survivin expression in human NSCLC cells. Cancer Res **67**, 4981–4988 (2007).
602. Juo, P., Kuo, C. J., Yuan, J. & Blenis, J. Essential requirement for caspase-8/FLICE in the initiation of the Fas-induced apoptotic cascade. Curr Biol **8**, 1001–1008 (1998).
603. Pingoud-Meier, C. et al. Loss of caspase-8 protein expression correlates with unfavorable survival outcome in childhood medulloblastoma. Clin Cancer Res **9**, 6401–6409 (2003).
604. Teitz, T. et al. Caspase 8 is deleted or silenced preferentially in childhood neuroblastomas with amplification of MYCN. Nat Med **6**, 529–535 (2000).
605. Miller, C. P. et al. NPI-0052, a novel proteasome inhibitor, induces caspase-8 and ROS-dependent apoptosis alone and in combination with HDAC inhibitors in leukemia cells. Blood **110**, 267–277 (2007).
606. Krueger, A., Schmitz, I., Baumann, S., Krammer, P. H. & Kirchhoff, S. Cellular FLICE-inhibitory protein splice variants inhibit different steps of caspase-8 activation at the CD95 death-inducing signaling complex. J Biol Chem **276**, 20633–20640 (2001).
607. Boatright, K. M., Deis, C., Denault, J.-B., Sutherlin, D. P. & Salvesen, G. S. Activation of caspases-8 and -10 by FLIP(L). Biochem J **382**, 651–657 (2004).
608. Chang, D. W. et al. c-FLIP(L) is a dual function regulator for caspase-8 activation and CD95-mediated apoptosis. EMBO J **21**, 3704–3714 (2002).
609. Kalkavan, H. & Green, D. R. MOMP, cell suicide as a BCL-2 family business. Cell Death Differ **25**, 46–55 (2018).
610. Souers, A. J. et al. ABT-199, a potent and selective BCL-2 inhibitor, achieves antitumor activity while sparing platelets. Nat Med **19**, 202–208 (2013).
611. Mason, K. D. et al. Programmed anuclear cell death delimits platelet life span. Cell **128**, 1173–1186 (2007).
612. Wilson, W. H. et al. Navitoclax, a targeted high-affinity inhibitor of BCL-2, in lymphoid malignancies: a phase 1 dose-escalation study of safety, pharmacokinetics, pharmacodynamics, and antitumour activity. Lancet Oncol **11**, 1149–1159 (2010).
613. Thomas, L. W., Lam, C. & Edwards, S. W. Mcl-1; the molecular regulation of protein function. FEBS Lett **584**, 2981–2989 (2010).
614. Zhang, B., Gojo, I. & Fenton, R. G. Myeloid cell factor-1 is a critical survival factor for multiple myeloma. Blood **99**, 1885–1893 (2002).
615. Xiang, W., Yang, C.-Y. & Bai, L. MCL-1 inhibition in cancer treatment. Onco Targets Ther **11**, 7301–7314 (2018).
616. Fresquet, V., Rieger, M., Carolis, C., García-Barchino, M. J. & Martinez-Climent, J. A. Acquired mutations in BCL2 family proteins conferring resistance to the BH3 mimetic ABT-199 in lymphoma. Blood **123**, 4111–4119 (2014).
617. Schuetz, J. M. et al. BCL2 mutations in diffuse large B-cell lymphoma. Leukemia **26**, 1383–1390 (2012).
618. Willis, T. G. & Dyer, M. J. The role of immunoglobulin translocations in the pathogenesis of B-cell malignancies. Blood **96**, 808–822 (2000).
619. Eichhorn, J. M., Alford, S. E., Sakurikar, N. & Chambers, T. C. Molecular analysis of functional redundancy among anti-apoptotic Bcl-2 proteins and its role in cancer cell survival. Exp Cell Res **322**, 415–424 (2014).
620. Hillert, L. K. et al. Dissecting DISC regulation via pharmacological targeting of caspase-8/c-FLIPL heterodimer. Cell Death Differ **27**, 2117–2130 (2020).

621. König, C., Hillert-Richter, L. K., Ivanisenko, N. V., Ivanisenko, V. A. & Lavrik, I. N. Pharmacological targeting of c-FLIPL and Bcl-2 family members promotes apoptosis in CD95L-resistant cells. Sci Rep **10**, 20823 (2020).
622. Shirley, S. & Micheau, O. Targeting c-FLIP in cancer. Cancer Lett **332**, 141–150 (2013).
623. Jo, E. B. et al. Combination therapy with c-met inhibitor and TRAIL enhances apoptosis in dedifferentiated liposarcoma patient-derived cells. BMC Cancer **19**, 496 (2019).
624. Ding, Y. et al. Identification of a small molecule as inducer of ferroptosis and apoptosis through ubiquitination of GPX4 in triple negative breast cancer cells. J Hematol Oncol **14**, 19 (2021).
625. Shlomovitz, I., Speir, M. & Gerlic, M. Flipping the dogma - phosphatidylserine in non-apoptotic cell death. Cell Commun Signal **17**, 139 (2019).
626. Chen, J., Kuroki, S., Someda, M. & Yonehara, S. Interferon-γ induces the cell surface exposure of phosphatidylserine by activating the protein MLKL in the absence of caspase-8 activity. J Biol Chem **294**, 11994–12006 (2019).
627. Klöditz, K. & Fadeel, B. Three cell deaths and a funeral: macrophage clearance of cells undergoing distinct modes of cell death. Cell Death Discov **5**, 65 (2019).
628. Zargarian, S. et al. Phosphatidylserine externalization, ‘necroptotic bodies’ release, and phagocytosis during necroptosis. PLoS Biol **15**, e2002711 (2017).
629. Huo, H. et al. Erastin Disrupts Mitochondrial Permeability Transition Pore (mPTP) and Induces Apoptotic Death of Colorectal Cancer Cells. PLoS One **11**, e0154605 (2016).
630. Neitemeier, S. et al. BID links ferroptosis to mitochondrial cell death pathways. Redox Biol **12**, 558–570 (2017).
631. Dan Dunn, J., Alvarez, L. A., Zhang, X. & Soldati, T. Reactive oxygen species and mitochondria: A nexus of cellular homeostasis. Redox Biol **6**, 472–485 (2015).
632. Paul, B. T., Manz, D. H., Torti, F. M. & Torti, S. V. Mitochondria and Iron: current questions. Expert Rev Hematol **10**, 65–79 (2017).
633. Cosentino, K. & García-Sáez, A. J. Mitochondrial alterations in apoptosis. Chem Phys Lipids **181**, 62–75 (2014).
634. Zhu, S. et al. Ferroptosis: A Novel Mechanism of Artemisinin and its Derivatives in Cancer Therapy. Curr Med Chem **28**, 329–345 (2021).
635. Wu, Y. et al. Ferroptosis in Cancer Treatment: Another Way to Rome. Front Oncol **10**, 571127 (2020).
636. Lee, J. S. et al. Statins enhance efficacy of venetoclax in blood cancers. Sci Transl Med **10**, eaaq1240 (2018).
637. Lin, K. H. et al. Systematic Dissection of the Metabolic-Apoptotic Interface in AML Reveals Heme Biosynthesis to Be a Regulator of Drug Sensitivity. Cell Metab **29**, 1217-1231.e7 (2019).
638. Xu, H.-D. & Qin, Z.-H. Beclin 1, Bcl-2 and Autophagy. Adv Exp Med Biol **1206**, 109–126 (2019).
639. Zhou, F., Yang, Y. & Xing, D. Bcl-2 and Bcl-xL play important roles in the crosstalk between autophagy and apoptosis. FEBS J **278**, 403–413 (2011).
640. Kitada, S. et al. Discovery, characterization, and structure-activity relationships studies of proapoptotic polyphenols targeting B-cell lymphocyte/leukemia-2 proteins. J Med Chem **46**, 4259–4264 (2003).
641. Lian, J. et al. A natural BH3 mimetic induces autophagy in apoptosis-resistant prostate cancer via modulating Bcl-2-Beclin1 interaction at endoplasmic reticulum. Cell Death Differ **18**, 60–71 (2011).
642. Maiuri, M. C. et al. BH3-only proteins and BH3 mimetics induce autophagy by competitively disrupting the interaction between Beclin 1 and Bcl-2/Bcl-X(L). Autophagy **3**, 374–376 (2007).
643. Lee, K. H., Cha, M. & Lee, B. H. Neuroprotective Effect of Antioxidants in the Brain. Int J Mol Sci **21**, E7152 (2020).
644. Weiland, A. et al. Ferroptosis and Its Role in Diverse Brain Diseases. Mol Neurobiol **56**, 4880–4893 (2019).
645. Yan, N. & Zhang, J. Iron Metabolism, Ferroptosis, and the Links With Alzheimer’s Disease. Front Neurosci **13**, 1443 (2019).
646. Zille, M. et al. Neuronal Death After Hemorrhagic Stroke In Vitro and In Vivo Shares Features of Ferroptosis and Necroptosis. Stroke **48**, 1033–1043 (2017).
647. Bao, W.-D. et al. Loss of ferroportin induces memory impairment by promoting ferroptosis in Alzheimer’s disease. Cell Death Differ **28**, 1548–1562 (2021).
648. Dumont, M. et al. Reduction of oxidative stress, amyloid deposition, and memory deficit by manganese superoxide dismutase overexpression in a transgenic mouse model of Alzheimer’s disease. FASEB J **23**, 2459–2466 (2009).
649. Karuppagounder, S. S. et al. N-acetylcysteine targets 5 lipoxygenase-derived, toxic lipids and can synergize with prostaglandin E2 to inhibit ferroptosis and improve outcomes following hemorrhagic stroke in mice. Ann Neurol **84**, 854–872 (2018).
650. Lan, B. et al. Extract of Naotaifang, a compound Chinese herbal medicine, protects neuron ferroptosis induced by acute cerebral ischemia in rats. J Integr Med **18**, 344–350 (2020).
651. Tuo, Q.-Z. et al. Tau-mediated iron export prevents ferroptotic damage after ischemic stroke. Mol Psychiatry **22**, 1520–1530 (2017).
652. Boudou-Rouquette, P. et al. Variability of sorafenib toxicity and exposure over time: a pharmacokinetic/pharmacodynamic analysis. Oncologist **17**, 1204–1212 (2012).
653. Li, Y., Gao, Z.-H. & Qu, X.-J. The adverse effects of sorafenib in patients with advanced cancers. Basic Clin Pharmacol Toxicol **116**, 216–221 (2015).

Acknowledgement

First of all, I would like to thank Prof. Dr. Markus Morrison (Rehm) for giving me the opportunity to work on this project under his wise supervision. With his acute observations and brilliant ideas, he has been a scientific role model to whom I would look up to for becoming a better researcher. His guidance, especially for the writing of the manuscript, has been essential for achieving this ambitious and satisfying goal and for that I am very grateful to him.

Thanks to Dr. Brona Murphy for supervising the project during the time I spent at RCSI. I sincerely appreciate the warm welcome she reserved to me. Her always positive attitude and her encouragement have greatly contributed to the success of my secondment.

A huge thanks goes to Nathalie Peters, an irreplaceable pilar of the Morrison's group and a lovely person I could always count on. Her experience, as well as her constant support, allowed me to solve many practical issues I encountered in these years, smoothening the bumpy journey of my PhD and making my time in the lab always enjoyable.

Many thanks also to Dr. Daniela Stöhr, one of the nicest persons I have ever met. Although very busy, she was the one who always took time to advise me and discuss scientific hypothesis with me. Her help and her kindness have been precious to me. By being such a "colourful" person, she brought joy also in my most difficult times in the lab. I won't forget that!

My appreciation goes also to all the past and present members of the Morrison's group, of the physiology department of RCSI as well as to the GLIOTRAIN people who have all contributed to make these three years an amazing experience, both personally and professionally. I have learned a lot from each of them, we laughed a lot and I am glad I shared this experience with them.

Infine, il più grande ringraziamento va a miei genitori Rita e Antonio che mi hanno sempre supportata con forza, costanza e pazienza, nonostante il dispiacere di avermi lontana. Spero che la mancata quotidianità vissuta insieme possa essere ripagata dall'orgoglio di avermi fatto raggiungere questo traguardo.